Applications of Asymmetric Rowland Geometries in Hard X-ray Spectroscopies

Anthony Joseph Gironda

A dissertation

submitted in partial fulfillment of the

requirements for the degree of

Doctor of Philosophy

University of Washington

2026

Reading Committee:

Gerald T. Seidler, Chair

Guozhong Cao

Brandi Cossairt

Juan Carlos Idrobo

Program Authorized to Offer Degree:

Materials Science and Engineering

University of Washington

Abstract

Applications of Asymmetric Rowland Geometries in Hard X-ray Spectroscopies

Anthony Joseph Gironda

Chair of the Supervisory Committee:

Gerald T. Seidler

Physics

Hard X-ray spectroscopy is widely used to characterize all states of matter in contemporary and relevant materials systems including but not limited to life sciences, catalyst materials, batteries and energy storage materials, pharmaceuticals, nuclear fuel and waste, and fossil fuels. At the core of these spectroscopy techniques is the measurement of X-ray absorption fine structure (XAFS), and the secondary process of X-ray fluorescence.

Both laboratory and synchrotron hard X-ray spectroscopies demand the use of high-resolution spectrometers to analyze scattered or fluorescing photons. In the laboratory, spectrometers are required for the measurement of both XAFS and X-ray emission spectroscopy (XES). At synchrotron light sources, advanced photon-in/photon-out techniques such as high energy resolution fluorescence detection X-ray absorption spectroscopy (HERFD-XAS), resonant inelastic X-ray scattering (RIXS) / resonant XES, and X-ray Raman Scattering (XRS) all require the use of a spectrometer to analyze outgoing photons. Across all of these disciplines, the state-of-the-art for large collection solid angles and point-focusing geometries for efficient

data collection at high resolution rely on the same diffractive optic: the spherically bent crystal analyzer (SBCA).

The employment of SBCAs for high energy resolution photon analysis across this suite of spectroscopy techniques are in the same symmetric geometry. The work within this dissertation details the characterization, commissioning, and application of asymmetric Rowland geometries of SBCAs to XAFS/XES, HERFD, and XRS. I propose that this is an overlooked and underutilized modality for spectrometer design and that it frequently enables improved energy resolution and a massively increased energy range for photon analysis; addressing the two largest shortcomings of SBCAs in conventional symmetric geometries. Most importantly, the use of SBCAs in asymmetric Rowland geometries can drastically reduce the number of unique optics required for a sufficient analysis energy range.

I detail the applications of this geometry in the design and construction of three separate spectrometers (laboratory XAFS/XES, synchrotron HERFD, synchrotron XRS), and in all three cases we find that it is lowering the resource barrier required for these techniques. The relevance of these developments for materials science research is substantial, and some representative applications are discussed and presented.

Dedications

With deep gratitude I dedicate this work to my father James, mother Jenine, and sister Rosemarie. Their support and faith in me is unwavering and I would not have completed this without them.

Acknowledgements

I'd like to thank Professor Gerald Seidler for his guidance and advisement the past 4.5 years. Our working relationship began with an impromptu email and a quick handshake, and I've been grateful for the course it has set me on ever since. I'd also like to thank Dr. Shelly Kelly, for overseeing my work and development at the Advanced Photon Source in my final year of study. Lastly, I owe a large heartfelt thank you to past and present lab members of the Seidler group: Samantha Tetef, Diwash Dhakal, Jared Abramson, Charles Cardot, and Yeu Chen.

Table of Contents

List of Figures

Chapter 5. Asymmetric Rowland Circle Geometries for Spherically Bent Crystal Analyzers in Laboratory and Synchrotron Applications

Chapter 8. Democratization of HERFD-XAS: High-Throughput Multi-Edge HERFD over 5-20 keV With a Single Optic Using Asymmetric Rowland Geometries

List of Tables

Chapter 1. Measuring XAFS

X-ray absorption fine structure (XAFS) is a powerful, chemical specific spectroscopy technique widely applied to solid, liquid, and solution chemistry in fields such as geochemistry, catalysis, and energy materials. This chapter provides a phenomenological overview of XAFS, basic theory, measurement, and concludes with some applications. Comprehensive reviews and textbooks are available from Bunker[1], Calvin[2], de Groot[3,4], Glatzel and Bergmann[5], and others[6,7].

1. Phenomenology

X-ray absorption spectroscopy (XAS) represents a broad suite of resonant and non-resonant techniques concerned with measuring the absorption coefficient, μ, as a function of photon energy, E. The Beer-Lambert law describes the attenuation of radiation intensity through a medium, as

$$I = I_0 e^{-\mu t} \quad (1)$$

where I_0 is the incident intensity, t is the sample thickness, and I is the transmitted intensity. Thus, a simple XAS experiment measures μ(E) by monitoring the incident and transmitted X-ray intensity through a sample over a range of photon energies. At most energies μ(E) changes smoothly and is roughly proportional to $1/E^3$, but at certain energies μ(E) rapidly increases – these so-called absorption edges are shown in Figure 1 for two different elements. The energy positions of the absorption edges are element specific and depend on the atomic number, Z, and they correspond to the binding energies of different electronic shells.

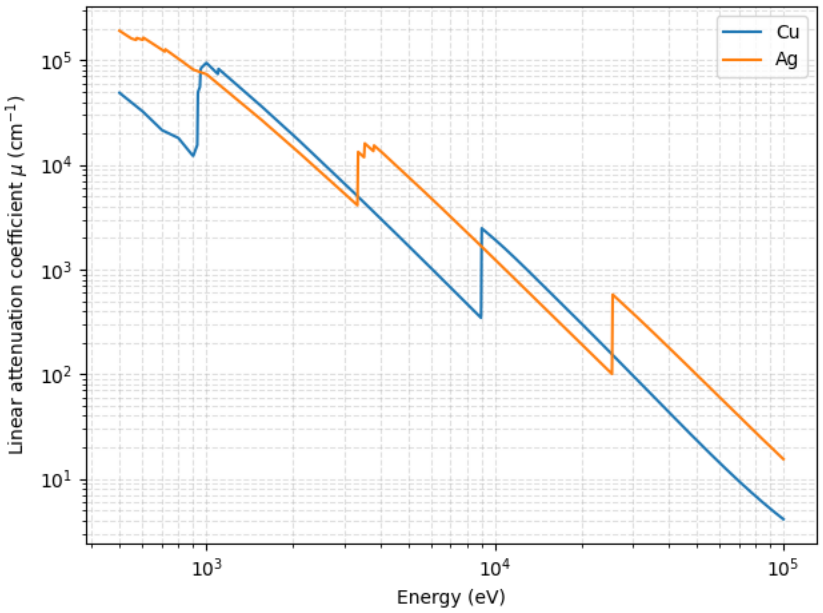

Figure 1. X-ray absorption coefficient, μ(E), of Cu and Ag on a log-log scale. The sudden increases in absorbance are absorption edges.

A closer examination of an absorption edge reveals additional structure. The normalized Fe *K*-edge absorption spectrum of Fe_2O_3 is shown in Figure 2. Note that we use the spectroscopic convention that *K*, *L*, and *M* edges refer to principal quantum numbers of 1, 2, and 3, respectively. The pre-edge features, white line peak, and oscillations extending several hundred eVs above the edge are referred to as X-ray absorption fine structure (XAFS). The XAFS can be divided into two regimes: X-ray absorption near edge structure (XANES) and extended X-ray absorption fine structure (EXAFS). XANES is the pre-edge features and white line of the absorption edge and can report oxidation state and local coordination (tetrahedral, octahedral, e.g.) of the probed atom. EXAFS are the oscillations extending above the edge and can report bond lengths, coordination number, and nearest neighbors of the absorbing atom.

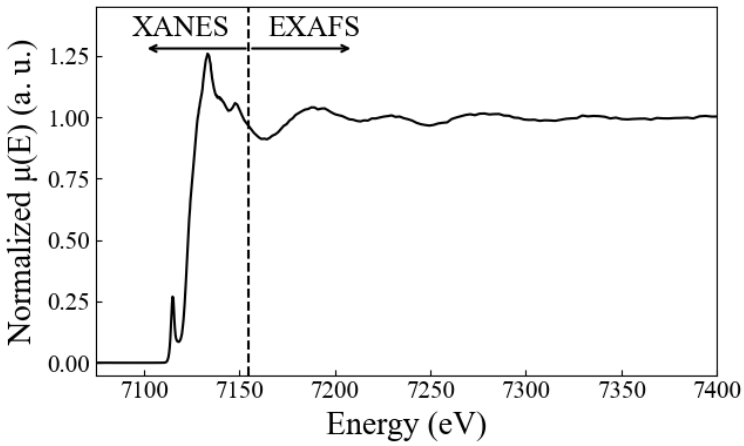

Figure 2. Edge-step normalized and background subtracted μ(E) of the Fe K-edge. The XANES and EXAFS regimes of the absorption edge structure are annotated.

The features and modulations of μ(E) in XANES and EXAFS result from the absorption event of the photon in the electronic structure of the probed atom. The corresponding absorption and excitation of K-edge XAFS is shown in Figure 3. Consider the Fe K-edge shown in Figure 2 as the incident photon energy is scanned. When the incident photon energy (E) is below the Fe 1*s* electron binding energy, μ(E) smoothly varies proportional to $1/E^3$. At incident energies at the K-shell binding energy, the 1*s* electron is excited above the Fermi level (E_{fermi}) into unoccupied electronic states of the valence band; this is shown in Figure 3 (left) and results in XANES. At incident energies several hundred eV's above the K-shell binding energy, the 1s electron is liberated and a photoelectron originating at the absorbing atom scatters around its nearest neighbors; this is shown in Figure 4 (right) and results in EXAFS.

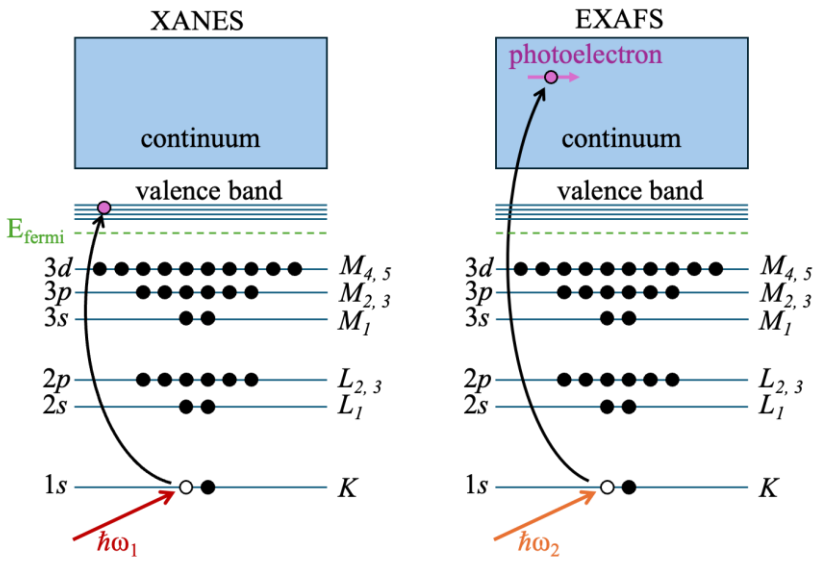

Figure 3. Electronic structure diagrams and photon absorption events resulting in **(Left)** XANES and **(Right)** EXAFS, depending on the energy of the incident photon, ħω.

Following the ideas of Stern et al.[8], the modulation of μ(E) above an absorption edge is commonly described as a result of the excited photoelectron originating at the absorbing atom scattering around its neighbors. As discussed, these EXAFS oscillations in μ(E) encode information on nearest neighbors and bond lengths around the absorbing atom. Treatment of the surrounding atomic array around the emitted photoelectron as a lattice of point scatterers allowed theory development to describe the total photoelectron wave function and the isolated oscillatory part, χ(k), in the so-called EXAFS equation[8] as

$$\chi(k) = \sum_j \frac{N_j f_j(k) e^{-2k^2\sigma_j^2}}{kR_j^2} \sin\left(2kR_j + \delta_j(k)\right) \qquad (2)$$

where *f(k)* is the scattering amplitude, *δ(k)* is the phase-shift, N is the number of neighboring atoms, *R* is the distance to the neighboring atom, and σ^2 is the mean-square-displacement in the bond distance *R*. The subscript *j* represents a coordination shell of identical atoms at

approximately the same distance from the absorbing atom. Thus, χ(k) is the summation of contributions from each scattering atom type in each coordination shell. The wave number of the photoelectron, k, in units of 1/ Å, is defined as

$$k = \sqrt{\frac{2m(E - E_0)}{\hbar^2}} \tag{3}$$

where E_0 is the absorption edge energy, m is the electron mass, and ħ is Planck's constant.

XAFS, and by extension EXAFS, is a local probe on the order of 1-5 Å around the absorbing atoms. Because of this, XAFS is suitable for the study of both crystalline and amorphous materials.

2. Detection Modes

There are several detection channels for monitoring μ(E). Depending on the detection or enforced by the binding energy of the absorption edge, XAFS experiments may be conducted in ambient conditions, He environments, or with entire spectrometers under ultra-high vacuum conditions. The two primary detection methods in the scope of this chapter and later discussed in the Instrumentation section are called transmission mode and total fluorescence yield.

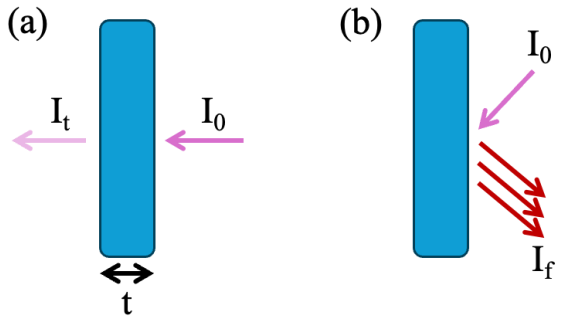

Figure 4. (a) Transmission mode and (b) fluorescence mode detection of XAFS

In transmission mode, the transmitted intensity (I_t) through a sample of uniform thickness (t) is monitored with respect to the incident intensity (I_0) as a function of photon energy. A diagram of transmission mode is shown in Figure 4 (a). Transmission mode requires homogeneous samples on the scale of the beam size, variations in sample density or pinholes result in so-called thickness effects and non-linearity[1,6]. Transmission measurements also require samples of 1 – 2 absorption lengths thick at the edge of interest for statistically optimal detection of I_t. Thus, transmission mode measurements are standard for hard X-ray spectroscopy of 3*d* *K*-edges and 5*d* *L*-edges where attenuation lengths are on the order of microns. For soft absorption edges where the attenuation lengths are less than a μm, transmission mode XAFS is typically not suitable. For transmission mode XAFS with reasonable sample thickness, the energy dependence of μ(E) is given by:

$$\mu(E) = \ln\left(\frac{I_0(E)}{I_t(E)}\right). \quad (4)$$

The fluorescence decay of the core-hole formed in a photon absorption event also presents a detection channel to monitor X-ray absorption. In the example of K-shell absorption, characteristic K_α and K_β fluorescence can occur as the electrons relax from the excited state and the intensity of this fluorescence is proportional to the X-ray absorption as a function of incident energy. This method is known as total fluorescence yield detection (TFY) and a diagram is shown in Figure 4 (b). TFY is suitable for dilute samples as non-linear effects (so-called "self-absorption") occur in concentrated samples[1,2,6]. For fluorescence mode XAFS of dilute samples, the energy dependence of μ(E) is proportional to:

$$\mu(E) \propto {I_f(E)}\Big/{I_0(E)}. \quad (5)$$

Other detection methods include total electron yield and Auger electron yield, both of which are surface sensitive and where the latter requires vacuum environments; these are more commonly used for thin films and surface science[9,10]. Partial fluorescence yield (PFY) detection XAFS, particularly high energy resolution fluorescence detection (HERFD), and non-resonant X-ray Raman Scattering (XRS) will be discussed in the following two chapters. The scope of the present chapter is limited to transmission and TFY XAFS.

3. Light Sources and Measurement

The measurement of XAFS requires a suitable X-ray source. Figure 5 shows the photon flux and spatial coherence of several X-ray light sources. Here, we focus on measurement of XAFS at synchrotron light sources and the measurement of XAFS in the laboratory with X-ray tubes. Other light source facilities such as X-ray free electron lasers are discussed elsewhere[11].

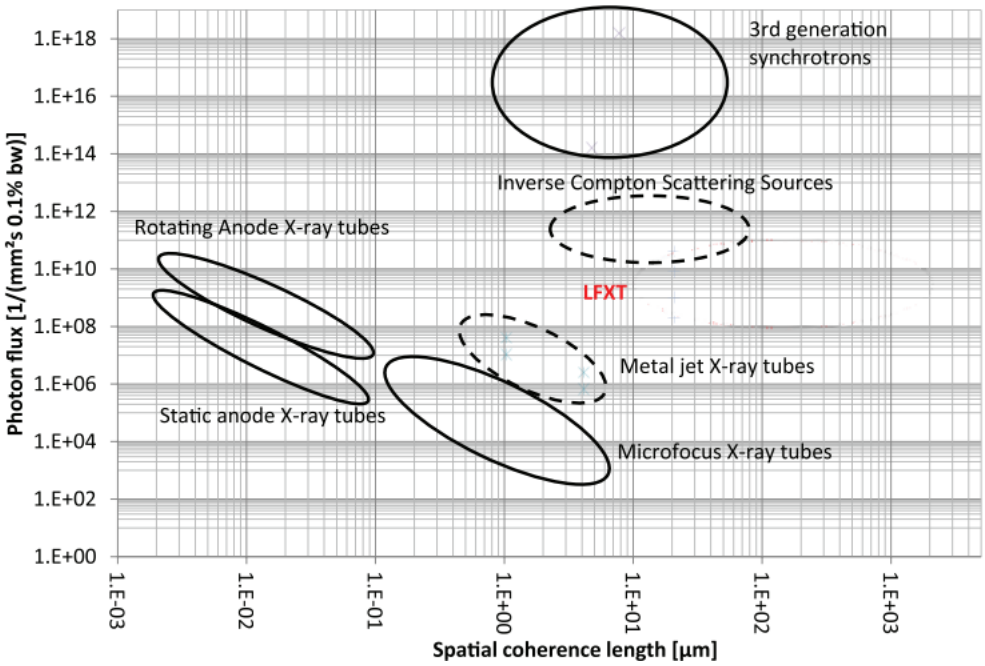

Figure 5. Photon flux and spatial coherence of different light sources[12].

a. Synchrotron

Synchrotron light sources accelerate electrons in a ring, and deviations to the electron's path can produce large amounts of hard X-ray radiation; this is accomplished with a bending magnet or undulator insertion device, for example. One synchrotron can support many insertion devices and thus many beamlines (X-ray spectroscopy, imaging, diffraction) exist at such a facility and operate simultaneously. 3rd generation synchrotron light sources are designed for low emittance[13]. A map of most 3rd generation hard X-ray synchrotron light sources is shown below.

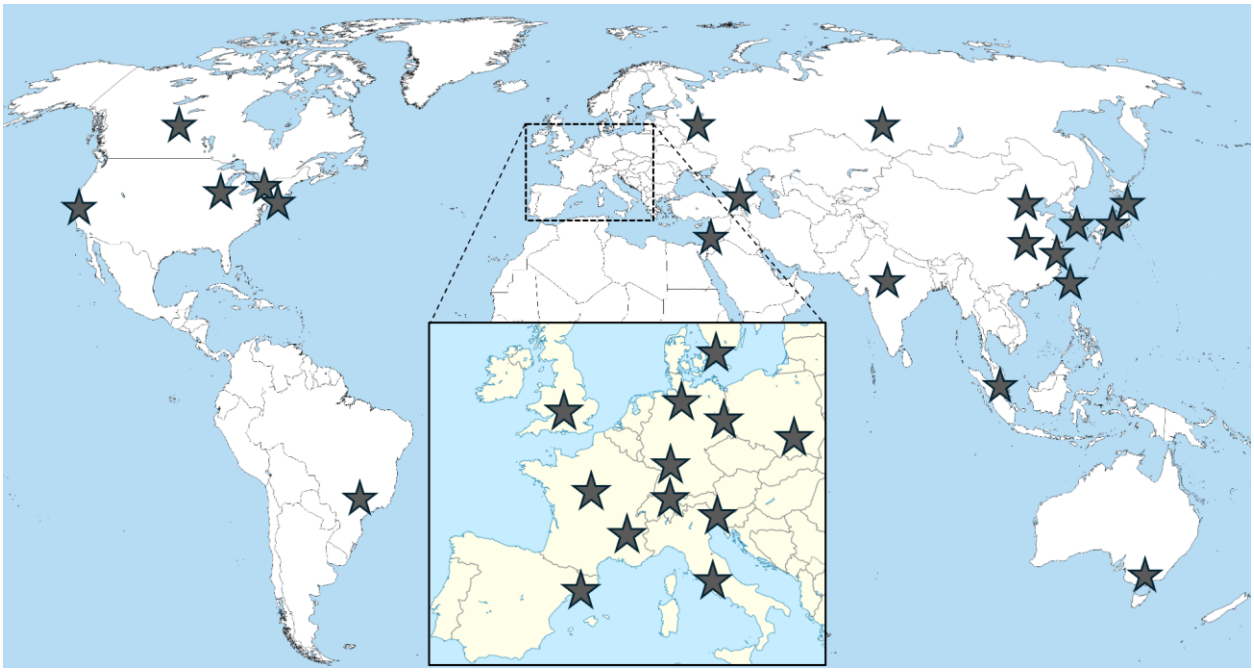

Figure 6. Map of most hard X-ray synchrotron light sources around the world.

Measurement of XAFS at the synchrotron is routine. Spectroscopy beamlines are equipped with a monochromator downstream of the insertion device or bending magnet. The result is a highly brilliant, monochromatically tunable X-ray source often ranging from ~4 – ~40 keV. XAFS measurements simply require scanning the monochromator over the absorption edge energy of interest. Signal intensities are typically monitored upstream and downstream of the

sample by ion chambers and fluorescence intensity monitored with a photon counting or spectroscopic detector[2].

The high flux of synchrotrons also lends the facilities for advanced photon-in/photon-out spectroscopy techniques. These are discussed in Chapter 3 and Chapter 4.

b. Laboratory

Laboratory XAFS is undergoing a so-called "rebirth"; XAFS begin in the laboratory, migrated to the synchrotrons in the 1970s, and is now a returning laboratory capability over the past two decades, enabled by improvements to bent crystal optics, X-ray tubes, and detectors. A historical perspective on laboratory XAFS is reported by Malzer et al[14].

The light source for laboratory XAFS measurements is an X-ray tube. A power spectrum from the a 50 keV X-ray tube is shown below, where characteristic emission lines from the anode material provide a flux of 10^8, and the underlying broad lower intensity spectrum is bremsstrahlung "braking" radiation.

We note the magnitudes different intensities from X-ray tubes and synchrotron light sources. Even X-ray tubes with improved line focus[12], rotating anodes[15,16], and liquid metal anodes[17–19] are ~6 orders of magnitude less than synchrotron fluxes. Furthermore, X-ray tubes have no monochromation – thus laboratory measurements require an X-ray spectrometer to analyze the spectrum at high energy resolution.

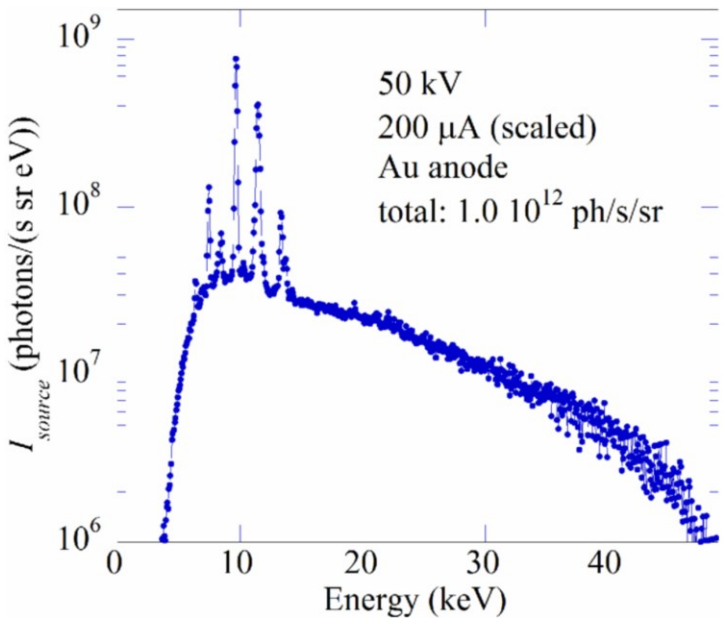

Figure 7. Broad polychromatic X-ray power spectrum, $I_0(E)$, from an electron-impact laboratory X-ray source. The smooth lower intensity "background" is bremsstrahlung and the intense lines are characteristic emission from the anode (Cu K_α, for example)[20].

Many modern laboratory X-ray spectrometers have been developed the last 20 years[20–27]. A review of laboratory based X-ray spectroscopies is provided by Zimmermann et al[28]. Here we limit the discussion to point focusing spectrometers – an in depth review of both focusing and dispersive spectrometers is found at the end of Chapter 4.

The operating principle of a laboratory XAFS spectrometer is described as the following. The energy spectrum from the X-ray tube source is monochromated, typically by a spherically bent crystal analyzer (SBCA). The SBCA is a diffractive X-ray optic with a bent profile such that it monochromates a narrow energy width (~1 eV) and provides nearly point focusing. The SBCA defines a focusing circle, the Rowland circle, where the X-ray source and detector are nominally arranged. A high resolution spectrum is collected by scanning the angle of the SBCA

while keeping the source and detector on circle. XAFS is measured by scanning the laboratory monochromator over the absorption edge of interest. A schematic of the laboratory monochromator for measuring XAFS is shown below. A larger discussion on bent analyzers and Rowland circle geometry is found in Chapter 2.

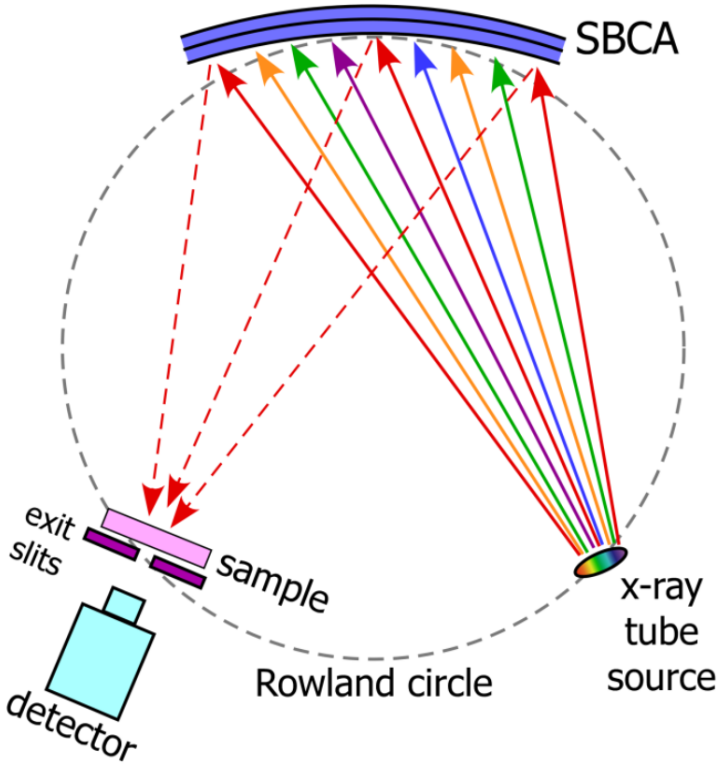

Figure 8. Schematic of the typical laboratory XAFS monochromator/spectrometer[20].

4. Applications

a. Assessing oxidation state of ex situ battery cathode materials

Vanadium pentoxide hydrate (VOH) is a promising Na^+ cathode material in the broader class of layered vanadium oxides[29–31]. However, the interatomic layer spacing of V_2O_5 is small in contrast to the large Na^+ ions. The interatomic spacing is tuned by hydrating V_2O_5 where water molecules increase the layer spacing. Strategies to enhance electrochemical performance included pre-intercalating the layers with large non-conducting ions such as Y^{3+} or K^+, the latter of which forms a unique crystalline phase (KVOH) in addition to intercalation[32]. The following study was part of broader work aimed to examine the structural integrity and cycling stability of KVOH when used as sodium ion battery cathodes[32]. XAFS was used to quantify the changes in formal oxidation state of the KVOH phase amongst several reference compounds by examined edge shifts in the V K-edge XANES.

Vanadium oxidation state of bulk samples and reference materials were characterized by XANES using a high-resolution laboratory-based hard x-ray monochromator. XANES spectra of samples and references are shown below in Figure 9 (left). The strong agreement of VOH, KVOH, and KVOHS indicate similar local chemistry, symmetry, and oxidation state of V in the bulk. However, here the minor shifts in the rising edge (Figure 9 (right)) were used to estimate the differences in formal valence of VOH, KVOH, and KVOHS with respect to known valence references. This is shown in Figure 11 the oxidation states calculated in Table 1, with inferred oxidation states of 4.82 ± 0.06, 4.84 ± 0.06, and 4.92 ± 0.06 for VOH, KVOHS, and KVOH respectively, showing subtle (if any) differences in V oxidation state in the bulk.

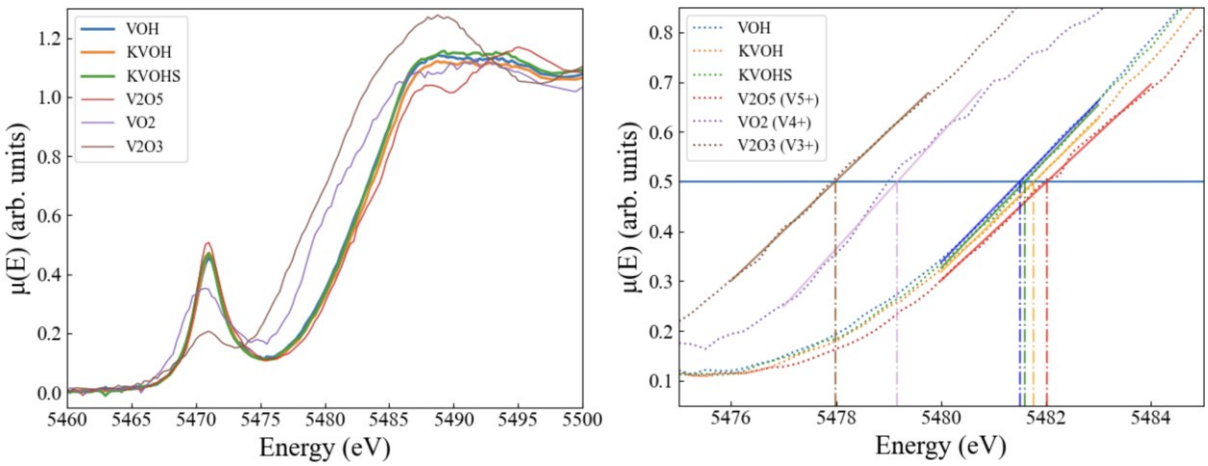

Figure 9. **(Left)** Normalized K-edge XANES spectra of V samples and reference material. Pre-edge features indicate similar local atomic coordination as V_2O_5 (V^{5+}), and shifts in the sample's rising edge indicate oxidation states of samples just below 5+. **(Right)** Linear regime and fits of the rising K-edge XANES. The energies corresponding to a normalized absorption of 0.5 were used to calculate oxidation state of V.

Table 1. Calculated oxidation states from the shifts in the rising K-edge.

Sample	E(μ) = 0.5	Inferred ox. state	Error
V_2O_3	5477.98	3	N/A
VO_2	5479.17	4	N/A
VOH	5481.50	4.82	±0.06
KVOHS	5481.56	4.84	±0.06
KVOH	5481.77	4.92	±0.06
V_2O_5	5482.00	5	N/A

b. Operando XANES of Ni_2P Nanoparticle Catalyst Corrosion

Earth-abundant electrocatalysts are a promising avenue for reducing greenhouse gas emissions in the manufacture of commodity petrochemicals[33–36]. Ni_2P is a promising earth-abundant catalyst that has been demonstrated for key reactions such as hydrogen evolution[37–40]. However, Ni_2P is susceptible to oxidation and corrosion; characterizing the instability of the nanoparticle and its degradation mechanisms is key before any scaling to industrialization. Here, a laboratory X-ray spectrometer was used with a custom x-ray transmissive electrochemical cell to enable *operando* Ni K-edge XANES measurements[41].

The application of XAFS enabled the measurement of several quantities during operation. First, the magnitude of the absorption edge (μ_0) is a a measure of the amount of absorbing Ni atoms in the X-ray beam. This was used as a tool to assess Ni dissolution during the corrosion of the cell at different potentials. Second, the collection of several reference XAFS spectra of relevant compounds and Ni valence allowed linear combination fitting to determine the Ni_2P electrode phase evolution as the cell was cycled, shown in Figure 10. The changing Ni *K*-edge XAFS signal during operation is shown in Figure 11.

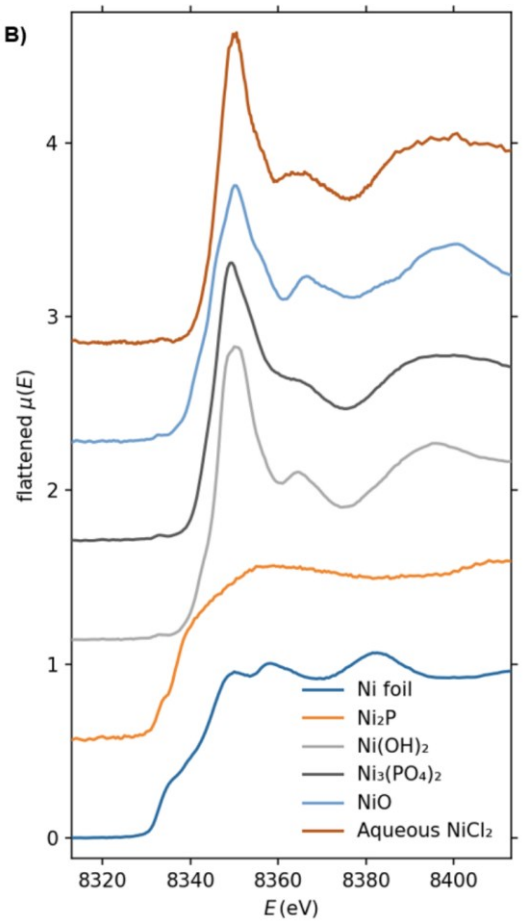

Figure 10. Ni *K*-edge XAFS of relevant reference spectra used for linear combination fitting and phase identification of the *operando* cell[41].

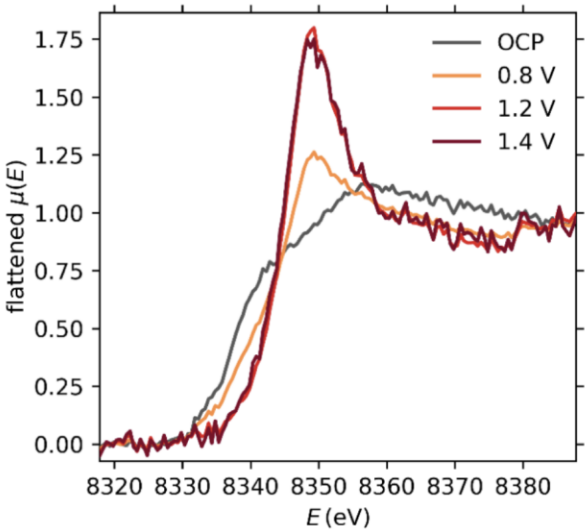

Figure 11. Ni *K*-edge XAFS of the Ni_2P electrode at different cell potentials[41]

5. References

1 G. Bunker, *Introduction to XAFS: a practical guide to X-ray absorption fine structure spectroscopy*, University Press, Cambridge, 1st ed., 2010.
2 S. Calvin, *XAFS for everyone*, CRC Press, Boca Raton, FL, Second edition., 2025.
3 F. de Groot and A. Kotani, *Core Level Spectroscopy of Solids*, CRC Press, Boca Raton, 2008.
4 F. de Groot, *Chem. Rev.*, 2001, **101**, 1779–1808.
5 P. Glatzel and U. Bergmann, *Coord. Chem. Rev.*, 2005, **249**, 65–95.
6 M. Newville, in *Spectroscopic Methods in Mineralology and Materials Sciences*, eds. G. S. Henderson, D. R. Neuville and R. T. Downs, Mineralogical Soc Amer & Geochemical Soc, Chantilly, 2014, vol. 78, pp. 33-+.
7 G. S. Henderson, F. M. F. de Groot and B. J. A. Moulton, in *Spectroscopic Methods in Mineralology and Materials Sciences*, eds. G. S. Henderson, D. R. Neuville and R. T. Downs, Mineralogical Soc Amer & Geochemical Soc, Chantilly, 2014, vol. 78, pp. 75-+.
8 D. Sayers, E. Stern and F. Lytle, *Phys. Rev. Lett.*, 1971, **27**, 1204-.
9 A. Erbil, G. S. Cargill III, R. Frahm and R. F. Boehme, *Phys. Rev. B*, 1988, **37**, 2450–2464.
10 C. T. Chantler, G. Bunker, P. D'Angelo and S. Diaz-Moreno, *Nat. Rev. Method. Prim.*, 2024, **4**, 89.
11 C. Pellegrini, *Eur. Phys. J. H*, 2012, **37**, 659–708.
12 S. Bartzsch and U. Oelfke, *Phys. Med. Biol.*, 2017, **62**, 8600.
13 C. Kunz, *J. Phys.-Condes. Matter*, 2001, **13**, 7499–7510.
14 W. Malzer, C. Schlesiger and B. Kanngiesser, *Spectroc. Acta Pt. B-Atom. Spectr.*, 2021, **177**, 106101.
15 P. Schardt, J. Deuringer, J. Freudenberger, E. Hell, W. Knüpfer, D. Mattern and M. Schild, *Med. Phys.*, 2004, **31**, 2699–2706.
16 T. Taguchi, J. Harada, A. Kiku, K. Tohji and K. Shinoda, *J. Synchrot. Radiat.*, 2001, **8**, 363–365.
17 G. Harding, A. Thran and B. David, *Radiat. Phys. Chem.*, 2003, **67**, 7–14.
18 O. Hemberg, M. Otendal and H. M. Hertz, *Appl. Phys. Lett.*, 2003, **83**, 1483–1485.
19 O. Hemberg, M. Otendal and H. M. Hertz, *Opt. Eng.*, 2004, **43**, 1682–1688.
20 G. T. Seidler, D. R. Mortensen, A. J. Remesnik, J. I. Pacold, N. A. Ball, N. Barry, M. Styczinski and O. R. Hoidn, *Rev. Sci. Instrum.*, 2014, **85**, 113906.
21 W. Blachucki, J. Czapla-Masztafiak, J. Sa and J. Szlachetko, *J. Anal. At. Spectrom.*, 2019, **34**, 1409–1415.
22 A. S. Ditter, E. P. Jahrman, L. R. Bradshaw, X. Xia, P. J. Pauzauskie and G. T. Seidler, *J. Synchrot. Radiat.*, 2019, **26**, 2086–2093.
23 E. P. Jahrman, W. M. Holden, A. S. Ditter, D. R. Mortensen, G. T. Seidler, T. T. Fister, S. A. Kozimor, L. F. J. Piper, J. Rana, N. C. Hyatt and M. C. Stennett, *Rev. Sci. Instrum.*, 2019, **90**, 024106.
24 J. Holburg, M. Mueller, K. Mann, P. Wild, K. Eusterhues and J. Thieme, *Anal. Chem.*, 2022, **94**, 3510–3516.
25 R. Bes, T. Ahopelto, A.-P. Honkanen, S. Huotari, G. Leinders, J. Pakarinen and K. Kvashnina, *J. Nucl. Mater.*, 2018, **507**, 50–53.
26 S. Praetz, M. Johansen, D. Kober, M. Tesic, C. Schlesiger, D. B. Ravnsbaek and B. Kanngiesser, *J. Anal. At. Spectrom.*, 2025, **40**, 2447–2461.

27 R. Fanselow, M. Sobstel, W. Blachucki and J. Szlachetko, *X-Ray Spectrom.*, 2023, **52**, 247–253.
28 P. Zimmermann, S. Peredkov, P. M. Abdala, S. DeBeer, M. Tromp, C. Mueller and J. A. van Bokhoven, *Coord. Chem. Rev.*, 2020, **423**, 213466.
29 C. Liu, Z. Neale, J. Zheng, X. Jia, J. Huang, M. Yan, M. Tian, M. Wang, J. Yang and G. Cao, *Energy Environ. Sci.*, 2019, **12**, 2273–2285.
30 Q. Wei, J. Liu, W. Feng, J. Sheng, X. Tian, L. He, Q. An and L. Mai, *J. Mater. Chem. A*, 2015, **3**, 8070–8075.
31 M. Tian, C. Liu, J. Zheng, X. Jia, E. P. Jahrman, G. T. Seidler, D. Long, M. Atif, M. Alsalhi and G. Cao, *Energy Storage Mater.*, 2020, **29**, 9–16.
32 Y. Lin, H. N. Ramesh, A. J. Gironda, L. Lin, X. Jia, Y. Guo, G. T. Seidler, T. Hu, U. Lassi and G. Cao, *Journal of Power Sources*, 2025, **653**, 237766.
33 I. Roger, M. A. Shipman and M. D. Symes, *Nat. Rev. Chem.*, 2017, **1**, 0003.
34 B. M. Hunter, H. B. Gray and A. M. Muller, *Chem. Rev.*, 2016, **116**, 14120–14136.
35 X. Li, J. Yu, J. Low, Y. Fang, J. Xiao and X. Chen, *J. Mater. Chem. A*, 2015, **3**, 2485–2534.
36 J. Liu, Y. Liu, N. Liu, Y. Han, X. Zhang, H. Huang, Y. Lifshitz, S.-T. Lee, J. Zhong and Z. Kang, *Science*, 2015, **347**, 970–974.
37 L. Wu, L. Yu, F. Zhang, B. McElhenny, D. Luo, A. Karim, S. Chen and Z. Ren, *Adv. Funct. Mater.*, 2021, **31**, 2006484.
38 E. J. Popczun, J. R. McKone, C. G. Read, A. J. Biacchi, A. M. Wiltrout, N. S. Lewis and R. E. Schaak, *J. Am. Chem. Soc.*, 2013, **135**, 9267–9270.
39 L.-A. Stern, L. Feng, F. Song and X. Hu, *Energy Environ. Sci.*, 2015, **8**, 2347–2351.
40 S. Z. Tasker, E. A. Standley and T. F. Jamison, *Nature*, 2014, **509**, 299–309.
41 R. A. Rivera-Maldonado, A. J. Gironda, A. Varughese, D.-Y. Kuo, H. Nguyen, D. Dean-Hill, J. E. Abramson, G. T. Seidler and B. M. Cossairt, *J. Phys. Chem. C*, 2025, **129**, 1165–1172.

Chapter 2. Bent Diffractive Optics and the Rowland Circle

1. Introduction

The operation of both laboratory and synchrotron hard X-ray spectrometers rely on either a dispersive or focusing optic element that "analyzes" radiation. For dispersive optics, this results in a spatial dispersion of analyzed energies on an area sensitive detector and enables a spectrum to be captured in a single shot, shown in Figure 1 (a). For focusing optics, this results in point-focusing and high resolution monochromation of radiation along a focusing circle, which is then scanned to collect a spectrum, shown in Figure 1 (b). The selection of an analyzer, (including its material, d-spacing, diameter, and surface profile) fundamentally determines the spectrometer design, energy range, and overall spatial and energy resolution. This chapter surveys the manufacture and use of Johann analyzers in Rowland geometry and the intrinsic, geometric, and source size contributions to the overall energy resolution of a spectrometer.

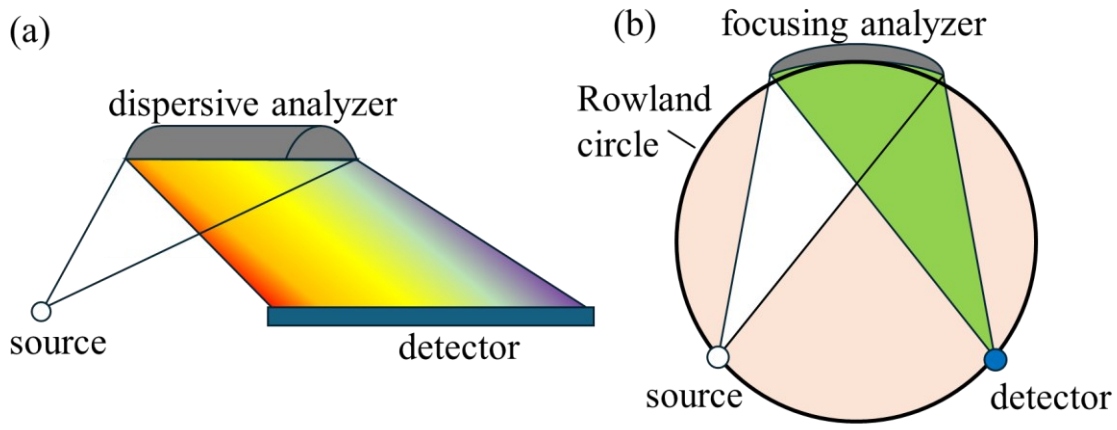

Figure 1. **(a)** Schematic of a dispersive crystal analyzer spatially separating a polychromatic point source across an area detector. **(b)** Schematic of a point-focusing crystal analyzer monochromatizing a polychromatic point source and focusing it onto a detector.

2. Diffraction

Hard X-ray absorption edges and emission lines studied typically range from 5 – 20 keV. Diffractive X-ray optics for photon analyses must have appropriate *d*-spacings for this energy range. In this regime, *d*-spacings on the order of atomic distances are required and perfect single crystals are typically used; monochromation is achieved by single crystal diffraction of the incident radiation and energy selected via Bragg's law.

a. Diffraction geometries for perfect single crystals

Diffraction scattering geometries can be transmissive through the crystal (Laue geometry) or reflective to the crystal's surface (Bragg geometry). Figure 2 (a) shows the symmetric Laue diffraction geometry of a perfect single crystal. The Bragg angle, θ_B, is the angle between the incident ray and diffracting planes and is the same angle for the exiting ray. The diffracting plane family with lattice spacing *d* is denoted by reciprocal lattice vector $\mathbf{G}_0$ and the crystal's surface

normal unit vector is shown as $\hat{\mathbf{n}}$. In a symmetric Laue geometry, these vectors are perpendicular and so the diffracting lattice planes are perpendicular to the crystal's surface. A similar depiction and description is shown in Figure 2 (b) for a symmetric Bragg geometry, note that $\mathbf{G}_0$ and $\hat{\mathbf{n}}$ are now parallel in the symmetric reflection geometry.

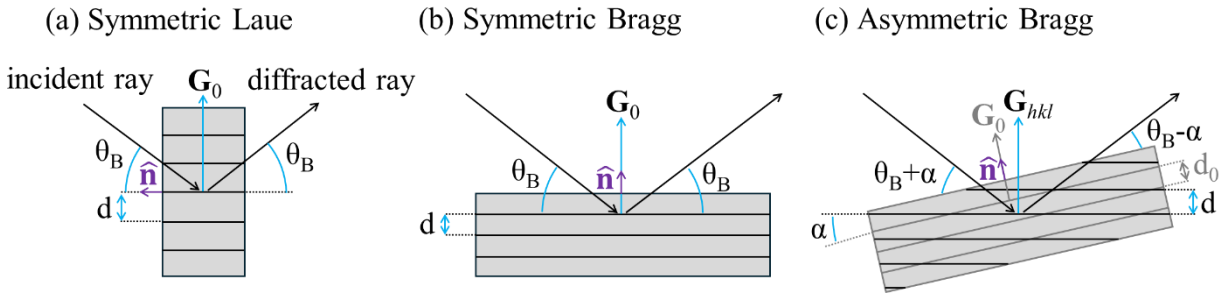

Figure 2. Diffraction schematic of a single crystal for **(a)** symmetric Laue transmission geometry, **(b)** symmetric Bragg reflection geometry and **(c)** asymmetric Bragg reflection geometry.

Similarly, asymmetric diffraction geometries are also allowed, shown for the Bragg geometry in Figure 2 (c) for a perfect crystal. In the asymmetric case, the diffracting plane family is now denoted as $\mathbf{G}_{hkl}$ which differs from the nominally surface coincident plane family $\mathbf{G}_0$. Notably these different plane families have different *d*-spacings, shown as d and d_0, respectively. The angle between these vectors/plane families is referred to as the asymmetry angle, α, and calculated by

$$\alpha = \cos^{-1}\left(\frac{\boldsymbol{G_0} \cdot \boldsymbol{G_{hkl}}}{\|\boldsymbol{G_0}\|\|\boldsymbol{G_{hkl}}\|}\right) \quad (1)$$

where *hkl* is the relevant crystal plane family. Note θ_B is still the angle between the incident ray and diffracting planes. In the case of asymmetric diffraction (Figure 2 (c)), the angle between the incident or diffracted ray with respect to the crystal's surface is $\theta_B + \alpha$ and $\theta_B - \alpha$, respectively.

b. Bragg's Law

Regardless of diffraction geometry, Bragg's law describes the conditions for the incident ray to be diffracted, given by

$$n\lambda = 2d \sin \theta_B \tag{2}$$

where n is the diffraction order (harmonic), λ is the diffracted wavelength, d is the interatomic distance between the diffracting planes, and θ_B is the Bragg angle in degrees, defined in Figure 2; noting that this assumes an index of refraction of unity and is only approximate – a more precise model requires dynamical diffraction theory. It is convenient to express Eq. (2) in terms of photon energy as

$$E\ (eV) = \frac{12398.5\ \text{eV} * \text{Å}}{2d \sin \theta_B} \tag{3}$$

where E is the diffracted photon energy and where the *d*-spacing is in units of Å. Perfect single crystals for hard X-ray optics are typically wafers of Si or Ge, both having the diamond face centered cubic crystal structure. The *d*-spacings of any Si or Ge plane family is given by

$$d_{Si}\ (\text{Å}) = \frac{5.4309\ \text{Å}}{\sqrt{h^2 + k^2 + l^2}} \tag{4}$$

$$d_{Ge}\ (\text{Å}) = \frac{5.6574\ \text{Å}}{\sqrt{h^2 + k^2 + l^2}} \tag{5}$$

where *h*, *k*, and *l* are the Miller indices of the diffracting plane. The numerator values are the lattice constants (a_0) of Si and Ge, respectively[1]. It is useful to define the diffracted energy at

backscatter, where $\theta_B = 90^o$. This value is the minimum photon energy that will diffract from a given crystal plane and is calculated by

$$E_0\ (eV) = \frac{12398.5\ \text{eV} * \text{Å}}{2d} \tag{6}$$

where E_0 is the analyzed energy at backscatter. A final useful identity for the spectroscopist is defining Bragg's law in terms of E_0 as

$$E(\theta_B) = \frac{E_0}{\sin \theta_B}. \tag{7}$$

By inspecting equations (3 – 7), some conclusions can already be drawn on spectrometer design. First, the meaningful d-spacing range for hard X-ray photon analysis from 5 – 20 keV is 1.2 – 0.3 Å and necessitates diffraction from crystalline planes. Second, over the typical scanning spectrometer operating range ($65^o \leq \theta_B \leq 85^o$) in the energy range of 5 –10 keV, a single reflection (*hkl*) can reliably cover 500 – 1000 eV; some examples are tabulated in Table 1. Third, sufficient photon energy analysis coverage from 5 – 20 keV requires many different reflections.

Table 1. Tabulated energy ranges for arbitrary E_0 values in the hard X-ray spectroscopy regime.

E_0 (eV)	$E(\theta_B=85^o)$	$E(\theta_B=65^o)$	Range (eV)
5000	5019	5538	519
7500	7529	8307	778
10000	10038	11076	1038
15000	15057	16614	1557
20000	20076	22152	2075

c. Structure Factor and Scattering Intensity

I review here some fundamentals of X-ray diffraction from single atoms and crystalline unit cells with the goal of providing context for X-ray analyzer optics and their function. A comprehensive treatment of kinematic and dynamical X-ray diffraction theory is available from Kittel[2], Als-Nielsen[3], or Cullity[4], as well as others.

The intensity of a given reflection (*hkl*) is dependent on its atomic and structure form factors. The atomic form factor, f, is a measure of the scattering intensity from an isolated atom and given by

$$f(\boldsymbol{q}) = \int \rho_e(\boldsymbol{r}) e^{-i\boldsymbol{q}\cdot\boldsymbol{r}} d\boldsymbol{r} \tag{8}$$

where $\rho_e(\mathbf{r})$ is the charge density of the scattering atom and $\boldsymbol{q}$ is the scattering vector (or momentum transfer) integrated over the volume $d\boldsymbol{r}$ the scattering electrons occupy[3]. The atomic form factor decreases with increasing q, thus the intensity of diffraction decreases with either decreasing θ_B or increasing photon energy. As a result, diffractive Bragg optics become steadily less efficient at higher photon energies, posing technical challenges for X-ray spectroscopy above 10 keV.

The structure factor, F, is the integration of the total charge distribution of all the atoms in the unit cell, given by

$$F(\boldsymbol{q}) = \int \rho_e(\boldsymbol{r}) e^{-i\boldsymbol{q}\cdot\boldsymbol{r}} d\boldsymbol{r} \tag{9}$$

where $\rho_e(\mathbf{r})$ is now the charge density of the entire unit cell[3]. For a unit cell composed of N atoms, the integration can be decomposed to a summation of individual form factors, f_n, of each atom and expressed as

$$F(\boldsymbol{q}) = \sum_{n=1}^{N} f_n e^{i\boldsymbol{q}\cdot\boldsymbol{r_n}}. \tag{10}$$

Because scattering intensity is only observed if the Bragg conditions are satisfied, the structure factor F_{hkl} of a given reflection can be written as

$$F_{hkl} = \sum_{n=1}^{N} f_n \exp\left[2\pi i(hx_n + ky_n + lz_n)\right] \tag{11}$$

where x_n, y_n, z_n are the fractional coordinates of each atom in the unit cell[2]. Finally, the structure factor (and so the scattering intensity) depends on the indices of the diffracting reflection, the crystal structure, and the atomic form factors of the atoms in the crystal structure (which decreases with increasing q and energy).

For a monoatomic diamond face centered cubic structure (corresponding to Si or Ge), the relative magnitude of the structure factor $|F_{hkl}|^2$ for a particular hkl is given by

$$|F_{hkl}|^2 = \begin{cases} 64f^2, & h+k+l = 4N \\ 32f^2, & h+k+l = 2N+1 \\ 0, & h+k+l = 4N+2 \end{cases} \tag{12}$$

Some further discussion and conclusions on the use of diffractive elements for photon analysis in spectrometers is evident on inspecting Eqs. 8 – 12. First, the intensity of the reflection depends on the atomic form factor which is greater for higher Z elements. Second, the atomic form factor is inversely proportional to q, thus scattering intensity decreases at higher energies and decreasing θ_B. Third, based on $|F_{hkl}|^2$, some reflections offer greater reflectivity than others – it is desirable to operate on $h+k+l=4N$ reflections when using Si or Ge, for example.

d. Darwin Width

There is a finite angular width over which diffraction occurs at a given Bragg condition for a sufficiently thin perfect crystal; this is an outcome of dynamical diffraction. This angular width (ω_D) is the so-called Darwin width and is given by

$$\omega_D = \frac{2r_e F_{hkl} \lambda^2}{\pi V \sin 2\theta_B} \tag{8}$$

where r_e is the classical electron radius, λ is the diffracted wavelength, and V is the volume of the unit cell[3]. Converting this angular width into an energy gives part of the intrinsic analyzer resolution, ΔE_{Darwin}, of the reflection before considering the shape of the optic profile, strain effects, manufacturing defects, etc. ΔE_{Darwin} / E is approximately constant for a given reflection[3]. ΔE_{Darwin} is relatively narrow compared to other contributing factors to overall spectrometer energy resolution, and its value is typically tabulated from online resources. For scale, some calculated examples are provided in Table 2. The values are small, thus Darwin width is not a limiting factor in dedicated XES, HERFD-XAS, and XRS spectrometers.

Table 2. Tabulated Darwin energy widths for Si reflections in the hard X-ray regime.

Reflection (*hkl*)	Energy (eV)	θ_B(°)	ΔE_{Darwin} (eV)
331	5000	84.6	0.075
531	7500	64.2	0.049
822	10000	75.6	0.030
975	15000	71.3	0.008

3. Rowland Circle Geometry

With the basis of diffraction established, a brief overview of Rowland circle geometry will be provided.

A geometric principle of rays originating from a point on a circle's perimeter is that any ray will refocus to another common point on the circle's perimeter. This geometric focusing geometry is shown in Figure 3. All rays from the point source refocus to a common point elsewhere. The break out view of Figure 3 shows that a common θ_B can be defined for each ray, and the normal vectors of these would-be diffracting planes coincide at a point on the focusing circle. This focusing geometry is known as Rowland geometry, wherein a diffractive optic with an appropriate surface profile can both monochromatize and focus a radiating point source. The analyzed photon energy is tunable by scanning θ_B and keeping the radiating source on the circle's perimeter. This is a generalization of the famous application of the same ideas to curved optical gratings[5].

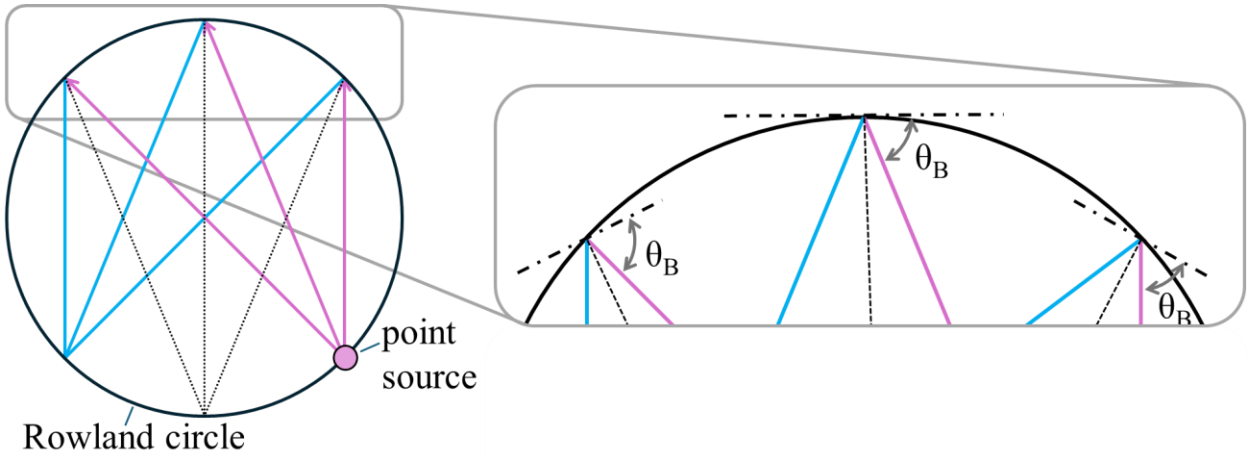

Figure 3. Symmetric Rowland circle focusing geometry, where a radiating point source on the focusing circle's perimeter is refocused. A common θ_B can be defined for any of the radiating rays incident on the circle's perimeter.

The Rowland circle geometry does not require reflective Bragg diffraction – a similar focusing configuration is achievable with transmission Laue geometry[6]. Furthermore, the Rowland circle geometry does not require a symmetric diffraction geometry as depicted in the diagrams here. Further discussion on the kinematics of a scanning Rowland circle and asymmetric Rowland geometries is found in subsequent chapters.

Next, we discus the Rowland circle crystal optic geometric profile in 2D and 3D. The profile of a single crystal diffractive optic for reflective Bragg geometry requires a circular bending radius equal to the diameter of the Rowland circle; the bending radius of the optic defines the Rowland circle[7]. The two common profiles of bent crystal analyzers are shown in Figure 4, the (a) Johannson[8] and (b) Johann[9] profiles. Johannson profiles perfectly follow the Rowland circle perimeter and require both bending and surface grinding of the crystal analyzer. Johann profiles approximate the Rowland circle perimeter and require only bending of the crystal analyzer; but the Johann approximation worsens at the analyzer's edges. Due to their ease of manufacture, Johann profiles are most common and are only consider for the following discussion.

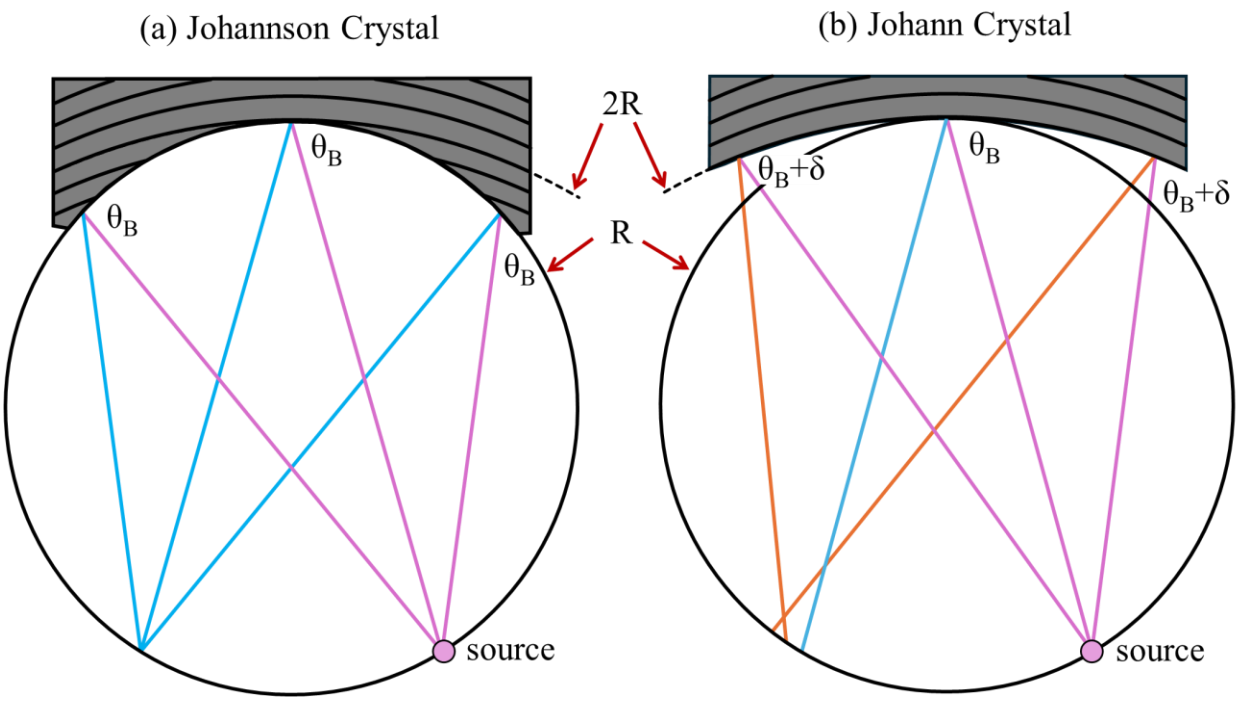

Figure 4. **(a)** Johannson and **(b)** Johann crystal analyzer profiles in Rowland circle focusing geometry. Both define the radius, R, of the Rowland circle by their radius of curvature, 2R.

The consequence of the Johann approximation is evident in Figure 4 (b). Consider a polychromatic radiating point source ('pink' on the figure) monochromated by the Johann optic. The incident angle at the center of the optic is θ_B as expected. At the analyzer edges, the incident angle is slightly larger by δ. Thus, the analyzed photon energy at the edges of the analyzer is slightly lower than the center which results in a low energy tail in the analyzer response function. This also causes a spatial dispersion of energies at the detector position. This is referred to as "Johann error", and is an energy degradation mechanism of Johann optics, quantified later in this chapter. In general, Johann error's impact on energy resolution worsens as θ_B moves away from backscatter, and as the ratio of optic diameter to optic bending radius increases (d_{optic} / R).

In three dimensions (i.e. perpendicular to the Rowland plane), the Johann profile is further approximated as a spherical radius of curvature. The consequence is an astigmatic focus when operating away from backscatter, shown in Figure 5. The ideal optic profile in three-dimensions would be toroidal, with the sagittal (out-of-plane) radius of curvature R_s and meridional (in-plane) radius of curvature R_m as shown in Figure 6. There has been effort to develope toroidal analyzers for Bragg spectrometers[10], but they are limited to a "correct" curvature at only a single θ_B, and an astigmatic focus returns everywhere else[11].

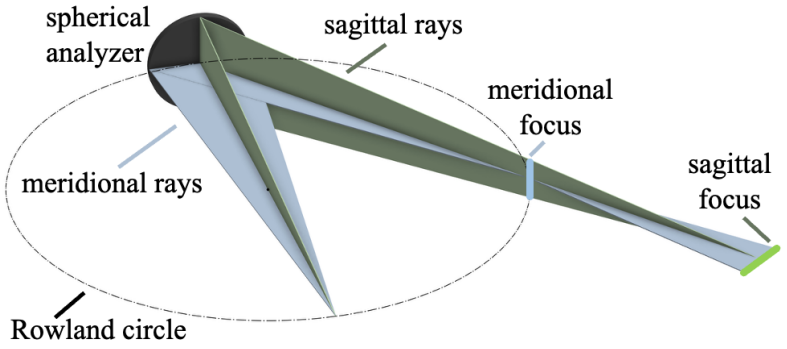

Figure 5. The astigmatic focus of a spherical analyzer

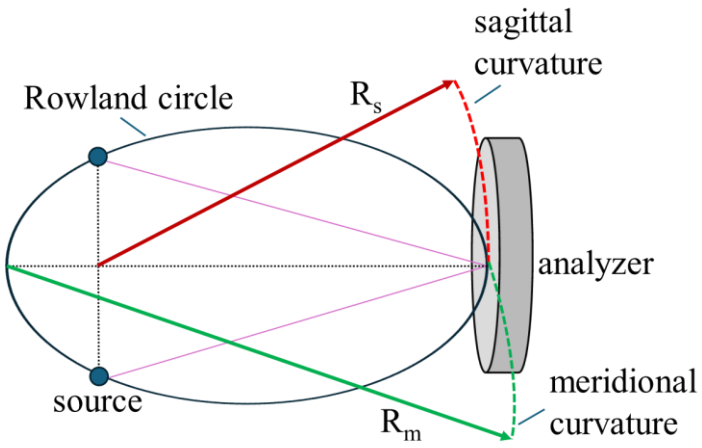

Figure 6. The toroidal analyzer profile to eliminate the astigmatic focus at a given θ_B. The out-of-plane sagittal curvature is defined by the axis between the source and refocusing point.

4. Spherically Bent Crystal Analyzers

Johann-type spherically bent crystal analyzers (SBCAs) are by far the most common hard X-ray diffractive optic for photon analysis in Rowland spectrometers[12–26]. SBCAs offer fine energy resolution (1-2 eV), large collection solid angle, and approximate point refocusing for efficient signal detection. As a result, laboratory XAFS and XES spectrometers and synchrotron HERFD-XANES, RIXS, and XRS spectrometers rely on SBCAs for high-resolution spectroscopy.

a. SBCA Manufacture

The necessity for high-purity, defect free single crystals for the semiconductor industry (Si, Ge) presents an inexpensive source of single crystal boules and wafers for diffractive optic manufacture, although alternative materials such as quartz[27], sapphire[28], and mica[29] are also sometimes used. The wafers are typically on the order of 300 μm thick and 100 mm in diameter. The difficulty in manufacture of SBCAs is in forming the wafer into a uniform spherical profile while mitigating strains in the wafer, which can cause variations in d-spacing and a worse intrinsic resolution of the optic. Broadly speaking, the manufacture of SBCAs requires the adhesion of the diffractive wafer to a rigid substrate or form with a spherical profile[30,31].

Before bonding, cutting the boule into wafers can introduce errors in the manufacture of the optic. Typically, a cut of the crystal is requested (e.g., 531 or 620) and the boule is cut at the appropriate angle for the wafer surface to be nominally parallel with the desired plane family. However, deviations between the cut analyzer surface and selected plane can occur. This angular deviation is referred to as crystal miscut, α_{miscut}, and introduces a small amount of asymmetry to

the diffraction geometry as shown in Figure 7. α_{miscut} is generally small (~0.1 to 0.5 deg) and can be accounted for in Rowland spectrometers by two-axis analyzer tilt stages[32] or by a tilt-free azimuthal rotation of the optic with a θ_B offset[33].

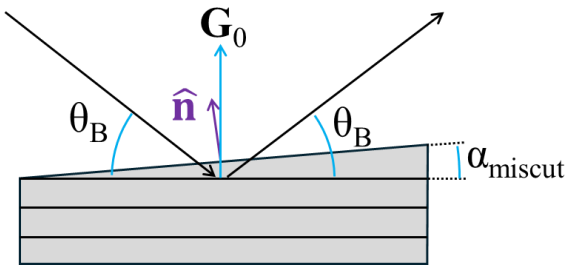

Figure 7. Exaggerated schematic depicting crystal miscut in a nominally symmetric Bragg diffraction geometry. Here $\mathbf{G}_0$ and $\hat{\mathbf{n}}$ are not parallel and separated by angle α_{miscut}.

The simplest bonding method is the use of a liquid adhesive such as a thermal curing epoxy or thermoplastic polymer to solidify and bond the wafer to a spherical glass substrate[34]. The wafer is elastically bent by a stamp or press into the form of the spherical substrate. This process requires a very thin layer of adhesive to ensure uniform distribution and high energy resolution is difficult to achieve relative to other techniques[35]. An exception is the so-called 'diced-flat' optic, by using ~12,000 independent diced Si square pixelites ~0.5 mm in width individually glued to a spherically substrate which can provide very high energy resolution as each pixelite is unstrained. The optic is "diced-flat" despite the overall spherical profile as each Si pixelite has a flat surface[30,31]. However, diced-flat optics require operating very close to backscatter as they become dispersive at smaller θ_B, and thus are limited to non-resonant inelastic X-ray scattering experiments[36], and easier methods for their manufacture have been developed.

Most contemporary SBCAs are manufactured by anodic bonding, shown in Figure 8. In anodic bonding, a hermetic seal is achieved between two materials without the use of an adhesive. In the anodic bonding process, Na^+ ions in the borosilicate glass substrate (anode) are driven by a voltage at elevated temperature to diffuse into a semiconductor wafer (cathode) while O^{2-} ions diffuse towards the glass substrate. A thin layer of oppositely charged ions are trapped near the substrate wafer interface; this electrostatic attraction results in the formation of a SiO_2 oxide layer at the interface and a permanent covalent bond remains after the driving potentials are removed[37]. This method was first applied to spherical X-ray optics by Verbeni et. al, 2005[30] and is a reliable manufacture technique for high-resolution SBCAs[36].

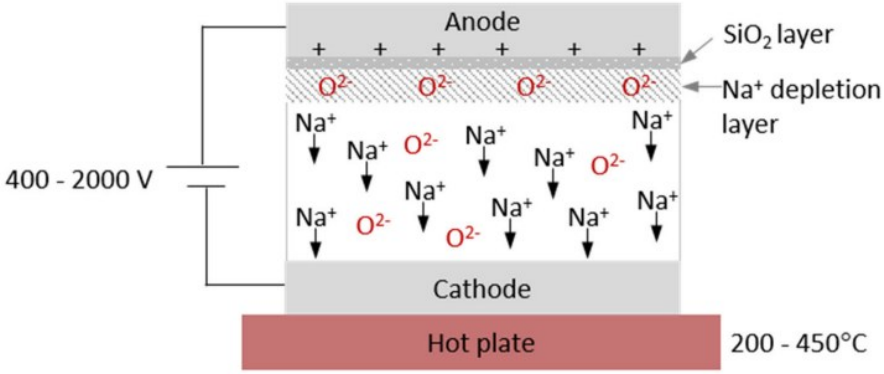

Figure 8. Anodic bonding process. Figure from Ketenoglu, 2021[37]. The anode is the glass substrate, the cathode is the semiconductor wafer.

An emerging adhesion method uses air pressure to temporarily adhere and shape a wafer or pixelated wafer against a spherical form. The benefits of this technique are only a library of flat diffractive wafers and a single vacuum form could function as a suite of SBCAs. The earliest example of temporary vacuum formed analyzers was demonstrated by Jahrman et al., 2018[10]. A Kapton film on the front face of the assembly pushed wafer against a CNC-machined spherical

or toroidal form when the chamber pumped down to vacuum. Later work applied vacuum pressure instead to the back of the wafer by using a microporous ceramic[38] or aluminum[39] spherical form, pulling the wafer into form.

Regardless of the adhesion method, the manufacture of SBCAs necessitates the minimization of strains in the wafer crystal for best resolution. In the pursuit of larger collection solid angle, SBCAs have trended towards tighter bending radius (0.5 m) while maintaining a large optic diameter (100 mm). This results in a significant manufacture challenge to accommodate and minimize the high strains on the wafer; the standard approach of elastically bending the wafer against the form is insufficient for this form factor. Instead, strain-relieving cuts are made on the wafer surface. The typical process involves cutting the 100 mm wafer into strips or squares of 10 – 15 mm in width. These elements are held together by a conductive tape (typically aluminum) during the anodic or epoxy bonding process against a spherical form. The resultant optic has improved energy resolution compared to an only elastically bent optic[40,41].

For an XRS, XES, HERFD-XANES, or laboratory XAFS spectrometer where the energy resolution requirements are ~1 eV, the contemporary optic is an anodically bonded 0.5-m SBCA either elastically bent, strip-bent, or diced-bent. Non-resonant inelastic x-ray scattering measurements requiring very high resolution (~100 meV) necessitate pixelated diced-flat SBCA, which are outside the scope of this chapter. Figure 9 shows 0.5-m curvature SBCA (a) bent, (b) sliced-bent, and (d) diced-bent, in addition to less common azimuthally sliced optics (c), (e).

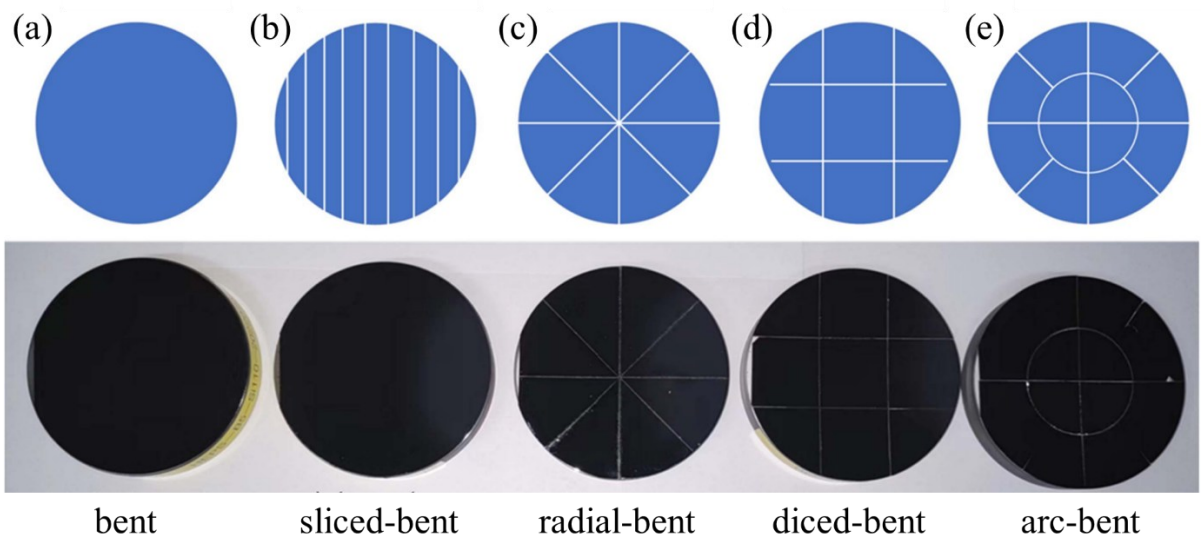

Figure 9. Different slice patterns for strain relieving SBCAs. Adapted from Diao, 2023[41].

b. Calculation of Strain Effects on Bent/Sliced/Diced SBCA Resolution

Understanding the effect of slicing, dicing, and mechanical strains on the wafer of an SBCA are crucial for the design and optimization of Rowland spectrometers. The equations describing the propagation of radiation through a deformed crystalline structure were described by both Takagi[42,43] and Taupin[44] in the 1960s. Significant research effort by Honkanen and collaborators the past two decades has developed the theory and method to calculate the elastic deformation of bent and strain-relieved cut crystal wafers[11,45–48]. The development and treatment of this theory will not be reviewed here, but it is noted that this provides the framework for the calculation of the intrinsic energy resolution of bent, sliced-bent, and radial-bent SBCAs discussed later in this chapter.

c. Typical Dimensions of an SBCA

A common supplier of Si and Ge bent, sliced, and diced SBCAs in the United States is XRS Tech LLC located in New Jersey. Their manufacture methods are proprietary, but it is a useful reference for SBCA dimensions; a computer aided design dimensioned drawing of a 0.5-m radius of curvature diced SBCA and isometric view are shown in Figure 10. Of note, the wafer is typically 300 μm thick and 100 mm in diameter anodically bonded to a 4" glass substrate[49]. The radius of curvature can vary as much as 20 mm from the target of 500 mm and is not known *a priori*. The square dicing is typically 10 x 10 mm, and the strip slicing 15 mm wide.

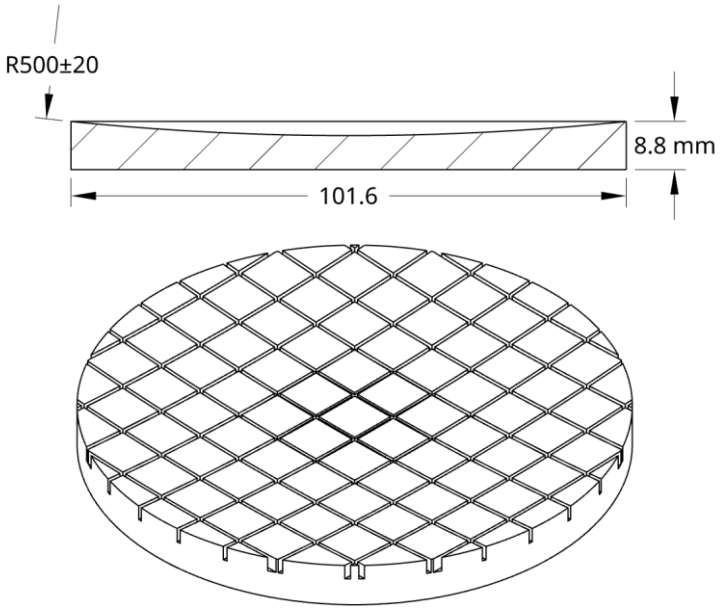

Figure 10. **(Top)** Dimensioned section view through the diameter of the nominally 0.5-m radius of curvature spherically bent crystal analyzer from XRSTech LLC, Freehold, NJ[49]. **(Bottom)** Isometric view of the spherical analyzer surface with a 10x10 mm square dice. The dicing cut depth is exaggerated for clarity and not to scale.

d. Solid Angle

A common metric for assessing scattered or fluorescing signal collection efficiency of an optic is the collected "solid angle", Ω, in steradians, sr. Consider a point source and SBCA in Rowland circle geometry near backscatter. The angular size of the optic, γ, is given by

$$\gamma\ (\text{rad}) = 2\sin^{-1}\left(\frac{d_{xtal}}{2R}\right) \tag{9}$$

where d_{xtal} is the diameter of the SBCA and R is the bending radius of the SBCA (or similarly the diameter of the Rowland circle). The solid angle is then given by the equation for subtended angle of a spherical cap on a unit sphere

$$\Omega\ (\text{sr}) = 4\pi\sin^2\left(\frac{\gamma}{4}\right). \tag{10}$$

Some small angle approximations can be made for convenience in (9) and (10), and Ω reduces to

$$\Omega\ (\text{sr}) \approx \pi\left(\frac{d_{xtal}}{2R}\right)^2. \tag{11}$$

Now, consider that a spherically radiating point source is 4π sr of solid angle. A 100 mm diameter, 1-m radius of curvature optic subtends ~8 msr of solid angle, or 0.06% of all the radiation emanating from the point source. Moving to 0.5-m radius of curvature increases the subtended solid angle by a factor of 4x, as shown in Figure 11.

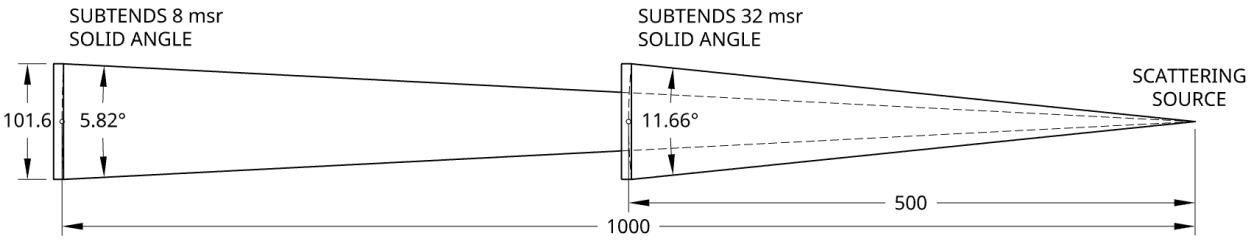

Figure 11. Schematic of the angular size and solid angle subtended of the XRSTech optics at 1-m and 0.5-m bending radius. A 4x improvement in signal collection is achieved per optic when going from 1-m to 0.5-m.

From this, some conclusions can again be drawn for spectrometer design and maximizing the signal acquisition efficiency. In the case of a single SBCA spectrometer, it is vastly beneficial to work at 0.5-m bending radius for the smaller instrument footprint and improved signal collection. Second, when smaller bending radii cannot be accommodated or the energy resolution compromised, building arrays of analyzers can also improve signal collection albeit with the added complexity of multiple Rowland circle trajectories in a scanning spectrometer[13,14,19,20]. Some discussion on the latter point in the context of multi-element HERFD-XANES instruments is found elsewhere in this dissertation.

5. Energy Resolution of SBCA Rowland Circle Spectrometers

Finally, in the design and commissioning of Rowland spectrometers, it is crucial to understand the energy resolution of the instrument and the X-ray source. This is particularly true while running an experiment or assessing the alignment of a spectrometer. We've divided the energy resolution of the spectrometer into three parts: intrinsic (the analyzer itself), geometric (the spread of θ_B due to the analyzer's surface), and source size (the volume of the radiating source w.r.t the Rowland circle and its placement nominally on the circle's perimeter).

a. Intrinsic Resolution

There are different definitions of the "intrinsic" resolution of an SBCA. We choose to define this as the contributions of Darwin width, crystalline defects, and strain effects from wafer bending and bonding that can cause variations in *d*-spacing. Thus, bent, sliced, and diced and diced SBCAs will have different intrinsic resolutions.

We begin with Darwin width, the angular acceptance size of a given reflection. The energy resolution due to ω_D is given by

$$\Delta E_{darwin} = \omega_D E \cot(\theta_B) \tag{12}$$

and ΔE_{darwin} is most dependent on the material and selected reflection (*hkl*). In the hard X-ray regime for Si and Ge (~10 keV), ω_D is on the order of 10 -100 μrad and ΔE_{darwin} is ~100 meV or less[50].

The other intrinsic resolution is the strain effects of wafer bending and bonding to make the spherical form. In general, elastic bending provides the largest degradation of energy resolution, followed by bent-sliced and then bent-diced, where bent-diced provides the best energy resolution. Sala et al.[51] provides an equation for estimating the resolution of spherically bent wafers as

$$\Delta E_{bent} = E \frac{\mathrm{t}}{R} \left(\frac{\cos^2(\theta_B - \alpha)}{\sin^2(\theta_B + \alpha)} - 2\upsilon \right) \tag{13}$$

where t is the absorption length of the material at the given photon energy and ν is its Poisson's ratio (0.22 for Si and 0.27 for Ge) and R is the Rowland circle diameter. However, there are no quick solutions for the resolution of bent-diced or bent-sliced SBCAs without resorting to strain calculations and modelling. Instead, it is easier to refer to experimentally characterized optics for the resolution of 0.5-m strain relieved SBCAs. In the case of bent-sliced 0.5-m Si SBCAs,

Rovezzi et al.[40] reports a resolution of ~0.4 eV. Thus, the overall intrinsic resolution of an SBCA is calculated by

$$\Delta E_{intrinsic} = \sqrt{\Delta E_{darwin}^2 + \Delta E_{strain}^2} \tag{14}$$

where ΔE_{strain} is the bent, diced, or sliced resolution, for example. Again, for Si and Ge SBCAs, the overall intrinsic resolution is on the order of 0.4 – 0.6 eV for strain relieved optics.

b. Geometric Contributions

Assuming a bent analyzer in Rowland circle geometry with a point source on the circle perimeter, energy degradation mechanisms result due to the range of θ_B made across the analyzer's surface as a result of the geometric profile of the analyzer. The Johann approximation for SBCA's results in a non-uniform θ_B in the Rowland plane. Additionally, the spherical approximation (rather than a toroidal surface) perpendicular/out-of the Rowland plane also results in a non-uniform θ_B on the optic's surface. The in-plane error is referred to as Johann error, ΔE_J, and the out-of-plane error we refer to as sagittal error, ΔE_s. Two equations for ΔE_J exist in literature, one provided by Sala et al.[51] and another cited here by Glatzel et al.[52] but reported by many others as

$$\text{Sala: } \Delta E_J = E \frac{\left[\frac{d_{xtal}}{R \sin(\theta_B + \alpha)}\right]^2}{8 \tan(\theta_B + \alpha)} \cot \theta_B \tag{15}$$

$$\text{Glatzel: } \Delta E_J = \frac{1}{2} \mathrm{E} \left(\frac{d_{xtal}}{2R}\right)^2 \cot^2(\theta_B + \alpha)\,. \tag{16}$$

Of the two equations, Eq. 16 is much more commonly reported in spectrometer design papers but is said to only be accurate close to backscatter. In practice, the most precise calculation of such geometric aberrations of SBCAs are reported by simulated ray tracing from

packages such as X-Ray Tracer (xrt)[53]. ΔE_s is often ignored as it is exponentially weaker than ΔE_J but is calculated by[52]

$$\Delta E_S = \frac{1}{2}\mathrm{E}\left(\frac{d_{xtal}}{2R}\right)^2 \cot^4(\theta_B + \alpha)\,. \tag{17}$$

The overall geometric contribution of the SBCA, $\Delta E_{geometric}$ is then given by the quadrature sum of ΔE_J and ΔE_s in the same fashion as Eq. 14.

c. Source size and off-circle contributions

The discussion and calculations of SBCAs in Rowland circle geometry have assumed a point source. In practice, the radiating source is volumetric. The size of the source causes a dispersion of θ_B incident on the analyzer and thus impacts energy resolution. This is also true even for a point source that is not placed on the Rowland circle perimeter. In both cases, this is referred to as source size broadening or "off-circle" contributions.

To calculate these, it is important to define a frame of reference with respect to the analyzer. This is described in Figure 12. To be technically correct, the "off-circle" contribution is given by displacements along s_x. It is immediately evident that the most unfavorable source dimension is s_z, as that lies along the dispersive direction of the SBCA and gives the biggest spread in energies for a given length.

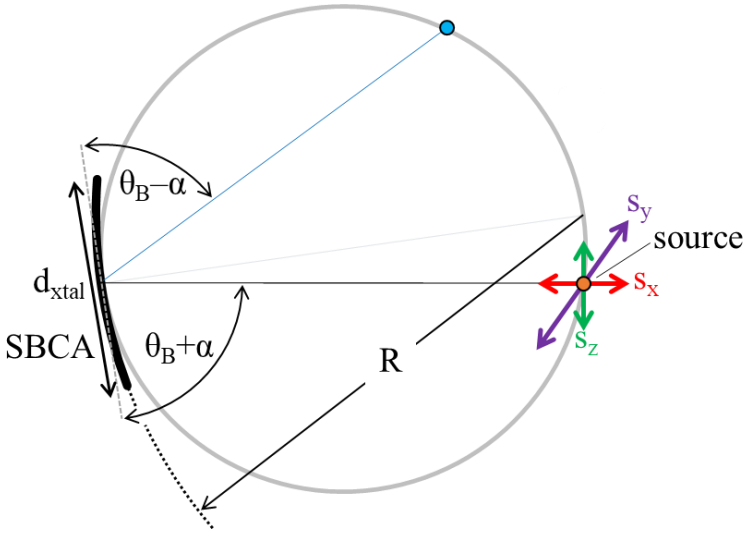

Figure 12. Cartesian coordinates for the calculation of source-size broadening in Rowland circle geometry. Note S_y is in-to/out-of the plane.

The energy resolution contributions in each direction are given by the following equations:

$$\Delta E_z = E \frac{s_z}{R \sin(\theta_B - \alpha)} \cot \theta_B \tag{18}$$

$$\Delta E_y = E \left[\frac{s_y}{R \sin(\theta_B - \alpha)}\right]^2 \tag{19}$$

$$\Delta E_x = E \frac{s_x}{R \sin(\theta_B - \alpha)} \cot^2 \theta_B \tag{20}$$

The overall source size contribution to energy resolution, ΔE_{size} is again given by the quadrature sum of these three quantities.

d. X-ray Source Resolution

In the case of synchrotron experiments, an upstream monochromator provides an already monochromatic beam incident upon the sample before a spectrometer is employed. This also

effects the overall resolution of spectrometer measurements at the synchrotron. We denote this as ΔE_{mono}. Typically, for a Si(111) double crystal monochromator operating at 10 keV the resolution is ~1.3 eV. In the case of laboratory measurements with an X-ray tube source, the spectrometer is the monochromator and thus this factor is not present.

e. Overall Resolution

We conclude with the obvious but worth stating equation for calculating the overall resolution of a Rowland geometry X-ray spectrometer employing SBCAs:

$$\Delta E = \sqrt{\Delta E_{intrinsic}^2 + \Delta E_{geometric}^2 + \Delta E_{size}^2 + \Delta E_{mono}^2} \tag{21}$$

6. References

1 T. Hom, W. Kiszenik and B. Post, *Journal of Applied Crystallography*, 1975, **8**, 457–458.
2 C. Kittel, *Introduction to solid state physics*, Wiley, Hoboken, NJ, 8th ed., 2005.
3 J. Als-Nielsen and D. McMorrow, *Elements of modern X-ray physics*, Wiley, West Sussex, 2nd ed., 2011.
4 B. D. Cullity, *Elements of x-ray diffraction*, Prentice Hall, Upper Saddle River, NJ, 3rd ed., 2001.
5 M. C. Hutley, *Diffraction gratings*, Academic Press, London ;, 1982.
6 N. Hiraoka, H. Fukui, H. Tanida, H. Toyokawa, Y. Q. Cai and K. D. Tsuei, *J Synchrotron Rad*, 2013, **20**, 266–271.
7 J. W. M. DuMond, *Rev. Sci. Instrum.*, 1947, **18**, 626–638.
8 T. Johansson, *Z. Physik*, 1933, **82**, 507–528.
9 H. H. Johann, *Z. Physik*, 1931, **69**, 185–206.
10 E. P. Jahrman, W. M. Holden, A. S. Ditter, S. A. Kozimor, S. L. Kihara and G. T. Seidler, *Rev. Sci. Instrum.*, 2019, **90**, 013106.
11 A.-P. Honkanen and S. huotari, *IUCrJ*, 2021, **8**, 102–115.
12 E. Kleymenov, J. A. van Bokhoven, C. David, P. Glatzel, M. Janousch, R. Alonso-Mori, M. Studer, M. Willimann, A. Bergamaschi, B. Henrich and M. Nachtegaal, *Rev. Sci. Instrum.*, 2011, **82**, 065107.
13 A. Tayal, D. S. Coburn, D. Abel, M. Rakitin, O. Ivashkevych, J. Wlodek, D. Wierzbicki, W. Xu, E. Nazaretski, E. Stavitskia and D. Leshcheva, *J. Synchrot. Radiat.*, 2024, **31**, 1609–1621.
14 J. M. Ablett, A. Berlioux, D. Prieur, J. Harrison, L. Heller, S. Gliga and J.-P. Rueff, *Rev. Sci. Instrum.*, 2025, **96**, 053104.
15 S. Hayama, R. Boada, J. Chaboy, A. Birt, G. Duller, L. Cahill, A. Freeman, M. Amboage, L. Keenan and S. Diaz-Moreno, *J. Phys.-Condes. Matter*, 2021, **33**, 284003.
16 M. M. Sala, K. Martel, C. Henriquet, A. Al Zein, L. Simonelli, C. J. Sahle, H. Gonzalez, M.-C. Lagier, C. Ponchut, S. Huotari, R. Verbeni, M. Krisch and G. Monaco, *J. Synchrot. Radiat.*, 2018, **25**, 580–591.
17 K. O. Kvashnina and A. C. Scheinost, *J. Synchrot. Radiat.*, 2016, **23**, 836–841.
18 P. Glatzel, A. Harris, P. Marion, M. Sikora, T.-C. Weng, C. Guilloud, S. Lafuerza, M. Rovezzi, B. Detlefs and L. Ducotte, *J. Synchrot. Radiat.*, 2021, **28**, 362–371.
19 B.-B. Mei, L.-X. Wang, S.-Q. Gu, X.-Z. Su, S. Zhang, Y. Wei, J.-Y. Ma, Z. Jiang and F. Song, *Nucl. Sci. Tech.*, 2024, **35**, 156.
20 P. Duan, S. Gu, H. Cao, J. Li and Y. Huang, *X-Ray Spectrom.*, 2017, **46**, 12–18.
21 I. Llorens, E. Lahera, W. Delnet, O. Proux, A. Braillard, J.-L. Hazemann, A. Prat, D. Testemale, Q. Dermigny, F. Gelebart, M. Morand, A. Shukla, N. Bardou, O. Ulrich, S. Arnaud, J.-F. Berar, N. Boudet, B. Caillot, P. Chaurand, J. Rose, E. Doelsch, P. Martin and P. L. Solari, *Rev. Sci. Instrum.*, 2012, **83**, 063104.
22 D. Sokaras, D. Nordlund, T.-C. Weng, R. A. Mori, P. Velikov, D. Wenger, A. Garachtchenko, M. George, V. Borzenets, B. Johnson, Q. Qian, T. Rabedeau and U. Bergmann, *Rev. Sci. Instrum.*, 2012, **83**, 043112.
23 S. Huotari, C. J. Sahle, C. Henriquet, A. Al-Zein, K. Martel, L. Simonelli, R. Verbeni, H. Gonzalez, M.-C. Lagier, C. Ponchut, M. Moretti Sala, M. Krisch and G. Monaco, *J Synchrotron Rad*, 2017, **24**, 521–530.

24 T. T. Fister, G. T. Seidler, L. Wharton, A. R. Battle, T. B. Ellis, J. O. Cross, A. T. Macrander, W. T. Elam, T. A. Tyson and Q. Qian, *Rev. Sci. Instrum.*, 2006, **77**, 063901.
25 G. T. Seidler, D. R. Mortensen, A. J. Remesnik, J. I. Pacold, N. A. Ball, N. Barry, M. Styczinski and O. R. Hoidn, *Review of Scientific Instruments*, 2014, **85**, 113906.
26 E. P. Jahrman, W. M. Holden, A. S. Ditter, D. R. Mortensen, G. T. Seidler, T. T. Fister, S. A. Kozimor, L. F. J. Piper, J. Rana, N. C. Hyatt and M. C. Stennett, *Review of Scientific Instruments*, 2019, **90**, 024106.
27 M. G. Honnicke, L. M. Bianco, S. A. Ceppi, C. Cusatis, X. Huang, Y. Q. Cai and G. E. Stutz, *J. Appl. Crystallogr.*, 2016, **49**, 1443–1453.
28 H. Yavas, E. E. Alp, H. Sinn, A. Alatas, A. H. Said, Y. Shvyd'ko, T. Toellner, R. Khachatryan, S. J. L. Billinge, M. Z. Hasan and W. Sturhahn, *Nucl. Instrum. Methods Phys. Res. Sect. A-Accel. Spectrom. Dect. Assoc. Equip.*, 2007, **582**, 149–151.
29 E. S. Joseph, E. P. Jahrman and G. T. Seidler, *X-Ray Spectrom.*, 2020, **49**, 493–501.
30 R. Verbeni, M. Kocsis, S. Huotari, M. Krisch, G. Monaco, F. Sette and G. Vanko, *Journal of Physics and Chemistry of Solids*, 2005, **66**, 2299–2305.
31 R. Verbeni, T. Pylkkänen, S. Huotari, L. Simonelli, G. Vankó, K. Martel, C. Henriquet and G. Monaco, *J Synchrotron Rad*, 2009, **16**, 469–476.
32 T. T. Fister, G. T. Seidler, L. Wharton, A. R. Battle, T. B. Ellis, J. O. Cross, A. T. Macrander, W. T. Elam, T. A. Tyson and Q. Qian, *Rev. Sci. Instrum.*, 2006, **77**, 063901.
33 D. R. Mortensen and G. T. Seidler, *J. Electron Spectrosc. Relat. Phenom.*, 2017, **215**, 8–15.
34 G. Klink and B. Hillerich, in *Micromachined Devices and Components IV*, SPIE, 1998, vol. 3514, pp. 50–61.
35 X. Liu, D. Zhang, X. Zeng, K. Zhang, P. Liu and T.-C. Weng, in *Seventh Asia Pacific Conference on Optics Manufacture and 2021 International Forum of Young Scientists on Advanced Optical Manufacturing (APCOM and YSAOM 2021)*, SPIE, 2022, vol. 12166, pp. 1785–1789.
36 E. Collart, A. Shukla, F. Gélébart, M. Morand, C. Malgrange, N. Bardou, A. Madouri and J.-L. Pelouard, *J Synchrotron Rad*, 2005, **12**, 473–478.
37 D. Ketenoglu, *Instrum. Sci. Technol.*, 2021, **49**, 545–559.
38 Z. Guo, Q. Diao, Y. Zhang, X. Jia, S. Jin, X. Gan, H. Zhang, Y. Tian, Q. Han, H. Qian, K. Ishii and W. Xu, *X-Ray Spectrom.*, 2025, **54**, 247–253.
39 A. H. Said, J. H. Kim, E. K. Aran and T. Gog, *J. Synchrot. Radiat.*, 2022, **29**, 749–754.
40 M. Rovezzi, C. Lapras, A. Manceau, P. Glatzel and R. Verbeni, *Rev. Sci. Instrum.*, 2017, **88**, 013108.
41 Q. Diao, Y. Zhang, S. Jin, S. He, J. Zeng, F. Bian, J. Yang, Z. Hong, H. Lian, X. Gan, H. Zhang, M. Li, P. Liu, D. Chen, Z. Guo and W. Xu, *J. Appl. Crystallogr.*, 2023, **56**, 1505–1511.
42 S. Takagi, *Acta Cryst*, 1962, **15**, 1311–1312.
43 S. Takagi, *J. Phys. Soc. Jpn.*, 1969, **26**, 1239–1253.
44 D. Taupin, DOI:10.3406/bulmi.1964.5769.
45 A.-P. Honkanen, R. Verbeni, L. Simonelli, M. M. Sala, G. Monaco and S. Huotari, *J. Synchrot. Radiat.*, 2014, **21**, 104–110.
46 A.-P. Honkanen, G. Monaco and S. Huotari, *J. Appl. Crystallogr.*, 2016, **49**, 1284–1289.
47 A.-P. Honkanen, R. Verbeni, L. Simonelli, M. M. Sala, G. Monaco and S. Huotari, *J. Synchrot. Radiat.*, 2017, **24**, 545–546.

48 A.-P. Honkanen, C. Ferrero, J.-P. Guigay and V. Mocella, *J. Appl. Crystallogr.*, 2018, **51**, 514–525.
49 XRS TECH LLC – x ray crystal analyzer, bent crystal, diced crystal, XES, XENS, XAFS, https://xrstech.com/, (accessed February 13, 2026).
50 T. Gog, D. M. Casa, A. H. Said, M. H. Upton, J. Kim, I. Kuzmenko, X. Huang and R. Khachatryan, *J. Synchrot. Radiat.*, 2013, **20**, 74–79.
51 M. M. Sala, K. Martel, C. Henriquet, A. Al Zein, L. Simonelli, C. J. Sahle, H. Gonzalez, M.-C. Lagier, C. Ponchut, S. Huotari, R. Verbeni, M. Krisch and G. Monaco, *J. Synchrot. Radiat.*, 2018, **25**, 580–591.
52 P. Glatzel, Other thesis, 2001.
53 K. Klementiev and R. Chernikov, in *Advances in Computational Methods for X-Ray Optics III*, SPIE, 2014, vol. 9209, pp. 60–75.

Chapter 3. X-ray Raman Scattering Background

1. Theory

This section provides a theory basis for inelastic X-ray scattering. The goal is to provide insight on the core-electron transitions inelastic scattering can probe and highlight similarities and differences with resonant XAFS. A complete foundational theory on resonant and non-resonant inelastic X-ray scattering is found in the textbook by Schulke[1].

Inelastic x-ray scattering (IXS) is an incoherent photon-in/photon-out scattering process where an incident photon interacts with the electron cloud and imparts some of its energy. This transferred energy can excite electrons or vibrational modes in the system and results in a scattered photon with less energy than its incident counterpart. The kinematics of this process are shown in Figure 1.

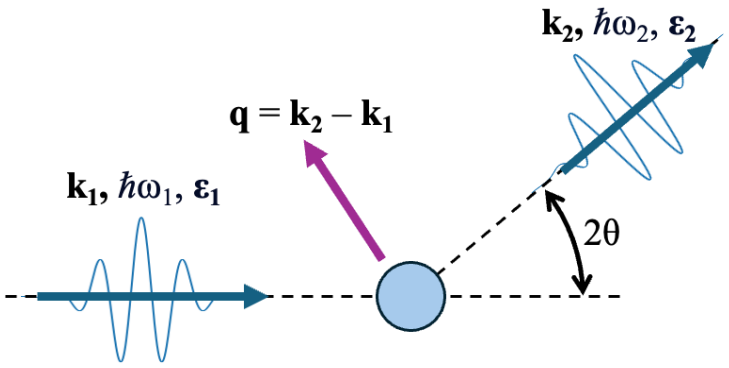

Figure 1. Schematic of the inelastic scattering process. An incident photon with wave vector $\mathbf{k}_1$, energy $\hbar\omega_1$, and polarization vector $\boldsymbol{\varepsilon}_1$ is inelastically scattered and imparts some energy and momentum exciting an electron to an unoccupied state. The remainder of the initial photon's energy and momentum are accounted for in the scattered photon. The scattering angle 2θ determines the momentum transfer, $\boldsymbol{q}$, of the scattering process.

IXS can probe different types of excitations depending on the magnitude of the energy loss of the incident and scattered photon, which can span losses of 1 meV to several keV. A schematic for the IXS energy loss spectrum is shown below[2]. Of particular interest is the core electron excitation on the order of a few 100 eVs, sometimes rereferred to as non-resonant inelastic x-ray scattering (NIXS or NRIXS)[3], but here will be defined as x-ray Raman scattering (XRS).

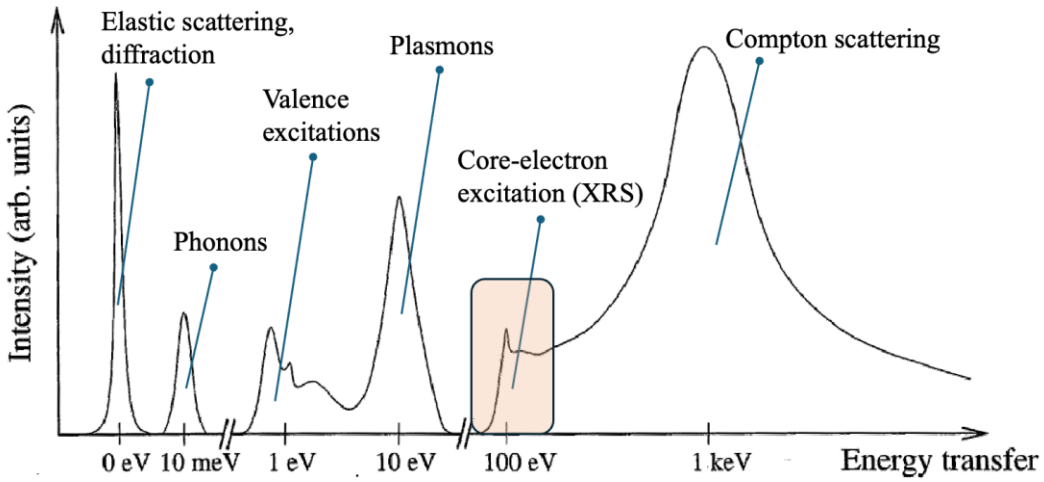

Figure 2. A diagram of the non-resonant IXS energy loss spectrum and the manner of excitations it can probe[2].

XRS is a photon-in photon out spectroscopy technique that is well suited for studying the soft x-ray absorption edges of lighter elements[4]. Because XRS studies the energy loss, the incident photon energy can be arbitrarily selected in the hard x-ray regime and experiments are performed in an ambient environment[5–7]. Studying soft electron binding energies with conventional techniques such as XAFS, electron-energy loss spectroscopy (EELS, the electron spectroscopy analogue of XRS as both measure the energy-loss function), and x-ray

photoelectron spectroscopy (XPS) require the sample and accompanying spectrometer system in vacuum and are highly surface sensitive[8].

The signal measured in XRS is proportional to the non-resonant portion of the double differential cross section given by

$$\frac{\mathrm{d}^2\sigma}{\mathrm{d}\Omega \mathrm{d}\omega} = \left(\frac{\mathrm{d}\sigma}{\mathrm{d}\Omega}\right)_{\mathrm{Th}} S(\boldsymbol{q}, \omega). \tag{1}$$

In this expression, $\left(\frac{\mathrm{d}\sigma}{\mathrm{d}\Omega}\right)_{\mathrm{Th}}$ describes the photon-electron coupling known as the Thomson scattering cross section

$$\left(\frac{\mathrm{d}\sigma}{\mathrm{d}\Omega}\right)_{\mathrm{Th}} = {r_e}^2 \left(\frac{\omega_2}{\omega_1}\right) (\hat{\boldsymbol{\varepsilon}}_1 \cdot \hat{\boldsymbol{\varepsilon}}_2)^2 \tag{2}$$

and $S(\boldsymbol{q}, \omega)$, the dynamical structure factor containing all information about the many-body electron system, is

$$S(\boldsymbol{q}, \omega) = \sum_{i,f} |\langle \mathrm{f}| \exp(i\boldsymbol{q} \cdot \boldsymbol{r}) |\mathrm{i}\rangle|^2 \delta\left(E_i - E_f + \hbar\omega\right) \tag{3}$$

where r_e is the classical electron radius, $(\hat{\boldsymbol{\varepsilon}}_1 \cdot \hat{\boldsymbol{\varepsilon}}_2)^2$ is the X-ray polarization factor, $\boldsymbol{q}$ is the momentum transfer ($\mathbf{k_2} - \mathbf{k_1}$, refer to Fig. 1), $\hbar\omega$ is the photon energy loss, and *i* and *f* are the electron's initial and final states[1]. A basis for all nonresonant IXS transitions (features of Fig. 2) is described by substituting Eqs. 2 and 3 into Eq. 1 as

$$\frac{\mathrm{d}^2\sigma}{\mathrm{d}\Omega \mathrm{d}\omega} = {r_e}^2 \left(\frac{\omega_2}{\omega_1}\right) \sum_{i,f} |\langle \mathrm{f}| \exp(i\boldsymbol{q} \cdot \boldsymbol{r}) |\mathrm{i}\rangle|^2 \delta\left(E_i - E_f + \hbar\omega\right). \tag{4}$$

The allowed electronic transitions XRS probes are momentum transfer ($\boldsymbol{q}$) dependent. XRS measurements within or beyond the dipole approximation is determined by the magnitude of $\boldsymbol{q} \cdot \boldsymbol{r}$, where $\mathbf{r}$ is the core radius of the probed element. $\mathbf{r}$ can be estimated as a_0/Z for core-electron excitations in the K-shell and $4a_0/Z$ for the L shell, where a_0 is the Bohr radius (0.53 Å)

and Z is the atomic number. The following discussion is divided into XRS measurements within the dipole limit ($\boldsymbol{q}\cdot\boldsymbol{r} \ll 1$) and beyond the dipole limit.

a. XRS within the dipole limit ($\boldsymbol{q}\cdot\boldsymbol{r} \ll 1$)

Consider the case where $\boldsymbol{q}\cdot\boldsymbol{r} \ll 1$. The transition operator $\exp(i\boldsymbol{q}\cdot\boldsymbol{r})$ of Eq. 4 can be expanded by a Taylor series as

$$\exp(i\boldsymbol{q}\cdot\boldsymbol{r}) \approx 1 + i\boldsymbol{q}\cdot\boldsymbol{r} - \frac{(i\boldsymbol{q}\cdot\boldsymbol{r})^2}{2} + \cdots, \tag{5}$$

and the evaluation of Eq. 5 is dominated by the second term, and mostly dipole transitions are probed ($\Delta l = \pm 1$). The dynamical structure factor (Eq. 3) then reduces to

$$S(\boldsymbol{q},\omega) \xrightarrow[\boldsymbol{q}\cdot\boldsymbol{r}\ll 1]{} \sum_{i,f} q^2 |\langle \mathrm{f}|\boldsymbol{q}\cdot\boldsymbol{r}|\mathrm{i}\rangle|^2 \delta\left(E_i - E_f + \hbar\omega\right) \tag{6}$$

which compared to the X-ray absorption coefficient, μ

$$\mu = \sum_{i,f} \frac{4\pi^2 e^2}{m^2 c\omega_1 n} |\langle \mathrm{f}|\boldsymbol{\varepsilon}\cdot\boldsymbol{r}|\mathrm{i}\rangle|^2 \delta\left(E_i - E_f + \hbar\omega_1\right) \tag{7}$$

shows proportionality between XRS within the dipole limit and the X-ray absorption process (XAFS)[9]. Thus, from inspection of Eq. 6 and 7, when within the dipole approximation, XRS probes the same states and provides the same information as XAFS.

b. XRS beyond the dipole limit ($\boldsymbol{q}\cdot\boldsymbol{r} \not\ll 1$)

When beyond the dipole approximation, XRS can probe non-dipole transitions beginning with $\Delta l = 0$ and $\Delta l = \pm 2$ transitions[9]. A greater depth of information is available from XRS as non-dipole transitions are forbidden in the resonant X-ray absorption process[10–16]. In the case of XRS outside the dipole approximation, higher order selection rules are relevant. Instead of a

Taylor series expansion approximation of the transition operator, at larger $\boldsymbol{q}$ an expansion of the transition operator in terms of spherical harmonics is preferred

$$\exp(i\boldsymbol{q}\cdot\boldsymbol{r}) = 4\pi\sum_{l,m} i^l j_l(qr) Y_{lm}^*(\hat{\boldsymbol{q}}) Y_{lm}(\hat{\boldsymbol{r}}) \tag{8}$$

$$\exp(i\boldsymbol{q}\cdot\boldsymbol{r}) = 4\pi\sum_{l,m} i^l j_l(qr) Y_{lm}^*(\theta_r,\varphi_r) Y_{lm}(\theta_q,\varphi_q) \tag{8}$$

where j_l are spherical Bessel functions and Y_{lm} are spherical harmonics with $\boldsymbol{r}$ and $\boldsymbol{q}$ vectors in spherical coordinates[4]. This can be substituted into the matrix element of the dynamical structure factor (Eq. 3) as

$$|\langle \mathrm{f}|\exp(i\boldsymbol{q}\cdot\boldsymbol{r})\,|\mathrm{i}\rangle|^2 = \sum_{l,m} |4\pi i^l \langle \mathrm{f}|j_l(qr)Y_{lm}(\hat{\boldsymbol{r}})|\mathrm{i}\rangle|^2. \tag{9}$$

From Eq. 9, the q dependence is in the spherical Bessel function (j_l). Within the dipole limit. As q increases, higher order transitions (quadrupole, octupole, etc.) gain weight in the dynamical structure factor[17]. As a result, XRS can probe the entirety of the unoccupied density of states beyond just dipole allowed transitions[18].

c. XRS Cross-section

The magnitude of the XRS cross-section is the biggest drawback of the technique compared to XAFS[19]. Photon cross-sections are shown below in Figure 3 for carbon and lead[20]. σ_{tot} is dominated by the photoelectric cross-section (resonant XAFS, for e.g.) whereas the XRS cross-section is a small fraction of the total incoherent scattering cross-section, σ_{incoh}. In both low- and high-Z elements, the XRS cross-section is many magnitudes smaller than the photoelectric cross-section and is an extremely weak signal of all photon-in/photon-out

interactions. As a result, highly brilliant photon sources, i.e. synchrotron X-ray light sources, and efficient collection of XRS signal are required for XRS measurements[1,4,9,19].

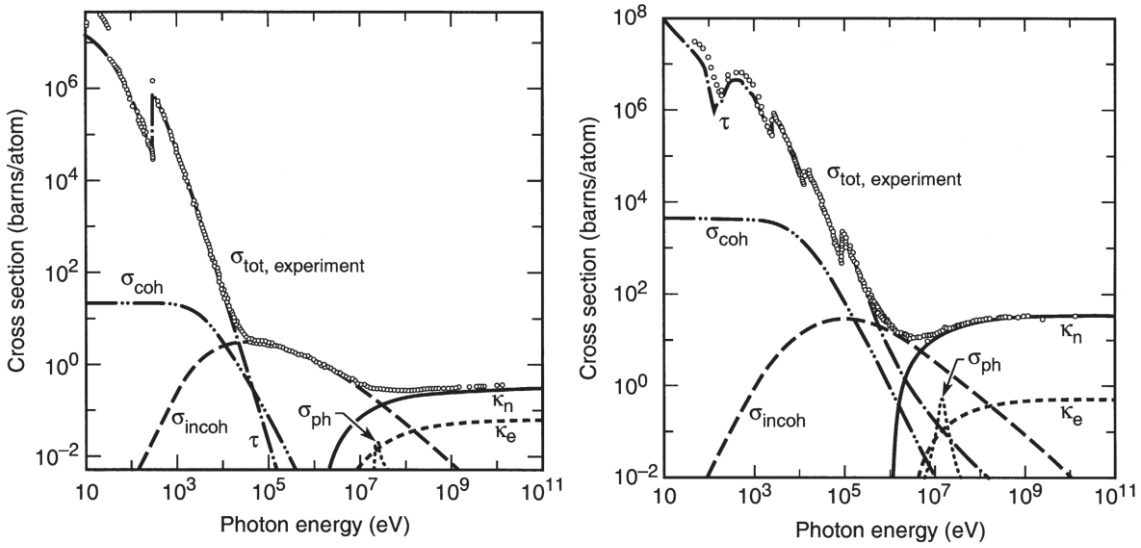

Figure 3. Photon cross-sections as a function of energy for carbon (left) and lead (right). The XRS cross-section is part of the incoherent scattering cross section, σ_{incoh}, and is magnitudes lower than the photoelectric cross-section, τ[20].

2. XRS Instrumentation and Measurement Techniques

XRS measurements require brilliant light sources due to the very small incoherent scattering cross-sections and thus are reserved for synchrotron sources or similar. The end station spectrometers are simple in principle and typically employ spherically bent crystal analyzers (SBCAs) in fixed, non-scanning Rowland circle geometries. A schematic of the upstream beamline and XRS spectrometer is shown below. The beamline provides a tunable (i.e., energy scannable) monochromatic beam (E_i) at the sample location. The scatterer, SBCA, and detector are arranged symmetrically on the Rowland circle. The SBCA, at fixed Bragg angle typically near backscatter for best energy resolution, analyzes a fixed photon energy (E_f) and focuses upon

the detector. The energy loss spectrum ($E_i - E_f$) is collected by scanning the monochromator energy while keeping the analyzed XRS spectrometer energy fixed.

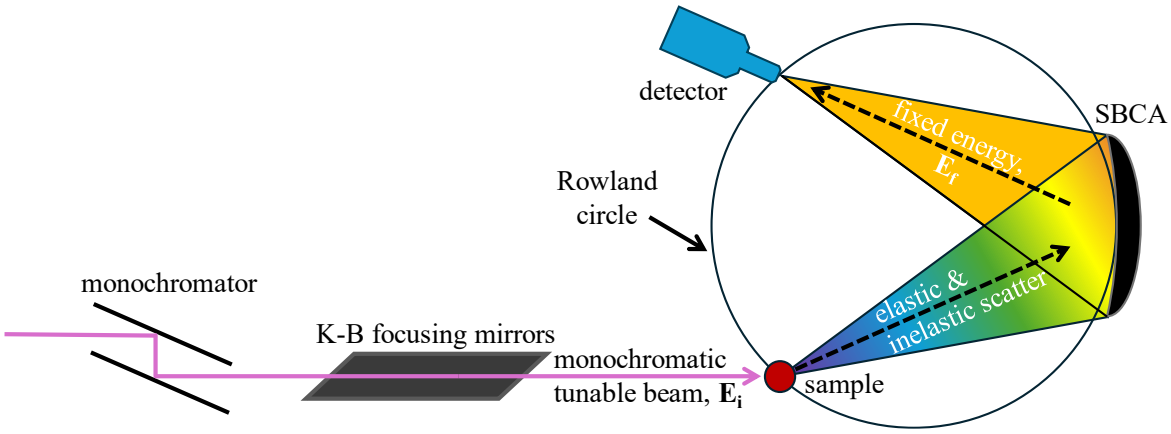

Figure 4. XRS beamline and measurement schematic. The beamline provides a tunable (i.e., energy scannable) monochromatic beam (E_i) at the sample location. The scatterer, SBCA, and detector are arranged symmetrically on the Rowland circle. The SBCA only focuses photons of a fixed energy (E_f) upon the detector.

In principle, XRS measurements are kinematically simple only requiring scattered x-ray analyzers in a static configuration while scanning incident photon energy *via* an upstream monochromator. In practice, XRS is hampered by extremely small scattering cross-sections, requiring brilliant light sources and efficient signal gathering for expedient data collection. With the advent of 3rd generation synchrotron light sources, several dedicated non-resonant IXS and XRS end stations have been constructed at dedicated user facilities[5–7,21–26].

a. XRS End stations

The following review of dedicated XRS synchrotron end stations is complete, with the exception of an IXS/XRS instrument at the Shanghai Synchrotron Research Facility. In general, an XRS spectrometer requires large collection solid angle for expedient measurement and reasonable signal-to-background ratio, Bragg angles near 90^{o} to minimize energy resolution degradation from optic aberrations, and large diameter Rowland circles (1-m) for space for sample environments. Unless noteworthy, the specifications (optic, optic diameter, source-detector clearance, detector) for each instrument are reported in Table 1 at the end of this section. All XRS end stations are in symmetric Bragg Rowland geometry.

i. Stanford Synchrotron Radiation Light source (SSRL): 6-2b

SSRL has a dedicated beam line (6-2b) for high resolution hard x-ray spectroscopy, with a 14-crystal analyzer spectrometer for high-q measurements at backwards scattering angle and a 40-crystal analyzer spectrometer for low-q measurements at forwards scattering angle[7]. The 6-2b XRS spectrometers are at fixed scattering angles and q-selection beyond the subtended scattering angle captured by an array is not possible. The platform can support simultaneous low-q and high-q detection using two detectors.

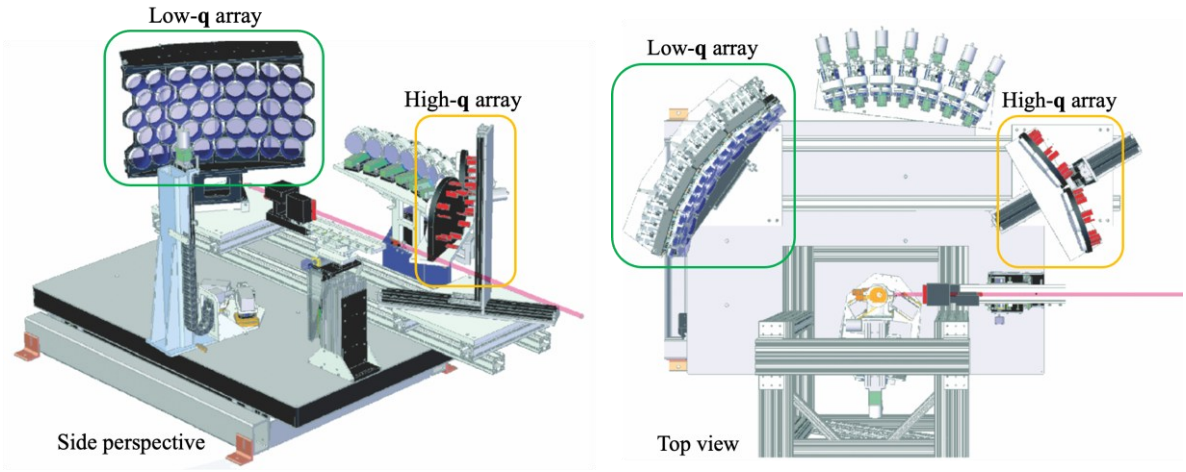

Figure 5. SSRL 6-2b XRS end station layout, with high-*q* and low-*q* analyzer arrays[7].

ii. SOLEIL: GALAXIES

The GALAXIES beamline has a dedicated IXS end station with two integrated analyzer systems (one single optic scanning spectrometer and a multielement array)[25]. The single optic is more suitable for resonant IXS so only the array will be described. Unlike 6-2b at SSRL, the GALAXIES multielement array is on a motorized arm with a circular degree of freedom around the sample which allows for a selection of scattering angles from 0 – 180 deg in the horizontal plane. Furthermore, the array has recently been upgraded from a 4-element array to a 40-element array; photographs of the instrument and the new 40-element array are shown below in Figure 6[25].

Figure 6. **(Left)** The two integrated spectrometers at the GALAXIES end station with the original 4-element NRIXS multi-analyzer array. **(Right)** The 40-element Si(110) 1-m SBCA multi-analyzer array upgrade[25].

iii. SPring-8: BL12XU

The Taiwan inelastic X-ray scattering beamline (BL12XU) hosts a non-resonant IXS and XRS end station at Spring-8[23], shown below in Figure 7. Similar to GALAXIES, the 15-element analyzer array is mounted on a circle curved rail for selecting scattering angle in the horizontal plane. However, here the array is also mounted on a motorized arm that can accommodate Rowland circle diameters from 1-m to 3-m, where larger diameters provide higher energy resolution with diminished collection solid angle.

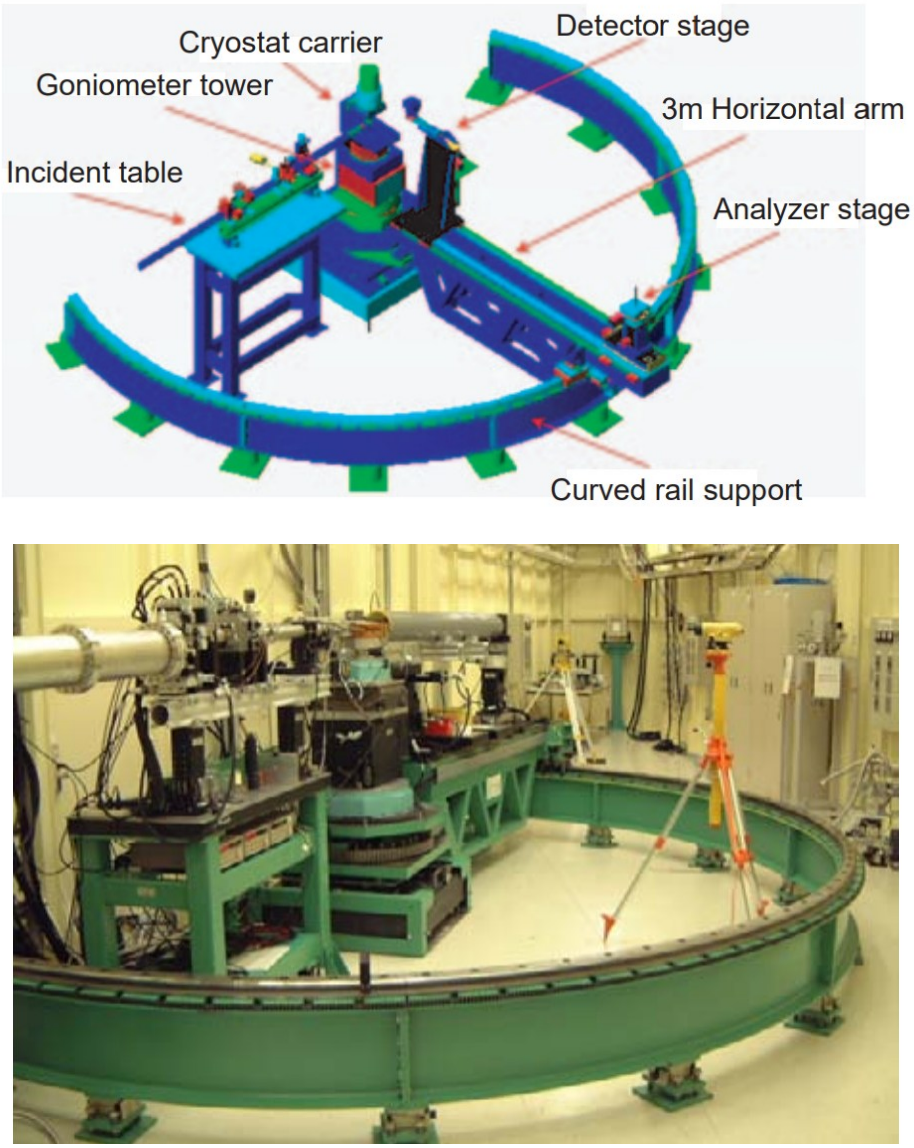

Figure 7. **(Top)** Design rendering of the BL12XU IXS end-station **(Bottom)** Photograph of the IXS end-station in a forward scattering geometry[23].

iv. PETRA III: P01

The P01 IXS/XRS spectrometer at PETRA III is a 12-element array on a circular rail in the vertical plane for free selection of scattering angle[21,26]. A schematic representation of the instrument is shown below with a transparent view of the array in Figure 8 (left). Unlike prior

examples, this instrument has a dedicated rigid enclosure around the array providing a He flight path through most of the spectrometer, shown in Figure 8 (right). A He flight path increases transmitted intensity and reduces stray scatter, thus improving signal-to-noise and collection efficiency.

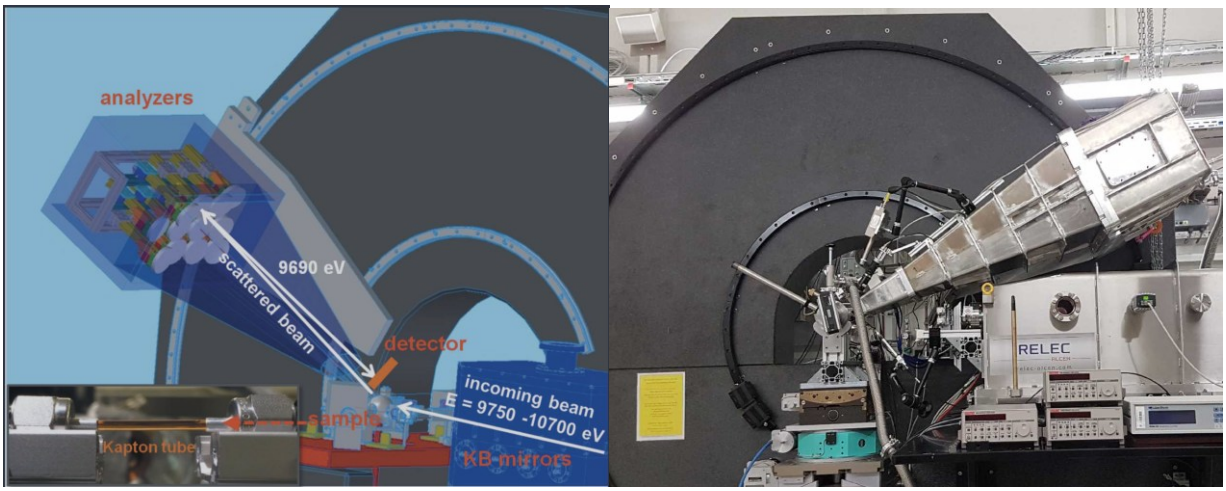

Figure 8. **(Left)** Design rendering of the P01 IXS/XRS 12-element spectrometer in a forward scattering geometry[26] **(Right)** Photograph of the P01 spectrometer in a back scattering geometry. A rigid enclosure provides a He flightpath through the spectrometer[21].

v. ESRF: ID20

The ID20 XRS spectrometer at ESRF consists of 6 modules, 3 in the horizontal scattering plane and 3 in the vertical scattering plane, each with continuous circular degree of freedom for selecting the momentum transfer studied[27]. Each module is a 12-element array of similar design to the PETRA III P01 spectrometer for a total of 72-elements; the ID20 instrument has the largest collection solid angle of all dedicated XRS end stations. Unlike P01, the ID20 instrument can measure XRS at six different q simultaneously.

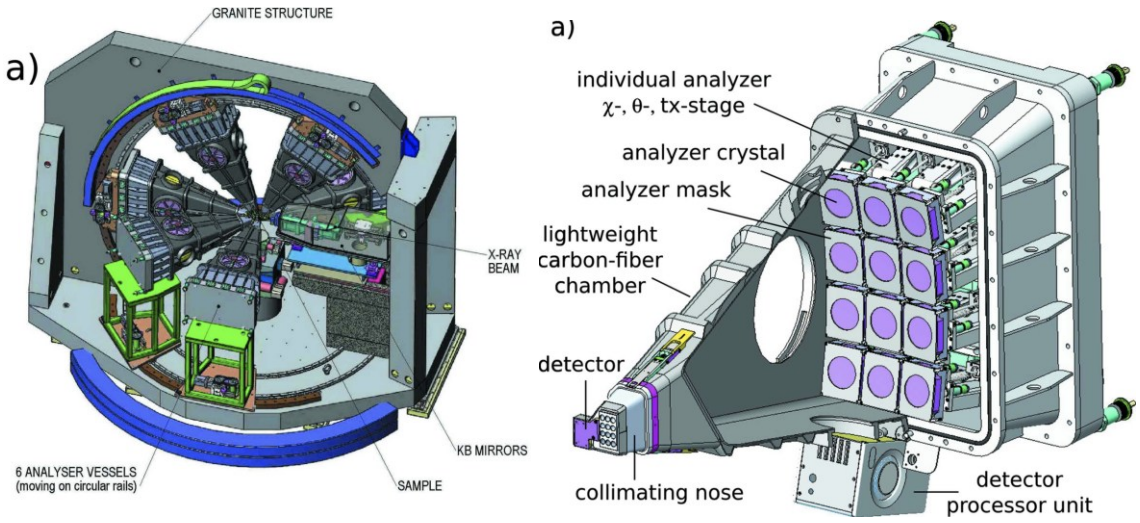

Figure 9. (Left) CAD rendering of the 6 module array of ID20's XRS spectrometer. (Right) A single array contains 12 1-m SBCA's each and its own pixelated area detector[6].

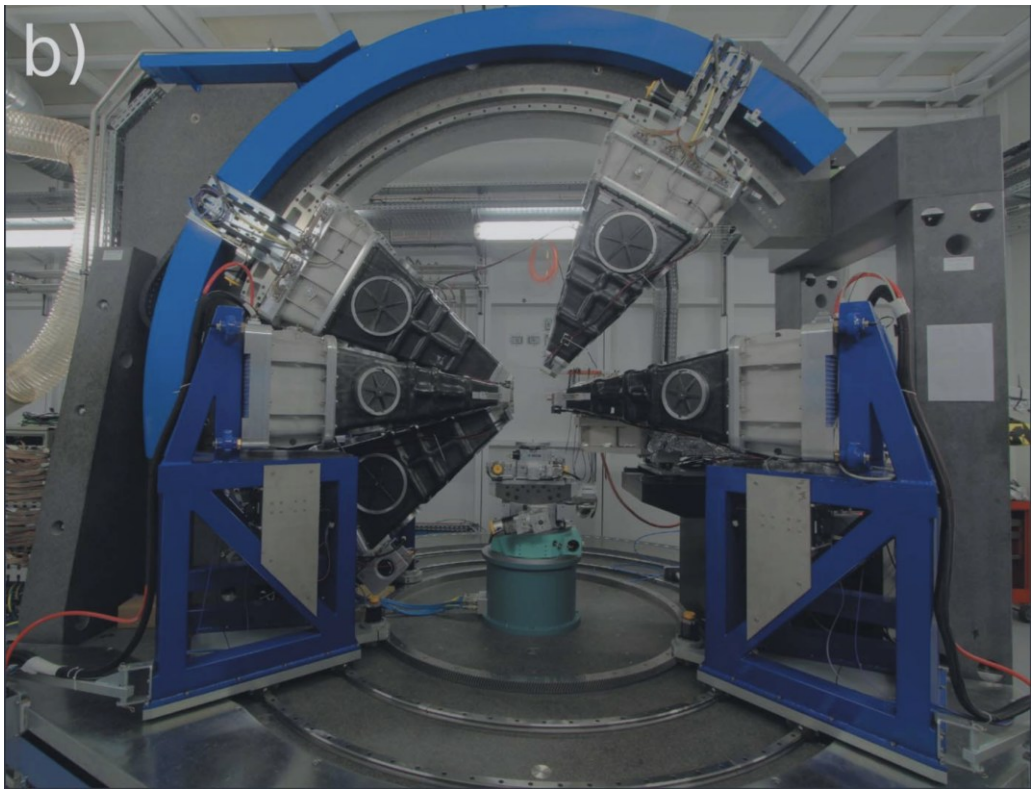

Figure 10. Photograph of the ID20 XRS spectrometer[6].

vi. Brazilian Synchrotron (Sirius): EMA

The extreme condition beamline (EMA) at Sirius is developing a dedicated XRS end station. A 36-element array is mounted on 6+2 diffractometer providing large freedom in selecting scattering geometry[24]; a rendering of the instrument is shown below in Figure 11. Instrumentation development was slowed due to funding freezes in 2019[28].

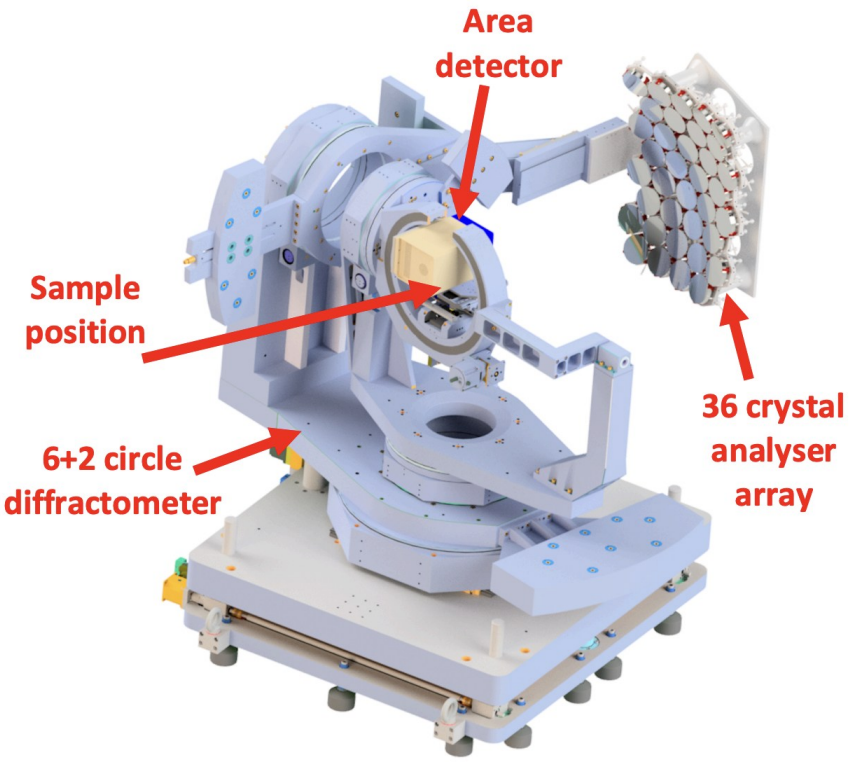

Figure 11. Rendered schematic of the XRS spectrometer at the EMA beamline[24].

vii. Advanced Photon Source (APS): 16-ID-D

The dedicated IXS / XRS spectrometer at Sector 16-ID-D at APS is targeted for *in situ* measurements of samples under high pressure[22]. The spectrometer uses a 17-element array consisting of three rows of analyzers along the vertical plane. Notably, these optics are 50 mm in diameter. A collimating slit at the detector is employed to reject background and improve signal collection efficiency; the author's note background rejection is critical for high-pressure experiments where signals are low and unwanted scatter from windows and pressure media can further contaminate signal.

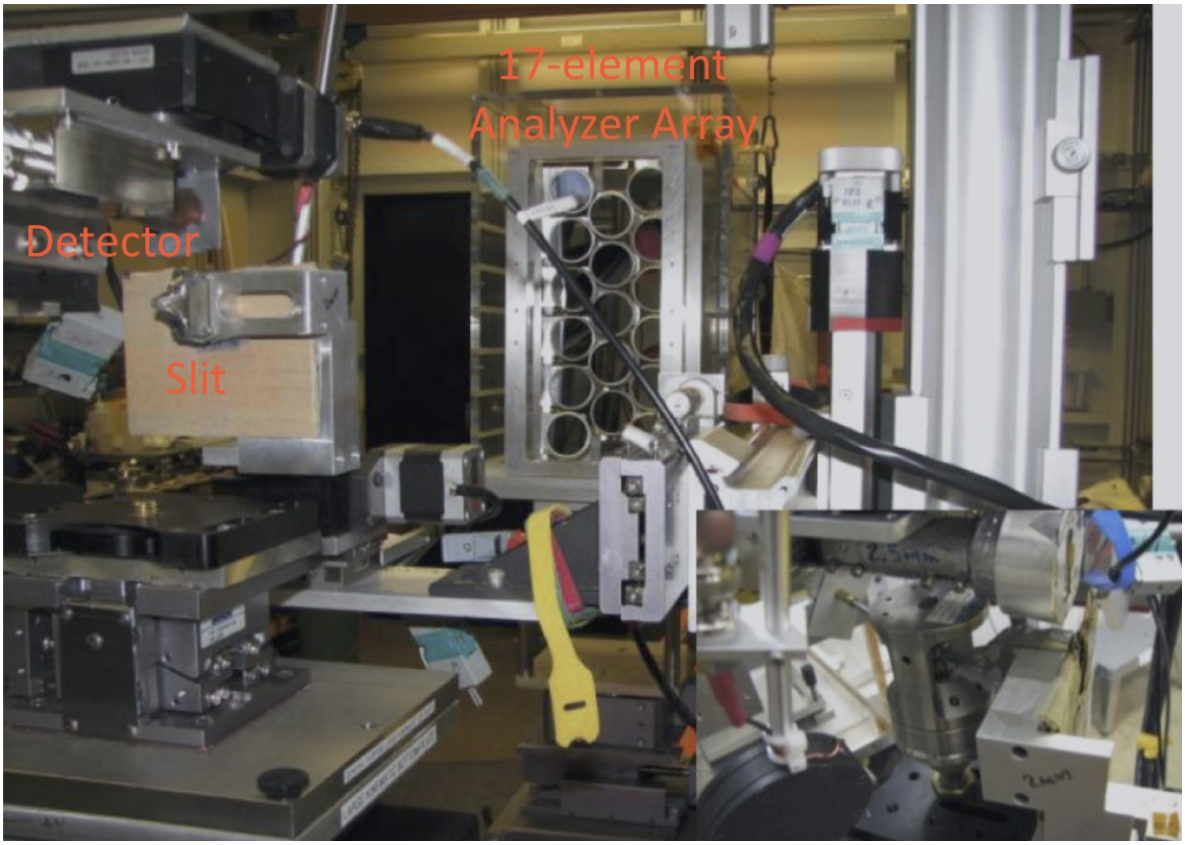

Figure 12. The 17-element IXS / XRS spectrometer at 16-ID-D of APS. The inset (bottom right) shows the sample environment which is a diamond anvil cell[22].

viii. APS: LERIX (decommissioned)

The "LERIX" XRS spectrometer at 20-ID of APS employs 19 SBCAs over a wide range of q arranged symmetrically on the Rowland circle[5]. The analyzers provide up to 19 simultaneous but independent measurements of *q*-dependent XRS and focus to their own independent detector at a fixed Bragg angle of 88.2°. Except for motorized degrees of freedom for tuning the optics, the instrument is entirely fixed. LERIX can simultaneously measure and distinguish momentum transfers from 0.8 – 10.1 $Å^{-1}$.

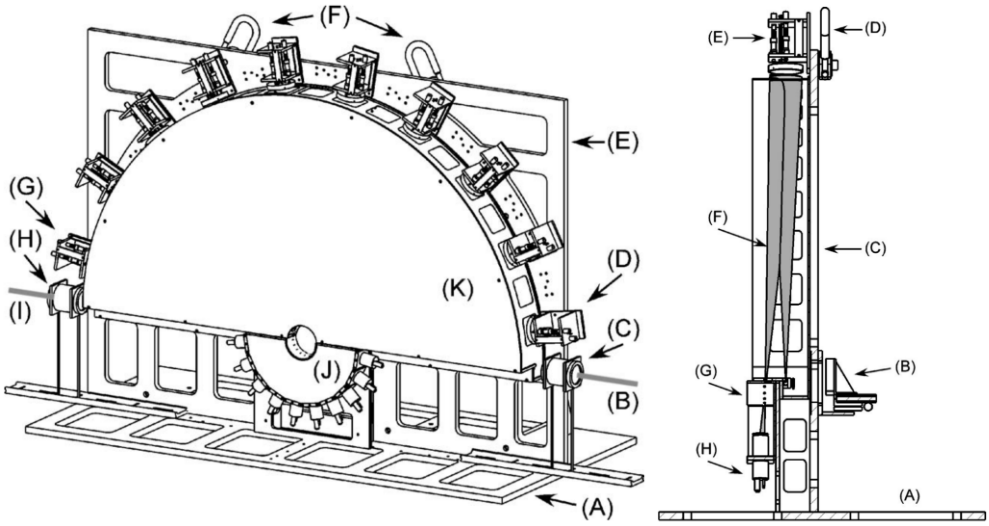

Figure 13. **(Left)** Perspective line drawing of the LERIX spectrometer with 10 of the 19 analyzers shown. **(Right)** Ray tracing schematic of a single SBCA collecting signal and focusing it to its associated detector[5].

b. Summary of Dedicated XRS End Stations

A summary of all dedicated XRS / NRIXS end stations at user facilities is shown below in Table 1, except for the SSRF instrument. The conclusions are the following. First, all instruments employ Johann-type SBCAs in symmetric Bragg diffraction Rowland circle focusing geometries with 1-m bending diameter for reasonable clearances between sample and detector, despite availability of 0.5-m optics. Second, a high number of optics (from 12 – 72) are needed for efficient signal collection. Third, only the LERIX, PETRA III, and ESRF instruments had dedicated rigid He flightpaths. Lastly, only the LERIX, SSRL, and ESRF spectrometers can support simultaneous q measurements.

Table 1. Summary of all dedicated synchrotron XRS end stations.

Facility	Beamline	Optic	# of optics	Solid angle (msr)	θ_B (°)	2θ (°)	Sample clearance (mm)	Detectors
SSRL[7]	6-2b	diced Si(110)	54	420	88	15–65, 125–165	70, 125	SDD
SOLEIL[25]	GALAXIES	diced Si(110)/ Si(111)	40	320	89	0–180	75	SDD APD PAD
SPring-8[23]	BL12XU	bent Ge(111)	15	120	88.9	5–175	75	SDD
PETRA III[21]	P01	bent Si(110)	12	95	88.3	0–180	125	PAD
ESRF[6]	ID20	bent Si(110)	72	450	88.9	0–175	75	PAD
Sirius[24]	EMA	---	36	280	---	---	---	---
APS[22]	16-ID-D	bent Si(111)	17	34*	87.7	0–90	65	SDD
APS[5]	LERIX	bent Si(111)	19	150	88.2	6–175	65	Sc

SDD – silicon drift diode, APS – avalanche photodiode, PAD – pixelated area detector, Sc – scintillator
*50 mm optic diameter

c. Sub-techniques Enabled by Area Detectors

The use of pixelated 2D area detectors in XRS instruments can improve energy resolution or be used to spatially image a scattering sample and its environment. These additional sub-techniques and methods will be discussed. We note the improved energy resolution with pixelated area detectors is general to all bent crystal spectrometers.

i. Improved Energy Resolution

All dedicated XRS end stations employ high resolution SBCAs in backscattering geometries, which minimizes the intrinsic, geometric, and source-size contributions to energy resolution. Even in this mitigating geometry, distortions and strains in the crystalline wafer can still reasonably degrade energy resolution. These strains result in a spatial dispersion of analyzed energies at the detector position.

Unlike a scintillator or spectroscopic detector, a photon counting pixelated 2D area detector records a complete spectrum for each pixel. Thus a spatial dispersion of energies at the SBCA focus can be corrected by shifting each pixel's spectrum to a centroid energy. The principle of sub-analyzer compensation and peak alignment to a centroid energy is shown in Figure 14. This so-called dispersion-compensation correction was first demonstrated by Huotari et al. (2005) using an area detector on the Rowland circle perimeter and post-processing to improve the energy resolution response function of a diced-flat SBCA[29]. This reduced cube-size contributions for IXS measurements and improved energy resolution from 213 meV to 23 meV at 9.9 keV[29].

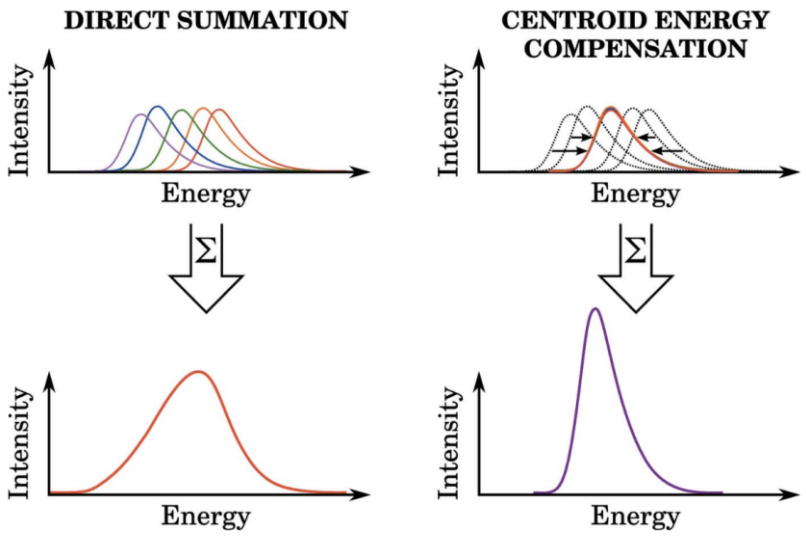

Figure 14. Post-processing dispersion compensation where the shifting of each pixel's spectrum before summation yields improved energy resolution[30].

An improvement to the technique was later reported by Honkanen et al. (2014)[30]. Placement of the area sensitive detector inside the Rowland circle further dispersed the imaging across the detector and allowed easier mapping of the energy distribution of the analyzer surface, shown in Figure 15. This method was demonstrated with XRS and improved the overall resolution from 1.0 eV to 0.46 eV.

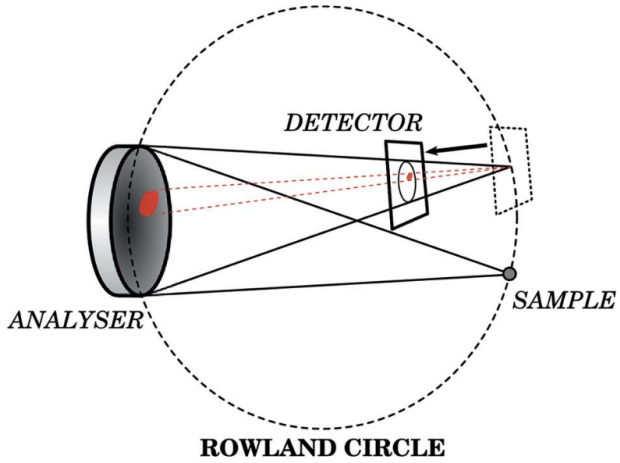

Figure 15. Off-focus imaging used to achieve a larger spatial dispersion of energy[30].

ii. "Direct Tomography"

When using a position sensitive detector on the Rowland circle perimeter, XRS can be used as phase-contrast mechanism for imaging. The transmission of the incident beam through a sample creates a line or volume scatterers along the Rowland circle. Any scattering point illuminated by the incident beam is projected by the SBCA to a unique point on the area detector, shown in Figure 16. Thus scanning the incident beam across a sample can map a 3D structure. The technique, so-called "direct tomography" (owing to it not requiring the reconstruction of many tomograms to make a 3D image) or "X-ray Raman imaging" was first reported by Huotari et al. (2011)[31]. Later improvements by Sahle et al. (2016) improved the spatial and statistical accuracy with the development of a reconstruction algorithm for imaging with multiple analyzers simultaneously[32]. This 3D mapping technique has been applied to systems such as carbon speciation of organic fossils[33].

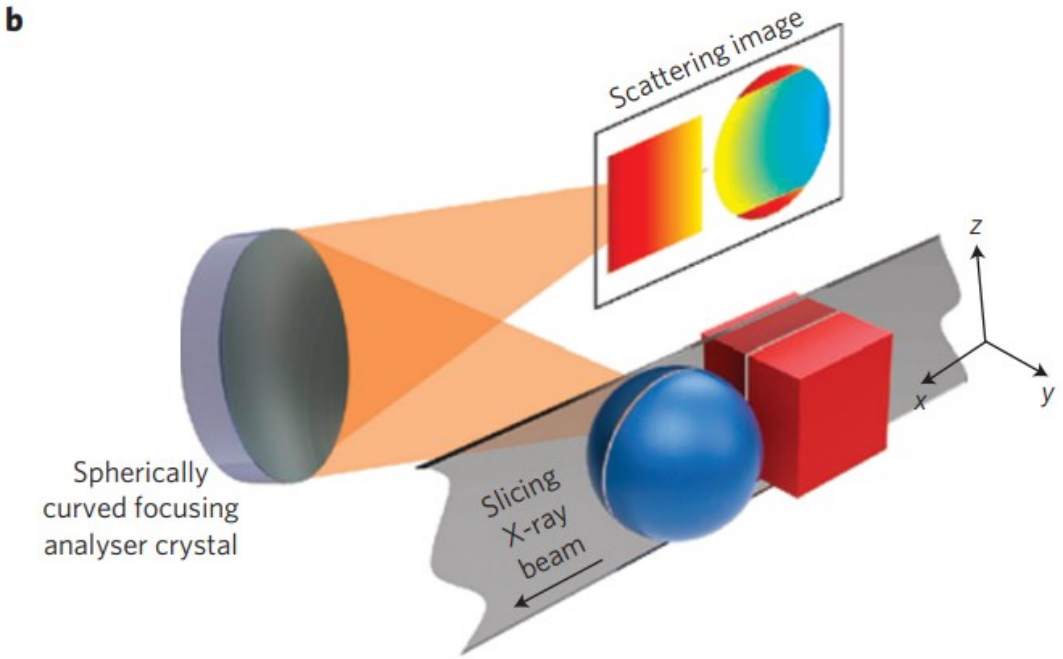

Figure 16. The direct tomography technique where each voxel illuminated by the incident beam is refocused by the SBCA to a unique point on the detector.[31]

The draw backs of the 3D mapping and particularly 4D spectral mapping of direct tomography are the slow acquisition times and prolonged beam exposure, which can damage organic samples. Recent work by Cazals et al. (2025) used a digital twin to reduce acquisition times by a factor of 10 for 4D XRS direct tomography spectral imaging[34]. More applications of direct tomography on radiosensitive samples may be seen in the future.

Frequently, a complete 4D spectral map of a sample is not necessary. Significant benefits exist for *in situ* and *operando* measurements where the sample is within an enclosure. Here, rather than direct tomography, we refer to this as X-ray Raman imaging. A pixelated area detector is used to spatially reject scatter from the sample enclosure, such as gaskets, pressure media, and cell windows and allow a region of interest selecting only sample scatter[35]. This significantly enhances signal acquisition by eliminating non-sample scatter. X-ray Raman imaging is frequently applied and optimized for *in situ* measurements of diamond anvil cells, an example is shown in Figure 17 below.

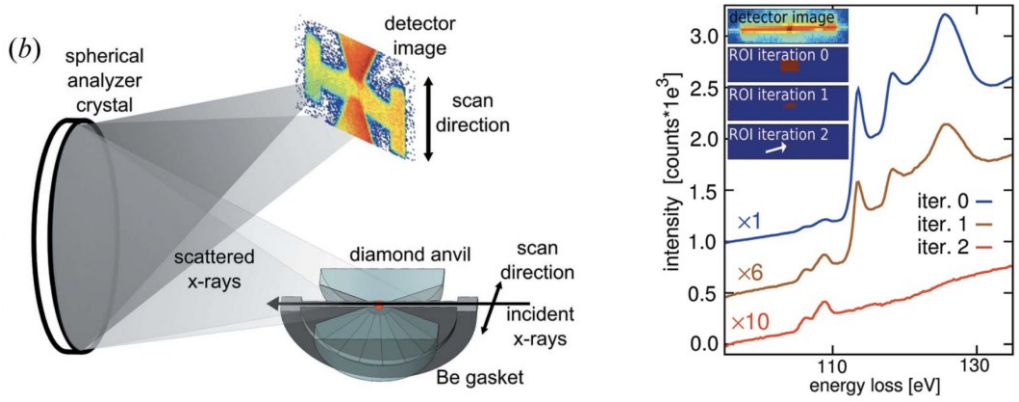

Figure 17. **(Left)** X-ray Raman imaging, used to spatially image a sample within an enclosure. Here, the beam is scanned to generate a 2D image through a diamond anvil cell[35]. **(Right)** With the beam fixed and transmitting through the center of the diamond anvil cell, a region of interest can select scatter from only the sample isolated from its surroundings, shown as the signal of "iter. 2" (red)[35].

3. XRS Applications

In the past 20 years, XRS has developed into a mature technique accomplishing science beyond demonstrative studies of simple model systems[36]. Here, we review and highlight some of the many applications of the technique across different fields of materials characterization.

a. High-pressure Science

Arguably the largest materials characterization niche XRS is applied to is high-pressure science, frequently *in situ* measurements within diamond anvil cells (DACs). XRS is one of the only X-ray techniques that can probe soft absorption edges of the bulk sample with sufficient penetrating power to do so *in situ*. Thus XRS is a valuable tool for high pressure studies, and several reviews of this application are provided by Lee et al.[37], Sahle et al[38], Hiraoka et al.[39], Sterneman and Wilke[40], and Hiraoka and Cai[41].

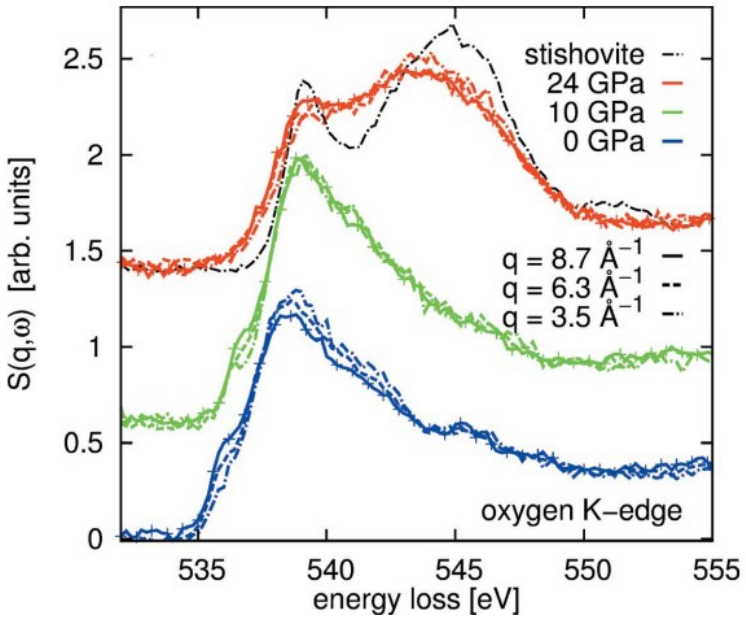

Figure 18. *In situ* XRS measurement of α-quartz O *K*-edge in a DAC at varying pressures. A change to six-fold coordination is observed at 24 GPa[35].

We highlight one such example from Sahle et al. (2017). Here, they monitor the O *K*-edge of α-quartz in a DAC at increasing pressure using XRS[35]. At ambient conditions, O is twofold coordinated with Si. As shown above in Figure 18, a broad feature in the O *K* XANES at 24 GPa indicate a transition to sixfold coordination. This is further proved by comparison to a stishovite reference sample, a known sixfold coordinated reference.

b. Battery Science

XRS is a powerful tool for bulk measurements of the conductive ions (Li, Na) or anions (O) *K*-edges, 3*d* transition metal cathode *L*-edges, and graphite electrode C *K*-edges at ambient conditions, often *in situ*. Here, we highlight some examples of XRS applied to battery materials.

Nonaka et al. (2019) used XRS to study the lithiation of lithium-intercalated graphite anodes[42]. A specially developed *in situ* cell was used for measurement, and C *K*-edge of LiC_6, LiC_{12}, and pure graphite were obtained during discharging of a Li-graphite pouch cell. The C *K*-edge at varying cell voltages is shown in Figure 19, and the spectral changes are attributed to change in electronic structure of the graphite electrode. Nonaka et al. highlights the technique for future studies of graphite electrodes.

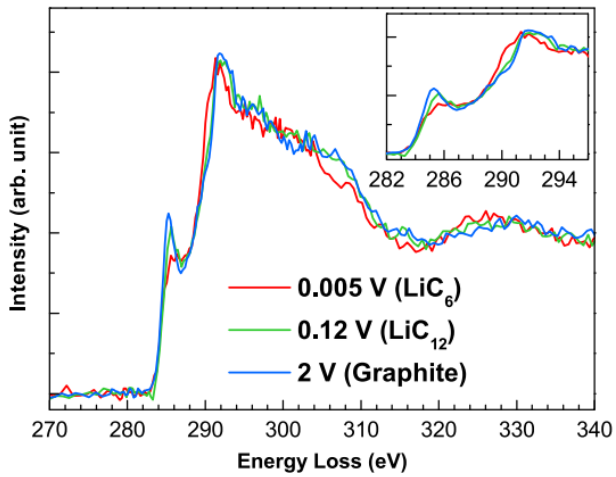

Figure 19. C *K*-edge XRS spectra of the *in situ* graphite coin-cell during discharging[42].

Fehse et al. (2019) used XRS to understand the charge compensation in electrodes. Here, they examined the Fe *L*-edge and O *K*-edge of a Li_2FeSiO_4 electrode using XRS[43]. The note the transition metal *L*-edge as a direct probe of redox activity. Figure 20 (left) shows a sensitivity to formal oxidation state and spin-state during the charge cycle of the battery[43]. Unlike Fe, they find the O K-edge formal oxidation state is unchanged during charging but note changes in a pre-edge feature and twin peak in the white line, shown in Figure 20 (right). The increase in oxygen pre-edge intensity is attributed to metal-oxygen hybridization[43].

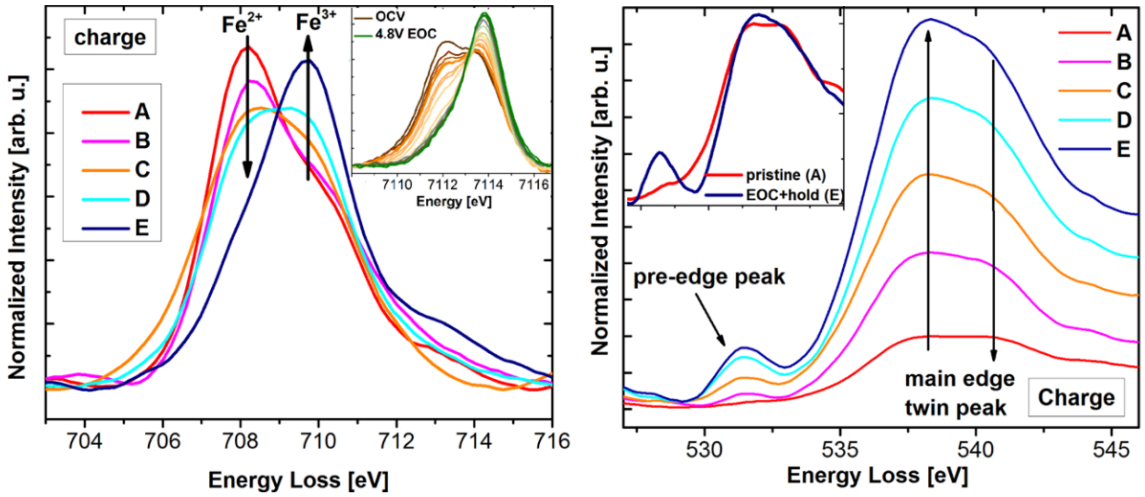

Figure 20. XRS *in situ* monitoring of a charging Li_2FeSiO_4 electrode's **(Left)** Fe *L*-edge and **(Right)** O *K*-edge. The electrode begins fully discharged in 'A' and fully charged in 'E'[43].

A final example is presented from Huang et al. (2024) where XRS was used to understand the lithiation of Li/SiO_x batteries[44]. Here, Li/SiO_x samples were electrochemically prepared to different lithiation states and measured *ex situ*. They find, after fitting the Li *K*-edge spectra (Fig. 21) to pseudo-Voigt peaks and comparing to theory, an earlier formation of Li_xSiO_y before Li_xSi during lithiation[44].

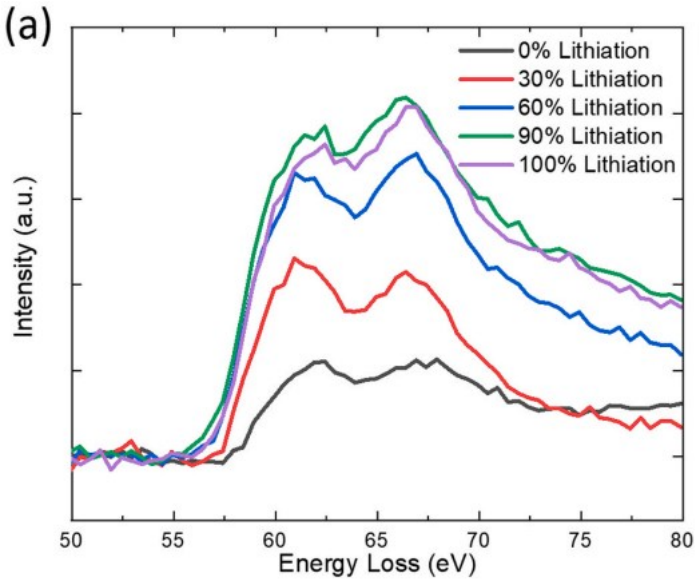

Figure 21. *Ex situ* Li *K*-edge XRS spectra at varying electrochemically prepared states of lithiation of Li/SiO_x[44].

c. Catalyst Science

XRS is also suitable for *ex situ* and *in situ* measurements of catalyst materials. Here, we report two contemporary applications of XRS to catalyst science.

Das et al. (2024) used XRS to characterize a $Ni/MgFeAlO_4$ catalyst for the dry production of methane[45]. A catalytic cell was prepared and measured *in situ* with flow. The cell was cycled from pristine to different phases of reduction / reoxidation, and held at these conditions during XRS measurements. The Al *L*-edge and O *K*-edge are shown in Figure 22. The Al is in the spinel support of the catalyst, and they find changes in the cation distribution in the spinel structure effects the Al white line intensity[45]. Combining theory with the O *K*-edge signal, they find the main peak and shoulder ratio of the white line indicative of electron transfer between the oxygen and transition metals[45].

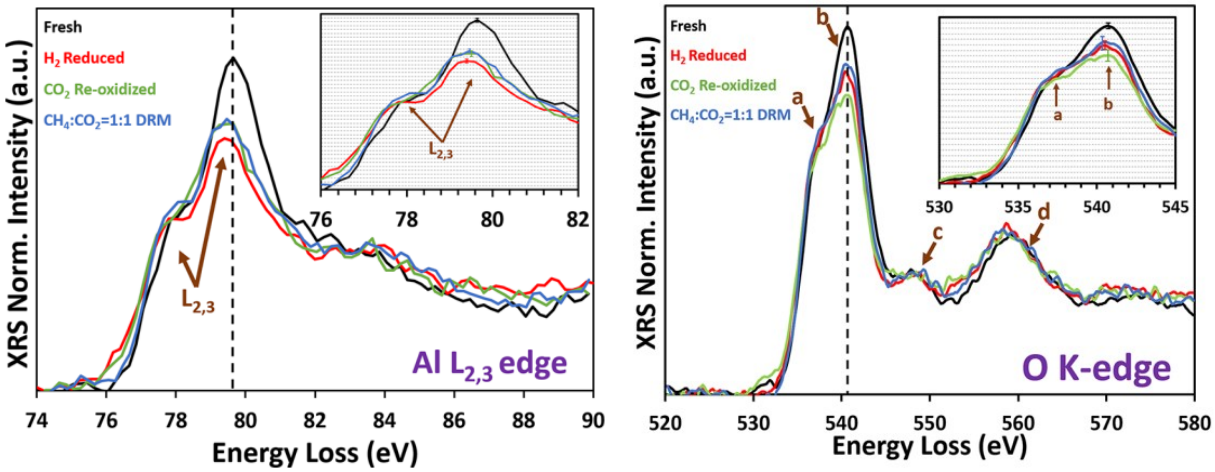

Figure 22. XRS spectra of a Ni/$MgFeAlO_4$, monitoring the **(left)** Al *L*-edge and **(right)** O *K*-edge[45].

Ceria (CeO_2)is an important catalyst support material for its ability to support oxygen vacancies. Longo et al. (2023) used XRS to measure the O *K*-edge (Figure 23) and Ce $N_{4,5}$-edge of a Au/CeO_2 catalyst during a CO oxidation reaction[46]. Combining XRS with density functional theory and multiple simulations, they find that the clustering of O vacancies is not limited to the surface but dispersed through the bulk of the ceria support[46].

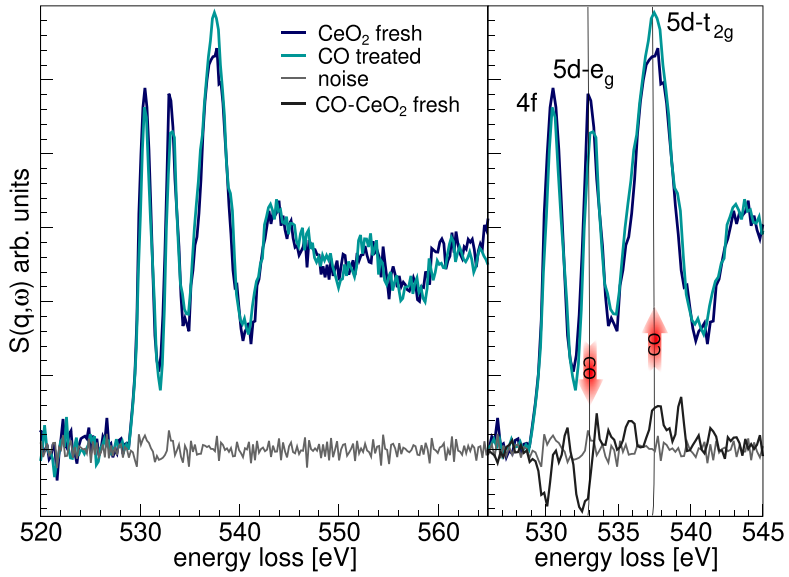

Figure 23. XRS O *K*-edge of CeO_2 before and after CO treatment. The right panel identifies subtle features by the difference of CeO_2 and CO-treated spectra[46].

d. Momentum Transfer Dependence

Lastly, XRS is also capable of momentum dependent measurements, as previously discussed in Section 1, and we aim to highlight some of the applications of *q*-dependent XAFS and its depth of information here.

Mattila et al. (2005) used *q*-dependent XRS spectra to investigate the electronic structure of a single crystal of MgB_2, a superconductor[13]. Their goal in a *q* dependent study was to separate different excitations (monopolar, dipolar, quadrupolar) at different *q*. They find a large density of p_{xy} and p_z states and highlight the p_{xy} density of states in the superconducting properties of MgB_2[13]. Their method combined experimental XRS measurements with theory calculations, *q* dependent B *K*-edge spectra are shown below in Figure 24.

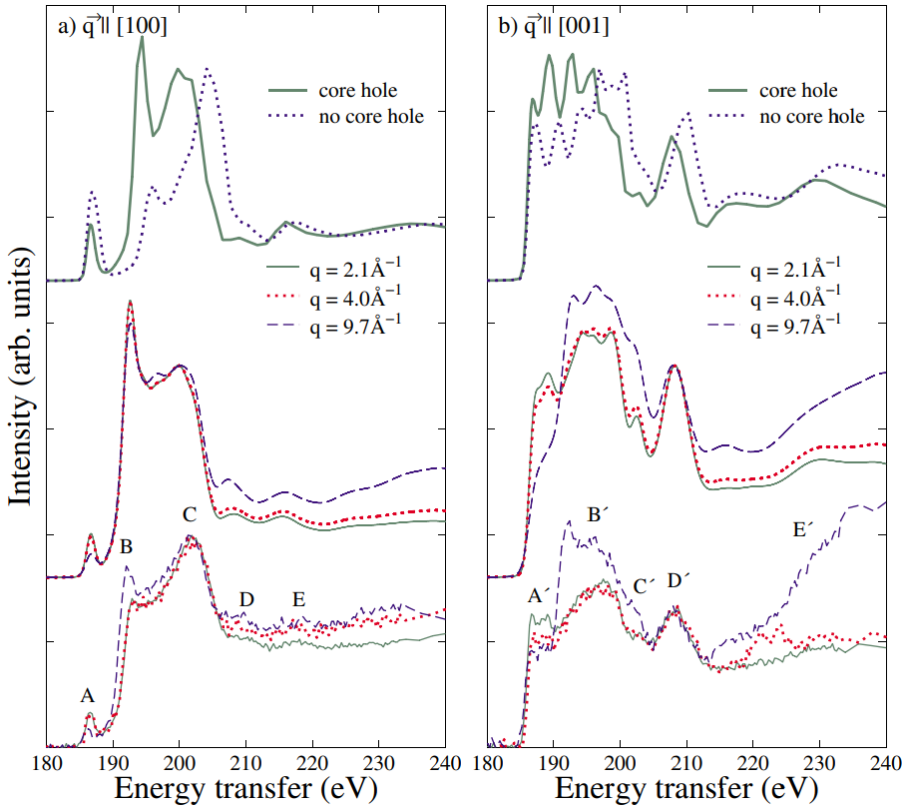

Figure 24. *q*-dependence of MgB_2 B *K*-edge measured *via* XRS in two orientations, **(left)** [100] and **(right)** [001].The experimental results are on the bottom, theory calculations are the center and top[13].

More generally, Fister et al. (2006) reports the *q*-dependent oscillations in the XRS measured dynamic structure factor above an absorption edge (extended X-ray absorption fine structure (EXAFS) analogue) can be enhanced with increasing *q*[10]. Simulations of the magnified oscillations with increasing *q* are shown below in Figure 25 for the Al L_2-edge. This was experimentally verified in the same work as a method for easier measurement of low-Z "EXAFS" *via* XRS. Later work by Huotari et al. (2011) reported on the analysis of XRS-EXAFS beyond the dipole limit, and found a diminishing signal-to-noise ratio with increasing *q* and increased sensitivity to multiple-scattering paths of the photoelectron at high *q* in the case of C *K*-edge EXAFS of polycrystalline diamond[16].

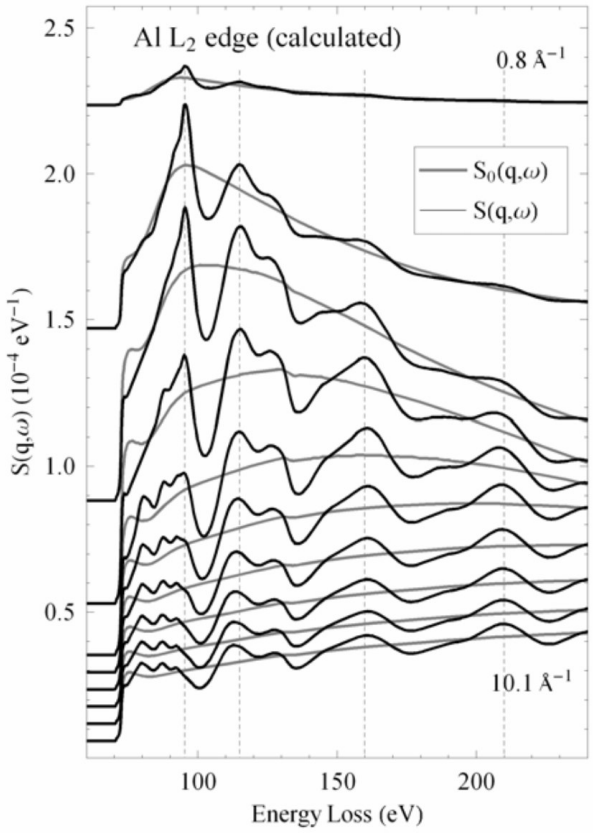

Figure 25. Theory calculated extended oscillations in the dynamical structure factor of the Al L_2-edge from 0.8 Å^{-1} to 10.1 Å^{-1} [10].

4. References

1 W. Schülke, *Electron dynamics by inelastic X-ray scattering*, University Press, Oxford, 1st ed., 2023.
2 S. Huotari, T. Pylkkänen, R. Verbeni, G. Monaco and K. Hämäläinen, *Nature Mater*, 2011, **10**, 489–493.
3 R. A. Gordon, G. T. Seidler, T. T. Fister, M. W. Haverkort, G. A. Sawatzky, A. Tanaka and T. K. Sham, *EPL*, 2008, **81**, 26004.
4 C. J. Sahle, A. Mirone, J. Niskanen, J. Inkinen, M. Krisch and S. Huotari, *J. Synchrot. Radiat.*, 2015, **22**, 400–409.
5 T. T. Fister, G. T. Seidler, L. Wharton, A. R. Battle, T. B. Ellis, J. O. Cross, A. T. Macrander, W. T. Elam, T. A. Tyson and Q. Qian, *Rev. Sci. Instrum.*, 2006, **77**, 063901.
6 S. Huotari, C. J. Sahle, C. Henriquet, A. Al-Zein, K. Martel, L. Simonelli, R. Verbeni, H. Gonzalez, M.-C. Lagier, C. Ponchut, M. Moretti Sala, M. Krisch and G. Monaco, *J Synchrotron Rad*, 2017, **24**, 521–530.
7 D. Sokaras, D. Nordlund, T.-C. Weng, R. A. Mori, P. Velikov, D. Wenger, A. Garachtchenko, M. George, V. Borzenets, B. Johnson, Q. Qian, T. Rabedeau and U. Bergmann, *Rev. Sci. Instrum.*, 2012, **83**, 043112.
8 D. Ketenoglu, *X-Ray Spectrom.*, 2022, **51**, 422–443.
9 T. T. Fister, G. T. Seidler, L. Wharton, A. R. Battle, T. B. Ellis, J. O. Cross, A. T. Macrander, W. T. Elam, T. A. Tyson and Q. Qian, *Rev. Sci. Instrum.*, 2006, **77**, 063901.
10 T. T. Fister, G. T. Seidler, C. Hamner, J. O. Cross, J. A. Soininen and J. J. Rehr, *Phys. Rev. B*, 2006, **74**, 214117.
11 J. A. Soininen, A. L. Ankudinov and J. J. Rehr, *Phys. Rev. B*, 2005, **72**, 045136.
12 S. A. Ceppi and G. E. Stutz, *J. Electron Spectrosc. Relat. Phenom.*, DOI:10.1016/j.elspec.2022.147207.
13 A. Mattila, J. A. Soininen, S. Galambosi, S. Huotari, G. Vankó, N. D. Zhigadlo, J. Karpinski and K. Hämäläinen, *Phys. Rev. Lett.*, 2005, **94**, 247003.
14 C. Sternemann, M. Volmer, J. A. Soininen, H. Nagasawa, M. Paulus, H. Enkisch, G. Schmidt, M. Tolan and W. Schülke, *Phys. Rev. B*, 2003, **68**, 035111.
15 R. A. Gordon, M. W. Haverkort, S. Sen Gupta and G. A. Sawatzky, in *14th International Conference on X-Ray Absorption Fine Structure (xafs14), Proceedings*, eds. A. DiCicco and A. Filipponi, IoP Publishing Ltd, Bristol, 2009, vol. 190, p. 012047.
16 S. Huotari, T. Pylkkanen, J. A. Soininen, J. J. Kas, K. Hamalainen and G. Monaco, *J. Synchrot. Radiat.*, 2012, **19**, 106–113.
17 J. A. Bradley, G. T. Seidler, G. Cooper, M. Vos, A. P. Hitchcock, A. P. Sorini, C. Schlimmer and K. P. Nagle, *Phys. Rev. Lett.*, 2010, **105**, 053202.
18 J. A. Soininen, A. L. Ankudinov and J. J. Rehr, *Phys. Rev. B*, 2005, **72**, 045136.
19 R. Georgiou, C. J. Sahle, D. Sokaras, S. Bernard, U. Bergmann, J.-P. Rueff and L. Bertrand, *Chem. Rev.*, DOI:10.1021/acs.chemrev.1c00953.
20 *X-ray Data Booklet*, Lawrence Berkeley National Laboratory, University of California, 2001.
21 C. Weis, G. Spiekermann, C. Sternemann, M. Harder, G. Vanko, V. Cerantola, C. J. Sahle, Y. Forov, R. Sakrowski, I. Kupenko, S. Petitgirard, H. Yavas, C. Bressler, W. Gawelda, M. Tolan and M. Wilke, *J. Anal. At. Spectrom.*, 2019, **34**, 384–393.
22 Y. M. Xiao, P. Chow, G. Boman, L. G. Bai, E. Rod, A. Bommannavar, C. Kenney-Benson, S. Sinogeikin and G. Y. Shen, *Rev. Sci. Instrum.*, 2015, **86**, 072206.

23 Y. Q. Cai, P. Chow, C. C. Chen, H. Ishii, K. L. Tsang, C. C. Kao, K. S. Liang and C. T. Chen, in *Synchrotron Radiation Instrumentation*, eds. T. Warwick, J. Arthur, H. A. Padmore and J. Stohr, Amer Inst Physics, Melville, 2004, vol. 705, pp. 340–343.
24 R. D. dos Reis, U. F. Kaneko, B. A. Francisco, J. Fonseca, M. a. S. Eleoterio and N. M. Souza-Neto, in *27th Airapt International Conference on High Pressure Science and Technology*, IoP Publishing Ltd, Bristol, 2020, vol. 1609, p. 012015.
25 J. M. Ablett, D. Prieur, D. Ceolin, B. Lassalle-Kaiser, B. Lebert, M. Sauvage, T. Moreno, S. Bac, V. Baledent, A. Ovono, M. Morand, F. Gelebart, A. Shukla and J.-P. Rueff, *J. Synchrot. Radiat.*, 2019, **26**, 263–271.
26 D. Ketenoglu, G. Spiekermann, M. Harder, E. Oz, C. Koz, M. C. Yagci, E. Yilmaz, Z. Yin, C. J. Sahle, B. Detlefs and H. Yavas, *J. Synchrot. Radiat.*, 2018, **25**, 537–542.
27 S. Huotari, C. J. Sahle, C. Henriquet, A. Al-Zein, K. Martel, L. Simonelli, R. Verbeni, H. Gonzalez, M.-C. Lagier, C. Ponchut, M. Moretti Sala, M. Krisch and G. Monaco, *J Synchrotron Rad*, 2017, **24**, 521–530.
28 Brazil's government freezes nearly half of its science spending, https://www.nature.com/articles/d41586-019-01079-9, (accessed March 3, 2026).
29 S. Huotari, G. Vankó, F. Albergamo, C. Ponchut, H. Graafsma, C. Henriquet, R. Verbeni and G. Monaco, *J. Synchrot. Radiat.*, 2005, **12**, 467–472.
30 A.-P. Honkanen, R. Verbeni, L. Simonelli, M. M. Sala, A. Al-Zein, M. Krisch, G. Monaco and S. Huotari, *J. Synchrot. Radiat.*, 2014, **21**, 762–767.
31 S. Huotari, T. Pylkkanen, R. Verbeni, G. Monaco and K. Hamalainen, *Nat. Mater.*, 2011, **10**, 489–493.
32 C. J. Sahle, A. Mirone, T. Vincent, A. Kallonen and S. Huotari, *J. Synchrot. Radiat.*, 2017, **24**, 476–481.
33 R. Georgiou, P. Gueriau, C. J. Sahle, S. Bernard, A. Mirone, R. Garrouste, U. Bergmann, J.-P. Rueff and L. Bertrand, *Science Advances*, 2019, **5**, eaaw5019.
34 L. Cazals, A. Desolneux, S. Huotari, L. Dalecky, C. Sahle, A. Mirone, S. X. Cohen and L. Bertrand, *Science Advances*, 2025, **11**, eadw5444.
35 C. J. Sahle, A. D. Rosa, M. Rossi, V. Cerantola, G. Spiekermann, S. Petitgirard, J. Jacobs, S. Huotari, M. M. Sala and A. Mirone, *J. Synchrot. Radiat.*, 2017, **24**, 269–275.
36 U. Bergmann, P. Glatzel and S. P. Cramer, *Microchem J.*, 2002, **71**, 221–230.
37 S. K. Lee, P. J. Eng and H. Mao, *Reviews in Mineralogy and Geochemistry*, 2014, **78**, 139–174.
38 C. J. Sahle, S. Petitgirard, G. Spiekermann, R. Sakrowski, N. Suomalainen, F. Gerbon, J. Jacobs, Y. Watier, C. Sternemann, M. Moretti Sala and V. Cerantola, *High Pressure Research*, 2024, **44**, 337–360.
39 N. Hiraoka, H. Fukui and T. Okuchi, *High Pressure Res.*, 2016, **36**, 250–261.
40 C. Sternemann and M. Wilke, *High Pressure Research*, 2016, **36**, 275–292.
41 N. Hiraoka and Y. Q. Cai, *Synchrotron Radiation News*, 2010, **23**, 26–31.
42 T. Nonaka, H. Kawaura, Y. Makimura, Y. F. Nishimura and K. Dohmae, *J. Power Sources*, 2019, **419**, 203–207.
43 M. Fehse, C. J. Sahle, M. P. Hogan, C. Cavallari, E. M. Kelder, M. Alfredsson and A. Longo, *J. Phys. Chem. C*, 2019, **123**, 24396–24403.
44 H.-J. Huang, C.-S. Hsu, J.-Y. Huang, S.-C. Haw, H.-Y. Chen, N. Hiraoka, Y.-F. Liao and C.-W. Hu, *J. Power Sources Adv.*, 2024, **29**, 100155.

45 S. K. Das, L. D'ooghe, N. V. Srinath, S.-A. Theofanidis, A. Longo, C. Sahle, K. Van Geem, H. Poelman, D. Poelman and V. Galvita, *ACS Catal.*, 2024, **14**, 1311–1323.
46 A. Longo, A. Mirone, E. D. C. Gallerande, C. J. Sahle, M. P. Casaletto, L. Amidani, S. A. Theofanidis and F. Giannici, *Cell Rep. Phys. Sci.*, 2023, **4**, 101699.

Chapter 4. High Energy Resolution Fluorescence Detected X-ray Absorption Spectroscopy Background, Applications, and Instrumentation

1. Core-hole Lifetime Broadening in XAS measurements

X-ray absorption spectroscopy (XAS) is a widely applied technique for studying the electronic structure of materials and probing the unoccupied density of states (DOS). For example, pre-edge features of the XANES can inform local symmetry (tetrahedral, octahedral) and orbital angular momentum character, whereas the position of the absorption edge can inform the formal oxidation state of the probed species[1].

The simplest measurement of XAS of the *K*-edge, for example, involves scanning the incident energy over the 1*s* binding energy of the probed element. Photo absorption occurs when the incident energy ≥ 1*s* binding energy, the 1s electron is excited to an intermediate state, and a core hole vacancy is left behind in the *K*-shell (Figure 1 (a)). This excited intermediate state with a core hole vacancy is short lived (~femtoseconds); an electron from a higher shell fills the core hole and releases energy, either characteristic fluorescence (see Figure 1 (b)) or through Auger electron decay.

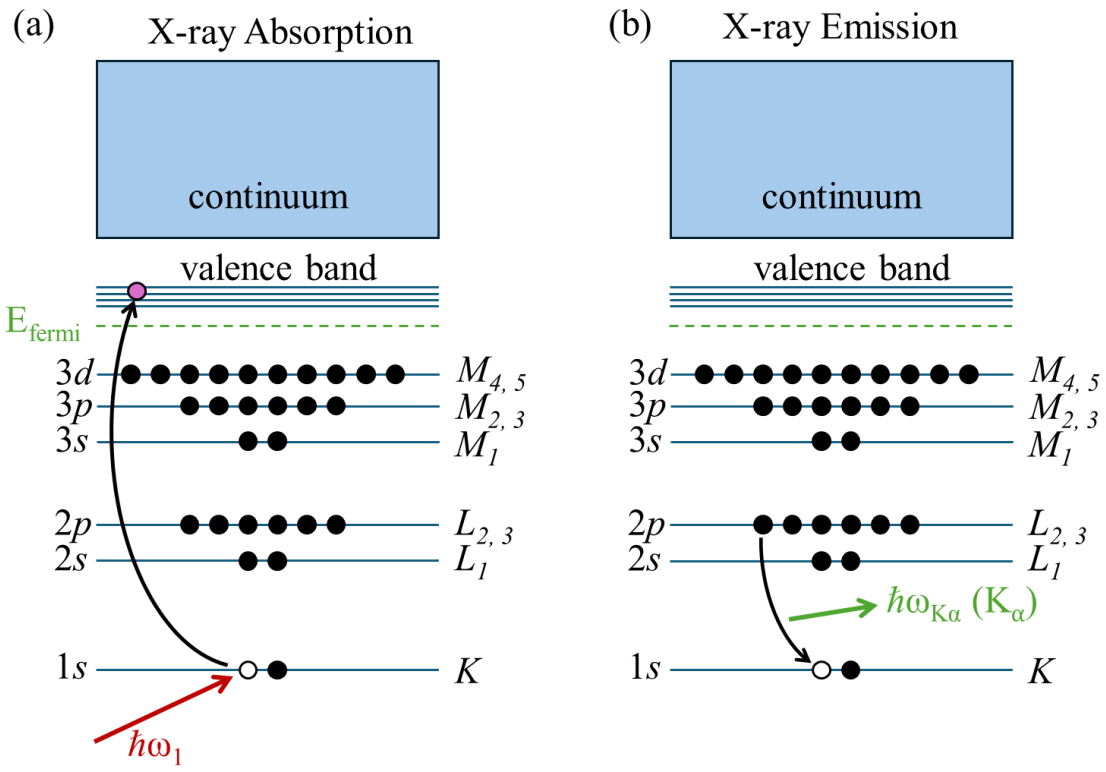

Figure 1. **(a)** The X-ray absorption process generates a core-hole and creates a short-lived excited state **(b)** The X-ray emission process fills the core-hole with an electron from a higher shell and a characteristic X-ray is fluoresced.

In the excited state following a photo absorption event (Fig 1 (a)), the Heisenberg uncertainty principle dictates that the short core-hole lifetime is inversely proportional to the energy uncertainty of the state. This energy uncertainty is termed the "natural line width" or more precisely, core-hole lifetime broadening. This intrinsic energy broadening is common to all X-ray absorption measurements and represents the energy resolution "limit" for an absorption edge. Even with the sharpest monochromator energy resolution, a transmission or total fluorescence mode XAFS spectrum will be broadened by the core-hole lifetime.

Core-hole lifetime increases with atomic number (Z) of the probed species and is also dependent on the absorption edge. For 3*d* transition metal K-edges, core-hole lifetime broadening is ~1.0 eV, for 5*d* transition metal L_1-edges and $L_{2,3}$-edges is ~10.0 and 5.0 eV, respectively, and for actinide L_1-edges and $L_{2,3}$-edges is ~14 eV and 7.0 eV, respectively. Tabulated theoretical and experimental core-hole lifetime broadenings for the periodic table are found elsewhere[2]. Broadly speaking, the natural line width of any *L*-edges and for *K*-edges with binding energies above 10 keV presents a real limit to the science possible from XANES measurements due to the smearing of near-edge features.

2. X-ray Emission Spectroscopy

The emission of a characteristic X-ray, in the case of Figure 1 (b), a K_α emission of a 2p electron filling a 1s core-hole, is referred to as X-ray fluorescence. Measuring a fluorescence spectrum at coarse resolution (>150 eV) is referred to as X-ray fluorescence (XRF) spectroscopy or the collection of an 'energy dispersive X-ray (EDX) spectrum . Detection of characteristic X-ray lines is a fast method for identifying the elements present in a system, shown in Figure 2.

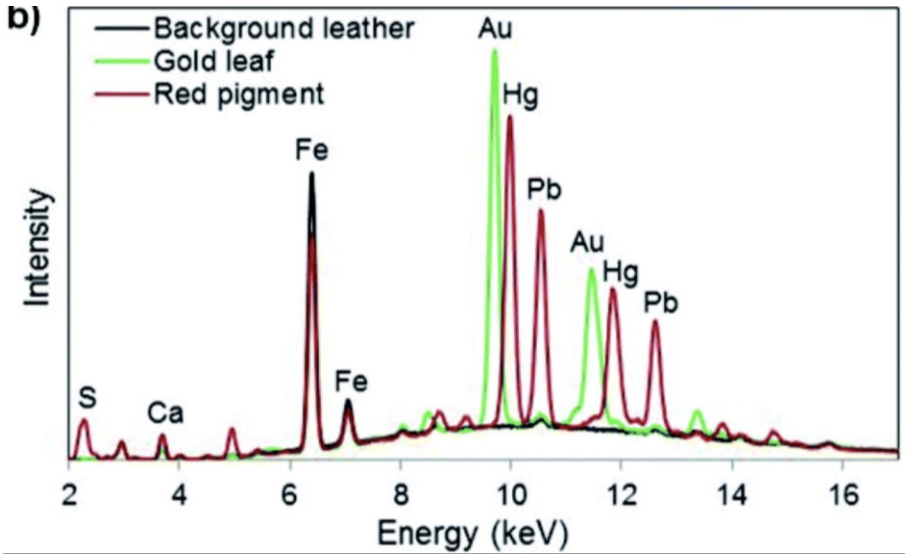

Figure 2. An XRF spectrum of a book cover from the *London* warship wreckage[3].

Collecting an XRF spectrum at high energy resolution we denote as X-ray emission spectroscopy (XES), a powerful spectroscopic tool for assessing the occupied electronic states of a system. When performed at the valence level, XES is frequently referred to as complementary to XAS, which probes the unoccupied density of states[4,5]. Furthermore, XES is a secondary process as demonstrated in Figure 1; a characteristic fluorescing photon is emitted in the filling of a core-hole made from a photo absorption event.

The "high-resolution" that differentiates XES from XRF is on the order of the core-hole lifetime broadening, ~1 – 5 eV. Notably, XES can be performed both in the laboratory with an X-ray tube[6–8] or at a light source such as a synchrotron[9–11]. In either case, this requires the use of a spectrometer to analyze the fluorescence; the final portion of this chapter is dedicated to reviewing XES spectrometers.

XES of core-shell characteristic fluorescence is a powerful technique for characterization materials. An example of the Cr K_α emission spectrum from Jahrman et al.[12] is shown below (Figure 3). The K_α peaks show sensitivity to the Cr oxidation state and this serves as a method to quickly assess Cr speciation as carcinogenic (Cr VI) and non-carcinogenic (Cr III). Note there are two peaks in the K_α emission spectrum unlike the single lines observed in the XRF spectrum of Figure 2. The doublet lines observed in XES is characteristic of all K_α spectra and are denoted as $K_{\alpha1}$ (higher energy) and $K_{\alpha2}$ (lower energy). K_α emission is from a $2p$ electron filling a $1s$ core hole. The doublet feature is a result of spin-orbit splitting in the $2p$ orbitals resulting in two different states ($2p_{1/2}$ and $2p_{3/2}$) with two slightly different binding energies. The intensity ratio of $K_{\alpha1}$ and $K_{\alpha2}$ is a consequence of the degeneracy of each spin state – $2p_{3/2}$ having 4 electrons and $2p_{1/2}$ having 2 electrons, the intensity ratio of $K_{\alpha1}$ to $K_{\alpha2}$ is 2:1.

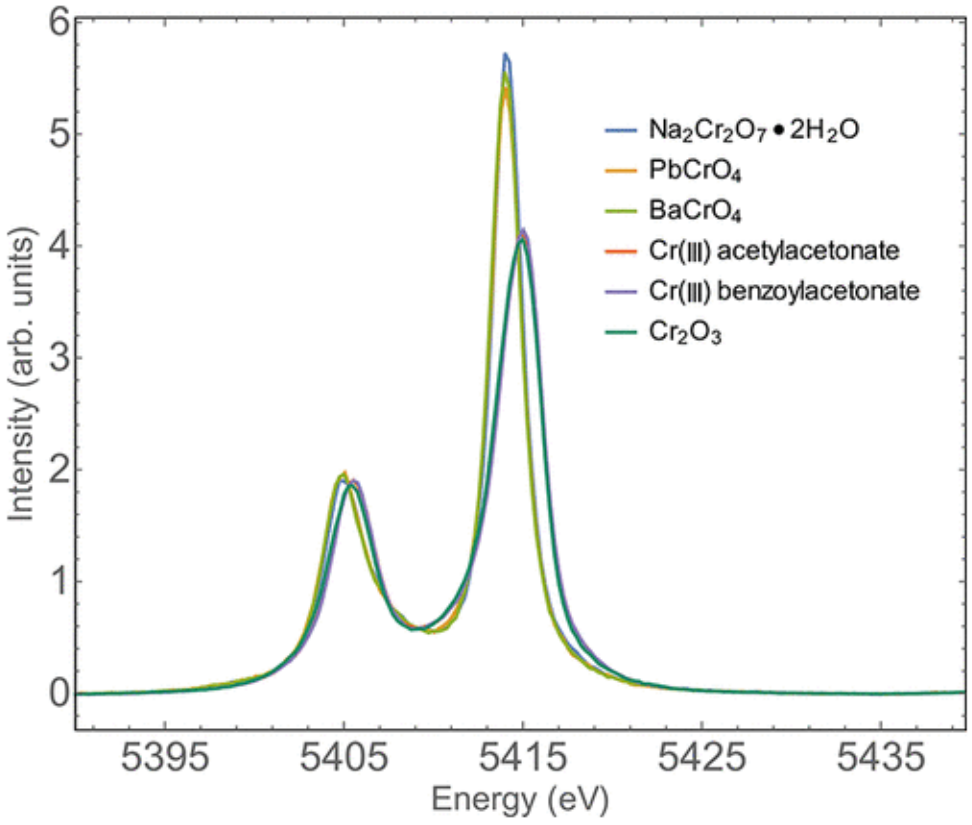

Figure 3. K_α XES of Cr samples and references. Spectral shifts are a result of Cr oxidation (6+ and 3+)[12]

Many core-to-core emissions are possible and can provide different information on the probed species. Instead of a 2*p* electron filling a 1s core-hole, a 3*p* electron filling a 1*s* core hole results in a K_β emission, at slightly higher energy than K_α owing to the electron filling from a higher shell. Due to 3*p*-3*d* exchange interaction when the 3*p* electron fills the 1s core hole and creates a 3*p* vacancy, K_β is sensitive to high/low spin. Figure 4 shows a satellite ($K_{\beta'}$) of varying intensity at lower energy of the $K_{\beta 1,3}$ main-line[13]. The intensity of this satellite is dependent on the spin of the fluorescing atom; a more intense satellite is observed with increasing number of unpaired 3*d* electrons. In the presented example, Rueff et al. observe a high to intermediate spin transition of $SrFeO_2$ with increasing pressure[13].

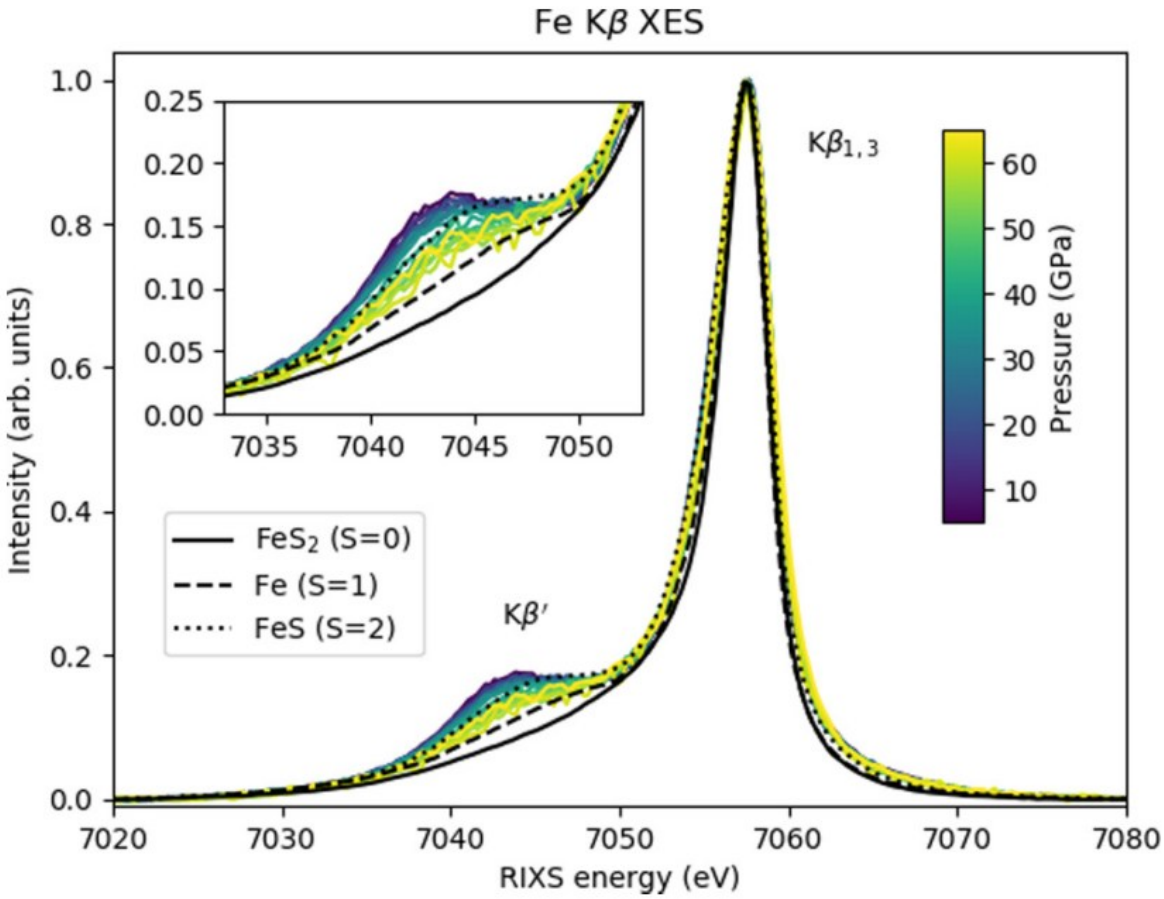

Figure 4. Fe K_β XES of SrFeO2 under pressure, plotted with high, low, and intermediate spin Fe reference spectra. The lower energy satellite beside the main line is sensitive to spin.[13]

In addition to core-to-core emissions, XES can also be used to detect valence-to-core (VtC) emissions. Continuing with the examples of the K-shell 1*s* absorption, the K-shell VtC characteristic emission would be from a valence electron filling the 1*s* core-hole. The VtC measures the occupied density of states near the Fermi level. It is a very local probe and can be highly sensitive to first shell coordination[14]. Figure 5 shows an example of Zn VtC of Zn^{2+} electrolytes in solution of increasing molarity from dilute to super concentrated[15]. The observed peaks in the VTC correspond to octahedral and tetrahedral coordination of aqueous Zn^{2+} with Cl^-

, and the isosbestic point indicates a linear combination of the two coordination geometries as a function of solution concentration.

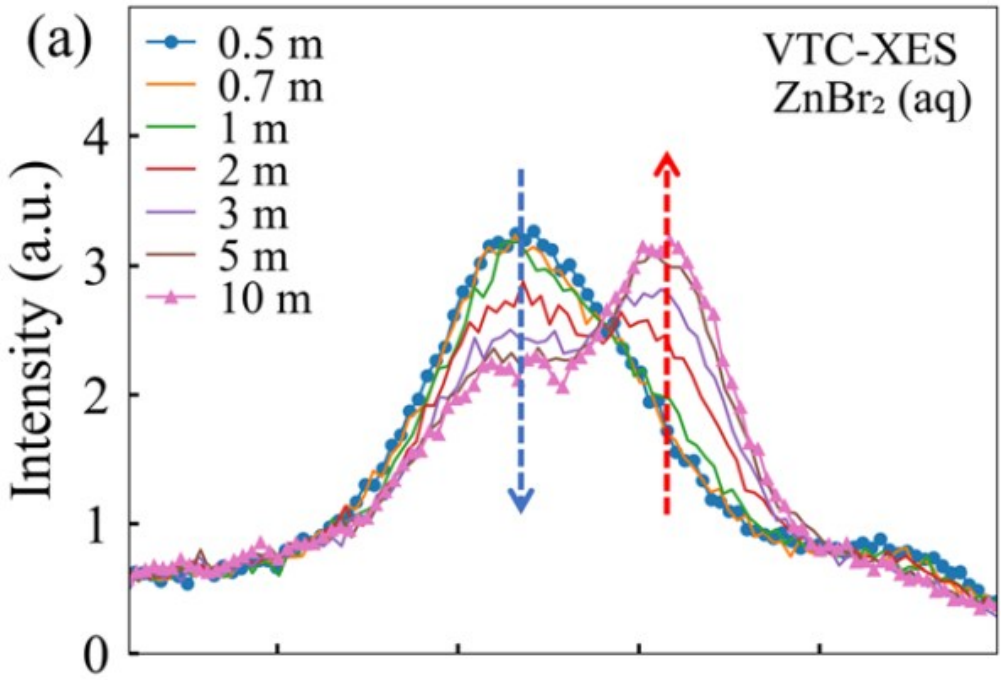

Figure 5. Zn K-shell VtC of Zn ions in solution. The coordination geometry around the Zn^{2+} correspond to the observed peaks (blue – octahedral, red – tetrahedral).[15] VtC is an extremely local probe.

3. High Energy Resolution Fluorescence Detection (HERFD) Background

With this XES background established, we return to the discussion of the intrinsic core-hole lifetime broadening of absorption edges. Reconsider the absorption process described in Figure 1 (a) and the emission process of Figure 1 (b). Consider an L_3 absorption event of a rare-earth ion. A $2p \rightarrow 4f$ absorption event occurs and leaves a core-hole in the L-shell with the associated intrinsic $2p$ core-hole lifetime previously discussed. Then, a $3d \rightarrow 2p$ emission occurs as a $3d$ electron fills the $2p$ core-hole and fluoresces. The $3d \rightarrow 2p$ fluorescence intensity is dependent on the number of $2p$ core-holes; thus monitoring $3d \rightarrow 2p$ fluorescence while the

incident energy is scanned over the 2*p* absorption edge would record XAFS. *However*, in the case that the 3*d* → 2*p* fluorescence is recorded at high resolution (~1 eV) while the 2*p* absorption edge is scanned, the experiment conducted will have measured the 2*p* → 4*f* absorption spectrum with the core-hole lifetime broadening of the 3d core-hole created from the 3*d* → 2*p* fluorescence.

In other words, this method of monitoring fluorescence of a specific emission at high resolution whilst scanning the absorption edge has replaced the 2*p* core-hole lifetime broadening with that of the 3*d* core-hole lifetime broadening. Notably, the 3*d* core-hole has much narrower resolution compared to the 2*p* core-hole and a sharper, higher resolution XAFS spectrum is recorded. This description mirrors the first demonstration of the technique from Hamalainen et al. in 1991 on the Dy L_3 edge whilst monitoring the $L_{\alpha 1}$ emission signal at high resolution with a crystal analyzer spectrometer[16]. The result of Hamalainen's experiment is shown in Figure 6 and a significant sharpening of the absorption edge is observed.

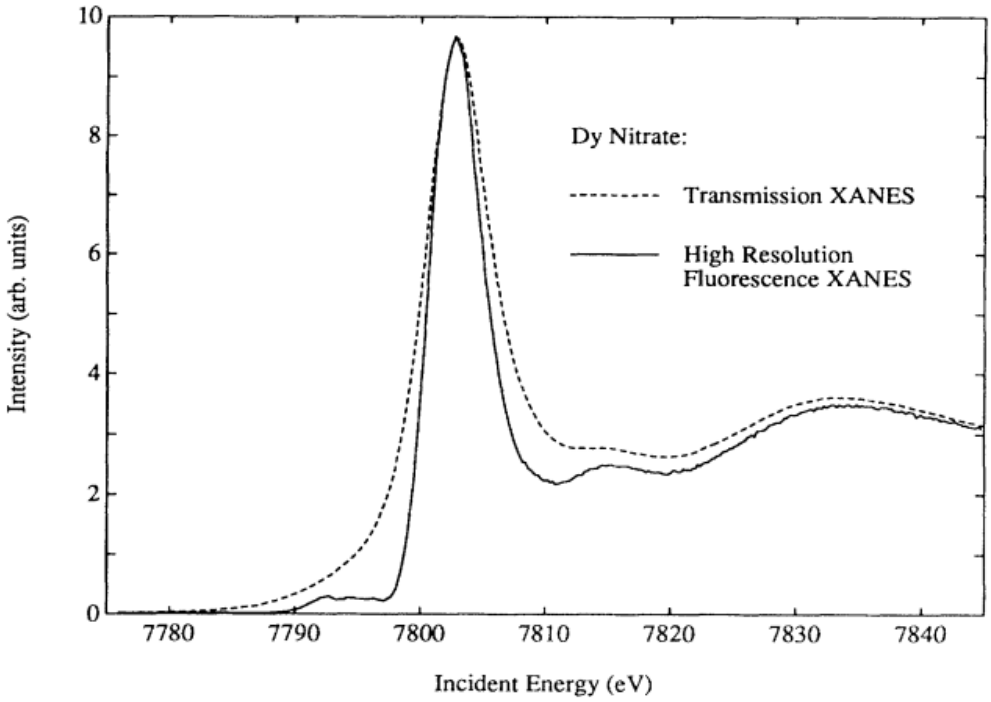

Figure 6. Transmission XAFS and HERFD-XAFS of the Dy L_3 absorption edge.[16]

Today, this technique is referred to as high-energy resolution fluorescence detection (HERFD) and is often seen denoted also as HERFD-XAFS, HERFD-XAS, HERFD-XANES, partial fluorescence yield (PFY)-XAFS or even high resolution (HR)-XAFS. It is in the larger umbrella of advanced X-ray spectroscopies known as photon-in/photon-out, referring to the incident absorbed and fluoresced photons. Furthermore, HERFD is an outcome of a particular spectroscopy known as Resonant Inelastic X-ray Scattering (RIXS), where a 2D energy plane of incident and scattered/fluoresced photons is recorded at an absorption edge and emission line[5,17,18]. HERFD is a "slice" through this RIXS plane. A discussion of RIXS is beyond the scope of this chapter.

HERFD measurements require a monochromatically tunable X-ray source and a spectrometer; effectively both the incident and fluoresced photons require a monochromator. Thus, HERFD is reserved for the synchrotrons and crystal analyzer spectrometers are employed to analyze the fluoresced photons at high resolution.

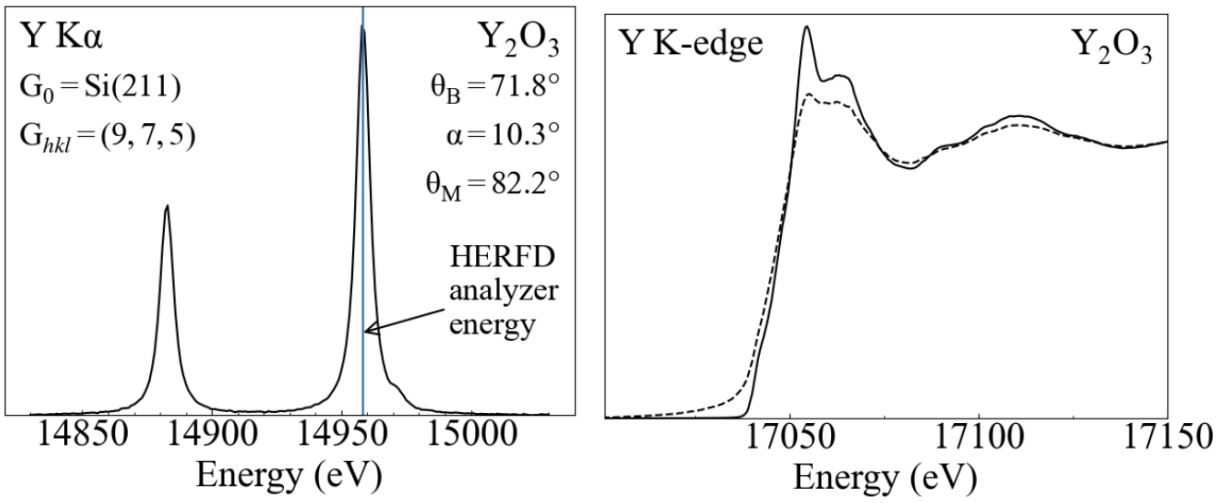

Figure 7. **(Left)** Y K_α emission XES with HERFD emission channel at $K_{\alpha 1}$ peak. **(Right)** The sharpened HERFD Y K-edge (solid) with traditional TFY XAFS (dashed).

4. Applications

a. Site-Selective XAFS

Consider, for example, the characteristic high-spin $K_{\beta'}$ feature of Figure 4 or the tetrahedral VtC feature of Figure 5. Using these examples, performing conventional XAFS on the mixed system of low- and high-spin Fe or tetrahedral and octahedral Zn yields XAFS that is a weighted combination of the different sites the probed species occupies. However, if HERFD is instead measured where the monitored emission channel corresponds to the high-spin $K_{\beta'}$ feature or the octahedral VtC signal, then the recorded XAFS would be site-specific to only high-spin Fe or octahedrally coordinated Zn. This is a powerful tool for materials characterization.

This HERFD technique was first proposed and outlined by de Groot (2000) in the context of catalysis research[19]. In catalyst science, the important chemistry typically occurs on the surface of, for example a nanoparticle, but conventional XAFS largely reports the chemistry of the bulk. Thus, site-selective HERFD can provide XAFS of , for example, a nanoparticle surface, in the case a suitable emission channel is present.

An early study demonstrating this approach was reported by Glatzel et al. (2002) on the Fe K-edge of Prussian Blue (PB), a mixed valence compound[20]. PB has two unique Fe sites with a bulk ratio of high-spin Fe^{3+} to low-spin Fe^{2+} of 4:3. Glatzel et al. determined the three most spin-sensitive HERFD channels in the PB Fe K_β emission spectrum by measuring Fe^{3+} (Fe_2O_3) and Fe^{2+} ($K_4Fe(CN)_6$) reference compounds, shown in Figure 8 (left). The measured XAFS was still admixtures of both Fe species in KB, but they were admixtures of “known” (assumed from the model compounds) high-spin:low-spin ratios[20]. The deduced site-selective EXAFS is shown in Figure 9 (right).

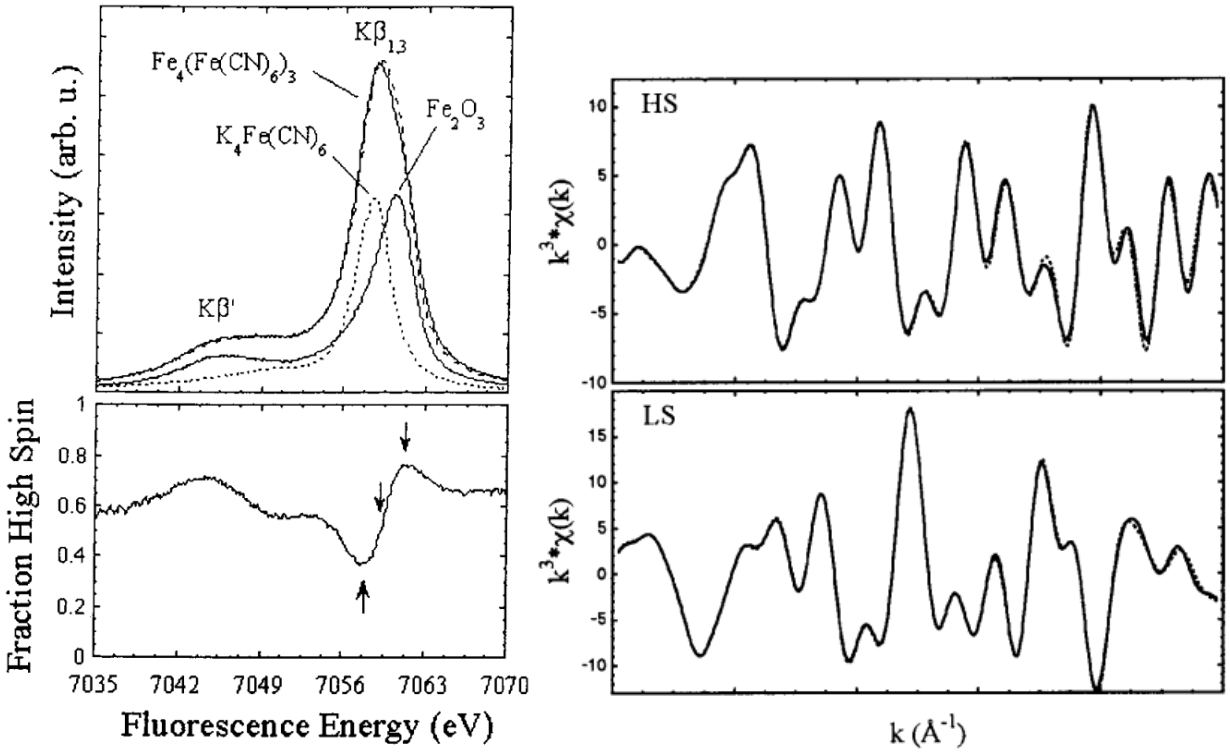

Figure 8. **(Left)** PB Fe K_β emission spectrum with Fe^{3+} and Fe^{2+} references. The lower panel shows the difference contrast between reference spectra and the three HERFD channels. **(Right)** Deduced site-specific Fe XAFS of high-spin (HS, top) and low-spin (LS, bottom)[20].

A similar technique following Glatzel et al.'s approach was applied to obtain site-specific HERFD XAFS for active sites of [FeFe]-hydrogenase (a mixed valence enzyme for biologic H_2 production)[21–24], for a Co Prussian Blue analogue measured *in situ*[25], and from a RIXS plane of Fe-doped lithium niobate crystals[26].

Site-specific HERFD has also been applied to nanoparticles, distinguishing sites at the surface from the bulk-like interior. The first example was presented by Kuhn et al. in 2011[27], where mixed valence Co nanoparticles were studied. The nanoparticles were assumed to have a metallic core and a Co-O/C shell with Co^{2+} valence. The Co HERFD data was acquired by measuring the entire RIXS plane and slicing where the Co $K_{\beta 1,3}$ differed the most between the

two valences, shown in Figure 9 (left). Like Glatzel et al.'s method, their measured HERFD result was admixtures of known quantities between Co^0 and Co^{2+} (Figure 9 (right)), which were decomposed into site-specific XAFS of the oxide shell and metallic core[27]. Later work from Kuhn et al. followed the same methodology to extract site-selective EXAFS of Co nanoparticles[28].

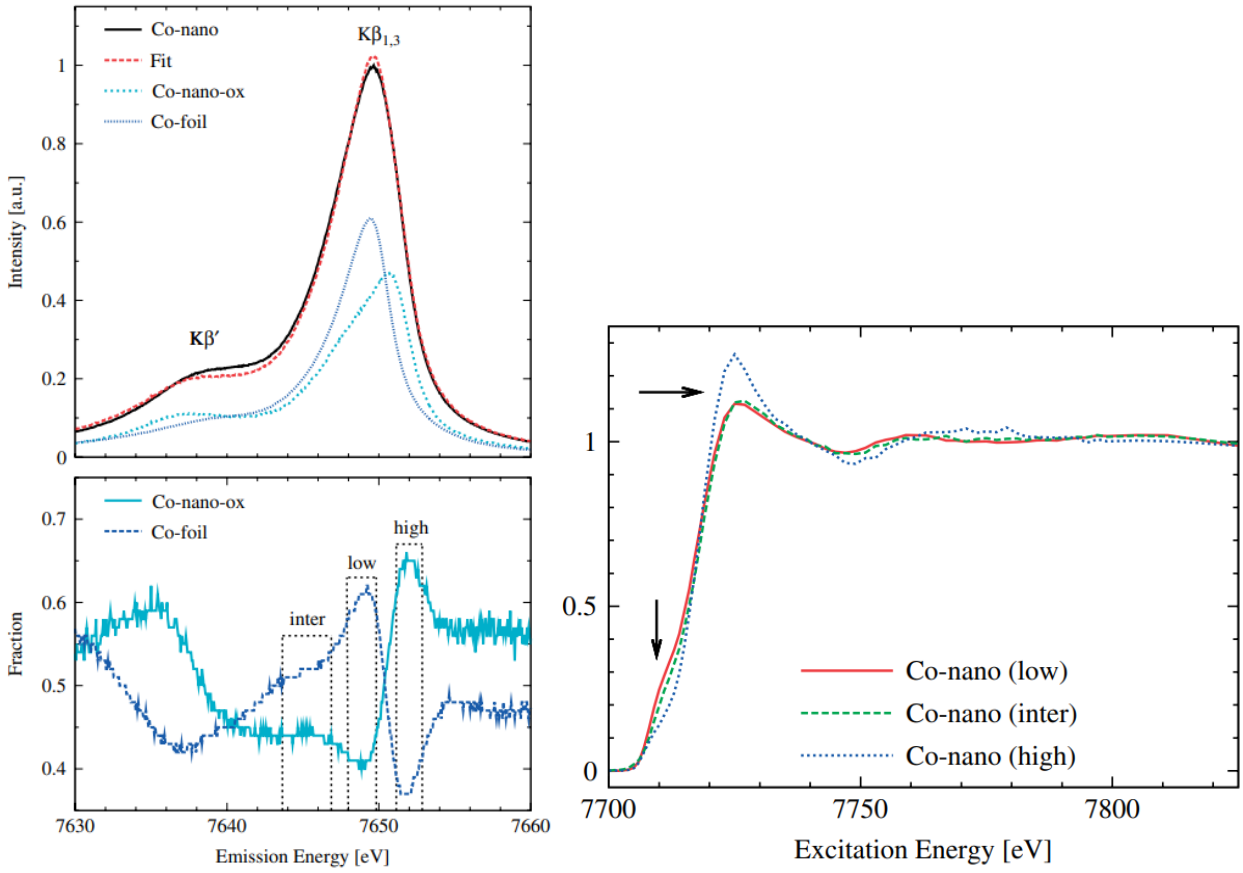

Figure 9. **(Left)** Co XES of the nanoparticle, oxidized nanoparticle, and metal foil. **(Right)** The HERFD Co^0/Co^{2+} mixtures measured at the three identified emission energies with the greatest distinction between Co^0 and Co^{2+}[27].

b. Catalyst Science

Generally, the enhanced resolution afforded by HERFD is beneficial to all studies of narrow XANES features. As an example, an *operando* applications of HERFD to catalyst research is highlighted here.

Friebel et al. used *operando* HERFD on a mixed Ni,Fe-oxyhydroxide ($Ni_{1-x}Fe_xOOH$) oxygen evolution reduction catalyst in alkaline electrolyte. HERFD revealed Fe^{3+} was octahedrally coordinated and the structure was nearly optimal for OER, whereas Ni sites were not active[29]. The local symmetry of the Ni and Fe sites at different operating potentials were informed by the pre-edge features shown in Figure 10, which are enhanced from HERFD. The centroid of the pre-edge feature also reports oxidation state of the transition metal.

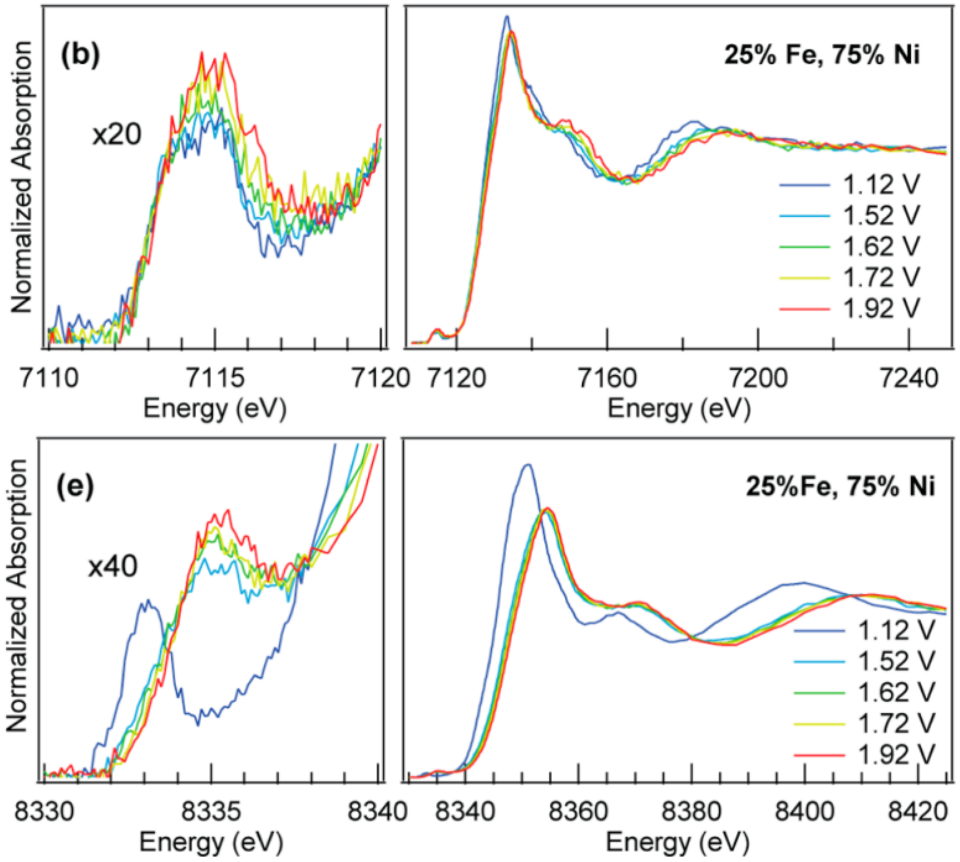

Figure 10. Pre-edge and main edge of the transition metal catalyst **(Top)** Fe *K*-edge and **(Bottom)** Ni *K*-edge[29].

c. Actinide Chemistry

Informative element specific probes are critical in actinide chemistry at all parts of the fuel cycle from mining, refining, waste disposal, and separations chemistry[30–32]. Understanding radionuclide mobility and solubility is paramount to nuclear waste storage and public safety. Several actinide chemistry dedicated beamlines have been developed[33–37] in addition to laboratory XAFS/XES spectrometers[38,39] for L- and M-shell spectroscopy on actinides. HERFD is a key part of this characterization suite; especially because theory and computational models of the many electron 5f elements are difficult[40] and the actinide edges have large core-hole lifetime broadening that hinders conventional XAFS. High resolution actinide XANES data obtained through HERFD improves both theory, computation, and analytical chemistry of these elements.

iii. L-edges

Here, Bes et al. (2016) compare an *ab initio* calculations from FDMNES to U L_3 absorption edge acquired through the FDMNES modelling software[41]. U L_3 HERFD was measured with the $L_{\alpha 1}$ emission channel. They find that the L_3 pre-edge feature is sensitive to local environment and valence state and good agreement between theory and experiment.

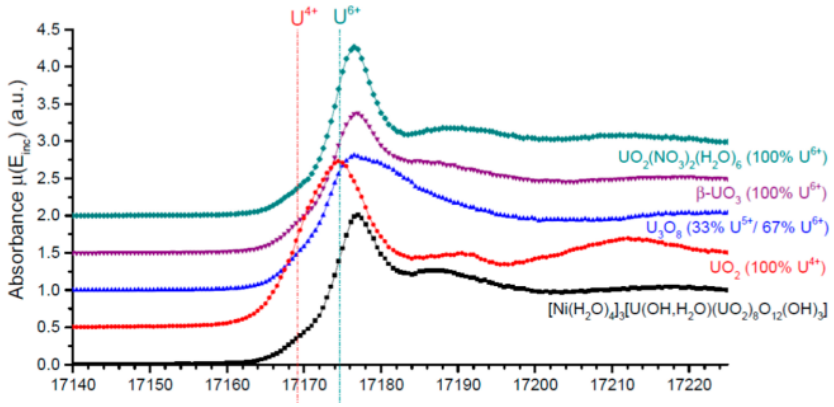

Figure 11. U L3 HERFD spectra of UO_2 compound and standard oxide references[41].

iv. M-edges

Actinide M-edges in the tender X-ray regime (~3.5 keV) such as the $M_{4,5}$ edge are more difficult to measure than their L_3 counterparts, owing to significant signal attenuation from air absorption. However, the M-edges can report the oxidation state, 5f occupancy, covalency, charge transfer effects, local symmetry, and speciation[42].

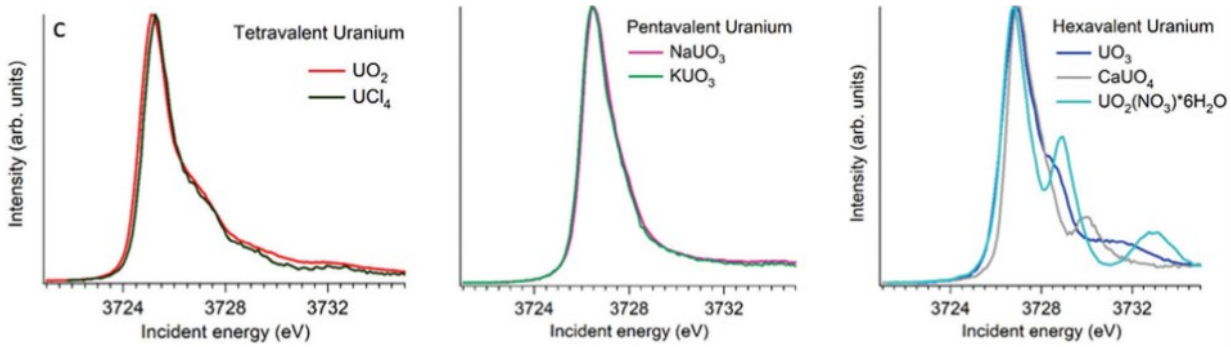

Figure 12. U M-edge HERFD data for 4+, 5+, and 6+ oxides in different crystal structures[42].

5. HERFD (and RIXS) Instrumentation

This chapter concludes with a review of the state-of-the art of scanning XES/RIXS/HERFD spectrometers. Both dispersive and point-focusing spectrometers are discussed. A large portion is spent on the point-focusing spectrometers, their reference frames, degrees of freedoms, and commonalities. Most notably is the prevalence of spherically bent crystal analyzers (SBCAs), the similar motorized degrees of freedom, and the multiplexing of scanning Rowland circles to maximize collection solid angle. We note here that all point focusing spectrometers reviewed operate in symmetric Rowland geometry and to our knowledge no dedicated asymmetric Rowland spectrometers have been overlooked.

a. Dispersive HERFD / RIXS Geometries

Generally, energy dispersive resonant inelastic x-ray scattering (RIXS) spectrometers are less common than their point focusing energy scanning counterpart. The pmost common energy dispersive spectrometers utilize a cylindrically bent crystal analyzer in a so-called von Hamos[43] geometry with an area detector; this allows a spectrum to be collected in a "single-shot". Energy dispersive spectrometers can require no moving parts and are mechanically and kinematically simple if motorized.

In the context of XES, and by extension RIXS where a two-dimensional energy plane of incident vs. emitted/scattered photon energy is collected, a dispersive set-up simplifies the data collection by collecting the photon-out spectrum in a single shot. These are particularly effective for pulsed light sources such as X-ray free electron lasers (XFELs) and suitable for time-dependent studies.

There are several drawbacks in the design of dispersive spectrometers; here I focus on those of von Hamos geometry with cylindrically bent diffractive optics. First, the focusing geometry yields a point to line focus. The large area of the line focus across a pixelated area detector results in a lower signal-to-background ratio than non-dispersive point focusing geometries. Second, only a small portion of the total solid angle analyzes a specific energy, thus dispersive set-ups are inefficient for only monitoring one emission channel. However, this can also be seen as a benefit if the goal is the collection of an entire RIXS plane to slice for HERFD later. Here, we review some dispersive set-ups used for XES, RIXS, and HERFD.

i. Review of Dispersive Instruments

One of the earlier dispersive hard X-ray RIXS spectrometers is reported by Mori et al developed and commissioning at the linear coherent light source (LCLS) at SLAC National Accelerator Laboratory in 2012 [27]. They used 16 cylindrically bent crystal analyzers (CBCAs) of 500 mm radius of curvature in a modified von Hamos geometry (Figure 13 (left)) to disperse the spectrum on a pixelated area detector. It is a "modified" von Hamos geometry because the out of plane CBCAs on the edges of the spectrometer have to be tilted so they diffract the same Bragg angles and energy range as the center CBCAs in the array, seen in Figure 13 (right). The spectrometer is motorized to scan the CBCA array vertically, allowing control of the dispersed energy range by changing the incident Bragg angles on the CBCA array; but the spectrometer is fixed during the collection of a scan. They report a resolution of 0.5 eV using Si(440) at 6.5 keV, and applications for XES, XRS and RIXS.

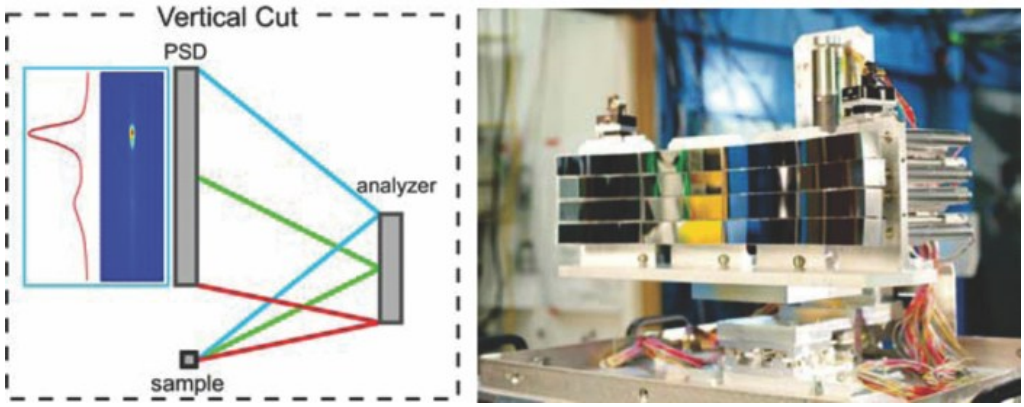

Figure 13. **(Left)** Von Hamos dispersive geometry of a flat crystal **(Right)** the LCLS dispersive spectrometer with 16 0.5-m radius CBCAs in a 4x4 array[44].

A later implementation specifically for RIXS studies is reported by Mei et al. in 2019 at the BL14W1 beamline of the Shanghai Synchrotron Radiation Facility[45]. Again, the dispersive set-up is accomplished in von Hamos geometry, described in Figure 14 (a) for CBCAs. Here, Jiang et al. report a spectrometer with a single Si(444) CBCA of 250 mm bending radius and 100 mm long in the dispersive direction; at 8 keV this provides an energy range of 575 eV. Unlike the prior spectrometer, here they use only one Si(444) CBCA and rely on harmonics and vertical translation to coarsely and finely adjust the dispersed energy range. The spectrometer is optimized specifically for *in situ K*- and *L*-edge RIXS of 3d and 5d transition metals from 8 – 9 keV.

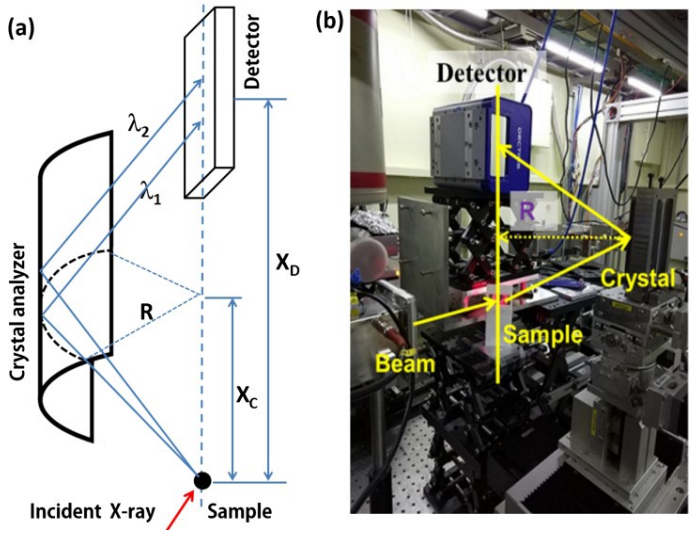

Figure 14. **(a)** Von Hamos geometry of a CBCA **(b)** the dispersive RIXS spectrometer at SSRF[45].

We conclude this brief review of dispersive RIXS instrumentation with the work from Ditter et al. in 2020[46]. Unlike the prior von Hamos spectrometers, Ditter et al. reports a RIXS spectrometer in a so-called dispersive Rowland refocusing (DRR) geometry. In a point-focusing spectrometer, a bent optic defines a focusing circle (the Rowland circle), and placement of a

radiating source on the circle's perimeter results in point-focusing elsewhere on the perimeter and a monochromatization of the X-rays, shown in Figure 15 (a). Placement of the radiating source inside the Rowland circle in DRR geometry results in a dispersion of energies along the circle perimeter, shown in Figure 15 (b).

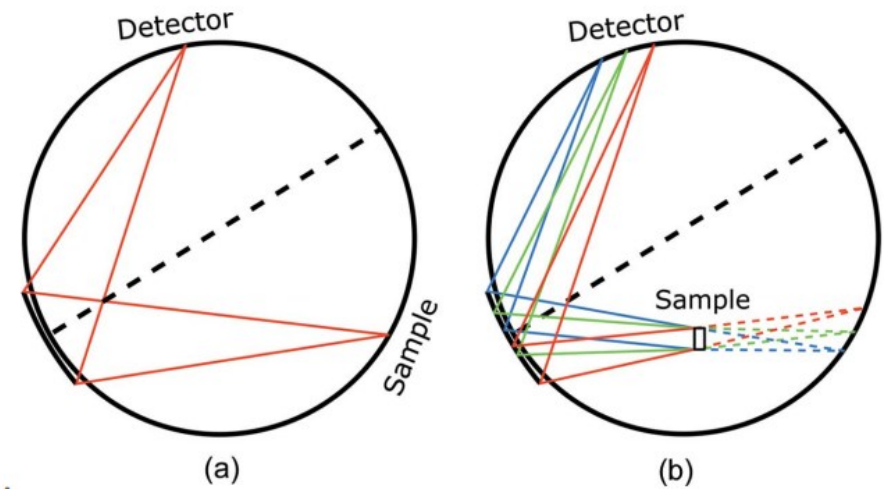

Figure 15. **(a)** Rowland circle geometry, yielding point-to-point focusing and monochromatization of an X-ray source and **(b)** dispersive Rowland refocusing (DRR) geometry, where placement of a source inside the Rowland circle yields a spatial dispersion of energy at the detector[46].

The advantage of DRR is an extremely compact dispersive spectrometer, Ditter reports the use of 100 mm curvature CBCA at median Bragg angles of 65 degrees[47]. The compact footprint of the DRR spectrometer lends it for use in soft or tender regime measurements such as S *K*-edge, as the entire spectrometer can easily be placed under He or vacuum and the flight paths are short. The instrument is shown in Figure 16 (b) and at the beamline in Figure 16 (a). They demonstrated the spectrometer at BL 4-3 of the Stanford Synchrotron Radiation Lightsource (SSRL), collecting RIXS on U *M*-edge and S *K*-edge in the soft X-ray regime. They

report the portability of the instrument is suitable for travel between unfocused beamlines and highlight the spectrometer for RIXS measurements even at non-dedicated end stations in the tender regime, of which there are only a few beamlines that operate in this energy range. Thus the flexibility of a portable instrument to make RIXS possible at any tender beamline is beneficial.

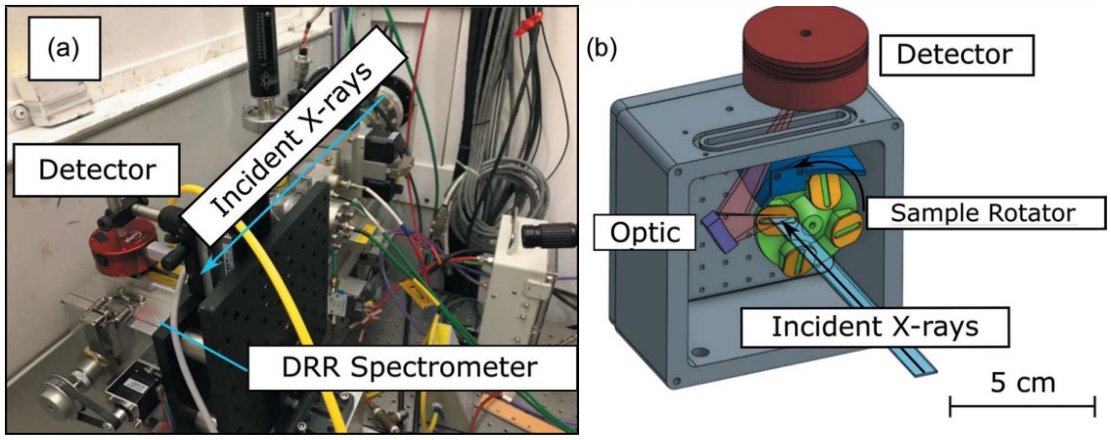

Figure 16. **(a).** The spectrometer in the synchrotron endstation **(b)** CAD rendering of the spectrometer and ray traced flight path[46].

b. Non-Dispersive Scanning HERFD / RIXS Geometries

The vast majority of photon-in/photon-out spectrometers for HERFD, and by extension RIXS and XES, utilize spherically bent crystal analyzers (SBCAs) in Rowland circle geometry. The relative ease of manufacture of Johann-type[48] SBCAs lends to their prevalence and application to these spectrometers. Nominally, during spectrometer operation the same Bragg angle is made across the entire SBCA, and point-focusing and monochromatization is achieved. This yields high signal-to-noise ratios and large collection solid angle at high resolution. A spectrum is collected by scanning the incident Bragg angle which scans the analyzed photon energy.

Mechanically, scanning the spectrometer during collection is non-trivial: the trajectory of the spectrometer elements need to remain on the Rowland circle perimeter to maintain best energy resolution. This becomes more challenging when arrays of optics are used, as each optic has its own scanning Rowland circle, and the arrays are typically designed for all the analyzers to refocus to a common point for maximum collection efficiency with a single detector.

We limit my discussion here only to symmetric Rowland geometries and detector placement at the meridional (on-circle) focus. This is to provide a thorough "state-of-the-art" as a basis for later discussion of asymmetric Rowland geometries and their applications to scanning XES/HERFD spectrometers. We focus here on two common reference frames of the point-focusing scanning spectrometer: the "table-scan" (Figure 17 (a)) and the "tilt-scan" (Figure 17 (b)) geometries. In both geometries, the source is fixed.

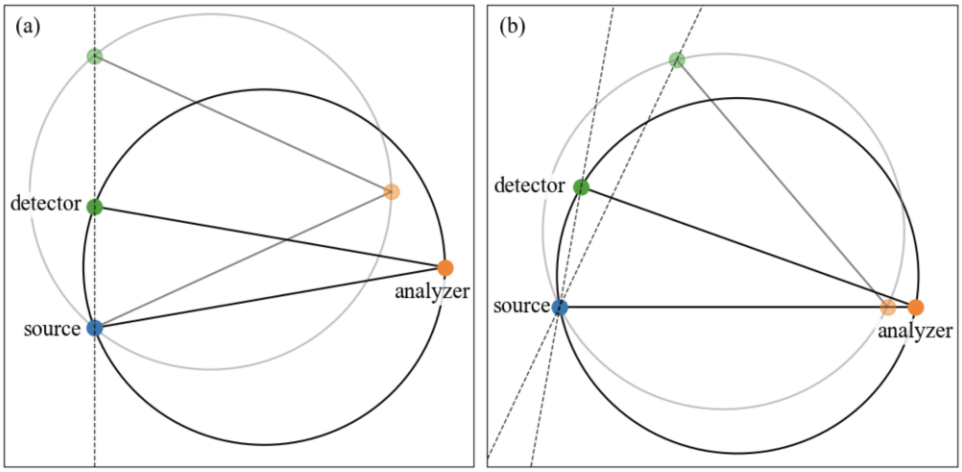

Figure 17. Scanning symmetric Rowland trajectories in two different reference frames: **(a)** table-scanning and **(b)** tilt-scanning.

The table-scan spectrometer translates the analyzer vertically to scan Bragg angle, and closer/further towards the sample to keep all elements on the Rowland circle. The analyzer only translates linearly. In a table-scan geometry, the detector is always vertically aligned with the

source, shown by the dashed vertical axis in Figure 17 (a). This trajectory can be accomplished with only linear translators and is kinematically simpler.

The tilt-scan spectrometer tilts the analyzer along the dispersive direction (i.e. tilts within the Rowland plane) to scan Bragg angle, and translates closer/further towards the sample to keep all elements on the Rowland circle. The analyzer both tilts and translates. In the tilt-scan geometry, the detector is always cantilevered in front of the source to remain on circle, and the angle of the axis between source and detector changes as the spectrometer scans in energy, shown by the two dashed lines in Figure 17 (b). This trajectory is kinematically more complex, and its simplest implementation requires the SBCA exactly at the rotation axis of a rotation/tilt/goniometer stage.

Lastly, note the detector placement with respect to the source as the spectrometer scans. This is crucial in the design of arrays of optics that scan the Rowland circle and refocus to a common point. In table-scanning, multiplexing is simple: revolving the analyzer around the vertical axis of source and detector patterns a plane with analyzer positions. A multiplexed table-scanning spectrometer will have all analyzers refocusing at the detector with no additional kinematic considerations, shown in Figure 18 (a), at all Bragg angles.

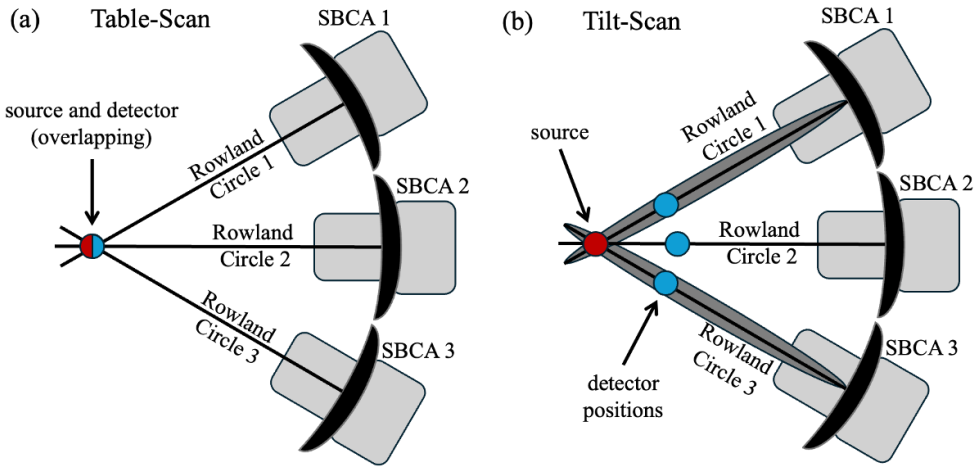

Figure 18. Top views diagrams of multiplexed **(a)** table scan and **(b)** tilt scan spectrometers.

Now consider multiplexing the tilt-scanning spectrometer. Choosing either of the two source-detector axes at two different Bragg angles to revolve the analyzers around patterns a plane with analyzer positions *that only focus to a common point at one Bragg angle*. Away from this Bragg angle, each Rowland refocuses to a different point and there is no coincidence; this is shown in Figure 18 (b). Additionally the patterned analyzers are no longer in the horizontal plane with respect to the source. Scanning the spectrometer whilst maintaining a common point focus of all analyzers is not trivial in tilt-scan geometry and requires an additional degree of freedom per SBCA.

However, the analyzer in the horizontal plane is highly favorable for *in situ* cells, which typically have exit or fluorescence windows in the horizontal plane. Tilt-scan geometry ensures the analyzers always have line of sight through *in situ* windows[49]. Additionally, with a linearly polarized X-ray source, tilt-scan geometries can eliminate elastic and inelastic scatter from being analyzed by keeping the optic orthogonal to the incident beam and in the plane of polarization for all Bragg angles.

HERFD and RIXS spectrometers are reviewed in the following order: (1) single optic table-scanning spectrometers, (2) multi-element table-scanning spectrometers, (3) single optic tilt-scanning spectrometers, (4) multi-element tilt-scanning spectrometers. This is loosely in ascending order of design complexity.

i. Single Optic Table Scan Spectrometers

(1) ESRF, Grenoble: BM30B/CRG-FAME

Hazemann et al. report a table-scanning single optic spectrometer for XES/HERFD measurements in 2008[50]. The spectrometer used a 0.5-m bending radius Johann-profile SBCA – typical for many contemporary scanning X-ray spectrometers owing to their increased collection solid angle than the older 1-m bending radius optics. A CAD rendering of the spectrometer is shown below in Figure 7. Linear translation motors in the "y" and "z" directions are used to scan the spectrometer with a Bragg angle range of 45 deg – 86 deg. Two additional rotation stages at the SBCA rotate the optic about the x- and z-axis, these are used to align the SBCA vertically (along z) and normal to the y-axis but are not relied on during scanning. The detector is a NaI scintillation photon-counting detector which only scans vertically along z. Hazemann notes the simplicity of the table scanning design, not requiring any goniometric tilt stages with large angular ranges. In total, their single optic system used 5 motorized degrees of freedom, requiring only 3 linear translating degrees of freedom to scan: SBCA-*y*, SBCA-*z*, and detector-*z*; but 2 additional rotation degrees of freedom for alignment.

They report an energy resolution of 1.4 eV at 8 keV and a significant coverage of K and L shell emission lines from 4-13.5 keV with a suite of only 4 Si optics. The energy range of the suite is significantly extended by working at lower Bragg angles (below 65 deg), but at the cost of degraded energy resolution.

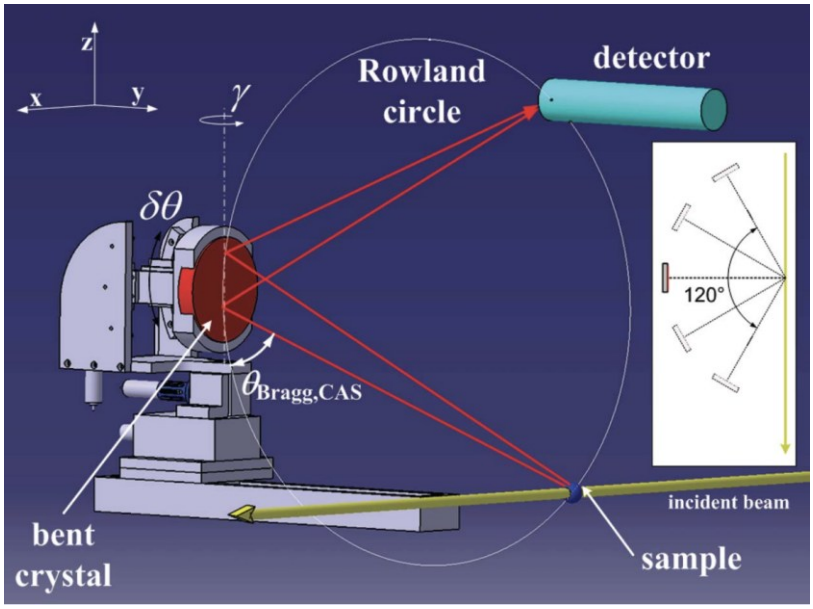

Figure 19. Single optic table-scanning spectrometer at CRG-FAME, ESRF[50].

ii. Multi Optic Table Scan Spectrometers

(1) ESRF: BM30B/CRG-FAME

LLorens et al. reported a high resolution five-crystal spectrometer for XES/HERFD at the same beamline as Hazemann et al[51]. They multiplexed (and replaced) the single-crystal spectrometer to enable fluorescence detection on dilute species. The degrees of freedom and energy ranges of the multiplexed spectrometer is identical to the single crystal spectrometer with the exception of the detector. Unlike the previous single optic prototype, the detector is now on a 3-axis linear translator with a rotation stage. In addition to the photon counting scintillator, a silicon drift diode (SDD) with resolution of 150 eV (Vortex-90ex) is employed for dilute fluorescence detection. They report an overall resolution of 1.4 eV at 8 keV. As previously stated, the multiplexing of table-scan geometry spectrometers is relatively simple – the detector always tracks vertically in-line above the sample, and thus multiplexing about the source-detector axis results in all Rowland circle's refocusing to the same point at any Bragg angle.

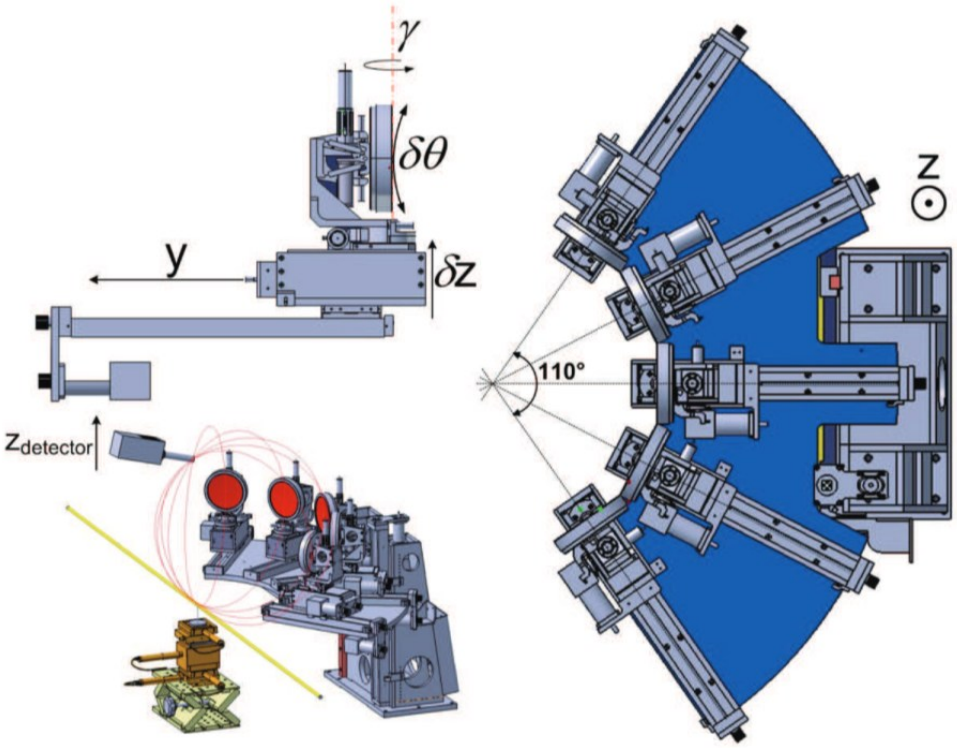

Figure 20. Schematic of the five crystal spectrometer at CRG-FAME, ESRF. The design and motorization of each module is fundamentally identically to the single optic prototype of Hazemann et al[51].

(2) Shanghai Synchrotron Radiation Facility (SSRF): BL14W1

A similar three crystal spectrometer is reported by Duan et al. at SSRF in 2016 for XES, HERFD, and RIXS[52]. The degrees of freedom on the optic for scanning and alignment are identical to those previously discussed. However, the instrument complexity is further simplified by using a common z-stage that translates all optics in tandem, in comparison to the previous instruments with individual z-stages for each optic, this is shown in Figure 21 (and a similar design in higher resolution in Figure 22). They report a 1.0 eV overall resolution at 6.5 keV.

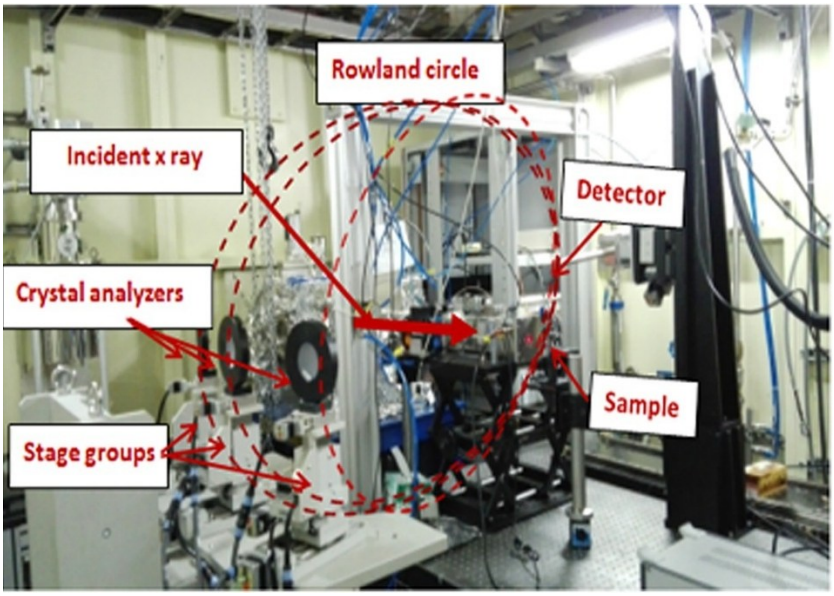

Figure 21. Picture of the three crystal spectrometer at BL14W1, SSRF. Here, the spectrometer is further simplified by a common z-stage for vertically translating all analyzers[52].

Unlike the prior spectrometers , here the Bragg angle range is limited to 71.5-88 deg. Due to this, this spectrometer requires many more unique SBCAs in the optic suite – they report coverage of the 3d transition metal Kβ emissions (Cr, Mn, Fe, Co, Ni, Cu, Zn) requires 7 SBCAs; in this case, as many unique analyzers as emission lines.

(3) SSRF: BL14W1 (2024)

An upgrade to the BL14W1 three-crystal spectrometer was published in 2024 by Mei et al, where the upgrade approximately doubled the collection solid angle with a seven-crystal spectrometer with a Bragg range of 73 to 86 deg operating from 3 – 20 keV shown in Figure 22[53]. This instrument is designed to operate in either table-scanning or tilt-scanning modes, enabled by a tilt stage on each SBCA that tilts the optic in the Rowland plane, but only table-

scanning is reported. The detectors used are a 4-element SDD (Vortex ME4) and a pixelated area detector (Pilatus 100K). They report a resolution of 0.8 eV at 6.5 keV.

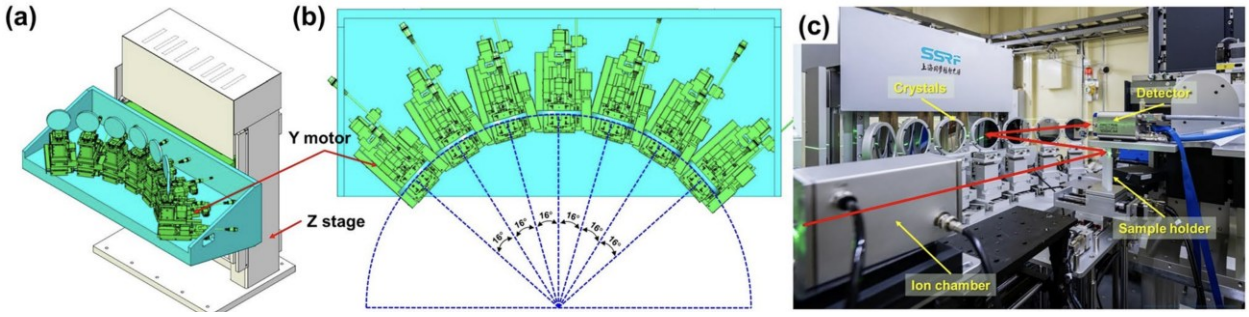

Figure 22. **(a)** isometric CAD view of the SSRL instrument with one common z-stage for all modules **(b)** top CAD view of the instrument **(c)** the pictured spectrometer in the hutch[53].

(4) SSRL: BL6-2

Here, Sokaras et al. design a 7-element table scanning spectrometer, this time with 1-m radius SBCAs and a Bragg range of 88-74 deg[54]. In terms of solid angle, this subtends about twice as much as a single SBCA at 0.5-m. Again, the z-table is common, shown clearly in Figure 23, and all optics focus to a single SDD. SBCAs are again motorized additionally for yaw and pitch adjustments for alignment. With bent-diced SBCAs and 1-m radius, they achieve a resolution of 0.5 eV at 6.5 keV.

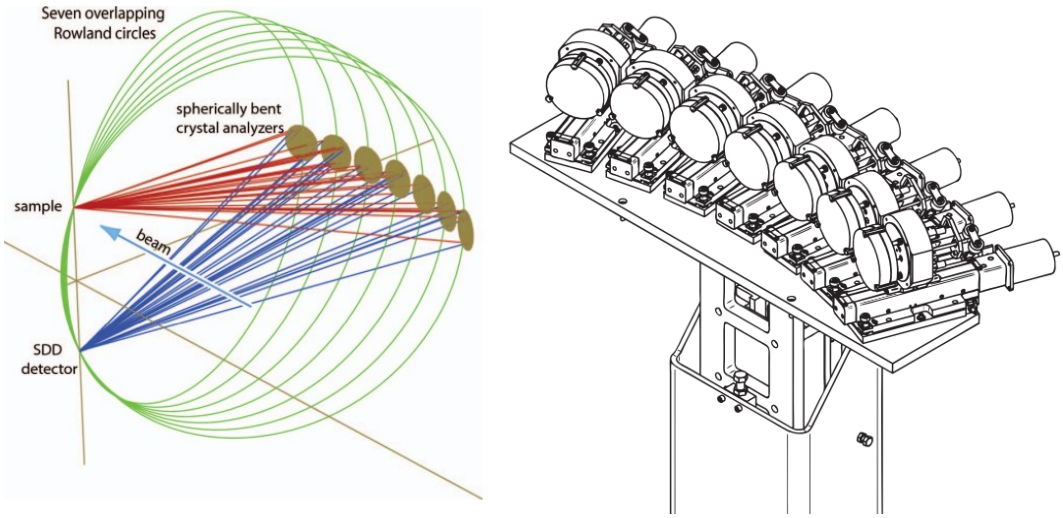

Figure 23. **(left)** the 7 overlapping Rowland circles and **(b)** isometric CAD view of the 7 element SSRL BL6-2 spectrometer[54].

We note the optic suite available if it is reported, as this is highly relevant when asymmetric operation is introduced in later chapters. A bar chart of energy ranges and SBCA cuts is reported by Sokaras for the BL6-2 spectrometer and is shown below. They report the use of 11 unique crystal analyzers for energy coverage of largely 3d transition metal K-shell and actinide L-shell features. 6 unique SBCAs were required for actinide L-shell coverage.

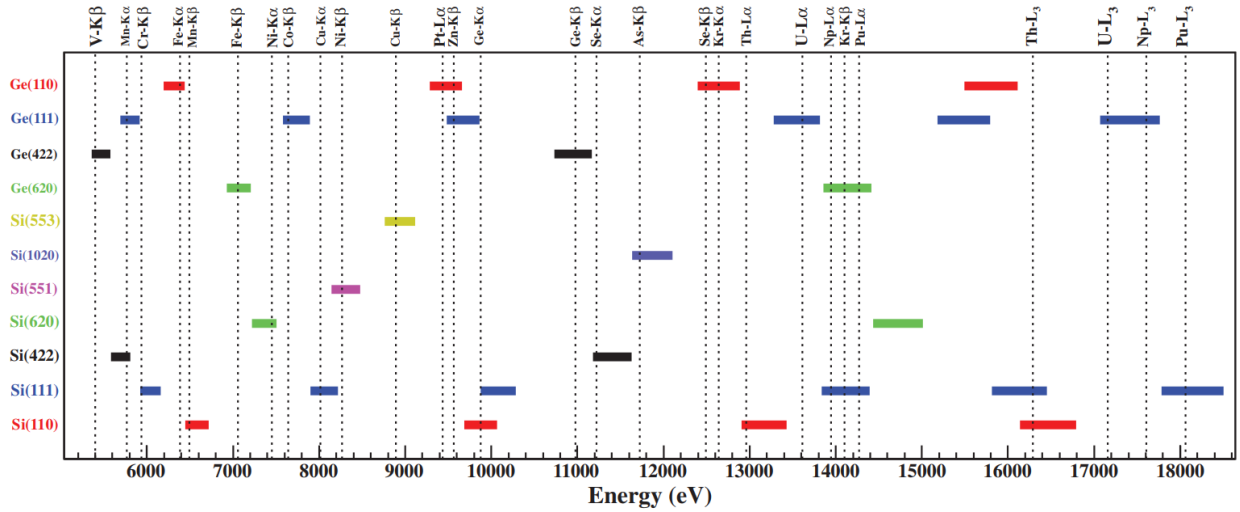

Figure 24. Optic suite and energy ranges of the SSRL spectrometer[54].

(5) SSRL: BL6-2 (2022)

The final table-scanning instrument is an updated 7-element spectrometer reported by Edwards et al (2022)[55]. Here, 7 1-m SBCAs are now arranged in a hexagonal pattern on a spherical array (see Fig 13) with a Bragg angle range of 64.5 to 82.6 degrees. All optics refocus to a single Vortex SDD detector and the same table-scan motorization and kinematics are present.

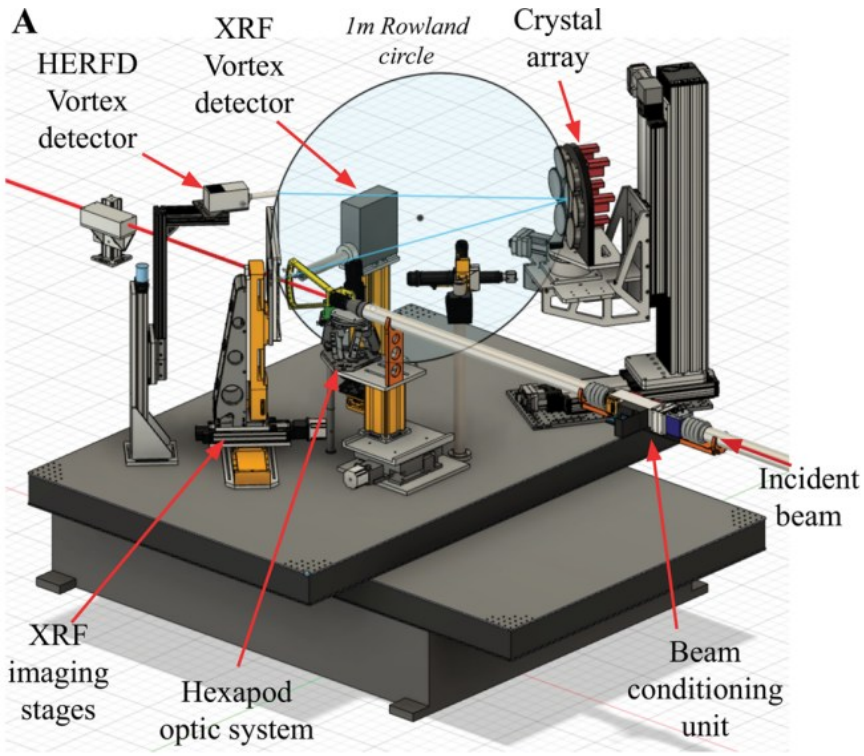

Figure 25. CAD model of the SSRL table-scanning spectrometer with hexagonal optic array[55].

The hexagonal array has 3 optics (the center horizontal row) in the familiar multiplexed geometry of the prior table-scan spectrometers; they are revolved around the vertical axis of sample and detector (Figure 26 (a), (c)). The array focuses to the SDD by individually tuning

each optic's pitch and yaw using two pusher motors (Figure 26 (b)), which is particularly important for the two rows of two optics on the top and bottom of the hexagonal array. The consequence of a common focus here is a degradation energy resolution for the four "out-of-plane" optics on the top and bottom rows of the array. This is improved by masking the SBCA edges in the dispersive direction (Figure 26 (d)). At 13.6 keV, the resolution of the array is 3 eV unmasked and 2.15 eV masked. The benefit of the hexagonal array is a smaller instrument footprint.

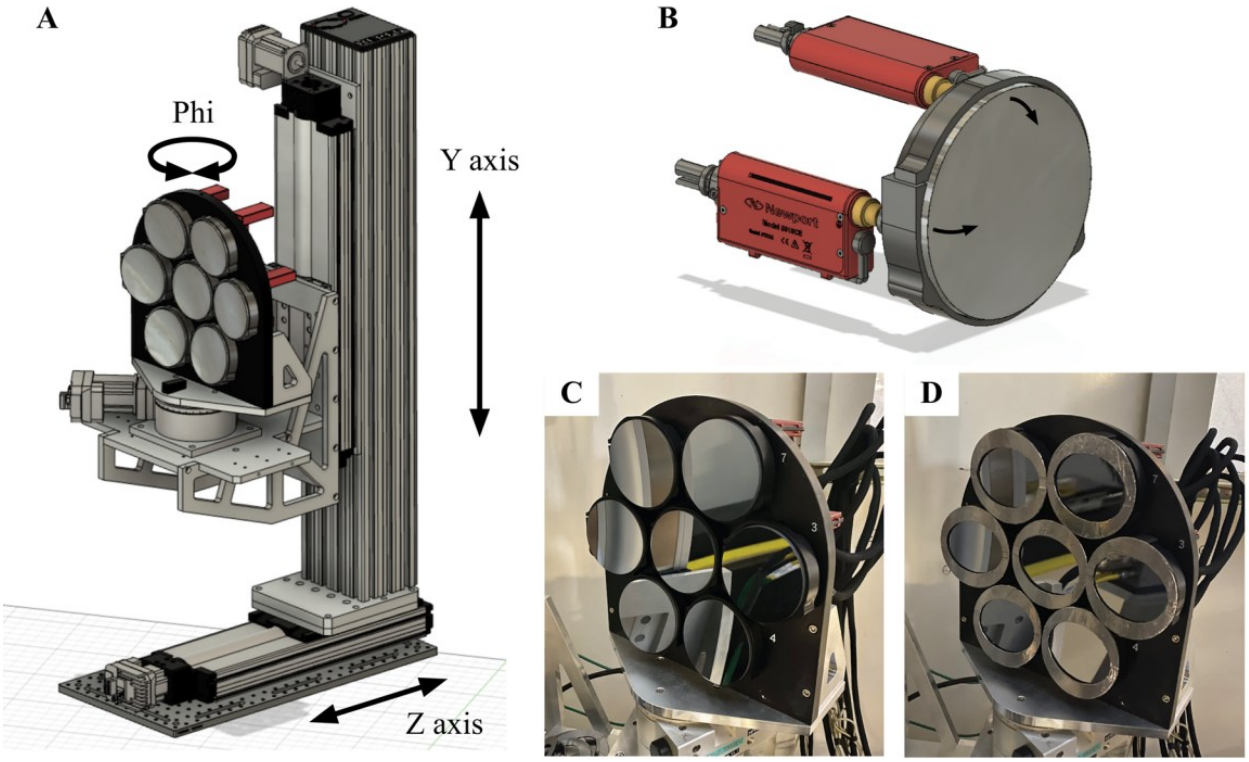

Figure 26. **(a)** CAD models of the hexagonal array and table-scanning motors **(b)** the pusher motors controlling pitch and yaw **(c)** the hexagonal array **(d)** the hexagonal array with analyzer edge masking in the dispersive direction[55].

iii. Single Optic Tilt Scan Spectrometers

(1) ESRF: ROBL

Kvashnina and Scheinost (2016) report a tilt-scan geometry scanning Johann spectrometer dedicated for XES and HERFD of actinides[56]. We note this is not the earliest spectrometer in this geometry but a convenient contemporary example. The instrument is shown in Figure 27, note the detector, in this case an avalanche photodiode, is now displaced by distance "DX" and the analyzer always remains in the horizontal plane in comparison to the table-scan geometry. The spectrometer operates from 3.5-25 keV with Bragg angles ranging from 65-89 degrees. In lieu of a goniometric tilt, the dispersive scanning of the 1-m radius SBCA is accomplished with a rotation stage the SBCA is side mounted to with the SBCA center lying along the rotation stage's axis.

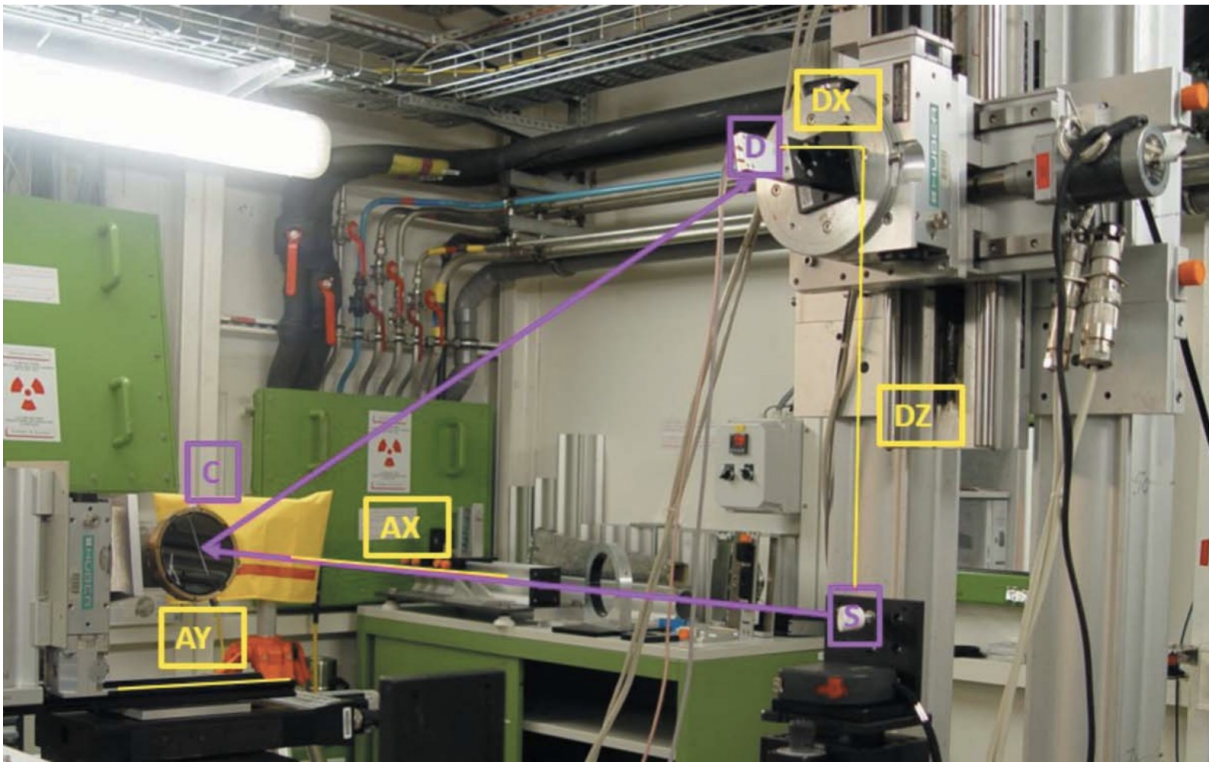

Figure 27. Single SBCA 1-m Rowland diameter tilt-scanning spectrometer at ROBL[56]

(2) ESRF: ID26

A similar set-up is reported by Rovezzi et al. (2016)[57]. Here, the spectrometer was constructed for the characterization of SBCAs manufactured at the facility to assess effects of strain-relieving the wafer on energy resolution. A thorough review of this design is not necessary, it is identical to the single optic ROBL set-up in all aspects of motorization. I note the relative simplicity of this tilt-scan geometry when only a single optic is employed.

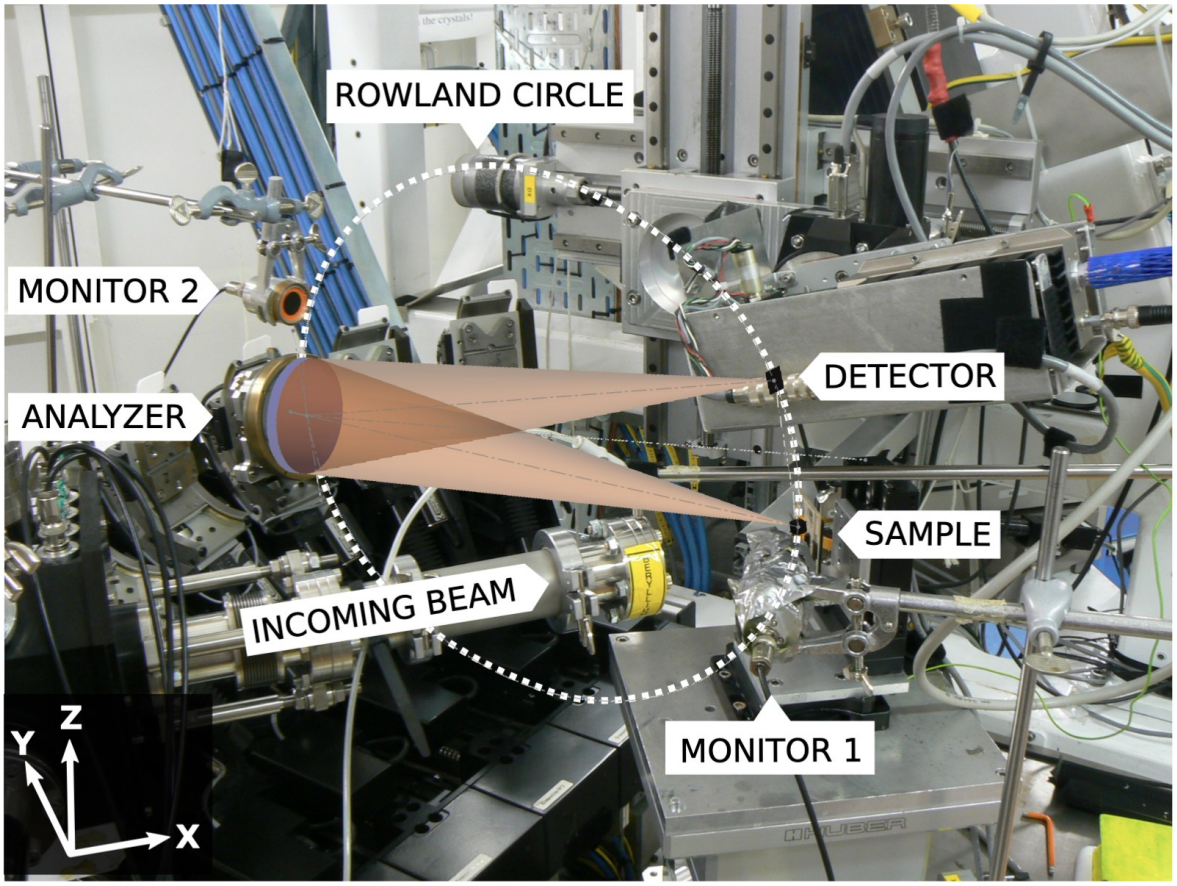

Figure 28. Single SBCA 0.5-m Rowland diameter tilt-scanning spectrometer at ID26. Identical in design to the ROBL instrument.[57]

iv. Multi Optic Tilt Scan Spectrometers

(1) NSLS-II: 8-ID

The review of multiplexed tilt-scanning spectrometers aims to proceed in increasing complexity. We begin with Tayal et al.'s work on a 5 analyzer tilt scanning spectrometer at NSLS-II (2024)[58]. An individual SBCA module is shown in Figure 29 (a), where four motorized degrees of freedom are required, pitch (dispersive direction), roll (alignment and steering), x (source-analyzer distance), and in their reference frame so-called "y" (vertical distance, which in most other examples is denoted as the z-direction) shown in Figure 29 (b). The pitch, i.e. dispersive scanning of Bragg angle, has a small stroke of ± 5°, so a full range of Bragg angles is reached by adjusting the manual angle offset of the SBCA w.r.t. the pitch stage.

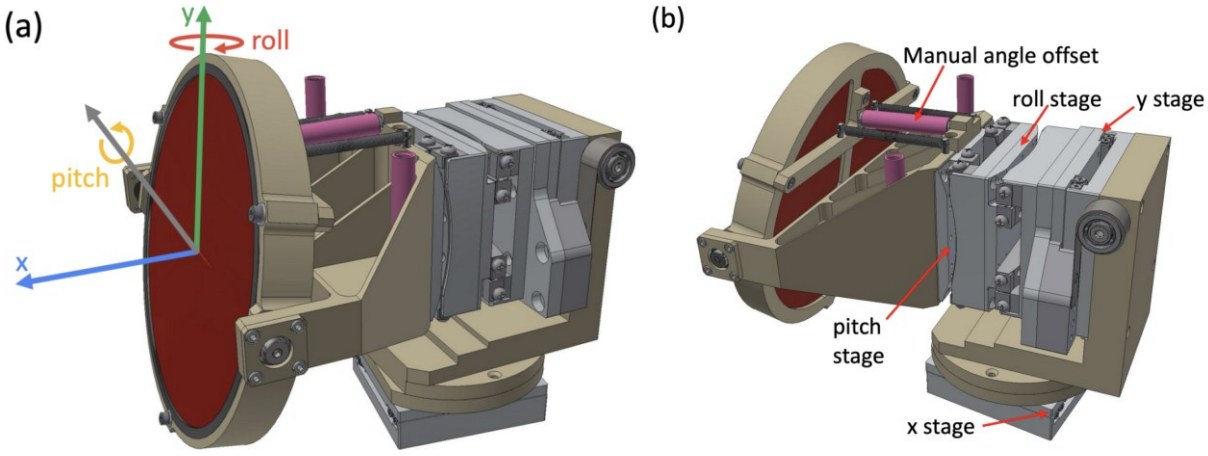

Figure 29. **(a)** degrees of freedom of each SBCA and **(b)** motorizations required.[58]

The arrangement of the modules in the five-element spectrometer is shown in Figure 30. The placement of modules on the array is first patterned around the vertical axis ("y"). Then, the y-stages of each module are adjusted to bring the optics on the wings (-2 & 2, -1 & 1) slightly above the horizontal plane w.r.t. the center module (0), forming an arc with the center module at the minima. Coarse placement of the array is accomplished with the common x-y stage beneath

the assembly, but this is not used during scanning. Coincidence of the refocusing point of each Rowland circle is achieved by scanning each modules y-stage (vertically) during an energy scan.

The authors note difficulty synchronizing the 22 motors (4 per SBCA minus the roll of the center optic, plus 3 for the detector) in addition to large overhead times when step scanning. The authors note in general, XES scans are accomplished by scanning pitch only of each SBCA while all other motors remain fixed, approximating the Rowland geometry over a narrow energy range.

There is an immediate increase in complexity compared to multiplexed table scan spectrometers – this is largely due to the requirement of vertical scanning of each SBCA to maintain Rowland circle focus coincidence at any Bragg angle; an additional degree of freedom not required in the single optic tilt-scan geometry.

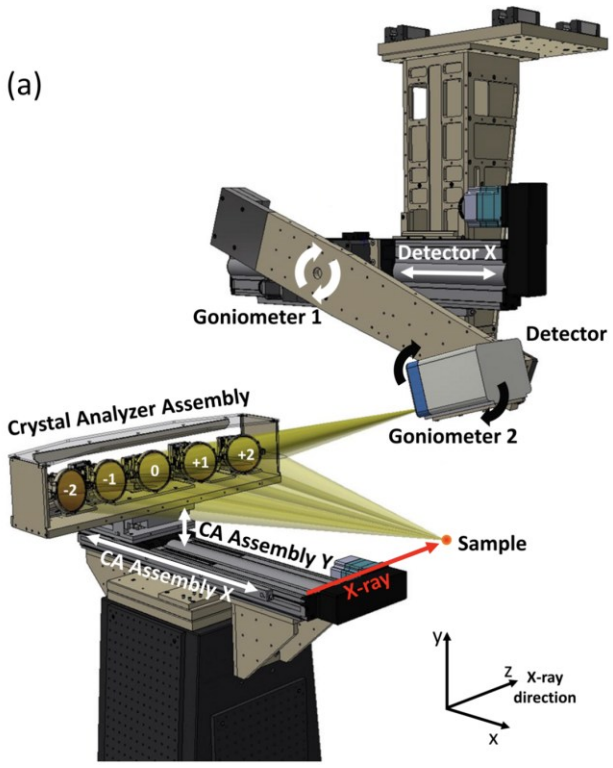

Figure 30. CAD rendering of the NSLS-II spectrometer[58].

(2) ESRF: ID20

Sala et al. report on the design of five element RIXS spectrometer at ID20 (2018)[59]. This is not a dedicated HERFD spectrometer but provides further basis for later discussion. The instrument design is based around identical modules (Figure 31, top left) supporting 1-m or 2-m SBCAs. Each SBCA is motorized with two translations and two tilts. The x, z, and theta are all required for scanning the energy of each SBCA and keeping the sample on the Rowland circle.

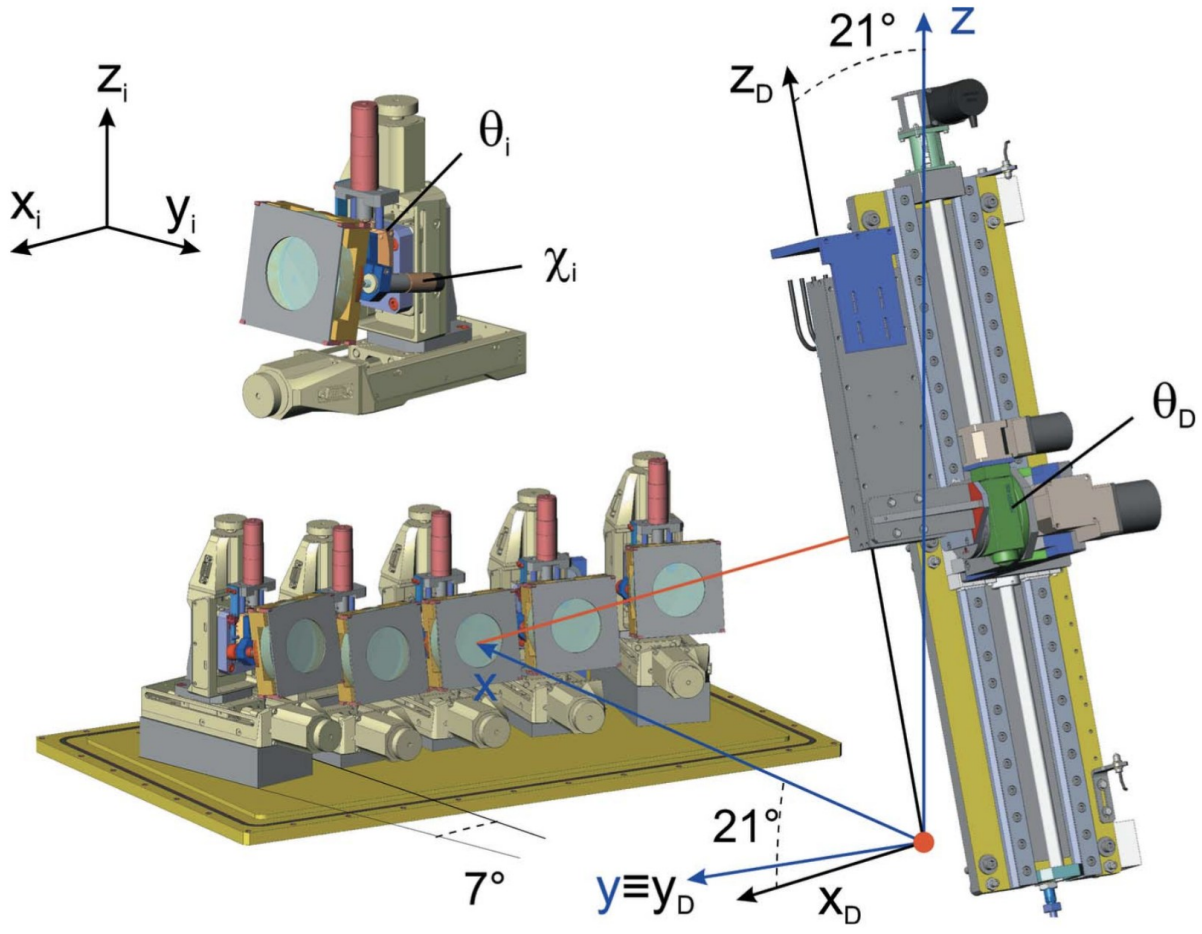

Figure 31. Multielement tilt-scanning spectrometer at ID20[59]

Here, the construction of the array is easiest visualized by revolving the center module about the "Z_D" axis. As this axis is not colinear with "z", it patterns the modules in an arc

through the horizontal plane, and is the reason for the spacers of different height (Fig. 31, grey blocks) beneath each SBCA module. An area detector is mounted on a vertically canted linear translator to eliminate the need for a second dedicated detector translation along ‘x’.

(3) SOLEIL: GALAXIES

Ablett et al. report on the design of a four element RIXS spectrometer, so-called MULTIXS, at the GALAXIES beamline (2025)[60]. Again, coincidence of the Rowland circle’s foci is achieved with an increasingly vertical offset towards the edges of the array as a function of Bragg angle, shown in Figure 32 (a) and (b). The instrument, rendered in Figure 33, has the same degrees of freedom as the prior instruments.

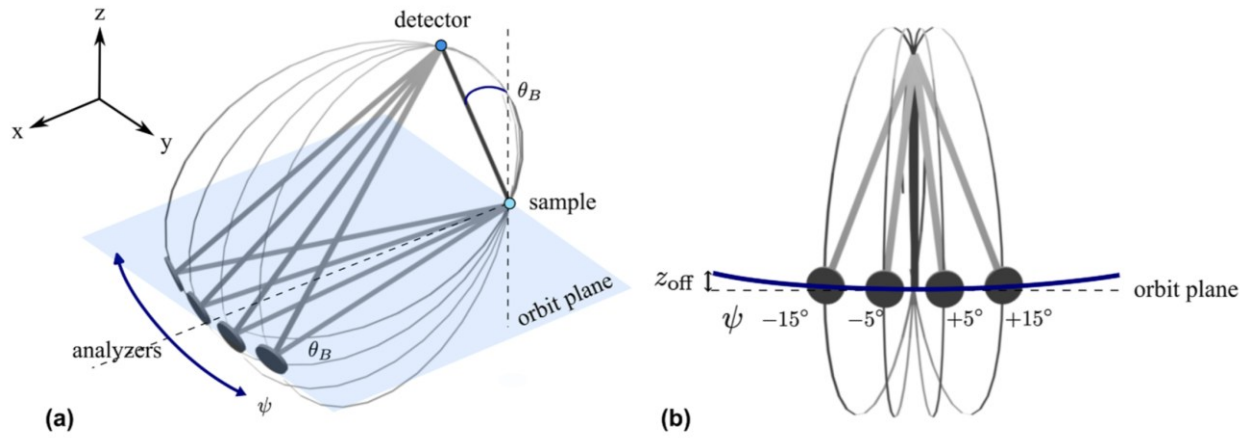

Figure 32. **(a)** Isometric view of the four Rowland circles of the MULTIXS spectrometer and **(b)** When patterning Rowland circles in this geometry by revolving around the sample-detector chord, a vertical offset out of the plane is required to maintain coincidence.[60]

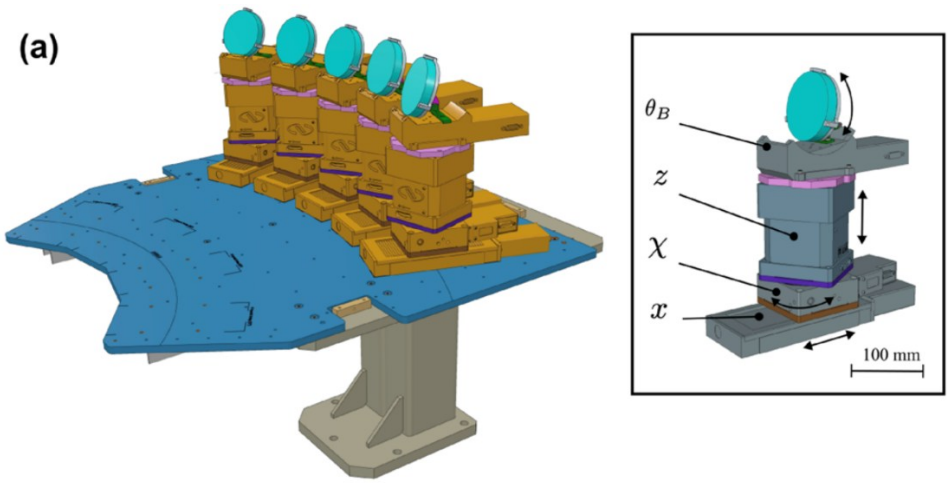

Figure 33. CAD rendering of the MULTIXS spectrometer. 4 or 5 SBCAs can be used depending on the radius of curvature (0.5-m or 1-m, respectively) of the optics.[60]

(4) Swiss Light Source: SuperXAS Beamline

A final instrument is presented here by Kleymenov et al. (2011) located at the Swiss Light Source[61]. The geometry and motorization is again identical to those previously discussed.

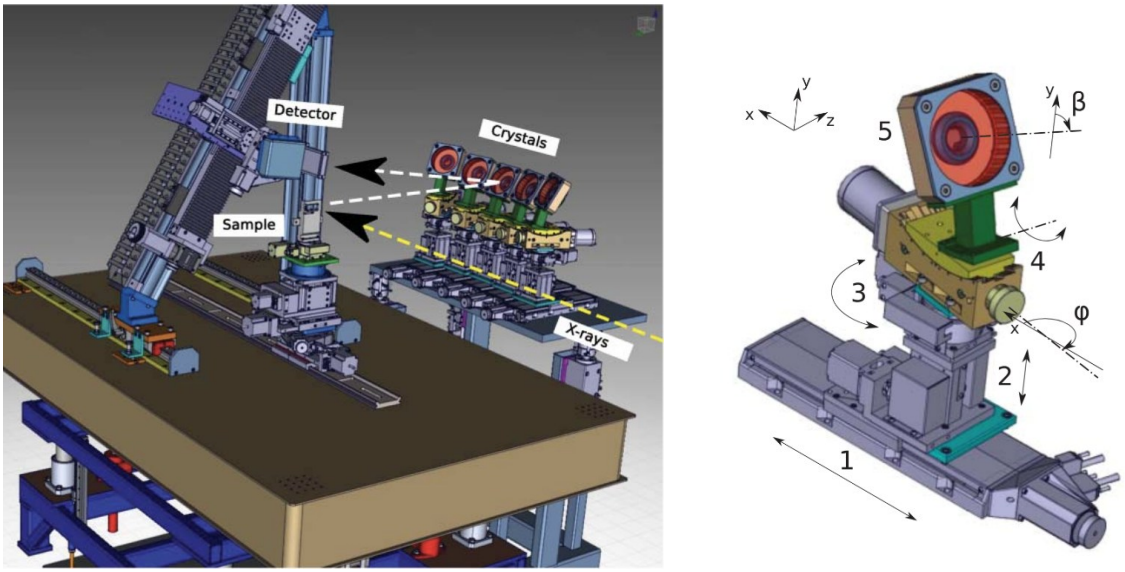

Figure 34. **(Left)** CAD rendering of the SuperXAS RIXS spectrometer. **(Right)** Motorized degrees of freedom per SBCA module.[61]

6. References

1 M. Newville, in *Spectroscopic Methods in Mineralology and Materials Sciences*, eds. G. S. Henderson, D. R. Neuville and R. T. Downs, Mineralogical Soc Amer & Geochemical Soc, Chantilly, 2014, vol. 78, pp. 33-+.

2 M. Abbate, F. Al Shamma, J. C. Fuggle and J. E. Inglesfield, in *Unoccupied electronic states: fundamentals for XANES, EELS, IPS, and BIS*, Springer-Verlag, Berlin ;, 1992, pp. 339–351.

3 F. Gherardi, *Anal. Methods*, 2021, **13**, 3731–3734.

4 U. Bergmann and P. Glatzel, *Photosynth. Res.*, 2009, **102**, 255–266.

5 F. M. F. de Groot, M. W. Haverkort, H. Elnaggar, A. Juhin, K.-J. Zhou and P. Glatzel, *Nat. Rev. Method. Prim.*, 2024, **4**, 45.

6 G. T. Seidler, D. R. Mortensen, A. J. Remesnik, J. I. Pacold, N. A. Ball, N. Barry, M. Styczinski and O. R. Hoidn, *Rev. Sci. Instrum.*, 2014, **85**, 113906.

7 J. E. Abramson, W. M. Holden, R. A. Rivera-Maldonado, A. Velian, B. M. Cossairt and G. T. Seidler, *J. Anal. At. Spectrom.*, 2023, **38**, 1125–1134.

8 D. Novichkov, A. Trigub, E. Gerber, I. Nevolin, A. Romanchuk, P. Matveev and S. Kalmykov, *J. Synchrot. Radiat.*, 2023, **30**, 1114–1126.

9 C. J. Sahle, F. Gerbon, C. Henriquet, R. Verbeni, B. Detlefs, A. Longo, A. Mirone, M.-C. Lagier, F. Otte, G. Spiekermann and S. Petitgirard, *J. Synchrot. Radiat.*, 2023, **30**, 251–257.

10 P. Jagodzinski, J. Szlachetko, J.-C. Dousse, J. Hoszowska, M. Szlachetko, U. Vogelsang, D. Banas, T. Pakendorf, A. Meents, J. A. van Bokhoven, A. Kubala-Kukus, M. Pajek and M. Nachtegaal, *Rev. Sci. Instrum.*, 2019, **90**, 063106.

11 P. Duan, S. Gu, H. Cao, J. Li and Y. Huang, *X-Ray Spectrom.*, 2017, **46**, 12–18.

12 E. P. Jahrman, G. T. Seidler and J. R. Sieber, *Anal. Chem.*, 2018, **90**, 6587–6593.

13 J.-P. Rueff, V. Baledent, K. Higashi and H. Kageyama, *Phys. Rev. B*, 2020, **102**, 235138.

14 M. Delgado-Jaime and S. De Beer, *Acta Crystallogr. Sect. A*, 2014, **70**, C218–C218.

15 D. Dhakal, D. M. Driscoll, N. Govind, A. G. Stack, N. Rampal, G. Schenter, C. J. Mundy, T. T. Fister, J. L. Fulton, M. Balasubramanian and G. T. Seidler, *Phys. Chem. Chem. Phys.*, 2023, **25**, 22650–22661.

16 K. Hamalainen, D. Siddons, J. Hastings and L. Berman, *Phys. Rev. Lett.*, 1991, **67**, 2850–2853.

17 P. Glatzel, T.-C. Weng, K. Kvashnina, J. Swarbrick, M. Sikora, E. Gallo, N. Smolentsev and R. A. Mori, *J. Electron Spectrosc. Relat. Phenom.*, 2013, **188**, 17–25.

18 S. Lafuerza, M. Retegan, B. Detlefs, R. Chatterjee, V. Yachandra, J. Yano and P. Glatzel, *Nanoscale*, 2020, **12**, 16270–16284.

19 F. M. F. de Groot, *Top. Catal.*, 2000, **10**, 179–186.

20 P. Glatzel, L. Jacquamet, U. Bergmann, F. M. F. de Groot and S. P. Cramer, *Inorg. Chem.*, 2002, **41**, 3121–3127.

21 N. Leidel, P. Chernev, K. G. V. Havelius, S. Ezzaher, S. Ott and M. Haumann, *Inorg. Chem.*, 2012, **51**, 4546–4559.

22 C. Lambertz, P. Chernev, K. Klingan, N. Leidel, K. G. V. Sigfridsson, T. Happe and M. Haumann, *Chem. Sci.*, 2014, **5**, 1187–1203.

23 P. Chernev, C. Lambertz, A. Bruenje, N. Leidel, K. G. V. Sigfridsson, R. Kositzki, C.-H. Hsieh, S. Yao, R. Schiwon, M. Driess, C. Limberg, T. Happe and M. Haumann, *Inorg. Chem.*, 2014, **53**, 12164–12177.

24 S. Mebs, R. Kositzki, J. Duan, L. Kertess, M. Senger, F. Wittkamp, U.-P. Apfel, T. Happe, S. T. Stripp, M. Winkler and M. Haurnann, *Biochim. Biophys. Acta-Bioenerg.*, 2018, **1859**, 28–41.
25 A. Bordage, V. Trannoy, O. Proux, H. Vitoux, R. Moulin and A. Bleuzen, *Phys. Chem. Chem. Phys.*, 2015, **17**, 17260–17265.
26 T. Vitova, J. Hormes, M. Falk and K. Buse, *J. Appl. Phys.*, 2009, **105**, 013524.
27 T.-J. Kuehn, W. Caliebe, N. Matoussevitch, H. Boennemann and J. Hormes, *Appl. Organomet. Chem.*, 2011, **25**, 577–584.
28 T.-J. Kuehn, J. Hormes, N. Matoussevitch, H. Boennemann and P. Glatzel, *Inorg. Chem.*, 2014, **53**, 8367–8375.
29 D. Friebel, M. W. Louie, M. Bajdich, K. E. Sanwald, Y. Cai, A. M. Wise, M.-J. Cheng, D. Sokaras, T.-C. Weng, R. Alonso-Mori, R. C. Davis, J. R. Bargar, J. K. Norskov, A. Nilsson and A. T. Bell, *J. Am. Chem. Soc.*, 2015, **137**, 1305–1313.
30 W.-Q. Shi, L.-Y. Yuan, C.-Z. Wang, L. Wang, L. Mei, C.-L. Xiao, L. Zhang, Z.-J. Li, Y.-L. Zhao and Z.-F. Chai, *Adv. Mater.*, 2014, **26**, 7807–7848.
31 D. Prieur, L. Amidani, E. F. Bazarkina, C. Hennig, E. L. Bright, A. Rossberg, C. L. Silva and K. O. Kvashnina, *Chem. Method.*, DOI:10.1002/cmtd.202400073.
32 A. Peterson and J. N. Wacker, *Nat. Rev. Chem.*, 2024, **8**, 408–409.
33 Y. Saitoh, Y. Fukuda, Y. Takeda, H. Yamagami, S. Takahashi, Y. Asano, T. Hara, K. Shirasawa, M. Takeuchi, T. Tanaka and H. Kitamura, *J. Synchrot. Radiat.*, 2012, **19**, 388–393.
34 A. C. Scheinost, J. Claussner, J. Exner, M. Feig, S. Findeisen, C. Hennig, K. O. Kvashnina, D. Naudet, D. Prieur, A. Rossberg, M. Schmidt, C. Qiu, P. Colomp, C. Cohen, E. Dettona, V. Dyadkin and T. Stumpf, *J. Synchrot. Radiat.*, 2021, **28**, 333–349.
35 P. Steier, K. Hain, U. Kloetzli, J. Lachner, A. Priller, S. Winkler and R. Golser, *Nucl. Instrum. Methods Phys. Res. Sect. B-Beam Interact. Mater. Atoms*, 2019, **458**, 82–89.
36 A. Zimina, K. Dardenne, M. A. Denecke, J. D. Grunwaldt, E. Huttel, H. Lichtenberg, S. Mangold, T. Pruessmann, J. Rothe, R. Steininger and T. Vitova, in *16th International Conference on X-Ray Absorption Fine Structure (xafs16)*, IoP Publishing Ltd, Bristol, 2016, vol. 712, p. 012019.
37 J. Rothe, S. Butorin, K. Dardenne, M. A. Denecke, B. Kienzler, M. Loeble, V. Metz, A. Seibert, M. Steppert, T. Vitova, C. Walther and H. Geckeis, *Rev. Sci. Instrum.*, 2012, **83**, 043105.
38 D. Novichkov, A. Trigub, E. Gerber, I. Nevolin, A. Romanchuk, P. Matveev and S. Kalmykov, *J. Synchrot. Radiat.*, 2023, **30**, 1114–1126.
39 R. Bes, T. Ahopelto, A.-P. Honkanen, S. Huotari, G. Leinders, J. Pakarinen and K. Kvashnina, *J. Nucl. Mater.*, 2018, **507**, 50–53.
40 K. O. Kvashnina, Y. O. Kvashnin and S. M. Butorin, *J. Electron Spectrosc. Relat. Phenom.*, 2014, **194**, 27–36.
41 R. Bes, M. Rivenet, P.-L. Solari, K. O. Kvashnina, A. C. Scheinost and P. M. Martin, *Inorg. Chem.*, 2016, **55**, 4260–4270.
42 K. O. Kvashnina and S. M. Butorin, *Chem. Commun.*, 2022, **58**, 327–342.
43 L. v. Hámos, *Naturwissenschaften*, 1932, **20**, 705–706.
44 R. Alonso-Mori, J. Kern, D. Sokaras, T.-C. Weng, D. Nordlund, R. Tran, P. Montanez, J. Delor, V. K. Yachandra, J. Yano and U. Bergmann, *Rev. Sci. Instrum.*, 2012, **83**, 073114.
45 B. Mei, S. Gu, X. Du, Z. Li, H. Cao, F. Song, Y. Huang and Z. Jiang, *X-Ray Spectrom.*, 2020, **49**, 251–259.

46 A. S. Ditter, W. M. Holden, S. K. Cary, V. Mocko, M. J. Latimer, E. J. Nelson, S. A. Kozimor and G. T. Seidler, *J. Synchrot. Radiat.*, 2020, **27**, 446–454.
47 W. M. Holden, O. R. Hoidn, A. S. Ditter, G. T. Seidler, J. Kas, J. L. Stein, B. M. Cossairt, S. A. Kozimor, J. Guo, Y. Ye, M. A. Marcus and S. Fakra, *Rev. Sci. Instrum.*, 2017, **88**, 073904.
48 H. H. Johann, *Z. Physik*, 1931, **69**, 185–206.
49 P. Glatzel, A. Harris, P. Marion, M. Sikora, T.-C. Weng, C. Guilloud, S. Lafuerza, M. Rovezzi, B. Detlefs and L. Ducotte, *J. Synchrot. Radiat.*, 2021, **28**, 362–371.
50 J.-L. Hazemann, O. Proux, V. Nassif, H. Palancher, E. Lahera, C. Da Silva, A. Braillard, D. Testemale, M.-A. Diot, I. Alliot, W. Del Net, A. Manceau, F. Gélébart, M. Morand, Q. Dermigny and A. Shukla, *J Synchrotron Rad*, 2009, **16**, 283–292.
51 I. Llorens, E. Lahera, W. Delnet, O. Proux, A. Braillard, J.-L. Hazemann, A. Prat, D. Testemale, Q. Dermigny, F. Gelebart, M. Morand, A. Shukla, N. Bardou, O. Ulrich, S. Arnaud, J.-F. Berar, N. Boudet, B. Caillot, P. Chaurand, J. Rose, E. Doelsch, P. Martin and P. L. Solari, *Rev. Sci. Instrum.*, 2012, **83**, 063104.
52 P. Duan, S. Gu, H. Cao, J. Li and Y. Huang, *X-Ray Spectrom.*, 2017, **46**, 12–18.
53 B.-B. Mei, L.-X. Wang, S.-Q. Gu, X.-Z. Su, S. Zhang, Y. Wei, J.-Y. Ma, Z. Jiang and F. Song, *Nucl. Sci. Tech.*, 2024, **35**, 156.
54 D. Sokaras, T.-C. Weng, D. Nordlund, R. Alonso-Mori, P. Velikov, D. Wenger, A. Garachtchenko, M. George, V. Borzenets, B. Johnson, T. Rabedeau and U. Bergmann, *Rev. Sci. Instrum.*, 2013, **84**, 053102.
55 N. P. P. Edwards, J. R. R. Bargar, D. van Campen, A. van Veelen, D. Sokaras, U. Bergmann and S. M. M. Webb, *Rev. Sci. Instrum.*, 2022, **93**, 083101.
56 K. O. Kvashnina and A. C. Scheinost, *J. Synchrot. Radiat.*, 2016, **23**, 836–841.
57 M. Rovezzi, C. Lapras, A. Manceau, P. Glatzel and R. Verbeni, *Rev. Sci. Instrum.*, 2017, **88**, 013108.
58 A. Tayal, D. S. Coburn, D. Abel, M. Rakitin, O. Ivashkevych, J. Wlodek, D. Wierzbicki, W. Xu, E. Nazaretski, E. Stavitskia and D. Leshcheva, *J. Synchrot. Radiat.*, 2024, **31**, 1609–1621.
59 M. M. Sala, K. Martel, C. Henriquet, A. Al Zein, L. Simonelli, C. J. Sahle, H. Gonzalez, M.-C. Lagier, C. Ponchut, S. Huotari, R. Verbeni, M. Krisch and G. Monaco, *J. Synchrot. Radiat.*, 2018, **25**, 580–591.
60 J. M. Ablett, A. Berlioux, D. Prieur, J. Harrison, L. Heller, S. Gliga and J.-P. Rueff, *Rev. Sci. Instrum.*, 2025, **96**, 053104.
61 E. Kleymenov, J. A. van Bokhoven, C. David, P. Glatzel, M. Janousch, R. Alonso-Mori, M. Studer, M. Willimann, A. Bergamaschi, B. Henrich and M. Nachtegaal, *Rev. Sci. Instrum.*, 2011, **82**, 065107.

Chapter 5. Asymmetric Rowland Circle Geometries for Spherically Bent Crystal Analyzers in Laboratory and Synchrotron Applications

This chapter is based on a manuscript that first appeared in "Journal of Analytical Atomic Spectroscopy" of the Royal Society of Chemistry.

Anthony J. Gironda, Jared E. Abramson, Yeu Chen, Mikhail Solovyev, George E. Sterbinsky, Gerald T. Seidler "Asymmetric Rowland Circle Geometries for Spherically Bent Crystal Analyzers in Laboratory and Synchrotron Applications." ***J. Anal. At. Spectrom.***, 2024, **39**, 1375-1387. (DOI: https://doi.org/10.1039/D3JA00437F)

1. Abstract

Spherically bent crystal analyzers (SBCAs) are the dominant high-resolution hard x-ray optic in the ongoing rebirth of laboratory-based x-ray absorption fine structure (XAFS) and x-ray emission spectroscopy (XES) as well as in synchrotron methods such as high energy resolution fluorescence detection (HERFD) and non-resonant x-ray Raman scattering (XRS). In the overwhelming majority of cases, SBCAs are implemented in a 'symmetric' configuration on the Rowland circle, wherein the diffracting crystal plane is nominally coincident with the analyzer surface. We report here comprehensive investigations of 'asymmetric' operation of SBCA on the Rowland circle, wherein the diffracting crystal plane is not coincident with the optical surface of the analyzer. First, we have developed a laboratory spectrometer for XAFS and XES that is

specialized for asymmetric SBCA operation. We find several benefits, including the capacity to use a single SBCA over a very wide energy range via '*hkl* hopping' and the frequent ability to eliminate Johann error, the most prevalent energy-broadening mechanism when using SBCA symmetrically on the Rowland circle. Second, we expand these ideas to synchrotron facilities with a demonstration study of HERFD and XRS where asymmetric operation also provided advantage. Our results suggest that large-array systems for HERFD augmented with an additional mechanical degree of freedom could streamline user operation and also indicate benefits to XRS in the asymmetric configuration, where larger solid angle, larger sample-to-detector distance, and decreased Johann error can be achieved simultaneously.

2. Introduction

Spherically bent crystal analyzers (SBCAs), specifically those with Johann-type profiles[1], are hard x-ray optics that provide a useful combination of large collection solid angle and fine energy resolution. This has resulted in their extensive use in the ongoing rebirth of laboratory-based x-ray absorption fine structure (XAFS) and x-ray emission spectroscopy (XES)[2–10] in addition to their historical and continued use as workhorse optics for high-resolution photon-in photon-out x-ray spectroscopy at synchrotron facilities.[11–18] With infrequent but valuable exceptions[19–22], such applications have been in a 'symmetric' Rowland circle configuration wherein the diffracting plane is nominally coincident with the surface of the SBCA diffracting wafer.

Here, we propose that asymmetric operation of SBCA on the Rowland circle is an underutilized opportunity. The basic parameters for asymmetric Rowland circle operation are defined in Fig. 1. In the Figure, note the asymmetry angle α, the need for a 'mechanical'

analyzer angle θ_M, and the inequality of the chord lengths ρ and d when $\alpha \neq 0$. The usual theorem for equality of inscribed angles still holds when $\alpha \neq 0$ so that the optic still functions as a monochromator in the Rowland plane, barring Johann error which will be discussed in detail later. Out-of-plane astigmatism at large α can become considerable, but we find that is not a significant limitation on energy resolution. It is not difficult to derive the dependence of the parameters in Fig. 1 on the Bragg angle, θ_B, and α, specifically

$$\begin{aligned} \rho &= D\sin(\theta_B + \alpha) \\ d &= D\sin(\theta_B - \alpha) \\ 2\theta &= 2\theta_B \\ \theta_M &= \theta_B + \alpha \end{aligned} \tag{1}$$

where D is the diameter of the Rowland circle or equivalently the radius of curvature of the Johann SBCA.

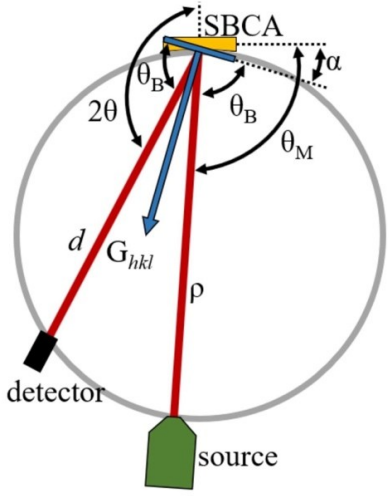

Figure 1. Diagram of spectrometer components during asymmetric operation in the reference frame of the SBCA. α denotes the angle between the diffracting plane for the reflection $\mathbf{G}_{hkl}$ and the plane at the optic's surface (nominally normal to the reciprocal lattice vector $\mathbf{G}_0$). Note the chord lengths d and ρ differ when $\alpha \neq 0$.

With this background established, we address the potential advantages of asymmetric operation as a central principle in spectrometer design. We denote by $\mathbf{G}_0$ the reciprocal lattice vector normal to the wafer surface and assume the wafer miscut is small. Choosing $\mathbf{G}_0$ is equivalent to choosing which wafer material and orientation to use in the optic, and it determines the useful energy range in symmetric operation -- Bragg angles below 60 deg generally suffer degraded energy resolution due to Johann error and source-size broadening. While analyzer harmonics sometimes enable high-resolution access to a few distinct energy ranges[23], both laboratory instruments and synchrotron facilities typically fabricate or acquire a suite of SBCAs having a variety of $\mathbf{G}_0$ vectors.

Asymmetric operation modifies these considerations. Any single crystal has a multitude of additional crystal planes at various angles to the surface. Each allowed reflection capable of diffraction in an asymmetric configuration gives an additional useful energy range dependent on its own *d*-spacing. Hence, as a first advantage, we show below that asymmetric operation of a single SBCA can permit high-resolution performance for photon energies from 5 keV through 10 keV and beyond with no gaps in the energy range. The good performance of many different reflections of various Miller indices (*hkl*) from a single analyzer is a major result of the present study, and we find it appropriate to introduce the term '*hkl* hopping' when a monochromator jumps between different Miller indices of a single SBCA to adjust energy range or to improve energy resolution, which we now address.

The second advantage of asymmetric operation is the minimization or even elimination of Johann error for SBCAs; prior work by Suortti and others for curved analyzers on the Rowland circle as well as asymmetric applications in other fields and other classes of optics motivates and supports this inquiry[21,22,24–35]. Briefly, Johann analyzers possess a radius of curvature for the

diffracting wafer that is equal to the diameter of the desired Rowland circle. This yields the necessary suface orientations but results in small displacements between the wafer surface and the Rowland circle at the analyzer edges with corresponding errors in the Bragg angle upon moving away from the analyzer center. There is consequently a characteristic low energy tail in the analyzer's energy response function[36].

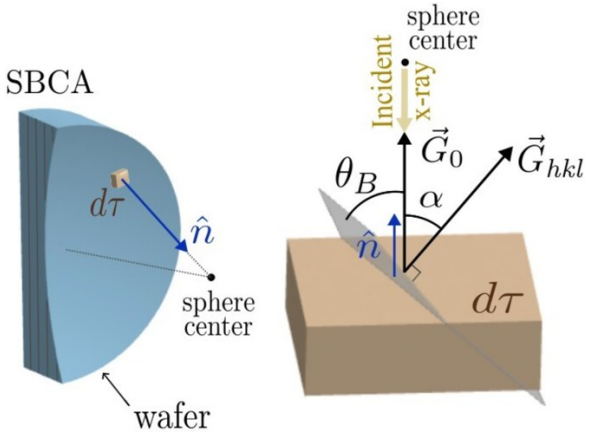

Figure 2. An infinitesimal single crystal element (right) of a spherically bent crystal analyzer (left), demonstrating a geometric argument for the elimination of Johann error in asymmetric Rowland geometries when the source is close to the sphere-center of the SBCA curved wafer.

The underlying principle for suppression of Johann error via asymmetric operation is illustrated in Fig. 2. As shown, consider the special case where all incident x-rays have an incoming path exactly normal to each infinitesimal crystallite that makes up the SBCA surface, i.e., the special case where a point source is located at the sphere center of the curved analyzer wafer surface. The key observation is that for every point on the analyzer surface, the angle between an arbitarily chosen reciprocal lattice vector $\mathbf{G}_{hkl}$ and the incident x-ray is the same everywhere on the surface. Hence, in this special case the Bragg angle is the same at every point on the surface and Johann error from the lack of coincidence between the edges of the analyzer

and the Rowland circle is eliminated. More generally, asymmetric operation allows operation with the source *closer to* the sphere center than is often possible symmtrically, and hence with dereased Johann error. We illustrate this later with XANES and XES measurements.

Finally, a third benefit comes from those special geometries that are expected to fully eliminate Johann error, as described by Fig. 2. Non-resonant x-ray Raman scattering (XRS), i.e., the non-resonant inelastic x-ray scattering from semicore levels, gives a hard x-ray analog to electron energy loss spectroscopy and allows x-ray spectroscopy on low-energy shells while using high-energy photons. This capability has seen sufficient demand that several dedicated facilities have been constructed at synchrotron facilities[37–41]. However, the extremely small cross-section for inelastic scattering from the semicore levels makes all XRS spectrometers subject to severe competition between the collection solid angle and the energy resolution. The best practice to date has been to use banks of 1-m SBCA as close as possible to a backscatter geometry in symmetric Rowland operation, together with considerable diligence to reject background scatter[12,14,17,18]. That being said, achieving highest energy resolution still requires analyzer masking to reduce Johann error; in some cases, small off-circle broadening is accepted as a compromise that aids with clearance between detector and the beam spot on the sample[13]. The more recently available 0.5-m SBCA having four times the solid angle of the older 1-m SBCA have not been used for XRS because their larger angular size results in far larger Johann error *in symmetric operation*. On the other hand, the Johann-rejection strategy of Fig. 2 provides a possible path toward simultaneously attaining large solid angle, fine energy resolution, and large clearance between sample and detector. XRS measurements are performed in so-called inverse-scanning mode where a single energy is chosen for the outgoing (analyzed) photon while

the incident monochromator is scanned to create the necessary range of energy losses: *the spectrometer must have low Johann error at only a single energy*.

In this paper we address all three of these proposed benefits. We describe a new laboratory-based XAFS and XES hard x-ray spectrometer specifically designed to enable easy exploration of asymmetric Rowland geometries. With this instrument we demonstrate *hkl* hopping over a broad energy range and also demonstrate the minimization of Johann error through choice of the favorable special geometry with the source near the spherical center of the analyzer. These benefits also appear in our preliminary synchrotron studies, where we use asymmetric reflections to access the otherwise inconvenient Zn $K\alpha_1$ for high-energy resolution fluorescence detection (HERFD) x-ray absorption spectroscopy and also use an optimal asymmetric configuration for XRS via an 0.5-m radius SBCA. This ensemble of results across laboratory and synchrotron venues supports the hypothesis that asymmetric operation of SBCA has been underutilized and suggests directions for further inquiry.

3. Laboratory Spectrometer Design and Operation

We now present the six main spectrometer systems in order: the x-ray enclosure, x-ray sources, the detector and its subassembly, the optic, the motorization of the primary Rowland circle degrees of freedom, the additional motorized degree of freedom used to rotate many different desired reflections into the Rowland plane, and the overall control software.

The spectrometer is housed in a steel enclosure, approximately 1.8-m wide by 1.5-m deep by 1.3-m tall. The slightly oversized enclosure provides ample space for special sample environments in the future such as a cryostat or additional equipment such as a potentiostat for *operando* electrochemical measurements. The computer-aided design (CAD) rendering in Fig. 3

shows the design of the spectrometer and its key components in Rowland circle geometries configured for XAFS and XES measurements in Fig. 3 (a) and (b), respectively. In XAFS mode (Fig. 3 (a)), a 100 W X-ray source (Varex VF-80 Pd-anode tube) with variable width entrance slits to adjust apparent source size is placed on-circle via manual slide. In XES mode (Fig. 3 (b)), a 3 kW X-ray source (Varex OEG-76H W-anode tube) with a preliminary 1 mm fixed-width entrance slit on the sample enclosure is placed on-circle via manual slide. A kinematic feature at the fixed source location ensures precise placement of radiation entrance slits on circle. A 100 W x-ray tube with a tungsten anode, but otherwise identical to the XAFS-mode source, was used for commissioning in XES measurements (not shown in the figure).

The detector is a silicon drift detector (SDD) with 150 mm^2 area sensing element (KETEK AXAS M-1) mounted on a motorized linear stage (Velmex XSlide) to adjust the detector-analyzer chord length. The optics are 0.5-m radius of curvature SBCAs (XRS Tech). The chord lengths and angular positioning of the detector and optic are motorized. The optic and detector subassemblies are concentrically mounted on the θ and 2θ rotation stages, respectively, of a repurposed goniometer from a commercial X-ray diffraction instrument (Bruker D8 Advance). The θ and 2θ stages of the goniometer are independent, allowing for the α offsets required in asymmetric operation. The entire goniometer-detector-optic subassembly is mounted on a motorized linear stage (Velmex tandem BiSlide) to adjust source-analyzer chord length, ρ.

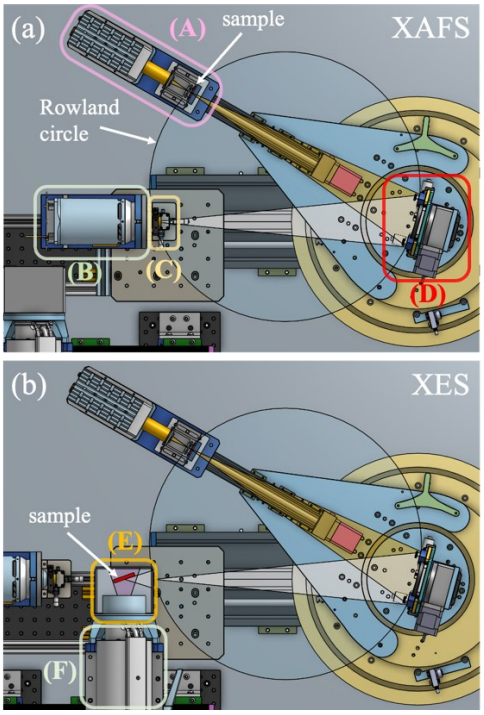

Figure 3. Top-view CAD renderings of the spectrometer configured for **(a)** XAFS and **(b)** XES measurements. The key components are outlined with boxes and labelled as follows: (A) detector, (B) 100 W XAFS source, (C) Adjustable-width XAFS entrance slit, (D) crystal analyzer and optic tower, (E) XES sample enclosure and entrance slit, and (F) 3 kW XES source.

For automated asymmetric operation, an additional motorized degree of freedom we refer to as the 'clock angle' or φ is required in the optic subassembly. This additional degree of freedom also enables motorized tilt-free correction of crystal miscut.[42] CAD renderings of the optic cartridge, the full optic tower assembly, and the φ rotation stage and direction are shown in the three panels of Fig. 4. The cartridge mounts concentrically on a small, motorized rotation stage (Velmex B5990TS). The fine adjustment *x*-*y* stage at the base of the optic tower aligned the optic on the rotation axis of the goniometer during spectrometer commissioning.

Recalling from the introduction the requirements for asymmetric Rowland configurations, the spectrometer achieves these geometries by using independent rotation and linear stages. Representative symmetric and asymmetric configurations are shown in CAD renderings in Fig. 5. Specifically, Fig. 5(a) shows a typical symmetric operation at an unfavorable θ_B far from backscatter, whereas Fig. 5(b) shows an asymmetric configuration at the same θ_B but satisfying the condition of $\theta_B + \alpha = 90$ deg, the configuration that is expected to eliminate Johann error, recall Fig. 2. It is important to note Fig. 5(a) and (b) could be at radically different energies because of the different *d*-spacings for $\mathbf{G}_0$ and $\mathbf{G}_{hkl}$. The purpose of the Figure is to demonstrate the difference in geometries in these different diffracting conditions. Note that the chord lengths between source-and-analyzer and analyzer-and-detector become unequal when $\alpha \neq 0$.

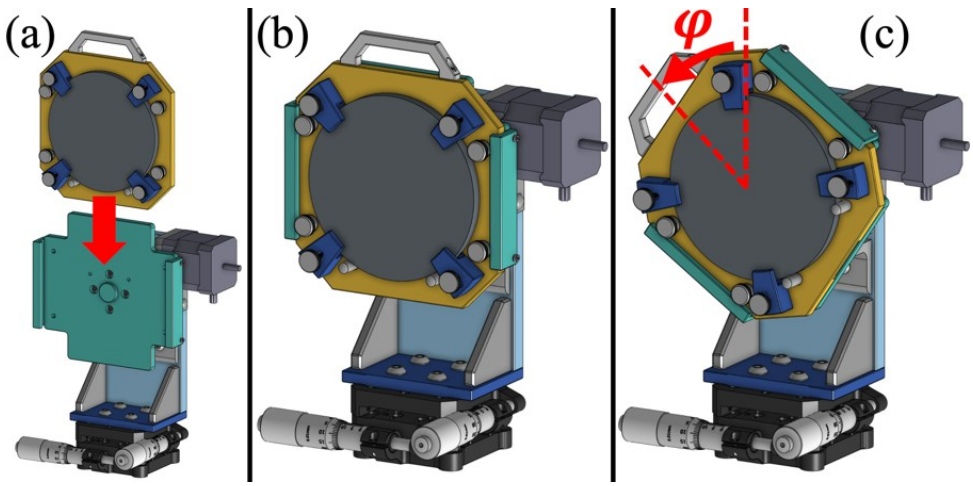

Figure 4. **(a)** An optic cartridge is loaded into the optic tower subassembly. **(b)** The fully assembled motorized optic tower which concentrically indexes the crystal on a motorized rotation stage. **(c)** The motorized azimuthal (φ) degree of freedom allows for tilt-free correction of crystal miscut and for automated asymmetric operation.

The spectrometer control software consists of two main components. First, a library of routines was written in Python (Jupyter) to generate ASCII files with component-by-component instructions for each step in any desired spectrometer scan. Second, LabView software was written to interpret the scan definition files and execute the desired measurements by commanding the motors and reading the detector. The LabView software can define measurement projects that perform sequences of measurements each parametrized by a different scan definition file including for successive scans using different $\mathbf{G}_{hkl}$. For both XAFS and XES, the energy is scanned by stepping the crystal angle θ_M and satisfying the Rowland circle geometry at a particular Bragg angle by driving the ρ, detector, and 2θ stages.

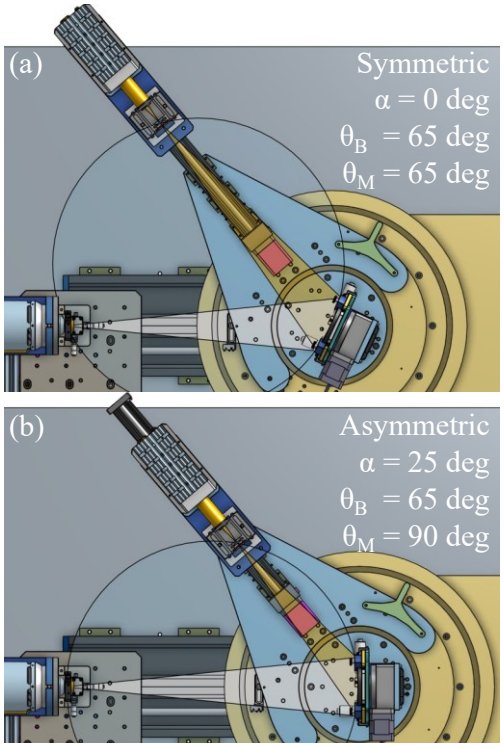

Figure 5. **(a)** Symmetric spectrometer operation at θ_B = 65 deg in XAFS mode. **(b)** Asymmetric spectrometer operation at the same θ_B with α = 25 deg, placing the source diametrically from the optic resulting in a monochromatic diffracted beam with no Johann broadening.

4. Methods

Ray tracing simulations are generated using the xrt Python package[43]. The ray tracing calculations use a 250-μm by 250-μm area source and a 100-mm diameter, 0.5-m SBCA in both symmetric and asymmetric Rowland circle configurations, thus approximating the experimental conditions. Calculations for the location of asymmetric reflections and their resulting energy ranges were performed in home-written software in Python (Jupyter).

XES and XAFS measurements were taken with the laboratory-based instrument described in Section II using only a 100 W source in both configurations. Studies were selected to demonstrate instrument capabilities to characterize the advantages of asymmetric operation. For XAFS, standard metal reference foils of Cu and Ni (EXAFS Materials) were used. To demonstrate the extended energy range afforded by asymmetric operation, a multi-component transition metal oxide sample was prepared for XES. Equal masses of V_2O_3, MnO, FeO, NiO, CuO, ZnO, and $SrTiO_3$ were dry milled together to homogeneously mix the sample. The multi-component powder was enclosed in a polyimide pouch for XES study.

XRS and HERFD-XANES measurements were performed at sector 25-ID of the Advanced Photon Source. This used a Si(111) double crystal monochromator and a set of Kirkpatrick-Baez mirrors to achieve an approximately 100 μm by 100 μm spot size on the sample. The monochromator was not detuned, and the resulting expected energy resolution is 1.2 - 1.3 eV at 8700 eV. An Eiger S 500K camera (Dectris Corp.) was used to measure the x-rays analyzed by the SBCA (XRS Tech) and an SDD (Hitachi, Vortex) was used to measure total fluorescence yield in the HERFD study. The HERFD sample was a ZnO film with embedded Ge nanocrystals, prepared by sequential sputtering of ZnO and Ge targets under reactive ZnO growth conditions[44]. The XRS sample was an 0.9-mm diameter cylinder of randomly oriented

graphite in a low-Z binder (mechanical pencil lead). For both studies the incident flux was ~$3x10^{12}$ ph/sec.

5. Results and Discussion

a. The Asymmetric Rowland Geometry in the Laboratory

We begin by illustrating a central motivation of asymmetric operation, i.e., the large number of crystal planes that are available and the consequently wide energy range that can be accessed with fine energy resolution for a single SBCA. See Fig. 6. In panel (a) we show the calculated locations for a large number of asymmetric reflections for a Si(551) analyzer in terms of the asymmetry angle α (radial direction in the polar plot) and the clock angle φ (azimuthal direction in the polar plot). Note that the $\mathbf{G}_0$=(551) reflection itself is at the center of the polar plot. In panel (b) we show an experimental survey of the (α, φ) space at θ_B= 82 deg and find excellent agreement with the calculations of panel (a). In addition, as shown by the color scale indicating the dominant energy detected at a given location, we observe that a very large energy range can likely be patched together by *hkl*-hopping between different asymmetric configurations. This type of study is readily performed in the laboratory because of the very broad bremsstrahlung spectrum of x-ray tubes. Panels (c) and (d) show analogous calculations and experimental results for a Si(221) analyzer. Miller indices in panels (b) and (d) were identified by consistency between the theoretical (α, φ) polar plot with all allowed reflections and the results of converting the observed energy of an experimental reflection to the sum of squared indices by Bragg's law.

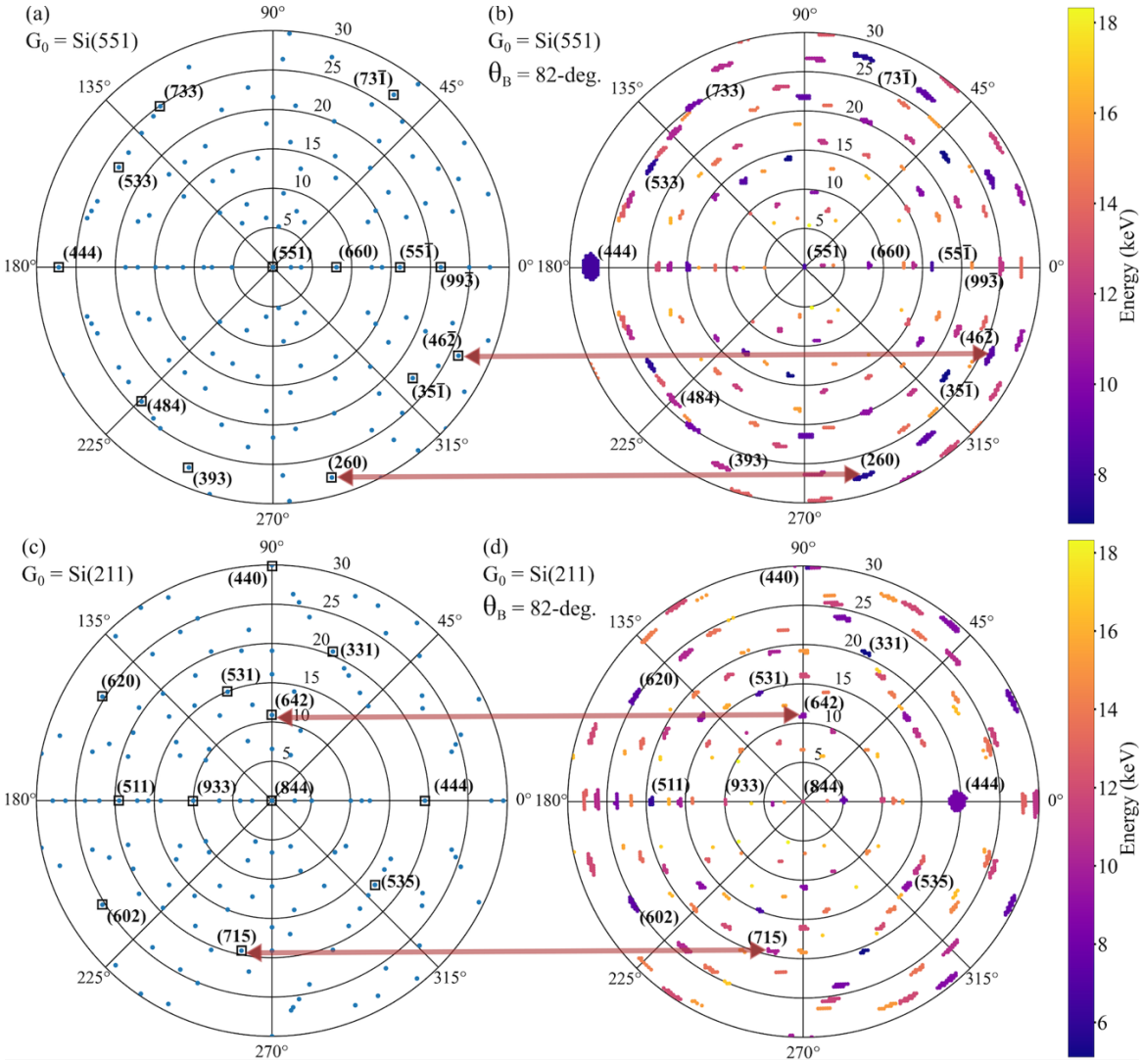

Figure 6. Polar plots in (α, ϕ) for calculated and measured reflections. (a) Calculated values of selected asymmetric reflections of a Si(551) analyzer. (b) Experimental data for Si(551) SBCA obtained by sampling phi-alpha space values at a fixed Bragg angle. (c) Calculated values of asymmetric Si(211) reflections. (d) Experimental data for Si(211) SBCAs. A threshold on reflection intensity was implemented to remove background in experimental data.

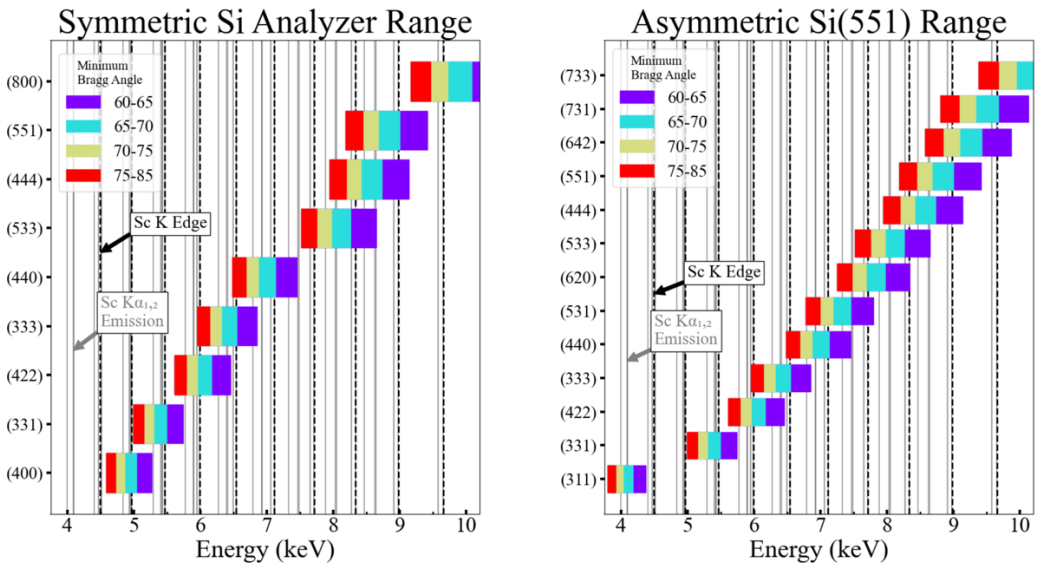

Figure 7. **(Left)** Diagram of the energy range achievable operating symmetrically with the Si SBCAs commonly used for transition metal XAS and XES: $\mathbf{G}_0$ = (100), (110), (111), (211), (331), (533), (551). The vertical gray lines indicate emission lines and the vertical black dashed lines indicate K-edges between 4 and 10 keV. **(Right)** Diagram of the energy range achievable operating asymmetrically with a Si(551) SBCA. Duplicate reflections, those that cover the exact same energy range at the same Bragg angle are omitted for clarity.

In both Fig. 6 (b) and (d) an azimuthal smearing is seen in the experimental results at large values of α near the borders of the pole plots. When at large asymmetries the chord length *d* from the SBCA to the detector becomes much smaller than the vertical radius of curvature of the analyzer, resulting in a significant vertical (perpendicular to the Rowland plane) extension and enlargement of the sagittal defocusing of the analyzed x-rays. The loss of intensity that occurs when the analyzed beam height is larger than the active diameter of the spectrometer's SDD is a confounding factor that leads to a trade-off between analyzed flux and the experimental convenience of asymmetric operation.

In Fig. 7 we compare the energy ranges of a conventional suite of SBCA operating symmetrically and the accessible diffraction planes of a single SBCA operated asymmetrically. This is investigated for the energy range of absorption edges and emission lines of the 3*d* transition metals. A comprehensive energy range is possible with a single analyzer operating asymmetrically and a suitable reflection is nearly always available that is close to the special condition (with the source moderately close to the analyzer spherical center) for a given emission or absorption edge. Hence, both a large energy range and high energy resolution should be expected with the Si(551) analyzer studied in the right panel of Fig. 7. We emphasize that there are complicated trade-offs between energy range coverage and analyzed flux (due to the vertical extent of the analyzed beam, described above), and we do not claim that Si(551) is necessarily optimal, although it does illustrate a favorable case for the argument being made here.

We next access a series of planes of the Si(551) SBCA on the amalgam XES, see Fig. 8. We measure Kα, Kβ, and valence-to-core (VTC) emission *en masse* with a single analyzer, demonstrating an expanded energy range through *hkl* hopping. The optimal reflections for the study are given in the left-hand side of Table 1; the experimental reflections used modestly differ in some cases. Fifteen emission lines spanning ~5 keV to ~14 keV were collected across seven elemental species using nine unique diffraction planes from the Si(551) analyzer. By comparison, under symmetric operation at useful Bragg angles the Si(551) crystal has an energy range of only ~8.2 – 9.3 keV and the same emission measurements would require a considerable number of separate Si optics, even if somewhat inferior Bragg angles were employed.

Table 1. Optimal asymmetric reflections for $\mathbf{G}_0$ = Si(551) and best symmetric counterparts for 3*d* transition metal XES, where both Si and Ge analyzers are considered for the symmetric case. For each emission line, the configuration expected to have the least Johann error is given in bold.

Emission	Energy (eV)	$\mathbf{G}_{hkl}$	θ_B (deg.)	α (deg.)	θ_M (deg.)	Best Si Symmetric Analyzer	θ_B (deg.)	Best Ge Symmetric Analyzer	θ_B (deg.)
V Kβ	5428	$(33\bar{1})$	66.47	21.31	**87.78**	(331)	66.47	(422)	81.49
Mn Kα	5900	(422)	71.44	23.84	**95.28**	(422)	71.44	(511) or (333)	74.81
Mn Kβ	6492	(333)	66.04	27.21	93.25	(440)	84.06	(531)	**86.94**
Fe Kα	6405	(333)	67.85	27.21	**95.06**	(511) or (333)	67.85	(440)	75.42
Fe Kβ	7059	(531)	73.11	13.97	**87.08**	(531)	73.11	(620)	79.04
Ni Kα	7480	(620)	74.87	27.67	**102.54**	(620)	74.87	(533)	73.87
Ni Kβ	8267	$(55\bar{1})$	80.49	16.1	**96.59**	(551) or (711)	80.49	(642)	82.7
Cu Kα	8046	(444)	79.45	27.21	106.66	(444)	**79.45**	(551) or (711)	76.55
Cu Kβ	8904	(731)	80.03	21.61	101.64	(731) or (553)	**80.03**	(800)	79.91
Zn Kα	8637	(642)	81.57	13.34	**94.91**	(642)	81.57	(553) or (731)	77.04
Zn Kβ	9570	(733)	77.56	24.95	102.51	(733)	77.56	(555) or (751)	**82.57**
Sr Kα	14,161	(884)	75.35	11.42	**86.77**	(777) or (11 5 1)	77.77	(991)	81.09
Sr Kβ	15,825	(12 6 2)	78.13	18.25	**96.38**	(13 3 3) or (995)	80.53	(13 5 3) or (11 9 1)	80.6

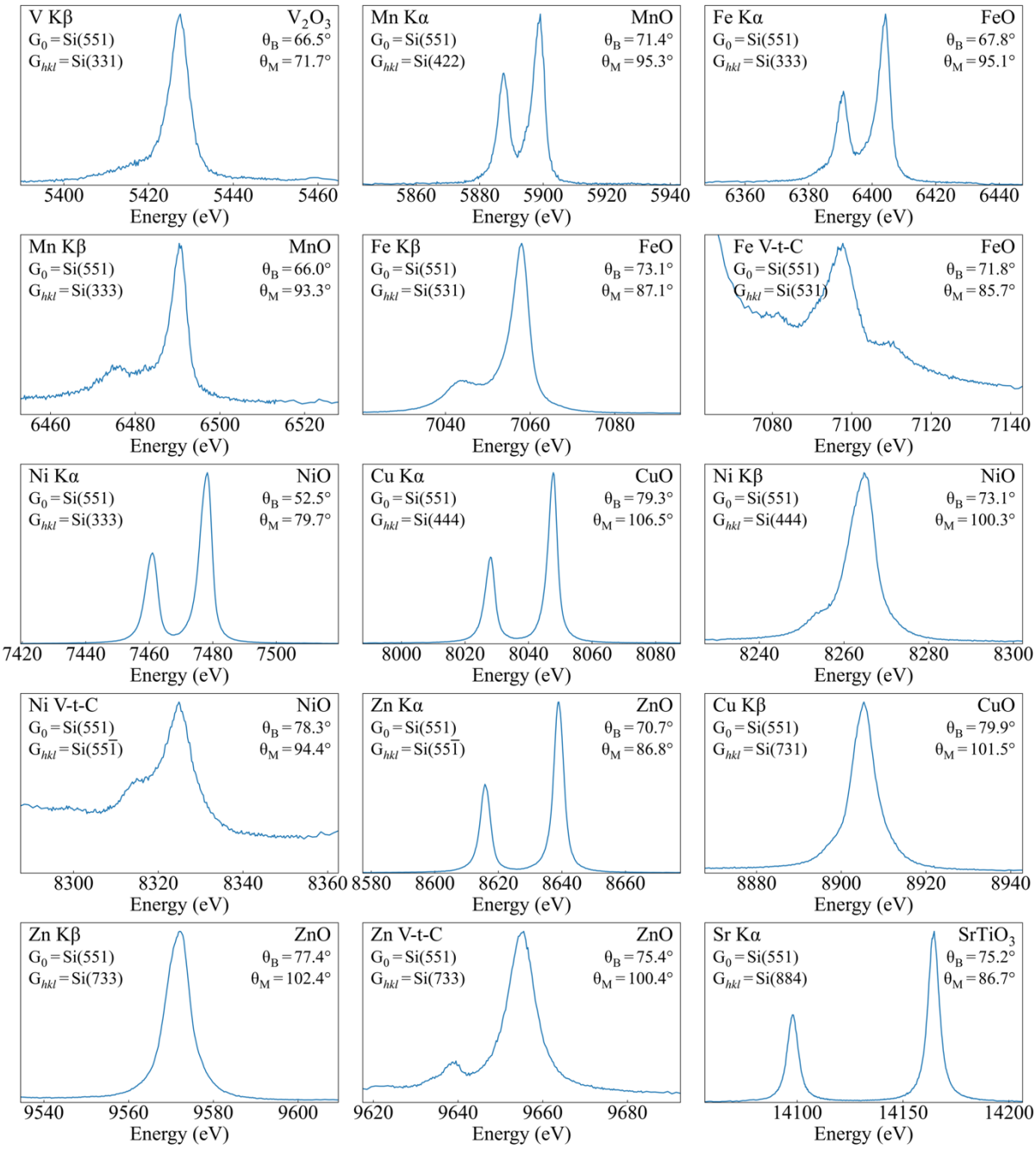

Figure 8. Emission lines measured asymmetrically with a Si(551) analyzer, arranged in order of ascending energy, presented with no background subtraction. The Bragg angle required to select the nominal energy of the emission line is given for each scan.

Having established the comprehensive advantage of a greatly increased energy range, we now address the proposed second benefit of asymmetric operation: an enhanced energy resolution compared to symmetric cases through elimination of Johann error when $\theta_B + \alpha = \theta_M \sim 90$ deg. Ray tracing simulations in Fig. 9 show the reduction of Johann error when approaching this special condition. Fig. 9 (a) shows an equatorial full-range broadening of ~9 eV at the analyzer edge of an SBCA at $\theta_B = 65$ deg. Fig. 9 (b), at the same photon energy, shows less than 10% as much broadening (with an opposite sign) for $\theta_B = 77.5$ deg and $\alpha = 14.9$ deg.

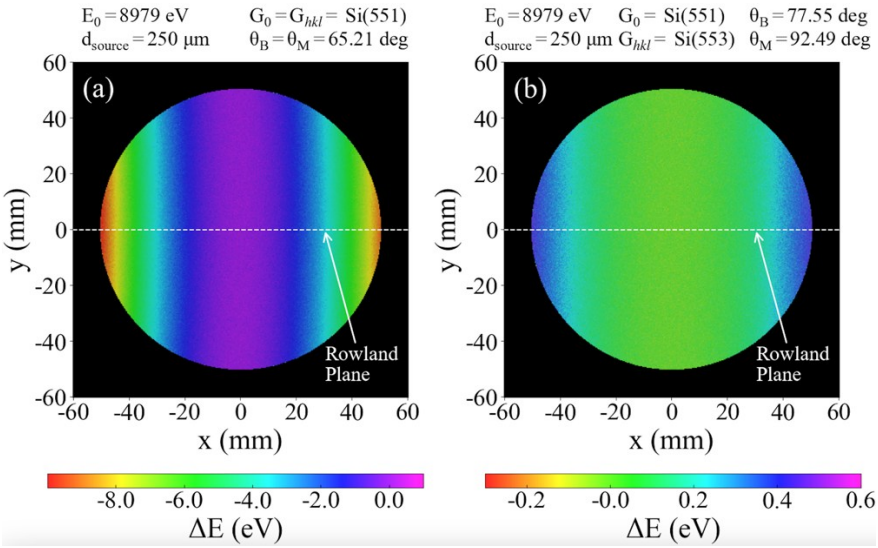

Figure 9. **(a)** XRT ray traced simulation of a Si(551) operated symmetrically far from backscatter, demonstrating Johann error as lower diffracted energies on the left and right sides of the crystal. **(b)** The same photon energy when using the asymmetric $\mathbf{G}_{hkl}$ = (553) reflection with the same analyzer. The crystal is optically near backscatter, resulting in elimination of Johann error.

The ray tracing results show the availability of an asymmetric plane at the same energy as its conventional symmetric counterpart but with improved energy resolution via reduction of Johann broadening. This is further illustrated in Fig. 10, which shows the energy response

functions corresponding to cases (a) and (b) of Fig. 9. The general consideration that Johann error is smallest when the source is near to the SBCA sphere center is also investigated in Table 1, where the most favorable cases with respect to this condition are shown in bold for each emission line. The asymmetric option from even the single favorable case of a Si(551) analyzer are always quite close to the best choices among Si or Ge analyzers used symmetrically and is generally better by this metric.

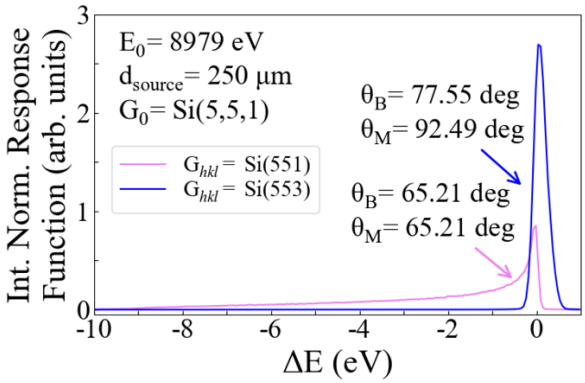

Figure 10. Symmetric and asymmetric energy response functions corresponding to Fig.9 (a) and (b), demonstrating the reduction of Johann error.

To show this Johann error reduction in practice, Cu and Zn Kβ XES on the amalgam sample were measured using both (somewhat unfavorable) symmetric and (rather favorable) asymmetric configurations. Fig. 11(a) and (b) shows significant difference in the width and symmetry of the characteristic emission. The symmetric spectrum is broadened with a tail primarily because of Johann error, as well as some contribution from source size broadening. Asymmetric reflections with θ_M near backscatter have improved energy resolution through elimination of Johann error. The effect is more evident in Fig. 11(b) as the symmetric Zn measurement is far from backscatter at $\theta_B = 58$ deg, so broadening is more pronounced. The standard deviation of the energy response function calculated via ray tracing in the asymmetric

case of the Zn measurement was 0.6 eV, compared to 4.6 eV in the symmetric case. The broadening in the asymmetric case is largely from source size effects.

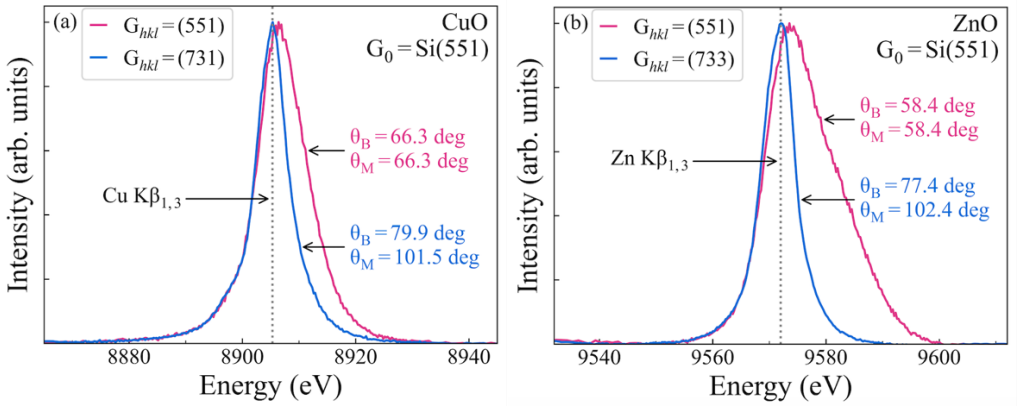

Figure 11. K$\beta_{1,3}$ emission spectra of (a) Cu and (b) Zn. Spectra were collected using the Si(551) SBCA symmetrically and with the most optimal asymmetric plane. Further from backscatter, the symmetric reflection analyzer response function broadens due to Johann error. On the other hand, the asymmetric reflection response function is narrow because of a mechanical analyzer angle, θ_M, close to 90 deg.

To further investigate energy resolution effects, we performed transmission mode XANES and EXAFS studies on metal reference foils in symmetric and asymmetric SBCA configurations. Fig. 12 shows Cu XANES, selected for the well-known shoulder feature in its rising edge, measured symmetrically and asymmetrically with and without analyzer masking and compared to synchrotron data. Johann error both broadens and shifts the spectra, as shown in the unmasked symmetric case having $\theta_B = \theta_M = 65.2$ deg at the absorption edge, and analyzer masking improves the energy resolution of the symmetric data. However, the asymmetric spectra are unaffected by analyzer masking as Johann error is eliminated in the optical configuration

with θ_B = 77.5 and θ_M = 92.5 deg, and the asymmetric spectra shows superb energy resolution with no loss of information compared to the synchrotron reference data.

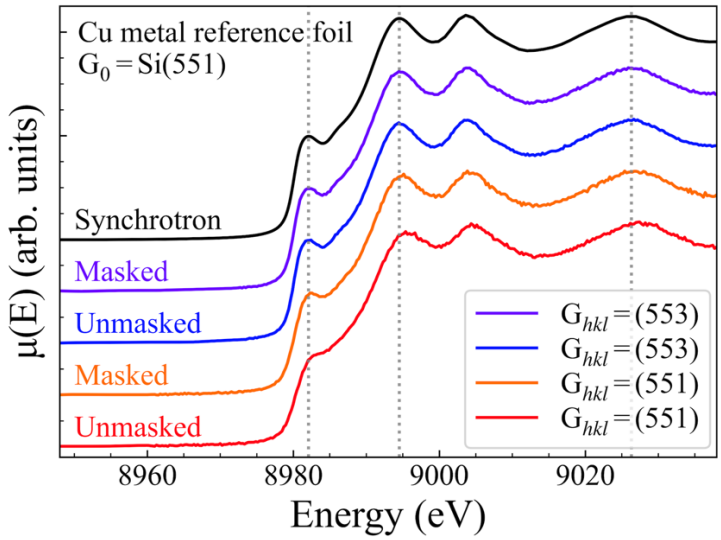

Figure 12. Cu K XANES measured using a Si(551) analyzer symmetrically and $\mathbf{G}_{hkl}$ = (553) reflection asymmetrically, compared to synchrotron results. At 8978.9 eV, $\theta_B = \theta_M$ = 65.2 deg symmetrically whereas θ_B = 77.5 and θ_M = 92.5 deg. The asymmetric configuration eliminates Johann error by operating mechanically at near backscatter. Masking the edges of the analyzer removes Johann broadening in the symmetric case, whereas masking in the asymmetric case shows no appreciable difference in energy resolution. Spectra are offset for clarity of presentation.

Next, the Ni K-edge EXAFS was measured symmetrically and asymmetrically using the Si(551) analyzer and reflections $\mathbf{G}_0$ = (551) and $\mathbf{G}_{hkl}$ = (55$\bar{1}$) and compared to synchrotron data. The raw EXAFS and χ(k) are shown in Fig. 13 (a) and (b). There is again no loss in information between synchrotron and laboratory XAFS. The symmetric and asymmetric results are identical here because the Johann broadening in the symmetric case has little effect for spectrally broad features over the large energy range studied.

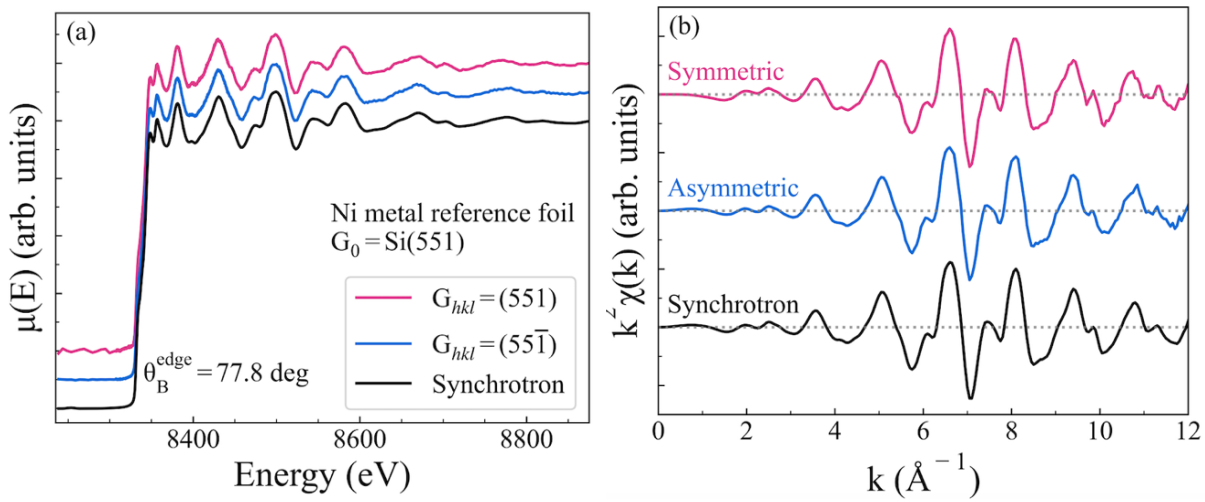

Figure 13. Ni K XAFS measured using a Si(551) analyzer symmetrically and with the $\mathbf{G}_{hkl} = (55\bar{1})$ reflection asymmetrically, compared to synchrotron results. Both spectra show agreement with synchrotron data. Spectra are offset for clarity of presentation.

b. **Synchrotron Measurements**

Having demonstrated some benefits of asymmetric Rowland geometry in laboratory x-ray spectroscopy, we extend the discussion to synchrotron x-ray measurements. Fig. 14 shows the asymmetric Rowland geometry of the monochromator for a HERFD-XANES measurement, tuned to the Zn $K\alpha_1$ emission energy for a study of a ZnO thin film. Note that while Si(642) is the preferred symmetric analyzer, it is an uncommon SBCA and in our case did not exist at any of the several beamlines performing XES or HERFD at our synchrotron, whereas the Si(211) is relatively common for its (422) reflection to study XES for vanadium. Fig. 15 shows the HERFD-XANES collected using the asymmetric $\mathbf{G}_{hkl} = (642)$ reflection of a Si(211) SBCA compared to total fluorescence yield (TFY) results, and shows significant suppression of the Zn K-shell lifetime broadening This result supports the use of asymmetric configurations for HERFD and XES at synchrotron light sources. The addition of 'clock angle' degrees of freedom

to the common designs for multi-SBCA arrays for HERFD[45,46] would therefore allow *hkl*-hopping with increased user convenience, i.e., when a single analyzer is favorable for all user-desired emission lines in a given study, jumping between the different energy ranges would not require changing the SBCA and retuning.

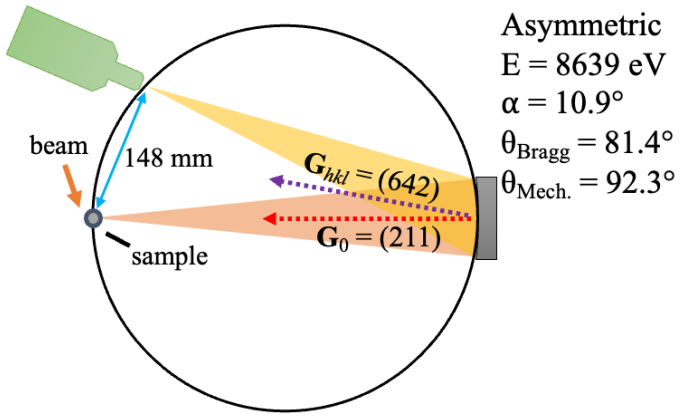

Figure 14. The asymmetric configuration implemented for HERFD-XANES measurements. Note the longer source-detector chord length (blue arrows), allowing greater flexibility in special sample environments and less size constraints than a symmetric counterpart.

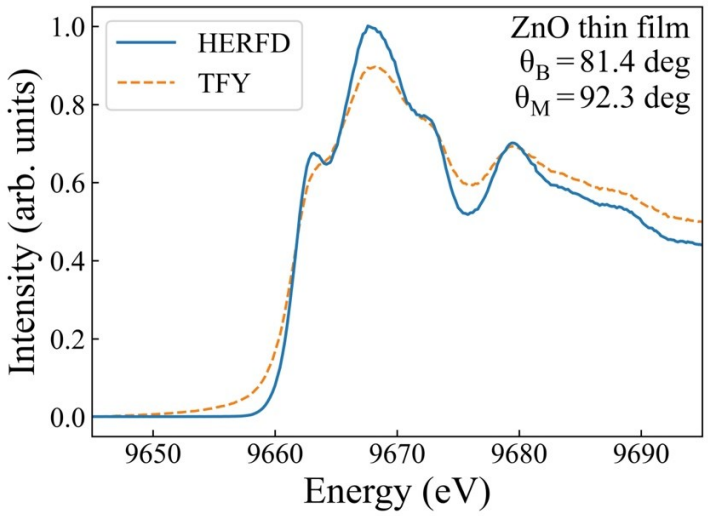

Figure 15. Zn HERFD-XANES measured with $\mathbf{G}_{hkl}$ = (642) of a Si(211) SBCA

We now move to our last study, a demonstration of XRS with an SBCA in an asymmetric configuration. Here we again used the Si(211) analyzer asymmetrically accessing the $\mathbf{G}_{hkl}$ = (642) reflection, approximately satisfying the condition $\theta_B + \alpha = \theta_M = 90$ deg at 8702.9 eV. The elastic line, measured by scanning the Si(111) double crystal monochromator, is shown in Fig. 16. The shape and (near) symmetry of the elastic peak illustrates a favorable energy response function for the experimental realization. The FWHM is 1.25 eV, which is comparable to the expected resolution of the Si(111) double crystal monochromator without second-crystal detuning, i.e., the analyzer is adding little broadening in this configuration. In addition, the source/sample-detector chord length of ~150 mm is quite large compared to that for synchrotron XRS spectrometers. This is beneficial due to the easier rejection of stray scatter and the larger clearance for special sample environments. This configuration is best used with a focused beam to avoid source broadening, given the ~81 deg Bragg angle. We note that asymmetric operation of curved analyzers have been used before to accommodate unequal source-analyzer and analyzer-detector chords required by ancillary equipment.[35,47] However, here we make use of asymmetric operation to get high energy resolution and large analyzer solid angle together with good sample-to-detector clearance. Similar resolutions are reported in a prior XRS study using the von Hamos (non-Rowland) configuration[48], but it should be noted that contemporary XRS end stations overwhelmingly use arrays of SBCAs.[12,14,17,18] The resulting wide energy scan of the inelastic x-ray scattering and the C K-edge XRS itself are shown in Fig. 17, main panel and inset, respectively. The results indeed agree with the well-known spectrum for graphite. While these results are preliminary, they build on the strength of the prior demonstrations in this paper and strongly suggest the use of 0.5-m radius SBCA in XRS measurement, especially when a study requires focusing and thus makes source broadening irrelevant.

We note one detail missing from our present study: 0.5-m SBCA are typically sliced for strain relief which raises the question of whether the XRS imaging modality that is now is common use[49,50] may exhibit some degradation. This is an important topic for further study.

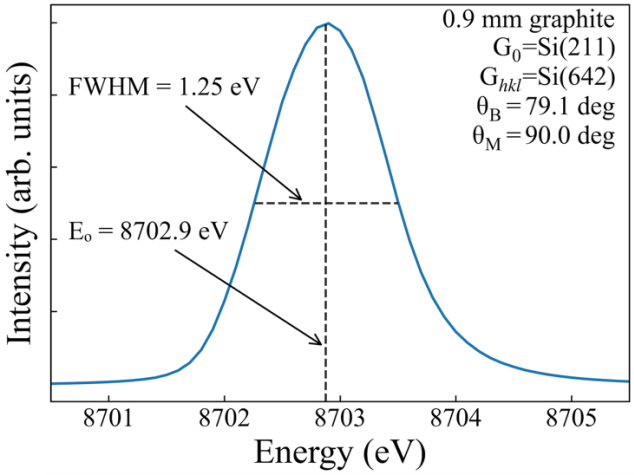

Figure 16. Elastic lines measured using a Si(211) analyzer asymmetrically $\mathbf{G}_{hkl}$ = (642), demonstrating Johann error elimination and narrowing of the analyzer response function when operated asymmetrically.

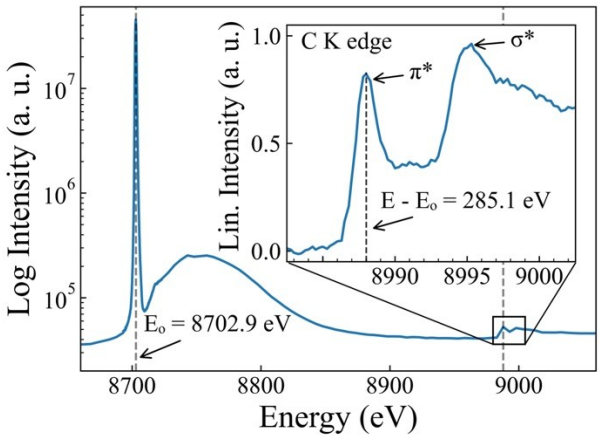

Figure 17. XRS of graphite showing elastic, inelastic, and XRS features of C K-edge. Measured with Si(211) using $\mathbf{G}_{hkl}$ = (642). The analyzer was mechanically at backscatter with a Bragg angle of 79.1 deg. The elastic peak FWHM is approximately 1.3 eV.

6. Conclusions

We investigate the merits of asymmetric Rowland geometries of spherically bent crystal analyzers (SBCAs) for laboratory based XAFS and XES as well as for synchrotron studies of high energy resolution fluorescence detection (HERFD) and x-ray Raman scattering (XRS). Several benefits of asymmetric operation are demonstrated. First, a single SBCA employed asymmetrically can use *hkl* hopping to access a large range of crystal planes and corresponding *d*-spacings, greatly extending the useful energy range with fine energy resolution compared to conventional symmetric operation. Second, by satisfying the condition that the source be at least relatively near to the SBCA sphere center, asymmetric Rowland geometries can mitigate or eliminate Johann error. Third, asymmetric Rowland geometries can significantly increase the clearance between sample and detector when the nominally perfect sphere-center geometry can be used. The combination of suppressed Johann error, larger solid angle (by use of the 0.5-m SBCA enabled by the elimination of Johann error), and large source-detector distance makes asymmetric operation an especially appealing paradigm for the design of future XRS endstations.

7. Acknowledgements

This work is supported by funding from the U.S. Department of Energy in the Nuclear Energy University Program under Contract No. DE-NE0009158. This research used resources of the Advanced Photon Source, a U.S. Department of Energy (DOE) Office of Science user facility operated for the DOE Office of Science by Argonne National Laboratory under Contract No. DE-AC02-06CH11357. We thank each of Mali Balasubramanian and Pieter Glatzel for useful discussions, Shelly Kelly and Chengjun Sun for beamline assistance, and Abdullah Ceylan and Abdul Rumaiz for providing the thin film sample studied by HERFD XAS.

8. References

1 H. H. Johann, *Z. Für Phys.*, 1931, **69**, 185–206.
2 W. M. Holden, O. R. Hoidn, A. S. Ditter, G. T. Seidler, J. Kas, J. L. Stein, B. M. Cossairt, S. A. Kozimor, J. Guo, Y. Ye, M. A. Marcus and S. Fakra, *Rev. Sci. Instrum.*, 2017, **88**, 073904.
3 G. T. Seidler, D. R. Mortensen, A. J. Remesnik, J. I. Pacold, N. A. Ball, N. Barry, M. Styczinski and O. R. Hoidn, *Rev. Sci. Instrum.*, 2014, **85**, 113906.
4 G. T. Seidler, D. R. Mortensen, A. S. Ditter, N. A. Ball and A. J. Remesnik, *J. Phys. Conf. Ser.*, 2016, **712**, 012015.
5 M. E. Mundy, D. Ung, N. L. Lai, E. P. Jahrman, G. T. Seidler and B. M. Cossairt, *Chem. Mater.*, 2018, **30**, 5373–5379.
6 E. P. Jahrman, W. M. Holden, A. S. Ditter, D. R. Mortensen, G. T. Seidler, T. T. Fister, S. A. Kozimor, L. F. J. Piper, J. Rana, N. C. Hyatt and M. C. Stennett, *Rev. Sci. Instrum.*, 2019, **90**, 024106.
7 D. R. Mortensen, G. T. Seidler, J. J. Kas, N. Govind, C. P. Schwartz, S. Pemmaraju and D. G. Prendergast, *Phys. Rev. B*, 2017, **96**, 125136.
8 D. R. Mortensen, G. T. Seidler, A. S. Ditter and P. Glatzel, *J. Phys. Conf. Ser.*, 2016, **712**, 012036.
9 R. A. Valenza, E. P. Jahrman, J. J. Kas and G. T. Seidler, *Phys. Rev. A*, 2017, **96**, 032504.
10 W. M. Holden, G. T. Seidler and S. Cheah, *J. Phys. Chem. A*, 2018, **122**, 5153–5161.
11 D. Sokaras, D. Nordlund, T.-C. Weng, R. A. Mori, P. Velikov, D. Wenger, A. Garachtchenko, M. George, V. Borzenets, B. Johnson, Q. Qian, T. Rabedeau and U. Bergmann, *Rev. Sci. Instrum.*, 2012, **83**, 043112.
12 M. Moretti Sala, K. Martel, C. Henriquet, A. Al Zein, L. Simonelli, C. Sahle, H. Gonzalez, M.-C. Lagier, C. Ponchut, S. Huotari, R. Verbeni, M. Krisch and G. Monaco, *J. Synchrotron Radiat.*, 2018, **25**, 580–591.
13 S. Huotari, C. J. Sahle, C. Henriquet, A. Al-Zein, K. Martel, L. Simonelli, R. Verbeni, H. Gonzalez, M.-C. Lagier, C. Ponchut, M. Moretti Sala, M. Krisch and G. Monaco, *J. Synchrotron Radiat.*, 2017, **24**, 521–530.
14 D. Sokaras, T.-C. Weng, D. Nordlund, R. Alonso-Mori, P. Velikov, D. Wenger, A. Garachtchenko, M. George, V. Borzenets, B. Johnson, T. Rabedeau and U. Bergmann, *Rev. Sci. Instrum.*, 2013, **84**, 053102.
15 E. Kleymenov, J. A. van Bokhoven, C. David, P. Glatzel, M. Janousch, R. Alonso-Mori, M. Studer, M. Willimann, A. Bergamaschi, B. Henrich and M. Nachtegaal, *Rev. Sci. Instrum.*, 2011, **82**, 065107.
16 I. Llorens, E. Lahera, W. Delnet, O. Proux, A. Braillard, J.-L. Hazemann, A. Prat, D. Testemale, Q. Dermigny, F. Gelebart, M. Morand, A. Shukla, N. Bardou, O. Ulrich, S. Arnaud, J.-F. Berar, N. Boudet, B. Caillot, P. Chaurand, J. Rose, E. Doelsch, P. Martin and P. L. Solari, *Rev. Sci. Instrum.*, 2012, **83**, 063104.
17 T. T. Fister, G. T. Seidler, L. Wharton, A. R. Battle, T. B. Ellis, J. O. Cross, A. T. Macrander, W. T. Elam, T. A. Tyson and Q. Qian, *Rev. Sci. Instrum.*, 2006, **77**, 063901.
18 R. Verbeni, T. Pylkkänen, S. Huotari, L. Simonelli, G. Vankó, K. Martel, C. Henriquet and G. Monaco, *J. Synchrotron Radiat.*, 2009, **16**, 469–476.
19 J. F. Seely, E. Galtier, L. T. Hudson, A. Henins and U. Feldman, *Appl. Opt.*, 2019, **58**, 5225–5232.

20 A. Bordage, M. Pápai, N. S. Sas, J. Szlachetko, M. Nachtegaal and G. Vankó, *Phys. Chem. Chem. Phys.*, 2013, **15**, 11088–11098.
21 P. Suortti, T. Buslaps, P. Fajardo, V. Honkimäki, M. Kretzschmer, U. Lienert, J. E. McCarthy, M. Renier, A. Shukla, T. Tschentscher and T. Meinander, *J. Synchrotron Radiat.*, 1999, **6**, 69–80.
22 P. Suortti, U. Lienert and C. Schulze, *Nucl. Instrum. Methods Phys. Res. Sect. Accel. Spectrometers Detect. Assoc. Equip.*, 1994, **338**, 27–32.
23 L. Simonelli, C. Marini, L. Ribo, R. Homs, J. Avila, D. Heinis, I. Preda and K. Klementiev, *J. Synchrotron Radiat.*, 2023, **30**, 235–241.
24 P. Suortti and W. Thomlinson, *Nucl. Instrum. Methods Phys. Res. Sect. Accel. Spectrometers Detect. Assoc. Equip.*, 1988, **269**, 639–648.
25 P. Suortti, P. Pattison and W. Weyrich, *J. Appl. Crystallogr.*, 1986, **19**, 336–342.
26 P. Suortti, P. Pattison and W. Weyrich, *J. Appl. Crystallogr.*, 1986, **19**, 343–352.
27 P. Pattison, P. Suortti and W. Weyrich, *J. Appl. Crystallogr.*, 1986, **19**, 353–363.
28 P. Suortti, U. Lienert and C. Schulze, *AIP Conf. Proc.*, 1997, **389**, 175–192.
29 P. Suortti, D. Chapman, J. R. Schneider and T. Tschentscher, *J. Appl. Crystallogr.*, 1992, **25**, 432–438.
30 E. Erola, V. Eteläniemi, P. Suortti, P. Pattison and W. Thomlinson, *J. Appl. Crystallogr.*, 1990, **23**, 35–42.
31 T. Matsushita and U. Kaminaga, *J. Appl. Crystallogr.*, 1980, **13**, 465–471.
32 A. Boeuf, S. Lagomarsino, S. Mazkedian, S. Melone, P. Puliti and F. Rustichelli, *J. Appl. Crystallogr.*, 1978, **11**, 442–449.
33 R. Caciuffo, S. Melone, F. Rustichelli and A. Boeuf, *Phys. Rep.*, 1987, **152**, 1–71.
34 S. G. Podorov, O. Renner, O. Wehrhan and E. Förster, *J. Phys. Appl. Phys.*, 2001, **34**, 2363.
35 R. Bartiromo, F. Bombarda and R. Giannella, *Nucl. Instrum. Methods Phys. Res.*, 1984, **221**, 453–459.
36 M. Moretti Sala, K. Martel, C. Henriquet, A. Al Zein, L. Simonelli, C. Sahle, H. Gonzalez, M.-C. Lagier, C. Ponchut, S. Huotari, R. Verbeni, M. Krisch and G. Monaco, *J. Synchrotron Radiat.*, 2018, **25**, 580–591.
37 D. Sokaras, D. Nordlund, T.-C. Weng, R. A. Mori, P. Velikov, D. Wenger, A. Garachtchenko, M. George, V. Borzenets, B. Johnson, Q. Qian, T. Rabedeau and U. Bergmann, *Rev. Sci. Instrum.*, 2012, **83**, 043112.
38 D. Sokaras, T.-C. Weng, D. Nordlund, R. Alonso-Mori, P. Velikov, D. Wenger, A. Garachtchenko, M. George, V. Borzenets, B. Johnson, T. Rabedeau and U. Bergmann, *Rev. Sci. Instrum.*, 2013, **84**, 053102.
39 Y. M. Xiao, P. Chow, G. Boman, L. G. Bai, E. Rod, A. Bommannavar, C. Kenney-Benson, S. Sinogeikin and G. Y. Shen, *Rev. Sci. Instrum.*, 2015, **86**, 072206.
40 Y. Q. Cai, P. Chow, C. C. Chen, H. Ishii, K. L. Tsang, C. C. Kao, K. S. Liang and C. T. Chen, *AIP Conf. Proc.*, 2004, **705**, 340–343.
41 J. M. Ablett, D. Prieur, D. Céolin, B. Lassalle-Kaiser, B. Lebert, M. Sauvage, T. Moreno, S. Bac, V. Balédent, A. Ovono, M. M, F. Gélebart, A. Shukla and J.-P. Rueff, *J. Synchrotron Radiat.*, 2019, **26**, 263–271.
42 D. R. Mortensen and G. T. Seidler, *J. Electron Spectrosc. Relat. Phenom.*, 2017, **215**, 8–15.
43 K. Klementiev and R. Chernikov, in *Advances in Computational Methods for X-Ray Optics III*, SPIE, 2014, vol. 9209, pp. 60–75.

44 A. Ceylan, A. K. Rumaiz, D. Caliskan, S. Ozcan, E. Ozbay and J. C. Woicik, *J. Appl. Phys.*, 2015, **117**, 105303.
45 N. P. Edwards, J. R. Bargar, D. van Campen, A. van Veelen, D. Sokaras, U. Bergmann and S. M. Webb, *Rev. Sci. Instrum.*, 2022, **93**, 083101.
46 P. Glatzel, A. Harris, P. Marion, M. Sikora, T.-C. Weng, C. Guilloud, S. Lafuerza, M. Rovezzi, B. Detlefs and L. Ducotté, *J. Synchrotron Radiat.*, 2021, **28**, 362–371.
47 P. Jagodziński, D. Banaś, M. Pajek, A. Kubala-Kukuś, Ł. Jabłoński, I. Stabrawa, K. Szary, D. Sobota, A. Warczak, A. Gumberidze, H. F. Beyer, M. Lestinsky, G. Weber, T. Stöhlker and M. Trassinelli, *J. Instrum.*, 2023, **18**, P11002.
48 N. Watanabe, H. Hayashi, Y. Udagawa, K. Takeshita and H. Kawata, *Appl. Phys. Lett.*, 1996, **69**, 1370–1372.
49 C. J. Sahle, A. D. Rosa, M. Rossi, V. Cerantola, G. Spiekermann, S. Petitgirard, J. Jacobs, S. Huotari, M. Moretti Sala and A. Mirone, *J. Synchrotron Radiat.*, 2017, **24**, 269–275.
50 C. J. Sahle, A. Mirone, T. Vincent, A. Kallonen and S. Huotari, *J. Synchrotron Radiat.*, 2017, **24**, 476–481.

Chapter 6. Asymmetric Rowland Geometries Enable Simplified and Improved X-ray Raman Scattering Spectrometers

This chapter is based on a manuscript prepared for submission to Journal of Synchrotron Radiation.

Anthony J. Gironda, Yeu Chen, Mark F. Wolfman, Cheng-Jun Sun, Gerald T. Seidler, Shelly D. Kelly

1. Abstract

X-ray Raman scattering (XRS) demands large collection solid angle while maintaining high energy resolution. Conventional spectrometers employ large arrays of typically 20 or more spherically bent crystal analyzers in symmetric Rowland circle geometries to maximize signal acquisition, wherein each analyzer is supported by three motorized degrees of freedom for alignment. The design of more compact XRS spectrometers using fewer optics with greater collection solid angle is hampered by trade-offs between tight sample-detector clearances and degraded energy resolution from Johann error. We address these trade-offs through *asymmetric* operation of spherically bent crystal analyzers, which presents several benefits: (1) suppression of Johann error allowing use of more tightly curved optics with larger solid angle, (2) alignment with only one mechanical degree of freedom per SBCA, (3) large clearances for detector

placement, and (4) imaging and spatial rejection of non-sample scatter with detector placement behind the Rowland circle at the sagittal focus. Here, we present the design and performance of a multielement XRS spectrometer that uses asymmetric Rowland geometry to achieve extremely high energy resolution (spectrometer resolution 0.3 – 0.4 eV) with 0.5-m analyzers with enough spatial resolution to significantly reject scatter from sample enclosures and windows. The instrument has ~10x fewer motorized degrees of freedom than would be common practice with 1-m SBCA having the same total collection solid angle. Hence, we demonstrate a much simplified, smaller, and more cost-effective path forward for XRS instrumentation.

2. Introduction

X-ray Raman scattering (XRS) is a non-resonant photon-in photon-out spectroscopy technique that provides X-ray absorption fine structure (XAFS)-like information from lower-energy absorption edges using hard x-rays. XRS is therefore bulk-sensitive and can determine oxidation state, local symmetry, and coordination environment of the probed element[1–3]. Furthermore, XRS can probe both dipole and non-dipole electronic transitions as a function of the momentum transfer, q, of the scattering process, providing more information on the unoccupied density of states [4–10]. Unlike electron-energy loss spectroscopy (EELS), X-ray photoemission spectroscopy (XPS), and soft/tender-edge XAFS[11], the hard X-rays in XRS avoid the short attenuation lengths, surface contaminant sensitivity, and vacuum flight paths that complicate those methods.

In the hard X-ray regime of XRS, photons readily penetrate cell windows and thin sample enclosures and thus XRS is a suitable probe for *in situ* measurements. XRS has been applied to studies of battery electrodes[12–15], catalyst materials[16–19], and energy conversion/storage

materials[20–23], with extensive use in high-pressure diamond-anvil cell (DAC) studies of geological samples[24–31]. A key feature of many of these *in situ* measurements is the rejection of scattered signal from cell windows, gaskets, and pressure media for background suppression using a pixelated area detector, so-called XRS imaging or direct tomography[32–34]. With increasingly brilliant light sources, *operando* battery and catalyst measurements are at the forefront of XRS capabilities; a handful of published examples exist from the past decade[35–38].

However, it is critical to recognize that XRS is a photon-starved spectroscopy technique; the Raman scattering cross-section is a small fraction of the total incoherent scattering cross-section, which is itself orders of magnitude smaller than the photoelectric cross-section. Consequently, acquisition times can be hours to days even with brilliant synchrotron light sources. As a result, XRS demands highly efficient spectrometers and strong background suppression.

Most dedicated XRS spectrometers use large arrays of Johann-type[39] spherically bent crystal analyzers (SBCAs) in symmetric Rowland geometries and collect spectra in inverse-scanning mode, where the analyzer energy is fixed while the incident photon energy is scanned to record the energy-loss spectrum. Representative implementations include the 72-analyzer system at the European Synchrotron Research Facility (ESRF) beamline ID20[40], the 54-analyzer system at the Stanford Synchrotron Radiation Lightsource (SSRL) beamline 6-2[41], and the now-decommissioned 19-analyzer "LERIX" system of the Advanced Photon Source (APS)[42]. Alternative approaches include a forward scattering bent Laue spectrometer for highly absorbing samples[43] and a dispersive von Hamos[44] spectrometer for spectral collection in a "single-shot"[45]. The design of smaller Johann-type point-focusing spectrometers using fewer optics with higher solid angle per optic (i.e. arrays of 0.5-m radius of curvature SBCA) is constrained by a tradeoff

between sample–detector clearance near backscatter and degraded energy resolution from Johann error away from backscatter.

Here, we focus on asymmetric Rowland geometries (in contrast to the above instruments) and their benefits to the design of a much simplified, lower-cost, high-throughput XRS spectrometer that retains the fine energy resolution needed for this technique. Asymmetric Rowland geometries employing SBCAs are underutilized for high-resolution hard X-ray spectroscopy. Recent work of Gironda et al.[46] showed that asymmetric operation of Johann-type SBCA in Rowland focusing geometry can greatly increase experimental flexibility for both synchrotron-based photon-in photon-out experiments and for laboratory-based high resolution absorption and emission spectroscopy. These observations were extended and formalized by the software package of Abramson et al.[47] for analyzer reflection selection and the ray-tracing discussion of Chen et al.[48].

The Chen et al. publication simulated two outcomes of asymmetric operation that guide best practice. First, Johann broadening, the dominant energy degradation mechanism of the optic when operating away from backscatter, is eliminated when the source is close to the spherical center of the SBCA in so-called “Johann normal alignment” (JNA). Second, although imaging resolution is degraded at the usual meridional focus on the Rowland circle perimeter when in asymmetric geometries, spatial resolution can be significantly recovered by instead operating at the sagittal focus behind the Rowland circle.

The present work presents the design and initial commissioning of an XRS spectrometer that utilizes these features of asymmetric operation to achieve high energy resolution, suitable detector clearances, and significant spatial resolution for rejecting scatter from container windows. In addition, we make use of the tilt-free approach first developed by Mortensen et al.[49]

and further developed in Gironda et al. to simplify the motorization needed for tune-up to only one translation per optic.

A six-element spectrometer with only six motorized degrees of freedom for alignment using 0.5-m radius of curvature bent-diced SBCAs in an asymmetric Rowland geometry has been constructed and commissioned at 25-ID-D of APS, with a monochromator-limited energy resolution of ~0.95 eV at 9.7 keV and inferred spectrometer energy resolution of 0.3 – 0.4 eV. Demonstration measurements were executed on the low-*q*, intermediate-*q* ("imaging"), and high-*q* optics. With the imaging optics, this platform is capable of spatially selecting scatter from the sample while rejecting scatter from other sources when used with a pixelated area detector off-circle at the sagittal focus, a key capability for *in situ* and *operando* measurements.

A spectrometer using instead the traditional approach of symmetric operation for 1-m analyzers on tilt plus translation modules would require ~24 SBCA and ~72 motorized degrees of freedom to obtain the same collection solid angle. These results demonstrate a simplified and more cost-effective path for high throughput, high resolution, lower resource optic arrays in XRS spectrometers.

The manuscript proceeds in the following order: Section 2 surveys the asymmetric Rowland geometry equations at the condition that suppresses Johann error. Section 3 describes the spectrometer design, including SBCA selection for asymmetric operation, mechanical renderings and diagrams, and the alignment procedure. Section 4 details methods and sample preparation. Section 5 presents simulated ray tracing and spectrometer performance results and demonstration measurements. Section 6 provides an outlook and future on the design of XRS instrumentation.

3. Asymmetric Rowland Geometry for XRS

The Rowland circle is a focusing configuration that uses a curved optic, here an SBCA, to monochromatize and focus scattered X-rays from the sample. The energy selection and focusing behavior are determined by the Bragg angle, θ_B, and the asymmetry angle, α, defined as the angle between the optic surface normal and the reciprocal lattice vector of the diffracting plane; see Figure 1. Because the SBCA is spherical, it is astigmatic: rays in the Rowland plane focus at the meridional line focus, f_m, located on the Rowland perimeter, while rays in the orthogonal plane focus at the sagittal line focus, f_s, located beyond the Rowland perimeter, shown in Figure 2. For any Rowland geometry, the dependence of the chord lengths and focal distances on θ_B and α is given by

$$\rho = R\sin(\theta_B + \alpha) \tag{1}$$

$$f_m = R\sin(\theta_B - \alpha) \tag{2}$$

$$f_s = -\frac{R\sin^2(\theta_B + \alpha)}{\sin(\theta_B - \alpha)\cos\big(2(\theta_B + \alpha)\big)} \tag{3}$$

where ρ is the source-analyzer chord and R is the radius of curvature of the SBCA[48,50]. When α is zero, these expressions define symmetric operation.

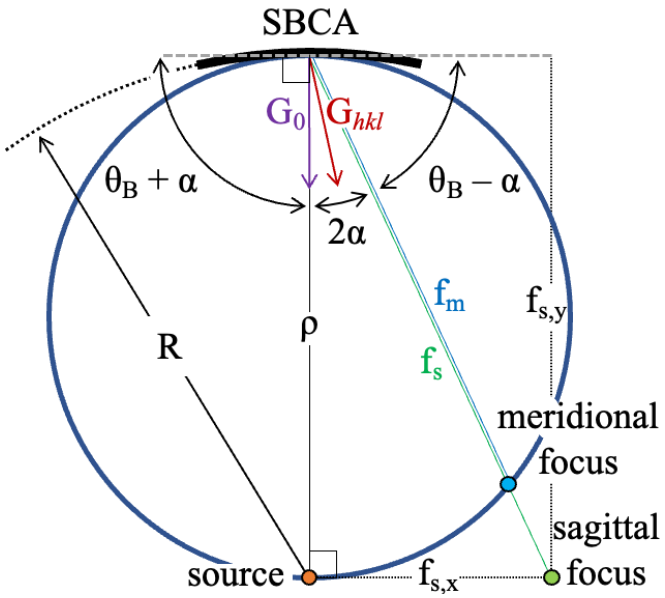

Figure 1. Diagram of asymmetric Rowland circle geometry in the JNA condition ($\theta_B + \alpha = 90^o$). At JNA, there is no Johann broadening. The asymmetry angle α is defined between the diffracting plane G_{hkl} and the surface cut plane G_0 reciprocal lattice vectors.

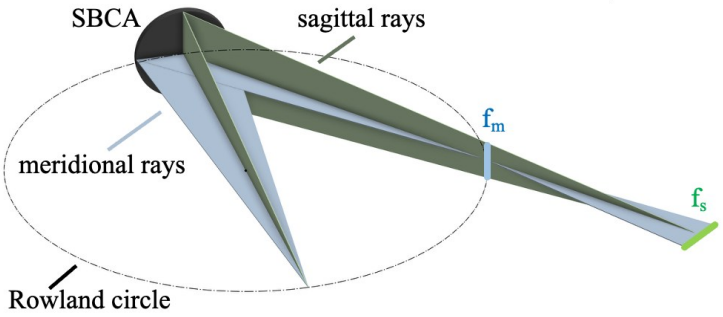

Figure 2. The astigmatic focus of a spherical lens. The meridional focus is perpendicular to the Rowland plane, while the sagittal focus is lies in the Rowland plane.

A special case arises when the X-ray source is placed at the SBCA's center of curvature. In this configuration the entire analyzer surface is illuminated at normal incidence resulting in a uniform Bragg angle, thus Johann error is eliminated[46,48,51,52]. This condition is defined by $\theta_B + \alpha = 90^o$ and was first termed "Johann Normal Alignment" (JNA) in Chen, et al. At JNA, Eqs. (1) – (3) reduce to

$$\rho = R \tag{4}$$

$$f_m = R\cos 2\alpha \tag{5}$$

$$f_s = \frac{R}{\cos 2\alpha}. \tag{6}$$

Geometrically, an important outcome of JNA is that the sagittal focus lies on a line perpendicular to ρ at the source position. This is shown by decomposing the components of the f_s vector (refer to Figure 1)

$$f_{s,y} = R \tag{7}$$

$$f_{s,x} = R\tan 2\alpha \tag{8}$$

observing that $f_{s,y}$,like ρ, is always equal to the radius of curvature at JNA. This suggests a particular simple motorization of detector placement.

For an XRS spectrometer operating in inverse-scanning mode, the spectrometer mechanics and energy remain fixed. Thus, a natural design choice is to place the scattering source at JNA in an asymmetric Rowland geometry with the detector at the sagittal focus. In this condition, there is no Johann error and the source-detector clearance $f_{s,x}$ depends only on α and can be freely tuned by appropriate selection of the optic's wafer cut, G_0, and diffracting plane family, G_{hkl}. Furthermore, revolving the analyzer about the $f_{s,x}$ axis generates a plane of analyzer positions for which all the sagittal foci are coincident. These geometric principles are central in the design of the present XRS spectrometer.

4. Spectrometer Design

In this section we present an overview of the spectrometer design and its components. First, we describe the rationale for selecting a preferred orientation of the crystal analyzer wafer and appropriate crystal planes for diffraction. Second, we describe the overall spectrometer layout, hardware, motorization. Third, we outline the alignment of the instrument.

a. Optic Selection

The expressions from Section 2 (Eqs. 4 – 8) show that, at JNA, the asymmetry angle α determines the Rowland geometry. Increasing α increases the source-detector clearance and eases space constraints, but also moves the Bragg angle θ_B farther from 90° which increases sensitivity to other energy broadening mechanisms such as source size broadening. For the 0.5-m radius of curvature SBCA, the ideal operating condition provides sufficient detector clearance while keeping α small (and thus θ_B closer to 90°).

A systematic search over wafer cuts G_0, diffracting plane families G_{hkl}, and the resulting α was conducted for the diamond cubic structure (corresponding to Si and Ge wafers) at JNA. This was accomplished using a modified version of the *hklhop* package by Abramson et. al[47].

For each candidate pair (G_0, G_{hkl}) we also computed the clock angle, φ, defined as the azimuthal rotation of the crystal that brings the selected G_{hkl} into the Rowland plane. The search was restricted to $\alpha < 15°$ and to analyzed energy between 5 and 12 keV at JNA. Higher scores were assigned to high reflectivity G_{hkl} with $h+k+l=4n$ and reflections with harmonics within the energy range. The best candidate optic was identified as Si(771). A polar plot of the available reflections of Si(771) in (α, φ) space is shown in Figure 3.

Next, we determined the corresponding sagittal focus positions satisfying the Bragg condition at JNA for a 0.5-m Si(771) SBCA. Figure 4 shows the detector clearances and energies

of the suitable G_{hkl} reflections. The (660) reflection at 9.7 keV was selected as the standard working energy of the spectrometer, given its available harmonics, relatively small α, and the ~100 mm detector clearance at JNA. Other reflections with different α and analyzed energy are reachable by rotating the clock angle φ of the optic and translating the detector along the sagittal focal-plane axis to the corresponding positions shown in Figure 4.

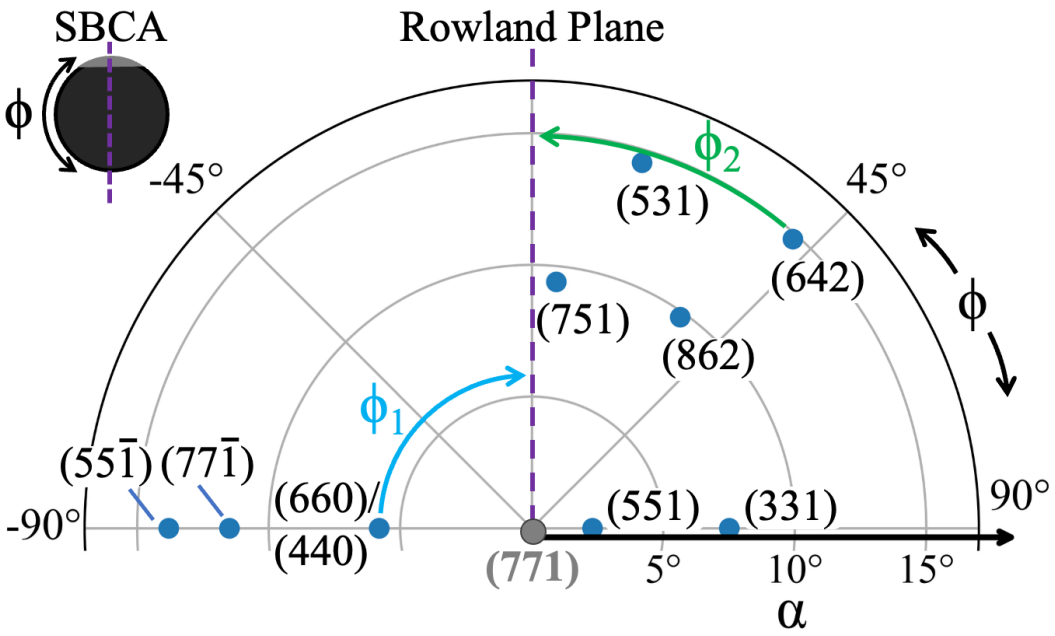

Figure 3. Polar plot of subset of asymmetric reflections for a Si(771) SBCA at JNA. Each point corresponds to a diffracting plane family G_{hkl}, each with a unique d-spacing and analyzed energy. The dashed vertical line denotes the Rowland plane, rotating the SBCA by a corresponding φ brings the selected G_{hkl} into this plane.

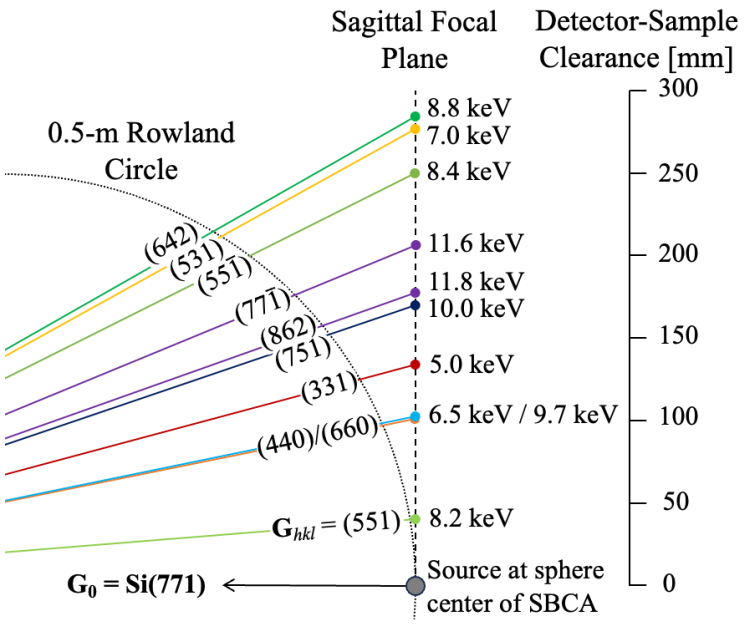

Figure 4. Detector clearances and energies for various asymmetric reflections for a 0.5-m Si(771) optic at JNA. Subset of G_{hkl} from 5-12 keV with $\alpha \leq 15°$. At JNA, the detector trajectory for the sagittal focus of different reflections is a straight line.

b. Mechanical Design and Hardware

The spectrometer is housed at the Sector 25-ID-D beamline at the Advanced Photon Source. A computer-aided design (CAD) rendering of the three arrays and their scattering geometries is shown in Figure 5. The instrument consists of three arrays of two 0.5-m optics at low, medium, and high momentum transfer (q). The intermediate q array is referred to herein as the imaging array because of its favorable line-of-sight for that purpose [33]. The spectrometer is at a fixed Bragg angle and thus cannot scan analyzed photon energy. The optics are arranged in the vertical scattering plane, where the polarization-dependent Thomson factor is maximized. The design of each module is identical. A wire frame (not shown) shapes and holds a He bag to reduce air scatter and improve count rate.

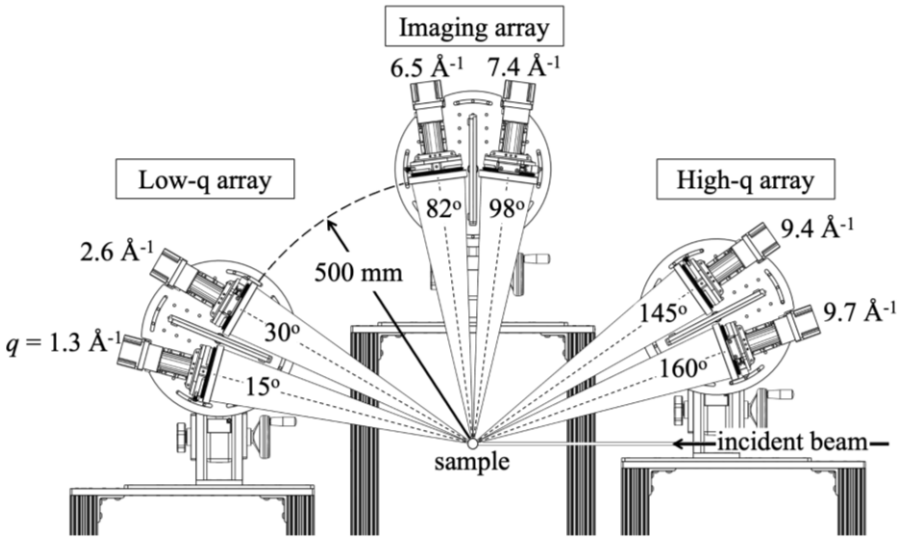

Figure 5. Front-view CAD rendering of the multielement spectrometer detailing the scattering geometry. Each array consists of two 0.5-m radius SBCA. The sample is placed diametrically at the sphere centers of all optics, and scatter from all optics is refocused to a common point. The scattering angle, measured relative to the incident beam, and the associated momentum transfers are shown for 9.7 keV analyzed photon energy.

A CAD rendering of a single array of two SBCA is shown in Figure 6. The scattering geometries of the different arrays was achieved by manually rotating the platter assembly to the desired scattering angle, allowing the design of the arrays to be identical. Each array positions two optic modules 15° apart in scattering angle. A manual linear stage, "z", (Velmex BiSlide) moves the array vertically with respect to the incident beam during tune-up and ensured the Rowland planes intersected the sample. A motorized stage linear stage, "ρ", (Velmex XSlide) under each optic subassembly allowed each optic to be tuned for best energy resolution regardless of manufacturing variations in bending radius. The 0.5-m bent-diced Si(771) SBCA optic (XRSTech) with 10 x 10 mm^2 square dicing is mounted concentrically on a manual rotation stage, "ϕ", (ThorLabs PRM2) for precise azimuthal rotation required for asymmetric operation

and for tilt-free beam steering[49]. A bent-diced analyzer was selected for superior energy resolution compared to bent or strip-bent analyzers [53] and to improve sagittal image quality compared to strip-bent.

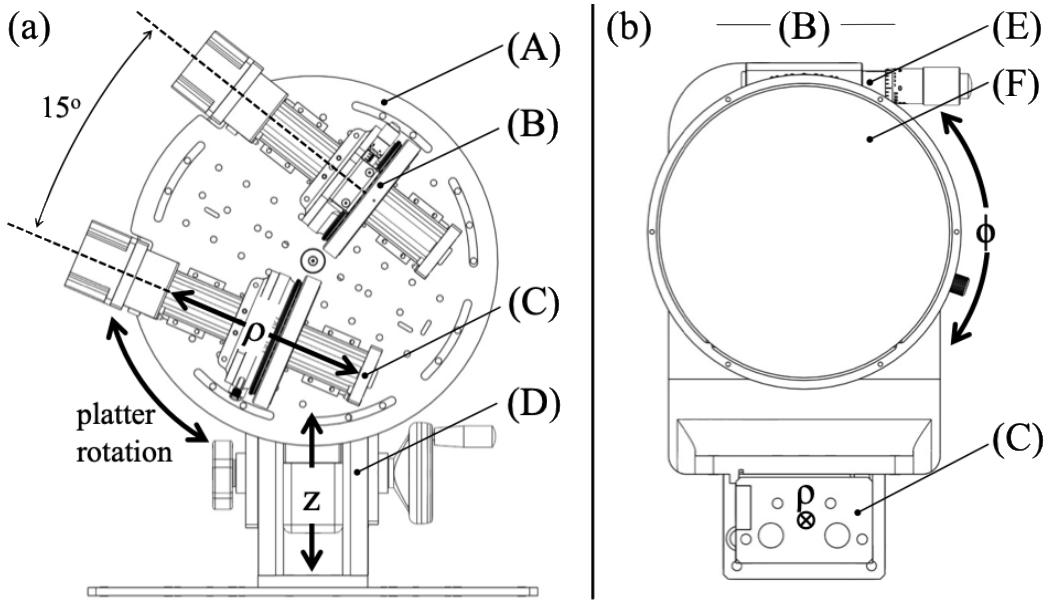

Figure 6. Front-view CAD renderings of (a) an array and (b) the optic subassembly. The key components are labelled as follows: (A) rotating platter, (B) optic subassembly, (C) motorized "ρ" linear stage, (D) manual "z" linear stage, (E) manual "ϕ" rotation stage, and (F) optic.

The system uses two detectors: a single-element silicon drift detector (SDD) with 50 mm^2 area sensing element (Vortex-EX) and a pixelated area detector with a square 14.1 x 14.1 mm^2 sensor and 55 x 55 um^2 pixel size (LAMBDA flex). The SDD, with energy resolution of 150 eV, was used for background rejection when measuring fluorescing samples. The area detector was used for initial alignment and for spatially rejecting scatter from sample enclosures when measuring with the imaging array. The present spectrometer implementation only detected with

one array at a time, i.e. simultaneous *q*-measurements with multiple arrays was not performed. Ongoing modifications to the detector configuration will allow this in the future.

The spectrometer operates in asymmetric Rowland geometry with the optic fixed diametrically from the scattering sample at JNA. The optic defines the 500 mm diameter Rowland circle, shown below in Figure 7. The detector is placed off-circle at the sagittal focus.

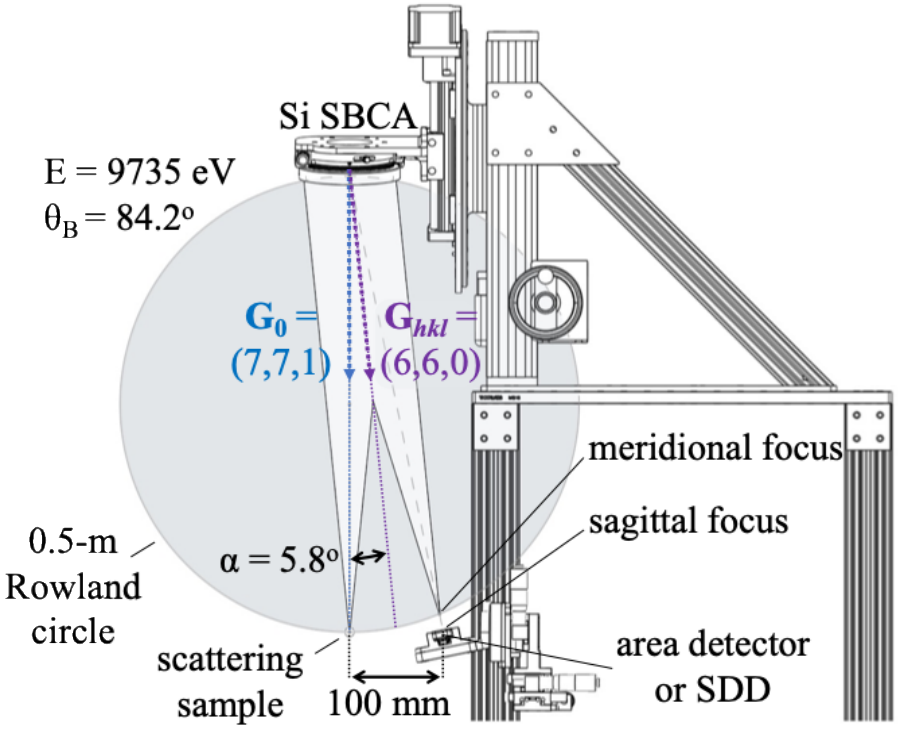

Figure 7. Side-view CAD rendering of a module and the asymmetric Rowland geometry at JNA.

c. Alignment

Pre-alignment was accomplished using a mechanical fiducial that extended from the center of each module to the sample position. The sample position was marked using a 20 mm depth of focus camera with a digital crosshair on the image. For each array, the mechanical fiducial was brought into focus on the camera at the sample position by adjusting the *z* stage (see Fig. 6 (a)) and manually pushing the arrays upstream/downstream and in/out with respect to the

beam direction. The in-board/out-board placement was determined with a planar laser level that projected a vertical plane along the beampath through the hutch. Next, the ρ stage was adjusted for each module until the sharpest elastic line at 9.7 keV was achieved (see Fig. 6 (b)). Finally, the manual ϕ stages were slightly detuned to separate the foci on an area detector to preserve energy resolution in the case analyzers were at slightly different energies.

5. Methods

a. Ray Tracing

Ray tracing was performed using the open-source software Xray Tracer (xrt) [54]. The simulations are purely geometric, and the effects of stress/strain and wafer dicing was not considered. The source is circular with a diameter of 50 μm, and the analyzer is 100 mm in diameter with 500 mm radius of curvature, matching the optic used.

b. Beamline Description

The spectrometer was commissioned at the Sector 25-ID-D beamline at APS. The X-ray source is a 2.8-mm canted undulator. Rh-coated high-heat load collimating mirrors provide harmonic rejection. X-rays are monochromatized by an Axilon Si(111) double-crystal monochromator with an energy range of 4 – 40 keV; a secondary double-bounce Si(220) channel cut monochromator further enhances energy resolution. At the elastic energy of the spectrometer (9735 eV), the widths of the primary and secondary monochromators are 1.5 eV and 0.9 eV with 15% detuning, respectively, measured by the rocking curve of a flat Si wafer downstream of the monochromators. A 300 mm long Kirkpatrick-Baez (KB) focusing mirror system provides a 30 um (H) x 300 um (V) beam spot 1.5 m downstream at the spectrometer's source (sample)

position. A flux of 1.0×10^{13} ph/s at 9.7 kV is delivered to the sample. Fluxes are monitored with ion chambers along the beam path and reported intensities were verified with a PIN diode.

c. Data Acquisition

The reported SiO_2 elastic lines, SiO_2 Compton profiles, BN diluted FeOOH elastic images, and BN diluted FeOOH Compton profiles were collected using the Lambda flex area detector. All other reported spectra were collected using the Vortex single element SDD. All measurements were made using the (660) reflection with a nominal analyzed energy of 9735 eV. A He path covering ~80% of the flight through the spectrometer was used in all reported measurements. Elastic lines were taken during the set-up of every measurement and intermittently during scans.

d. Data Processing

For area detector data, appropriate regions of interest (ROIs) and pixel thresholds were applied home-written Python code in a Jupyter environment to extract spectra. An ROI was also applied to the energy dispersive spectra from the SDD to extract spectra. All spectra presented are normalized by an I_0 ion chamber that monitored the flux after the focusing mirrors. After normalizing, spectra were rescaled back to counts by selecting the maximum of the Compton peak to rescale to. The energy loss scale is set to 0 eV at the peak of the elastic line. In the case several scans were taken, scans were summed together after normalizing and rescaling and the total dwell times (sum of all scans) are reported.

When presenting absorption edge data outside the context of the Compton profile, the pre-edge region was fitted to a Pearson VII right-side tail function to model and subtract the Compton background. When reporting $q \cdot r$, the core radius r was estimated as a_0/Z for the K shell and $4a_0/Z$ for the $L_{2,3}$ shell, where a_0 is the Bohr radius (0.53 Å) and Z is the atomic number.

e. Samples

SiO_2 measurements were conducted using fused quartz glass slides of 150 μm thickness. Greater thicknesses reported were accomplished by stacking slides together. Pure goethite (FeOOH), iron oxide (FeO), and graphitized carbon pellets without binder were prepared by cold pressing to form approximately 1-mm thick (thk.) pellets. A mixed stoichiometry sodium *closo*-borate $(Na_2B_{10}H_{10})_{0.5}(Na_2B_{12}H_{12})_{0.5}$ 1-mm thick pellet was also pressed and then heat-sealed into aluminized mylar pouches under a dry Ar environment. For demonstrating imaging resolution, a 5 wt% goethite 95 wt% boron nitride loose powder mixture was hand milled and loaded into two receptacles: a washer with a Kapton window spacer 1 mm from the powder surface and a quartz capillary 1.5 mm in diameter with 50 μm wall thickness.

6. Results and Discussion

Here, we report results from simulated ray tracing and spectra measured with the instrument. First, we quantify the energy resolution trade-offs going from 1-m to 0.5-m radius of curvature SBCA, and how asymmetric JNA configurations eliminate this constraint. Next, we present instrument characterization data on the energy resolution and q-range. Then, we demonstrate an imaging capability to spatially select scatter for air-sensitive samples with Kapton windows and powders in capillary on the imaging array. We continue this example by showing XRS oxidation sensitivity on a transition metal *L*-edge of pure reference samples. Next, we show an O *K*-edge measurement on the high-*q* array. Lastly, we present data collected with the low-q array.

a. Ray Tracing Simulations

For a given optic diameter, the Johann approximation worsens as bending radius decreases and as θ_B moves further from backscatter, leading to increased Johann error and degraded energy resolution. This constrains XRS instruments to use larger radius of curvature (RoC) SBCA, typically 1-m, that subtend modest collection-solid angle to preserve energy resolution, and even in these cases the optic is occasionally masked along the dispersive plane. In contrast, operation at JNA eliminates Johann error and allows tighter radius SBCAs with much larger collection solid angle to be used without penalty to energy resolution.

To illustrate the effect of bending radius, Bragg angle, and asymmetry on the energy response of the analyzer, we performed ray-tracing simulations. Figure 8 shows the calculated energy response across the surface of a 100 mm diameter Johann SBCA at 9.7 keV for several representative Rowland geometries, corresponding to the (6,6,0) reflection.

In Figure 8, (a) represents a conventional symmetric 1-m radius configuration near backscatter ($\theta_B = 88.5^o$), typical of existing XRS instruments using banks of SBCA. The response is nearly uniform across the analyzer and Johann error is minimal. In (b) the RoC is reduced to 0.5-m. This increases the collection solid angle from 8 msr to 32 msr and leads to slightly more Johann error and a minimal effect on energy resolution. However, the source-detector clearance decreased from 50 mm to 25 mm going from (a) to (b), which would greatly constrain an XRS instrument.

To achieve acceptable clearance at 0.5-m, θ_B must be further from backscatter. In Figure 8, (c) shows the 0.5-m symmetric configuration at $\theta_B = 84.2^o$; where the source-detector clearance is recovered but Johann error significantly worsens. Finally, (d) shows the 0.5-m RoC asymmetric configuration at the same θ_B but with $\alpha = 5.8^o$ at JNA. This corresponds to operation

of the XRS spectrometer using the Si(7,7,1) optic and (6,6,0) reflection. As discussed in Chen, et al., there is no energy dispersion, demonstrating Johann error suppression while providing a source-detector clearance of 100 mm. The ability to get a large source-detector clearance with good energy resolution using asymmetric operation was shown in Gironda, et al.

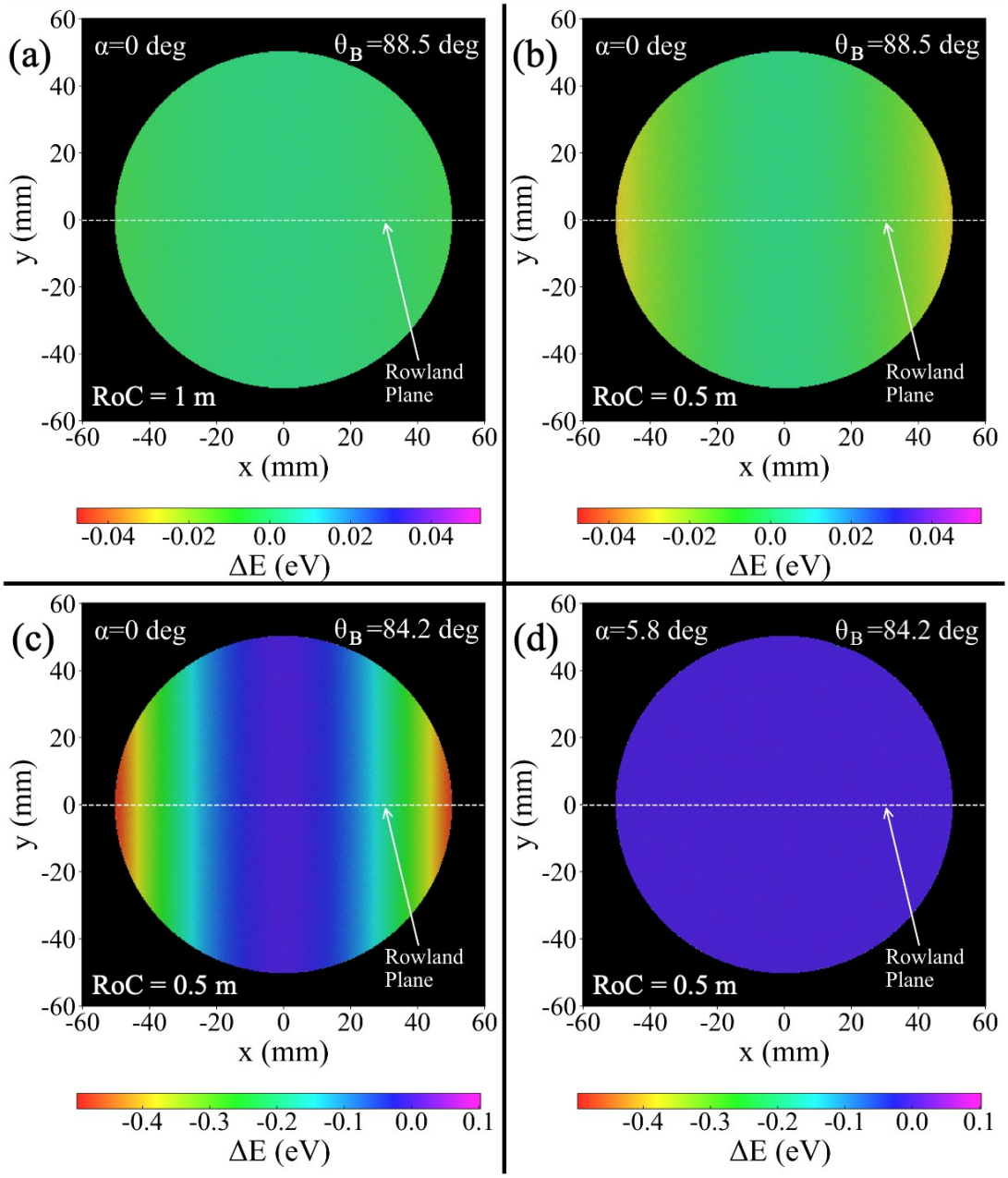

Figure 8. XRayTracer (xrt) simulations of the energy response function across the surface of a 100-mm diameter Johann SBCA for different Rowland geometries and radius of curvatures. Panels show: (a) symmetric 1-m radius near backscatter ($\theta_B = 88.5°$); (b) symmetric 0.5-m radius at the same Bragg angle; (c) symmetric 0.5-m radius at $\theta_B = 84.2°$; and (d) asymmetric 0.5-m radius at $\theta_B = 84.2°, \alpha = 5.8°$(JNA).

b. Energy Resolution and *q*-Range

The spectrometer energy resolution was quantified by the full width half max (FWHM) of the elastic line. Figure 9 shows the elastic line from each crystal analyzer. A high-energy tail is present for all analyzers, and this asymmetry was unaffected by masking both the dispersive (in-Rowland plane) and non-dispersive (out-of Rowland plane) edges of the analyzer. Energy resolutions are summarized in Table 1, but range between 0.95 and 1.0 eV for all optics, which we note is effectively monochromator-resolution limited as the upstream secondary mono has an energy resolution of 0.9 eV. By quadrature deconvolving the overall resolution and the monochromator resolution, the SBCA energy resolution contributions are estimated in the final column.

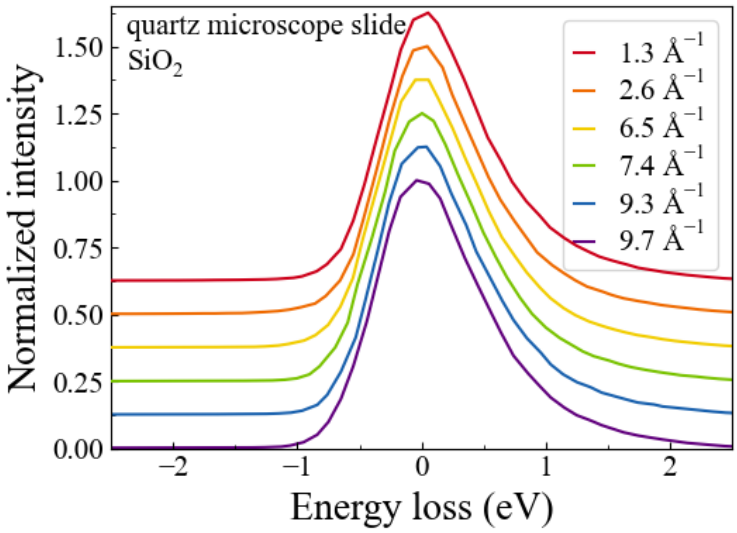

Figure 9. Peak normalized elastic lines of a quartz microscope slide (SiO_2) from each optic array: low-*q* (*q* = 1.3, 2.6 Å^{-1}), imaging (*q* = 6.5, 7.4 Å^{-1}), and high-*q* (*q* = 9.3, 9.7 Å^{-1}). Spectra have been shifted in energy and vertically offset for clarity.

Table 1. Summary of optic parameters and measured energy resolution using the (660) reflection from a Si (771) SBCA.

Scattering Angle (deg.)	q (Å-1)	Analyzed Energy (eV)	θB (deg.)	θB+α (deg.)	FWHM Energy Resolution (eV)	SBCA Resolution (eV)
15	1.3	9728.7	84.61	90.38	0.95	0.30
30	2.6	9730.2	84.52	90.29	0.94	0.27
82.5	6.5	9733.0	84.34	90.12	0.97	0.36
97.5	7.4	9733.3	84.33	90.10	0.98	0.39
145	9.3	9737.0	84.12	89.88	0.98	0.39
160	9.7	9739.9	83.95	89.72	0.99	0.41

The q-range of the spectrometer was demonstrated by measuring the Compton profile of an SiO_2 quartz microscope slide in all scattering geometries, shown in Figure 10. Note the sample thicknesses and measurement geometries: low-*q* (*q* = 1.3, 2.6 *Å^{-1}, 300* μm thick sample, transmission geometry*),* imaging (*q* = 6.5, 7.4 Å^{-1}, 300 μm thick sample tilted 22° from vertical*),* and high-*q* (*q* = 9.3, 9.7 Å^{-1}, 750 μm thick sample, reflection geometry*).* The O *K*-edge is visible for the medium and high-*q* measurements. For initial commissioning, the measurements were not made simultaenously using all three arrays.

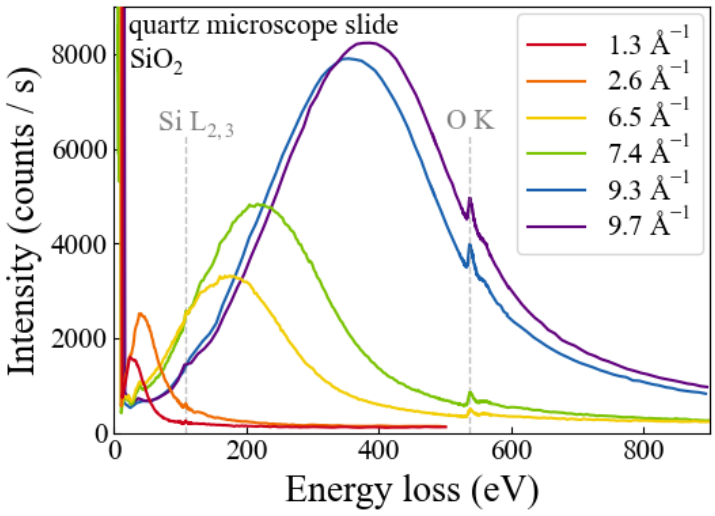

Figure 10. Compton profiles of a quartz microscope slide (SiO_2) from each optic array. Vertical dashed lines denote Si $L_{2,3}$ and O K absorption edge features of the sample. The spectra are unscaled with respect to the relative scattering volume.

c. Imaging and Spatial Rejection of Non-Sample Scatter Using Imaging Array

XRS Johann spectrometers with pixelated detectors can spatially reject scatter from sample enclosures including diamond anvil cells, as previously discussed in Section 1. By rejecting non-sample scatter, the signal-to-noise ratio (SNR) is improved and acquisition times are reduced. This capability is particularly crucial for *in situ* and especially *operando* measurements in the future where flow plug cell walls or windows would otherwise contribute to Poisson noise.

Two representative XRS imaging applications are for (1) radioactive or air-sensitive pellets enclosed in a sealed environment and (2) samples in a capillary such as an *operando* plug-flow catalyst reactor. In both situations, imaging is used to reject non-sample scatter from the enclosure or capillary. Proof of principle measurements are shown in Figure 11 with the elastic

images shown. In Figure 11 (a), a diluted FeOOH pellet with a 1 mil Kapton window displaced from the pellet surface was imaged and an ROI completely selects the sample scatter and rejects the window scatter. In Figure 11 (b), dilute FeOOH loose powder in a capillary was imaged through the capillary's diameter and again, an ROI that rejects the capillary walls and selects the powder is shown. We note that when θ_B is away from backscatter, sufficient spatial resolution is only possible at the sagittal focus. Additional discussion on this imaging behavior is found in Chen et al.

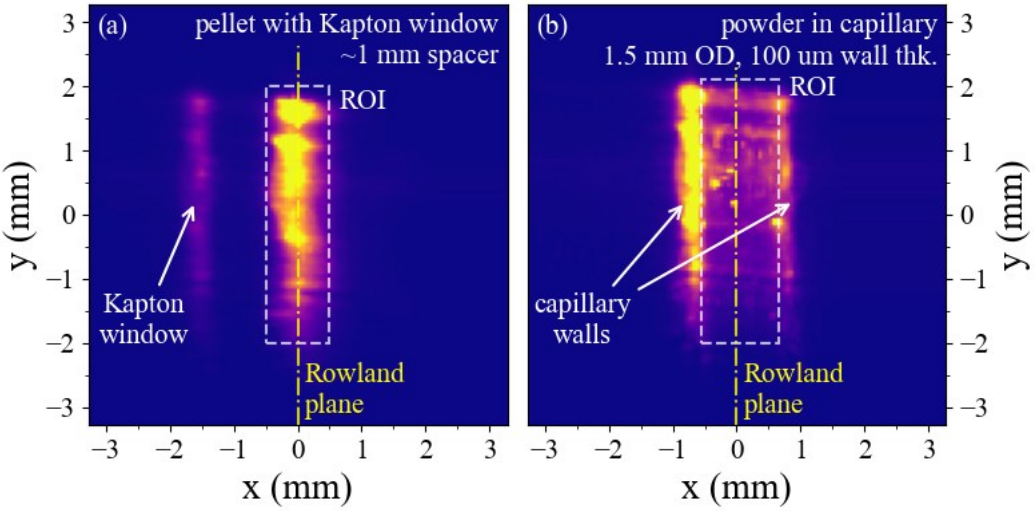

Figure 11. Pixelated area detector images at the sagittal focal plane the elastic energy for (a) BN diluted FeOOH pellet in an air-tight Kapton pouch, separated from the Kapton window by a spacer and (b) BN diluted FeOOH in a quartz capillary. Images are at the sagittal focus of the 7.4 $Å^{-1}$ optic in the imaging array.

Next, the Compton profile and Fe $L_{2,3}$-edge was measured to show the benefits of spatial rejection of non-sample scatter. Figure 12 shows the Compton profiles corresponding to the powder filled capillary from Figure 11 (b). Without imaging capability, all signal shown in panel 11 (b) would be included in the XRS spectra. As a result, the feature of interest Fe $L_{2,3}$ sits on a

Compton background from the capillary walls and the contained powder. With imaging, the ROI ideally selects only the powder, and the Compton background is reduced. The signal-to-noise ratio (SNR) of the non-imaging and imaging situations is 0.098, and 0.138, respectively, a significant improvement. However, we note that the Fe $L_{2,3}$ signal decreased by 20% when using a tight ROI. Extending the ROI would recover the Fe $L_{2,3}$, signal but would include Compton scatter from the capillary.

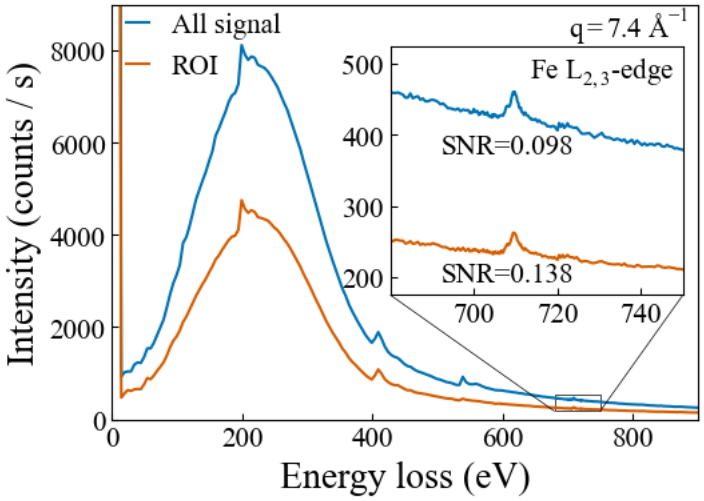

Figure 12. Compton profile of BN diluted FeOOH in a SiO_2 quartz capillary measured at 7.4 $Å^{-1}$ with a single optic in the imaging array for no ROI (i.e. scatter from capillary and sample) and for the ROI shown in Fig. 11 (b). B, N, and O K-edges are visible in the Compton spectrum, the inset plot shows the Fe $L_{2,3}$ edge.

d. Spectrometer Demonstrations

We conclude our results with demonstration measurements from the low-*q*, imaging, and high-*q* optics. We note all spectra were measured with a single optic with resolution of 1.0 eV and used the SDD. Low-*q* measurements of the B and C K-edges are reported in Figure 13 (a) and (b). Both were measured in a transmission geometry, and the *closo*-borate was air-sensitive and enclosed in heat sealed aluminized pouch.

Imaging and high-*q* optic measurements were demonstrated with two iron oxide samples in a reflection geometry. Figure 13 (c) shows an edge shift between Fe^{2+} and Fe^{3+} of the Fe $L_{2,3}$-edge measured at medium-*q*. Figure 13 (d) shows the O *K*-edge of the same samples.

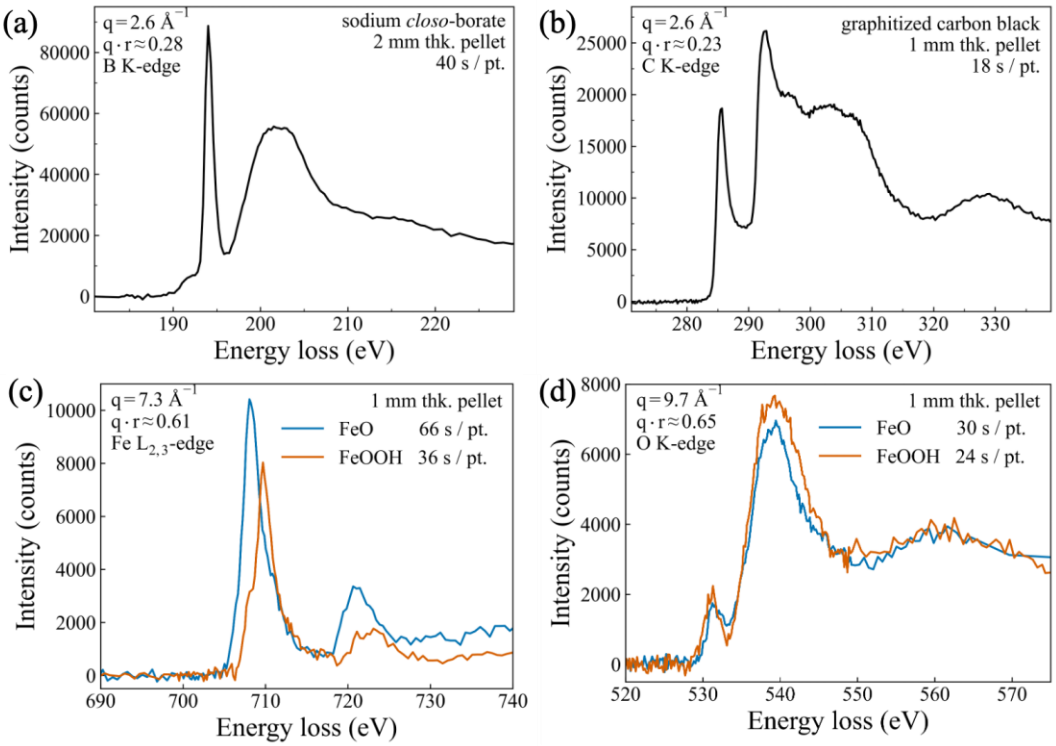

Figure 13. Demonstration XRS measurements made with the spectrometer. All spectra were measured with a single optic using an SDD (a) *in situ* B *K*-edge of a sodium *closo*-borate pellet sealed in an aluminized pouch (b) *ex situ* C *K*-edge of graphite (c) *ex situ* Fe $L_{2,3}$ of an Fe^{2+} and Fe^{3+} sample and (d) *ex situ* O *K*-edge of the same samples as (c).

7. Summary and Conclusion

We show that a six-element XRS spectrometer in an asymmetric Rowland geometry with 0.5-m radius SBCAs can deliver performance suitable for materials characterization with comparable energy resolution to symmetric 1-m radius SBCA configurations. Furthermore, we show that this is accomplished with an extreme reduction in spectrometer size and complexity, such as by the use of only six motorized degrees of freedom for alignment, as opposed to the 72 motorized degrees of freedom that would be needed for the 24 1-m SBCA that would capture the same total solid angle.

The asymmetric Rowland geometry in the Johann Normal Alignment (JNA) configuration with 0.5-m SBCA enables 100 mm working distances between source and detector whilst preserving a total energy resolution of ~1.0 eV and a spectrometer energy resolution of 0.3 – 0.4 eV. Future testing with improved incident beam energy resolution could indicate the limits of this design. Furthermore, experimental or ray tracing investigations into energy resolution at even great asymmetries could potentially provide even larger source/detector clearance at 0.5-m.

The spectrometer spans a q range from 1.3 $Å^{-1}$ to 9.7 $Å^{-1}$ at 9.7 keV. However, the present implementation does not support simultaneous data collection from multiple arrays and data collection from both optics in the same array is only possible with the area detector. Doing so with energy discrimination would require a second SDD or an additional degree of freedom (a tilt) to tune the analyzer energies to the exact same value so a single SDD could be used without compromising energy resolution. The imaging results highlight an unexpected capability of the asymmetric geometry with diced analyzers. The use of the sagittal focus is required for any spatial imaging at Bragg angles away from backscatter when asymmetric.

The drawback of asymmetric geometries at 0.5-m is an increase in sagittal and meridional focal spot sizes and a reduction in the *q*-resolution per optic compared to 1-m. Furthermore, the spectrometer is still operating at Bragg angles further from backscatter, where source-size and other broadening mechanisms contribute more strongly to energy resolution. The present geometry occupies a favorable regime where the benefits in clearance and solid angle outweigh these penalties. Despite this, a single 0.5-m optic subtends four times the collection solid angle of its 1-m counterpart and the present system is demonstrated as capable. Future upgrades to larger arrays with additional optics could rapidly outpace 1-m systems.

These results validate the use of asymmetric Rowland geometry at JNA as a central design strategy for smaller XRS spectrometers. The relatively compact footprint and low number of optics suggest a practical pathway for upgrading existing hard X-ray spectroscopy beamlines to XRS capability. The demonstration measurements reported here were collected in a few hours with a single analyzer. For a hard x-ray spectroscopy beamline, installing one or a few 0.5-m asymmetric analyzers and a suitable detector could enable routine *ex situ* XRS measurements without significant resource investment.

8. Acknowledgements

This research used resources of the Advanced Photon Source, an Office of Science User Facility operated for the U.S. Department of Energy (DOE) Office of Science by Argonne National Laboratory, and was supported by the U.S. DOE under Contract No. DE-AC02-06CH11357, and the Canadian Light Source and its funding partners. We also thank James N. Burrow for preparing and providing the sodium *closo*-borate sample for measurement.

9. References

1 U. Bergmann, P. Glatzel and S. P. Cramer, *Microchem J.*, 2002, **71**, 221–230.
2 C. J. Sahle, A. Mirone, J. Niskanen, J. Inkinen, M. Krisch and S. Huotari, *J. Synchrot. Radiat.*, 2015, **22**, 400–409.
3 R. Georgiou, C. J. Sahle, D. Sokaras, S. Bernard, U. Bergmann, J.-P. Rueff and L. Bertrand, *Chem. Rev.*, DOI:10.1021/acs.chemrev.1c00953.
4 T. T. Fister, G. T. Seidler, C. Hamner, J. O. Cross, J. A. Soininen and J. J. Rehr, *Phys. Rev. B*, 2006, **74**, 214117.
5 S. Huotari, T. Pylkkanen, J. A. Soininen, J. J. Kas, K. Hamalainen and G. Monaco, *J. Synchrot. Radiat.*, 2012, **19**, 106–113.
6 C. Sternemann, M. Volmer, J. A. Soininen, H. Nagasawa, M. Paulus, H. Enkisch, G. Schmidt, M. Tolan and W. Schülke, *Phys. Rev. B*, 2003, **68**, 035111.
7 A. Mattila, J. A. Soininen, S. Galambosi, S. Huotari, G. Vankó, N. D. Zhigadlo, J. Karpinski and K. Hämäläinen, *Phys. Rev. Lett.*, 2005, **94**, 247003.
8 J. A. Soininen, A. L. Ankudinov and J. J. Rehr, *Phys. Rev. B*, 2005, **72**, 045136.
9 S. A. Ceppi and G. E. Stutz, *J. Electron Spectrosc. Relat. Phenom.*, DOI:10.1016/j.elspec.2022.147207.
10 R. A. Gordon, M. W. Haverkort, S. Sen Gupta and G. A. Sawatzky, in *14th International Conference on X-Ray Absorption Fine Structure (xafs14), Proceedings*, eds. A. DiCicco and A. Filipponi, IoP Publishing Ltd, Bristol, 2009, vol. 190, p. 012047.
11 D. Ketenoglu, *X-Ray Spectrom.*, 2022, **51**, 422–443.
12 M. Fehse, C. J. Sahle, M. P. Hogan, C. Cavallari, E. M. Kelder, M. Alfredsson and A. Longo, *J. Phys. Chem. C*, 2019, **123**, 24396–24403.
13 K. Mukai, T. Nonaka, T. Uyama and Y. F. Nishimura, *Chem. Commun.*, 2020, **56**, 1701–1704.
14 T. Nonaka, H. Kawaura, Y. Makimura, Y. F. Nishimura and K. Dohmae, *J. Power Sources*, 2019, **419**, 203–207.
15 C. Cavallari, S. Radescu, M. Dubois, N. Batisse, H. Diaf and V. Pischedda, *J. Phys. Chem. C*, 2020, **124**, 24747–24755.
16 A. Longo, A. Mirone, E. D. C. Gallerande, C. J. Sahle, M. P. Casaletto, L. Amidani, S. A. Theofanidis and F. Giannici, *Cell Rep. Phys. Sci.*, 2023, **4**, 101699.
17 J. G. Moya-Cancino, A.-P. Honkanen, A. M. J. van der Eerden, R. Oord, M. Monai, I. ten Have, C. J. Sahle, F. Meirer, B. M. Weckhuysen, F. M. F. de Groot and S. Huotari, *ACS Catal.*, 2021, **11**, 809–819.
18 S. K. Das, L. D'ooghe, N. V. Srinath, S.-A. Theofanidis, A. Longo, C. Sahle, K. Van Geem, H. Poelman, D. Poelman and V. Galvita, *ACS Catal.*, 2024, **14**, 1311–1323.
19 S. K. Das, A. Longo, E. Bianchi, C. V. Bordenca, C. J. Sahle, M. P. Casaletto, A. Mirone and F. Giannici, *ChemPhysChem*, DOI:10.1002/cphc.202400742.
20 P. S. Miedema, P. Ngene, A. M. J. van der Eerden, D. Sokaras, T.-C. Weng, D. Nordlund, Y. S. Au and F. M. F. de Groot, *Phys. Chem. Chem. Phys.*, 2014, **16**, 22651–22658.
21 P. S. Miedema, P. Ngene, A. M. J. van der Eerden, T.-C. Weng, D. Nordlund, D. Sokaras, R. Alonso-Mori, A. Juhin, P. E. de Jongh and F. M. F. de Groot, *Phys. Chem. Chem. Phys.*, 2012, **14**, 5581–5587.
22 A. Longo, L. F. Liotta, D. Banerjee, V. La Parola, F. Puleo, C. Cavallari, C. J. Sahle, M. M. Sala and A. Martorana, *J. Phys. Chem. C*, 2018, **122**, 1003–1013.

23 C. J. Sahle, S. Kujawski, A. Remhof, Y. Yan, N. P. Stadie, A. Al-Zein, M. Tolan, S. Huotari, M. Krisch and C. Sternemann, *Phys. Chem. Chem. Phys.*, 2016, **18**, 5397–5403.
24 C. Sternemann and M. Wilke, *High Pressure Res.*, 2016, **36**, 275–292.
25 A. Nyrow, J. S. Tse, N. Hiraoka, S. Desgreniers, T. Buening, K. Mende, M. Tolan, M. Wilke and C. Sternemann, *Appl. Phys. Lett.*, 2014, **104**, 262408.
26 C. Weis, C. Sternemann, V. Cerantola, C. J. Sahle, G. Spiekermann, M. Harder, Y. Forov, A. Kononov, R. Sakrowski, H. Yavaş, M. Tolan and M. Wilke, *Sci Rep*, 2017, **7**, 16526.
27 M. Elbers, C. Schmidt, C. Sternemann, C. J. Sahle, S. Jahn, C. Albers, R. Sakrowski, H. Gretarsson, M. Sundermann, M. Tolan and M. Wilke, *Phys. Chem. Chem. Phys.*, 2021, **23**, 14845–14856.
28 C. Weis, G. Spiekermann, C. Sternemann, M. Harder, G. Vankó, V. Cerantola, C. J. Sahle, Y. Forov, R. Sakrowski, I. Kupenko, S. Petitgirard, H. Yavaş, C. Bressler, W. Gawelda, M. Tolan and M. Wilke, *J. Anal. At. Spectrom.*, 2019, **34**, 384–393.
29 C. J. Sahle, J. Niskanen, C. Schmidt, J. Stefanski, K. Gilmore, Y. Forov, S. Jahn, M. Wilke and C. Sternemann, *J. Phys. Chem. B*, 2017, **121**, 11383–11389.
30 A. Nyrow, C. Sternemann, J. S. Tse, C. Weis, C. J. Sahle, K. Mende, D. C. F. Wieland, V. Cerantola, R. A. Gordon, G. Spiekermann, T. Regier, M. Wilke and M. Tolan, *J. Anal. At. Spectrom.*, 2016, **31**, 815–820.
31 S. Petitgirard, C. J. Sahle, W. J. Malfait, G. Spiekermann, I. Blanchard, E. S. Jennings, M. Cotte and M. Murakami, *Phys. Rev. B*, 2022, **105**, 134106.
32 C. J. Sahle, A. D. Rosa, M. Rossi, V. Cerantola, G. Spiekermann, S. Petitgirard, J. Jacobs, S. Huotari, M. Moretti Sala and A. Mirone, *J Synchrotron Rad*, 2017, **24**, 269–275.
33 S. Huotari, T. Pylkkänen, R. Verbeni, G. Monaco and K. Hämäläinen, *Nature Mater*, 2011, **10**, 489–493.
34 C. J. Sahle, A. Mirone, T. Vincent, A. Kallonen and S. Huotari, *J Synchrotron Rad*, 2017, **24**, 476–481.
35 A. Jonas, S. Erat, N. Ryzhkov, A. Rulev, K. Frenzel, H. Wang, G. F. C. Mejica, J. G. T. Tomacruz, O. Paredes, D. Sokaras, B. Beckhoff and A. Braun, *MRS Adv.*, DOI:10.1557/s43580-025-01397-3.
36 A. Braun, D. Nordlund, S.-W. Song, T.-W. Huang, D. Sokaras, X. Liu, W. Yang, T.-C. Weng and Z. Liu, *J. Electron Spectrosc. Relat. Phenom.*, 2015, **200**, 257–263.
37 U. Boesenberg, D. Sokaras, D. Nordlund, T.-C. Weng, E. Gorelov, T. J. Richardson, R. Kostecki and J. Cabana, *Carbon*, 2019, **143**, 371–377.
38 M. C. Cendejas, O. A. P. Mellone, U. Kurumbail, Z. Zhang, J. H. Jansen, F. Ibrahim, S. Dong, J. Vinson, A. N. Alexandrova, D. Sokaras, S. R. Bare and I. Hermans, *J. Am. Chem. Soc.*, 2023, **145**, 25686–25694.
39 H. H. Johann, *Z. Physik*, 1931, **69**, 185–206.
40 S. Huotari, C. J. Sahle, C. Henriquet, A. Al-Zein, K. Martel, L. Simonelli, R. Verbeni, H. Gonzalez, M.-C. Lagier, C. Ponchut, M. Moretti Sala, M. Krisch and G. Monaco, *J Synchrotron Rad*, 2017, **24**, 521–530.
41 D. Sokaras, D. Nordlund, T.-C. Weng, R. A. Mori, P. Velikov, D. Wenger, A. Garachtchenko, M. George, V. Borzenets, B. Johnson, Q. Qian, T. Rabedeau and U. Bergmann, *Rev. Sci. Instrum.*, 2012, **83**, 043112.
42 T. T. Fister, G. T. Seidler, L. Wharton, A. R. Battle, T. B. Ellis, J. O. Cross, A. T. Macrander, W. T. Elam, T. A. Tyson and Q. Qian, *Rev. Sci. Instrum.*, 2006, **77**, 063901.

43 N. Hiraoka, H. Fukui, H. Tanida, H. Toyokawa, Y. Q. Cai and K. D. Tsuei, *J Synchrotron Rad*, 2013, **20**, 266–271.
44 L. v. Hámos, *Naturwissenschaften*, 1932, **20**, 705–706.
45 R. Alonso-Mori, J. Kern, D. Sokaras, T.-C. Weng, D. Nordlund, R. Tran, P. Montanez, J. Delor, V. K. Yachandra, J. Yano and U. Bergmann, *Rev. Sci. Instrum.*, 2012, **83**, 073114.
46 A. J. Gironda, J. E. Abramson, Y. Chen, M. Solovyev, G. E. Sterbinsky and G. T. Seidler, *J. Anal. At. Spectrom.*, 2024, **39**, 1375–1387.
47 J. E. Abramson, Y. Chen and G. T. Seidler, *J. Anal. At. Spectrom.*, 2025, **40**, 817–824.
48 Y. Chen, A. J. Gironda, Y. Shen, A. D. Taylor and G. T. Seidler, *J. Anal. At. Spectrom.*, 2025, **40**, 836–847.
49 D. R. Mortensen and G. T. Seidler, *J. Electron Spectrosc. Relat. Phenom.*, 2017, **215**, 8–15.
50 P. Suortti, U. Lienert and C. Schulze, *Nucl. Instrum. Methods Phys. Res. Sect. A-Accel. Spectrom. Dect. Assoc. Equip.*, 1994, **338**, 27–32.
51 P. Suortti, T. Buslaps, P. Fajardo, V. Honkimäki, M. Kretzschmer, U. Lienert, J. E. McCarthy, M. Renier, A. Shukla, T. Tschentscher and T. Meinander, *J. Synchrot. Radiat.*, 1999, **6**, 69–80.
52 M. M. Sala, K. Martel, C. Henriquet, A. Al Zein, L. Simonelli, C. J. Sahle, H. Gonzalez, M.-C. Lagier, C. Ponchut, S. Huotari, R. Verbeni, M. Krisch and G. Monaco, *J. Synchrot. Radiat.*, 2018, **25**, 580–591.
53 R. Verbeni, M. Kocsis, S. Huotari, M. Krisch, G. Monaco, F. Sette and G. Vanko, *Journal of Physics and Chemistry of Solids*, 2005, **66**, 2299–2305.
54 K. Klementiev and R. Chernikov, in *Advances in Computational Methods for X-Ray Optics III*, SPIE, 2014, vol. 9209, pp. 60–75.

Chapter 7. Proof-of-Principle Characterization of Superionic Conducting Hydridoborate Based Solid State Electrolyte Using X-ray Raman Scattering Spectroscopy

1. Introduction

Battery systems and infrastructure are a critical technology for energy storage and large-scale energy delivery[1]. Conventional rechargeable batteries have solid electrodes and liquid electrolyte and have become ubiquitous for their low-cost, ease of manufacture, and high energy and power density. However, the upper limit energy density of conventional lithium-ion batteries is being approached[2]. Furthermore, liquid electrolytes pose safety concerns as a flammable organic liquid[3]. Thus, alternative battery technologies such as sodium-ion and solid-state batteries are a lower cost and higher safety alternative with the potential to deliver greater energy and power density than conventional lithium-ion batteries[4–7].

Solid state electrolytes present a promising future for Na and Li solid-state batteries[8]. Solid electrolytes have been historically overlooked due to assumed slow kinetics in solid systems; if the ionic conductivity is overcome they offer many benefits compared to their liquid counterpart. Unlike liquid electrolyte, solid electrolytes serve as functional separators between anode and cathode and only Li/Na ions are mobile[9]. Thus, the dissolution of transition metals into the electrolyte (leaching) cannot occur, unlike in liquid electrolytes. Furthermore, in liquid electrolytes, both ions and anions are mobile and concentration gradients form in the electrolyte while current flows which reduces cell current; again this cannot occur in solid electrolytes[10].

Lastly, many inorganic solid electrolytes are stable at room temperature and are a higher safety alternative to conventional liquid organic electrolytes.

Metal *closo*-borates are an emerging inorganic solid state electrolyte salt with large $B_nH_n^{2-}$ polyhedral anions[11]. These materials are superionic conductors and stable at room temperature but undergo phase transitions at higher temperatures. However, some equal molar mixtures of *closo*-borates are stable beyond room temperature and undergo no such phase transitions making them suitable for use in batteries[12,13]. $(Na_2B_{10}H_{10})_{0.5}(Na_2B_{12}H_{12})_{0.5}$ is one such mixture with 3-4 magnitudes greater room-temperature ionic conductivity than its components; the electrolyte is compatible with both sodium metal anodes and sodium cathode materials and has been realized in several laboratory-scale solid state battery devices[12,13]. More broadly, hydridoborate-based solid electrolytes are a rapidly growing class of materials for solid state batteries[11,14], but are difficult to characterize with X-ray spectroscopy.

X-ray Raman Scattering (XRS) presents a potential characterization method for the entire class of hydridoborates. Traditional resonant X-ray absorption spectroscopy fine structure (XAFS) or X-ray photoemission spectroscopy (XPS) are not suitable for characterizing the low-Z metal hydridoborates as the measurements require a vacuum environment and suffer from high surface sensitivity and low penetration depths[15]. However, XRS is a non-resonant technique that is a bulk-sensitive element specific probe that can provide XAFS equivalent data with large penetration depths and can be performed in air[16–18]. In the future, XRS may be a key *operando* technique for studying both the metal ion (Na, Li) and boron anion (B, H) local chemical environment in solid state electrolytes while the battery cycles.

Here, we use XRS as a proof-of-principle demonstration measurement to collect XANES information on the $(Na_2B_{10}H_{10})_{0.5}(Na_2B_{12}H_{12})_{0.5}$ system.

2. Methods

a. Sample Preparation

The prepared sample chemistries measured were $Na_2B_{10}H_{10}$, $Na_2B_{12}H_{12}$, and a 50/50 molar combination $(Na_2B_{10}H_{10})_{0.5}(Na_2B_{12}H_{12})_{0.5}$, herein referred to as B10, B12, and B10/12 respectively. High density 1 mm thick pellets were cold pressed without additional binder and heat-sealed into aluminized mylar pouches under a dry Ar environment. XRS measurements were made through the pouch without breaching its atmosphere.

b. Beamline Description and Measurement

Measurements were conducted at Sector 25-ID-D at the Advanced Photon Source. An unfocused rectangular beam 200 (V) x 500 (H) μm^2 delivered a 6 x 10^{12} ph/s flux at the sample position. XRS was performed using a prototype single-element spectrometer in an asymmetric Rowland geometry in so-called inverse scanning mode, described in Figure 1. The spectrometer used a 0.5-m radius of curvature Si(211) optic (XRSTech) on the 755 reflection in a configuration that suppressed energy resolution degradation from Johann error. The analyzed photon energy was 11.5 keV. The XRS measurements were executed at a momentum transfer of 8.6 $Å^{-1}$ set by the incident photon energy and scattering angle (90º). An Eiger 500K pixelated area detector (DECTRIS) was placed 62.6 mm off-circle at the sagittal focus.

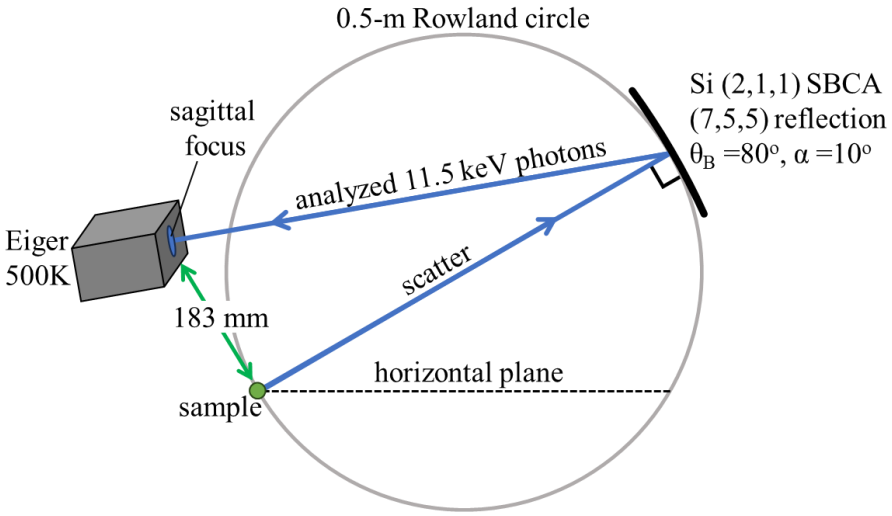

Figure 1. The Rowland circle geometry for the XRS measurements. The spectrometer remained fixed while the incident beam energy was scanned. Note the incident beam on the sample is pointing into the page making a scattering angle of 90°; the momentum transfer of the experiment was 8.6 $Å^{-1}$.

c. Data Processing

Spectral data was extracted from the image stacks using a home-written Python package and normalized by an upstream ion chamber signal along the beam path. All presented data are normalized. An unconstrained non-negative least squares linear combination fitting of the spectra was performed using the scipy library.

3. Results & Discussion

Spectral data was extracted from the image stacks with a region of interest (ROI) that selected only signal from the BH pellets, shown in Figure 2. A unique ROI that contained a B K-edge signal was selected for the 3 sample chemistries. By rejecting scatter from the aluminized pouch, the signal-to-background of the B K-edge is increased and the Poisson noise of the spectra is reduced.

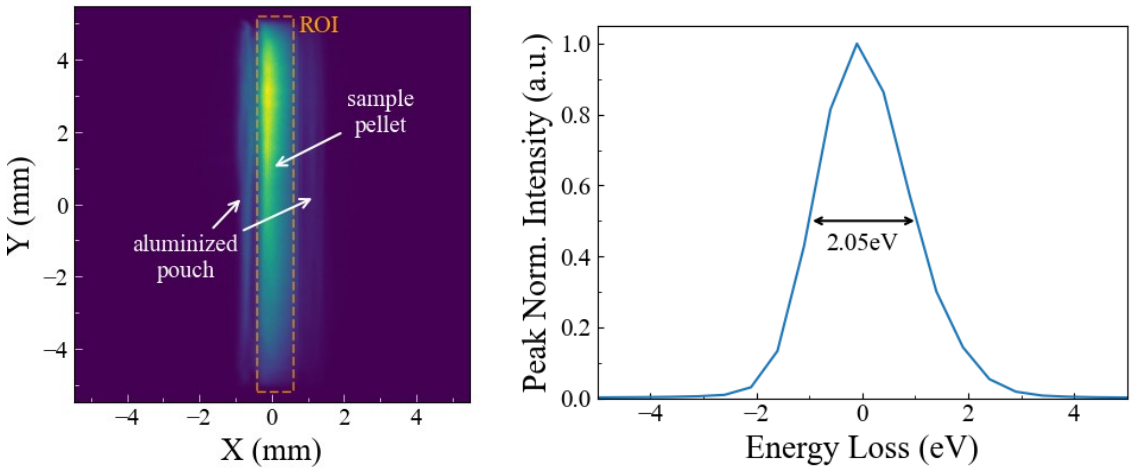

Figure 2. **(left)** Summed image stack of an XRS scan. The region of interest (ROI) show selects signal from the sample pellet and rejects scatter from the enclosing aluminized pouch. **(right)** Peak normalized elastic line from the measurements with a full width half max (FWHM) of 2.05 eV.

The overall energy resolution of the measurements was ~2.0 eV, determined by the full width half max (FWHM) of the elastic line shown in Figure 2. The elastic line sets the origin of the energy loss spectrum.

XRS measurements and the resultant normalized spectra are shown in Figure 3. Panel (a) shows the inelastic X-ray scattering spectrum collected on all 3 samples on a semi-log scale. The B10/12 spectra shows the elastic line, Na L-edge, and B K-edge absorption features. The broad featureless background these edges sit upon is the Compton spectrum. Due to time constraints, only the B K-edge regime was scanned for the B10 and B12 chemistries.

Data analysis of the B K-edge requires background subtraction and normalization of the spectra. This was accomplished by a linear fit of the pre-edge region, shown in Figure 3 panel (b). For spectral changes in the near-edge regime, this is an acceptable model.

The linear fitted background subtracted B K-edge spectra are shown in Figure 3 panel (c). Limitations in data collection time resulted in fewer counts in the B12 spectra, but the signal noise is comparable to the B10/12 and B10 datasets. Figure 3 panel (d) shows the normalized XANES regime for the three samples. The B10/12 mixture appears to be a linear combination of its constituent compounds.

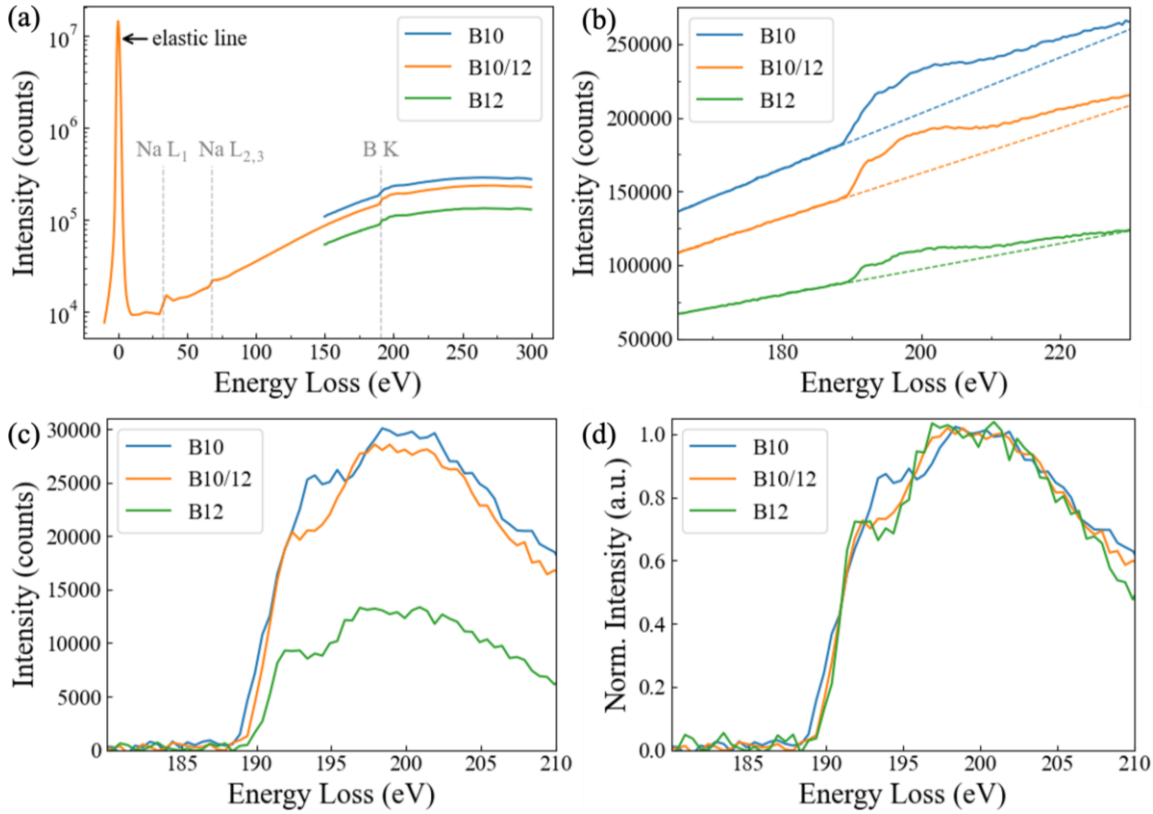

Figure 3. **(a)** The summed inelastic spectra collected from the samples. A wider scan on the B10/12 sample shows the elastic line and Na L-edge features. **(b)** The linear fits to the B K pre-edge region. **(c)** The pre-edge subtracted B K-edge feature of the three chemistries. **(d)** The normalized B-K-edge absorption feature of the samples.

To test this hypothesis, a linear-combination fit over the energy loss window of 180 – 210 eV was performed with the B10 and B12 spectra. The sum of squared residuals between the measured B10/12 spectra and the modeled a*$y_{B10}(x)$ + b*$y_{B12}(x)$ was minimized. The result of the

linear combination fitted spectrum overlaid on the B10/12 measured spectrum is shown in Figure 5. The best fit solution was determined with weights of 0.360 ± 0.045 and 0.635 ± 0.045 for B10 and B12, respectively. The errors are 1 standard deviation, corresponding to a 65% confidence interval. There was negligible difference between the constrained (a+b=1) and unconstrained models. The calculated R^2 was 0.997, indicating a good fit over the specified energy loss range and that B10/12 is well-described by a linear superposition of B10 and B12 spectra.

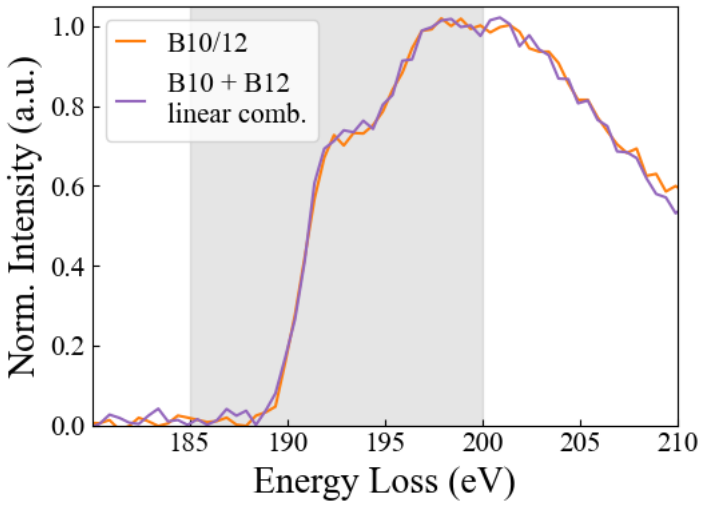

Figure 4. The normalized B10/12 B K-edge feature and the linear combination fit spectrum from the B10 and B12 data with 0.36 and 0.63 weights, respectively. The grey region is the fitted domain.

The expected mixture of the linear combination was 50/50, however, the mixture weights don't directly correlate to mass fraction – the calculated weights from the best fit are on a "per-boron atom" basis, and need to be appropriately scaled by the fraction of B10 and B12 boron atoms in the mixture. Doing so, the mixture determined by linear-combination fitting scaled by B

atoms is 43% ± 5% B10 and 53% ± B12, which is modestly agreeable to the expected 50/50 mole fraction.

4. Conclusions

Reference and mixture XRS data was collected on three *closo*-borate samples, where the mixture is a known superionic conductor. Spectral features in the near-edge structure of the mixture were successfully fitted using a linear-combination of the reference data.

Most constraints in this experiment were instrument specific; significant losses in XRS signal intensity were costly in the data acquisition time and statistics of the collected spectra. The prototype spectrometer was only 30^{o} above the horizontal plane, resulting in the polarization-dependent Thomson factor being reduced by a factor of 4. Furthermore, the use of an all-odd *hkl* reflection of the crystal analyzer reduced the spectrometer efficiency by another factor of 4. Measuring at a lower momentum transfer would also result in more oscillator strength and intensity of the B K-edge with respect to the underlying Compton background, improving signal to noise ratio. Lastly, measuring with a focused beam and at lower incident energy would result in improved energy resolution and sharper spectral features.

5. References

1 Z. Zhu, T. Jiang, M. Ali, Y. Meng, Y. Jin, Y. Cui and W. Chen, *Chem. Rev.*, 2022, **122**, 16610–16751.
2 M. Li, C. Wang, Z. Chen, K. Xu and J. Lu, *Chem. Rev.*, 2020, **120**, 6783–6819.
3 Z. Chen, K. Wang, P. Pei, Y. Zuol, M. Wei, H. Wang, P. Zhang and N. Shang, *Nano Res.*, 2023, **16**, 2311–2324.
4 D. Larcher and J.-M. Tarascon, *Nat. Chem.*, 2015, **7**, 19–29.
5 J.-Y. Hwang, S.-T. Myung and Y.-K. Sun, *Chem. Soc. Rev.*, 2017, **46**, 3529–3614.
6 S.-W. Kim, D.-H. Seo, X. Ma, G. Ceder and K. Kang, *Adv. Energy Mater.*, 2012, **2**, 710–721.
7 P. K. Nayak, L. Yang, W. Brehm and P. Adelhelm, *Angew. Chem.-Int. Edit.*, 2018, **57**, 102–120.
8 H. Aziam, B. Larhrib, C. Hakim, N. Sabi, H. Ben Youcef and I. Saadoune, *Renewable and Sustainable Energy Reviews*, 2022, **167**, 112694.
9 A. Joshi, D. K. Mishra, R. Singh, J. Zhang and Y. Ding, *Appl. Energy*, 2025, **386**, 125546.
10 X. He, D. Bresser, S. Passerini, F. Baakes, U. Krewer, J. Lopez, C. T. Mallia, Y. Shao-Horn, I. Cekic-Laskovic, S. Wiemers-Meyer, F. A. Soto, V. Ponce, J. M. Seminario, P. B. Balbuena, H. Jia, W. Xu, Y. Xu, C. Wang, B. Horstmann, R. Amine, C.-C. Su, J. Shi, K. Amine, M. Winter, A. Latz and R. Kostecki, *Nat. Rev. Mater.*, 2021, **6**, 1036–1052.
11 L. Duchêne, A. Remhof, H. Hagemann and C. Battaglia, *Energy Storage Materials*, 2020, **25**, 782–794.
12 J. B. Grinderslev, T. S. S. Kjær, L. N. Skov and T. R. Jensen, *J. Mater. Chem. A*, 2025, **13**, 15031–15039.
13 L. Duchêne, R.-S. Kühnel, D. Rentsch, A. Remhof, H. Hagemann and C. Battaglia, *Chem. Commun.*, 2017, **53**, 4195–4198.
14 T. A. Dobbins, *Molecules*, DOI:10.3390/molecules26113239.
15 D. Ketenoglu, *X-Ray Spectrom.*, 2022, **51**, 422–443.
16 U. Bergmann, P. Glatzel and S. P. Cramer, *Microchem J.*, 2002, **71**, 221–230.
17 R. Georgiou, C. J. Sahle, D. Sokaras, S. Bernard, U. Bergmann, J.-P. Rueff and L. Bertrand, *Chem. Rev.*, DOI:10.1021/acs.chemrev.1c00953.
18 C. J. Sahle, A. Mirone, J. Niskanen, J. Inkinen, M. Krisch and S. Huotari, *J. Synchrot. Radiat.*, 2015, **22**, 400–409.

Chapter 8. Democratization of HERFD-XAS: High-Throughput Multi-Edge HERFD over 5-20 keV With a Single Optic Using Asymmetric Rowland Geometries

This chapter is based on a manuscript prepared for submission to Journal of Synchrotron Radiation.

Anthony J. Gironda, Yanna Chen, Yeu Chen, Mark F. Wolfman, Shelly D. Kelly, Gerald T. Seidler

1. Abstract

High-energy resolution fluorescence detection X-ray absorption spectroscopy (HERFD-XAS) is a powerful chemical specific probe for K- and L-absorption edges. However, HERFD-XAS spectrometers require as many as 10 or more unique sets of crystal analyzers for sufficient energy coverage of emission lines, greatly increasing the up-front instrument cost and a long-term operational cost of often 1-2 days to swap crystal sets; present conventional instrumentation is not well-suited for dynamic, on-the-fly changes of user science goals studying multiple edges at different energies. Here, we report a HERFD-XAS spectrometer innovation utilizing asymmetric Rowland geometries with detector placement off-circle at the sagittal focus. With one additional degree of freedom (an azimuthal rotation of the analyzer face), we demonstrated that one single spherically bent crystal analyzer can access over 10 emission lines from 5-20 keV with no hands-on user intervention, hardware changes, or optic swapping. This presents an

avenue for rapid high-throughput, low-cost HERFD-XAS for any hard X-ray spectroscopy beamline.

2. Introduction

X-ray photon-in/photon-out spectroscopies such as X-ray emission spectroscopy (XES) [1], high energy resolution fluorescence detection X-ray absorption spectroscopy (HERFD-XAS) [2,3], and resonant inelastic X-ray scattering (RIXS) [4] are advanced synchrotron techniques widely applied to fields such as actinide chemistry [5,6], catalyst science [7,8], and life sciences [9,10], and have become routine characterization tools at hard X-ray spectroscopy beamlines. These techniques typically share a common Bragg angle scanning spectrometer design wherein spherically bent crystal analyzers (SBCAs) in symmetric Rowland geometry analyse fluorescing/scattered photons [11,12]. Johann profile SBCAs [13] provide both high energy resolution (1-2 eV), large collection solid angle, and approximately point-focusing at the detector position [14]. We focus here on their use in XES/HERFD-XAS spectrometers.

However, XES/HERFD measurements are also constrained by the conventional symmetric scanning Rowland spectrometer: the useful energy range per SBCA is only ~600 eV when operating at 5 – 10 keV. Sufficient coverage of, for example, the 3*d* transition metal K_α and K_β emission lines require nearly as many unique SBCAs as emission lines. There are three costs associated with the conventional spectrometer modality. First, a significant up-front resource cost for instrumentation. Second, instrument scientists are typically required for swapping and potentially recalibrating SBCAs to analyze different energy ranges; for large arrays this can take upwards of 1 –2 days of beamtime and is often scheduled in advance. This incurs a long-term operational cost and limits the flexibility of experiment design for user-science. And third, an experiment may require a crystal or crystal set that are not owned by the

beamline and thus the science is not possible. Present symmetric scanning Rowland spectrometers are not flexible platforms for studying multiple edges at different energies in quick succession.

With notable but seldom examples [15,16], asymmetric Rowland geometries are presently underutilized in the design and operation of high-resolution hard X-ray photon-in/photon-out spectrometers. Recent work with a laboratory X-ray spectrometer demonstrated two significant benefits of asymmetric operation of SBCA [17]. First, the energy range of a single optic can be greatly expanded by so-called "*hkl*-hopping", where an additional degree of freedom (azimuthal rotation of the analyzer) enabled access to many reflections of the optic without swapping. Second, that asymmetric operation frequently allows the suppression and occasionally elimination of Johann error, an aberration causing energy resolution degradation, without masking the analyzer. These observations were extended and formalized in a software package for asymmetric analyzer reflection selection [18] and a ray-tracing study of the analyzer response function and focusing behavior when asymmetric [19].

We note two typical scanning geometries for the conventional symmetric XES/HERFD Rowland spectrometer: a table scan geometry (Figure 1 (a)), where the analyzer translates above the horizontal plane and the detector is always vertically aligned with the source [20–22], and a tilt scan geometry (Figure 1(b)), where the analyzer, always in the horizontal plane, tilts in the dispersive direction and the detector is not vertically aligned with the source [23–29]. We focus here on the tilt scan geometry with the goal of presenting asymmetric as both a new design strategy for future instrumentation and a potential "retrofit" to pre-existing tilt scanning XES/HERFD spectrometers.

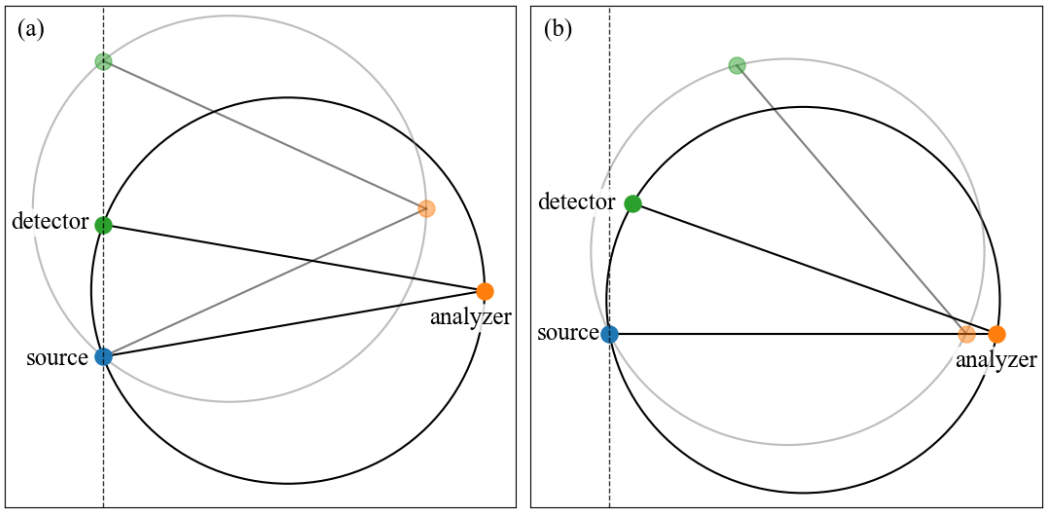

Figure 1. Trajectories of a symmetric (a) table scan and (b) tilt scan Rowland geometries. For HERFD/XES, the beam ('source') is in-to/out-of the page.

We report the design and commissioning of a tilt scan Rowland geometry XES/HERFD spectrometer. A key design strategy for the detector placement when *hkl*-hopping utilizes the astigmatic focus of the SBCA, shown in Figure 2. Detector placement and tracking behind the Rowland circle at the sagittal focus simplifies the detector trajectory to be mostly vertical and frequently places the detector vertically in line above the source. By using a single Si(211) analyzer asymmetrically and *hkl*-hopping, we measured emission lines and performed K- and L_3-edge HERFD-XAS at ~1.5 eV resolution from 5 – 10 keV with no changes in spectrometer set-up. With the same single analyzer, we also demonstrate measurements on 4d transition metal K-edges as surrogates for actinide L-edges with spectrometer energies up to 18 keV at ~4.0 eV resolution. Asymmetric XES/HERFD spectrometers require many fewer analyzers than conventional symmetric ones, and present HERFD as a high throughput technique capable of analyzing vastly different photon energies without requiring intervention of a beamline scientist to change optics. This mode of operation is automatable and user trainable.

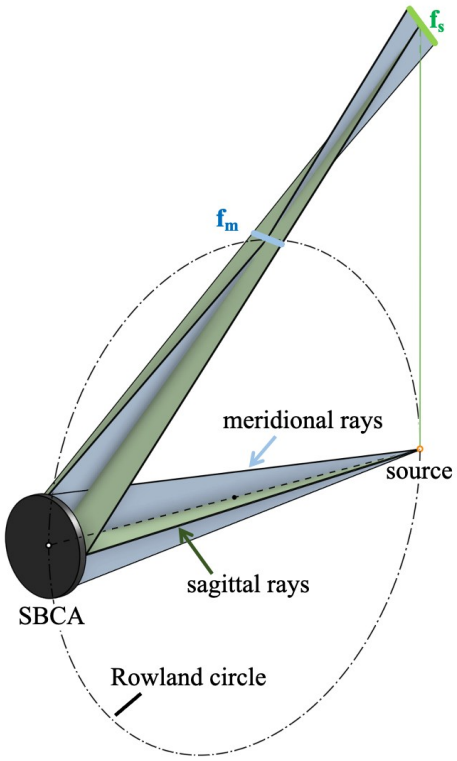

Figure 2. Diagram of the astigmatic focus of the analyzer in the asymmetric JNA Rowland geometry, wherein the source is diametrically located from the analyzer on the Rowland circle. The meridional focus is perpendicular to the Rowland plane and on the focusing circle perimeter whereas the sagittal focus lies within the Rowland plane and beyond the focusing circle perimeter. In this reference frame at JNA, the sagittal focus is located directly in-line above the source

3. Asymmetric Spectrometer Rowland Geometry

When operating asymmetrically, the diffracting plane family ($\mathbf{G}_{hkl}$) differs from the nominally surface coincident "cut" plane family ($\mathbf{G}_0$) of the optic. The asymmetry angle (α) between these plane families for cubic crystal structures (Si, Ge, e.g.) is defined by

$$\alpha = \cos^{-1}\left(\frac{\boldsymbol{G_0} \cdot \boldsymbol{G_{hkl}}}{\|\boldsymbol{G_0}\|\|\boldsymbol{G_{hkl}}\|}\right) \tag{1}$$

for a given asymmetric reflection. We note that under asymmetric operation of a single optic using many reflections for an expanded energy range, α can vary significantly.

The Rowland geometry of the spectrometer arranges the fluorescing source and optic in the horizontal plane and places the detector at the sagittal focus. The variables of the asymmetric Rowland circle in this reference frame are denoted in Figure 3. For convenience, we define a so-called mechanical angle (θ_M) as

$$\theta_M = \theta_B + \alpha \tag{2}$$

where θ_B is the Bragg angle of the diffracting plane. Physically, θ_M is the angle between the SBCA's center surface tangent and the fluorescing source (see Fig. 3).

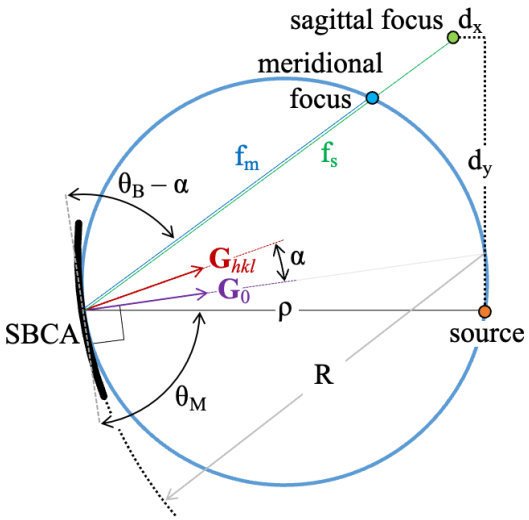

Figure 3. Diagram of asymmetric Rowland circle geometry with sagittal detector displacements shown w.r.t a fixed fluorescing source. The asymmetry angle α is defined between the diffracting plane $\mathbf{G}_{hkl}$ and the surface cut plane $\mathbf{G}_0$ reciprocal lattice vectors.

The chord relations in asymmetric Rowland geometry are given by

$$\rho = R\sin(\theta_M) \tag{3}$$

$$f_m = R\sin(\theta_B - \alpha) \tag{4}$$

$$f_s = -\frac{R\sin^2(\theta_M)}{\sin(\theta_B - \alpha)\cos(2\theta_M)} \tag{5}$$

where R is the bending radius of the SBCA (equivalently the diameter of the Rowland circle), ρ is the chord from source to SBCA, and f_m and f_s are the meridional (on-circle) and sagittal (behind-circle) astigmatic focal lengths of the SBCA, respectively [19]. The extents of these focal spots assuming geometric lenses and an on-circle point source is given by

$$w_m = 2(f_s - f_m)\tan\left(\frac{d_{xtal}}{2f_s}\right) \tag{6}$$

$$h_s = 2(f_s - f_m)\tan\left(\frac{\gamma}{2}\right) \tag{7}$$

where w_m is the width of the meridional focus (perpendicular to the Rowland plane) and h_s is the height of the sagittal focus (within the Rowland plane) [19]. These focal sizes also depend on the diameter of the optic, d_{xtal}, and the angular size of the optic in the Rowland plane viewed from the source, γ, given by

$$\gamma = 2\tan^{-1}\left(\frac{d_{xtal}\sin\theta_M}{2\rho}\right). \quad (8)$$

The trajectory of the sagittal focus, and thus the displacements of the detector with respect to the source (refer to Fig. 3), is given by

$$d_x = f_s\cos(2\theta_B^c) - \rho \quad (9)$$

$$d_y = f_s\sin(2\theta_B^c) \quad (10)$$

where θ_B^c is the complement angle of θ_B.

Now, we consider a special configuration of asymmetric Rowland geometry where the source is placed on-circle diametrically from the optic at the spherical center of the radius of curvature (ρ = R); we define this geometry as "Johann Normal Alignment" (JNA). Here, $\theta_M = \theta_B + \alpha = 90^o$ and Johann error is eliminated [17,19,30,31]. At JNA, $d_x = 0$ and the sagittal focus is located directly above the fluorescing source. Figure 4 shows 0.5-m Rowland circle trajectories at three different α (i.e. three different $\mathbf{G}_{hkl}$ and analyzed energy ranges), and in for each case when JNA is satisfied the sagittal focus is vertically in line with the source.

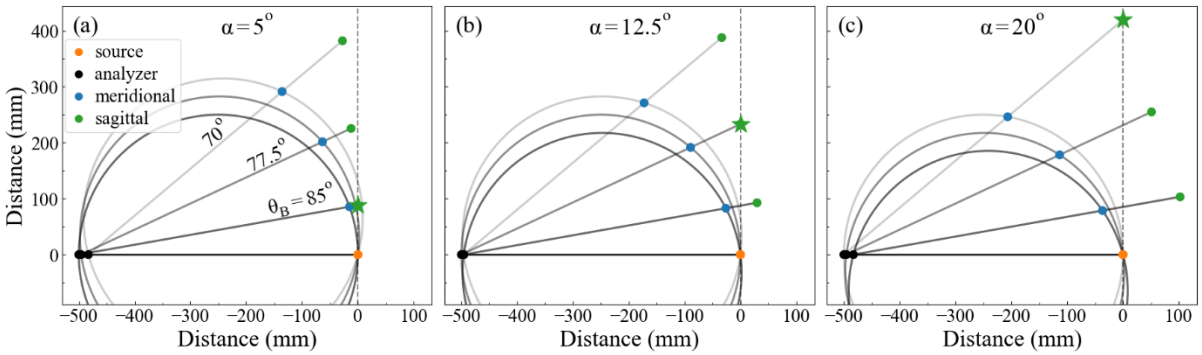

Figure 4. Side view of asymmetric Rowland circle geometry at three different asymmetries (panels (a), (b), (c)) at select θ_B. The JNA condition ($\theta_M = \theta_B + \alpha = 90^o$) is denoted by a star at the sagittal focus. At JNA, the sagittal focus is located directly above the source shown by the dashed vertical axis.

As mentioned in the introduction, this reference frame is very common for usual symmetric spectrometers. Here, a particular challenge in the design of an asymmetric scanning Rowland spectrometer with detector tracking at the conventional meridional focus is the non-equivalence of ρ and f_m at increasing α. This always results with the detector cantilevered in front of the source, closer towards the analyzer (refer to Fig. 4, the meridional point in all cases), which complicates the flight path for He boxes and requires both significant horizontal and vertical displacement of the detector to remain on circle.

Thus, the design strategy for a kinematically simpler and more convenient asymmetric spectrometer in this reference frame instead detector tracks the off-circle sagittal focus and prioritizes reflections only where the analyzed energy is at or close to JNA ($\theta_M = 90^o$). This simplifies the detector tracking to require only significant vertical displacement, and relatively little horizontal displacement.

4. Spectrometer Description

The spectrometer utilizes a single SBCA in asymmetric Rowland circle geometry. A computer aided design (CAD) rendering in Figure 5 details the components and motorized degree of freedom. The source remains fixed while the spectrometer scans. The instrument employs a 0.5-m radius of curvature sliced Si(211) SBCA (XRSTech) arranged in the horizontal plane to eliminate any elastic/inelastic photons from being analyzed. The optic is mounted concentrically to a motorized azimuthal rotation stage (Velmex B5990TS), which we refer to as the 'clock angle' or ϕ, shown in the section view 'A' of Figure 5. This additional degree of freedom enables automated asymmetric operation and is required to rotate the selected $\mathbf{G}_{hkl}$ into the vertical Rowland plane for *hkl*-hopping, and can also be used for tilt-free correction of wafer miscut when symmetric [32]. The analyzer is permanently mounted on a cartridge that kinematically mounts to the azimuthal ϕ subassembly, preserving concentricity and orientation when swapping analyzer cartridges.

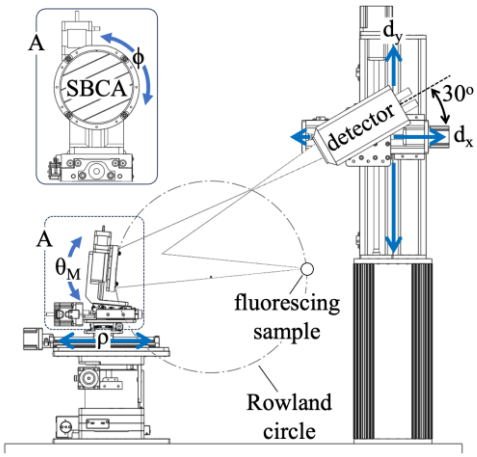

Figure 5. Side-view CAD rendering of the 0.5-m spectrometer. Degrees of freedom are labelled with blue arrows. The detector is placed at the sagittal focus at a fixed angle of 30°. The section view 'A' shows the front face of the SBCA subassembly and the additional azimuthal motorized degree of freedom, ϕ, required for automated asymmetric *hkl*-hopping.

The spectrometer scans in angle, θ_M, by a tilt stage (Kohzu SA10A-RT01) beneath the azimuthal subassembly. Kinematic alignment features place the apex of the SBCA on the rotation axis of the θ_M tilt stage. The θ_M subassembly is designed to scan the analyzer equidistant around JNA ($\theta_M = 90^o$) with a range of $80^o – 100^o$. The absolute θ_B range of a given asymmetric reflection depends on α. The source is kept on circle while the spectrometer scans by a linear translation stage, ρ (Velmex Xslide), beneath the θ_M tilt subassembly. The stroke and resolution of the spectrometer motors are described in Table 1.

Table 1. Motorization specifications for scanning the spectrometer.

Name	Description	Stroke	Resolution
θ_M	Analyzer dispersive rotation	±10°	0.002°
ϕ	Analyzer azimuthal rotation	±180°	0.01°
ρ	Analyzer translation	395–600 mm	75 μm
d_x	Detector horizontal translation	-45–80 mm	75 μm
d_y	Detector vertical translation	80–460 mm	75 μm

The spectrometer uses an Eiger 500K (Dectris) pixelated area detector with a 77.2 x 38.6 mm^2 sensing area and 450 μm thick Si sensor. The detector is side mounted so the longer dimension of the sensing area lies along the Rowland plane and is tipped down 30^o so the diffracted rays from the analyzer are approximately normal to the sensor. The detector is placed behind the Rowland circle at the sagittal focus by linear translation stages d_x and d_y (Velmex Bislide and Velmex Tandem Bislide). In this frame of reference and operating around JNA, the sagittal focus is mostly located vertically above the source.

Table 2. Calculated spectrometer parameters for several emission lines asymmetrically accessed with a 0.5-m Si(211) SBCA.

Emission	**Energy**	$\mathbf{G}_{hkl}$	**φ**	θ_B	**α**	θ_M	**ρ**	d_x	d_y	h_s	**η**
	(eV)		(°)	(°)	(°)	(°)	(mm)	(mm)	(mm)	(mm)	
Nd Lα1	5227.6	(3, 3, 1)	67.8	72.13	20.51	92.65	499.5	19.4	373.3	49.5	2.6
Co Kα1	6930.9	(5, 3, 1)	112.2	76.99	14.96	91.95	499.7	9.6	248.7	25.1	2.5
Fe Kβ1	7059.3	(5, 3, 1)	112.2	73.06	14.96	88.02	499.7	-10.2	328.7	33.1	1.9
Fe V-t-C	7110.0	(5, 3, 1)	112.2	71.77	14.96	86.73	499.2	-17.1	356.3	36.3	1.8
Co Kβ1	7649.1	(5, 3, 3)	0.0	78.11	5.05	83.16	496.4	-11.2	213.8	10.5	1.2
Cu Kα1	8046.3	(4, 4, 4)	0.0	79.37	19.47	98.84	494.1	57.9	214.7	32.3	4.7
Zn Kα1	8637.2	(6, 4, 2)	90.0	81.48	10.89	92.37	499.6	8.2	155.6	11.9	2.7
Re Lα1	8652.0	(6, 4, 2)	90.0	80.85	10.89	91.74	499.8	6.0	167.3	12.6	2.5
Cu Kβ1	8903.9	(5, 5, 3)	39.2	79.97	16.92	96.89	496.4	38.3	195.3	24.9	4.1
Pt Lα1	9442.0	(7, 3, 3)	180.0	81.71	4.04	85.75	498.6	-5.4	146.9	5.3	1.3
Zn Kβ1	9570.4	(7, 3, 3)	180.0	77.49	4.04	81.54	494.6	-11.2	225.6	10.9	1.2
As Kα1	10543.4	(7, 5, 3)	67.8	80.51	9.65	90.17	500.0	0.5	172.1	11.4	2.1

By *hkl*-hopping, a single analyzer can access many asymmetric reflections granting an expanded energy range. The Rowland circle parameters for several emission lines are tabulated in Table 2 from Eqs. 1—10. The enlarged sagittal focal size when asymmetric is quantified by taking the ratio of the asymmetric reflection's sagittal extent to the meridional extent of the same reflection but if accessed symmetrically (i.e. $\mathbf{G}_{hkl} = \mathbf{G}_0$); this focal extent factor is denoted by η, the last column of Table 2. For example, Cu K$_{\beta 1}$ measured asymmetrically with Si(211) accessing the (553) reflection has a sagittal extent h_s of 24.9 mm; had it been measured symmetrically with a Si(553) optic the meridional extent w_m is 6.1 mm, so η = 24.9 mm / 6.1

mm = 4.1. η serves as a metric for detection inefficiency when operating asymmetrically at the sagittal (off-circle) focus compared to symmetric operation at the meridional (on-circle) focus.

Pre-alignment of the spectrometer utilized a 0.5-m metal rod with an aperture that kinematically mounted to the base plate of the spectrometer; the beam was steered through the center of the aperture to set the position of the spectrometer to a known fiducial. X-ray alignment required determining the radius of curvature of the Si(211) optic. This was done by measuring the elastic line width on the (444) reflection at JNA while varying ρ. The radius of curvature was determined at the ρ value that yielded the sharpest energy resolution. Regular spectrometer operation required a Bragg angle offset, θ_B^{offset}, at JNA to calibrate the energy scale for an asymmetric reflection before proceeding to an XES or HERFD scan.

5. Methods

a. Beamline Description

All measurements and commissioning were carried out at Sector 25-ID-C of the Advanced Photon Source. The beamline's X-ray source is a 2.8-mm canted undulator. Rh-, Si-, and Pt-coated stripes on a high-heat load collimating mirror provided harmonic rejection. A 4 – 40 keV monochromatized energy range is provided a Si(111) double-crystal monochromator which was 15% detuned. A 300 mm Kirkpatrick-Baez focusing mirror system provided a 10 x 10 μm^2 micro focused beam spot 400 mm downstream. At 10 keV, a flux of $1x10^{13}$ ph/s was delivered at the sample. Intensities were monitored with ion chambers at several segments along the beam path.

b. Software and Data Processing

Images captured with the area detector were processed in Python using a region of interest (ROI) and a pixel threshold to select signal and extract spectra. XES spectra are presented with a background subtraction, this background was determined with an off-signal ROI. XAFS and HERFD spectra were normalized following standard practice in Athena. Sets of SBCAs for asymmetric energy coverage was surveyed using a modified version of *hklhop*[18].

c. Samples and Measurement

The samples were mostly transmission and fluorescence beamline standards. Layered samples of powders prepared on tape were CuO, Cu_2O, Na_2ReO_4, Y_2O_3, and MoO_3. Non-diluted pressed pellets were Nd_2O_3, Fe_3O_4, As_2S_3 contaminated soil, and Pt catalyst on TiO_2 support. Individual PEG diluted pellets were 10 wt% ZnO, 5 wt% CoO, and 50 wt% ZrO_2.

All measurements were made in air except for Nd, which used a He flight path through the spectrometer. Overall energy resolutions were assessed by the full width half max (FWHM) of the elastic line from the spectrometer. Total fluorescence yield was recorded with a Vortex-ME4 spectroscopic silicon drift detector below 15 keV and a passivated implanted planar silicon detector with no energy discrimination above 15 keV.

The presented experimental results were all performed with the spectrometer described except for the slice orientation dependent focus images which begins the Results section. That work was done with a prototype asymmetric spectrometer of similar operating principles – a description of that instrument and the 25-ID-C beamline parameters is found in the SI.

6. Results

The results begin with a survey of asymmetrically operated SBCA energy ranges and a suite of analyzers for maximum energy coverage. Next, we describe the spectrometer's energy resolution and performance. Then we demonstrate *hkl*-hopping for K- and L-edge XES in the energy ranges of 4-10 keV, and discuss the effect of slice orientation on the sagittal focus quality. Lastly, we demonstrate spectroscopy capability at 10-20 keV on surrogate L-edges of actinides.

a. Survey of Unique SBCAs for Energy Coverage

By *hkl*-hopping, a comprehensive energy range can be stitched together by accessing many reflections. We present asymmetric operation as a low cost design strategy for scanning spectrometers, where a few asymmetrically operated optics can replace an entire suite of symmetrically operated optics. To demonstrate this, we surveyed common cuts of Si and Ge analyzers for their coverage of the 3d transition metal $K_{\alpha 1}$ and $K_{\beta 1}$ emissions when used asymmetrically. A subset of some of the best analyzers for this range is shown in Figure 1(a).

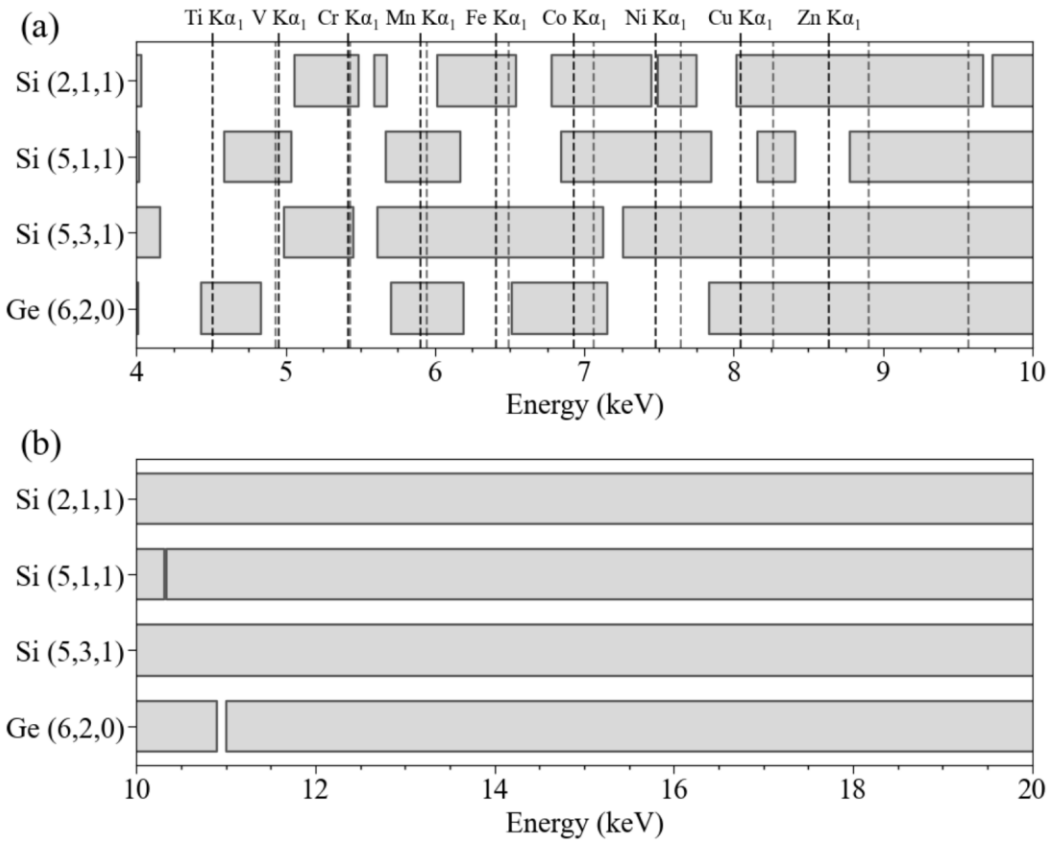

Figure 6. *hkl*-hopped energy ranges for a subset of SBCAs for θ_B = [65°, 88°], θ_M = [80°, 100°], α = [0°, 21°] at **(a)** 4-10 keV with 3d transition metal $K_{\alpha 1}$ (black, labelled) and $K_{\beta 1}$ (gray, unlabelled) emissions and **(b**) 10-20 keV. Ranges assume sufficient detector translation.

When operating asymmetrically, significant coverage of relevant emission lines can be achieved with a small number of SBCAs. First, a two analyzer SBCA suite (Si(211) and Si(511)) can cover all 3d transition metal $K_{\alpha 1}$ and $K_{\beta 1}$ emissions except for Ti $K_{\alpha 1}$. Similarly, a single analyzer (Si(531)) covers all the energy targets greater than 5 keV. If the θ_B low limit is extended to 60°, one Si(531) analyzer covers all emission targets except for Ti $K_{\alpha 1}$. With this modified range, Si(531) and Ge(620) could cover the entire 3d transition metal $K_{\alpha 1}$ and $K_{\beta 1}$ emission lines

from Ti to Zn. We note that these coverages do not include an energy width around the emission line energies and assume sufficient detector range of motion.

A relatively careful selection of SBCAs is required for maximum coverage with minimum unique analyzers in the range of 4 – 10 keV; and we find a comprehensive energy range for the 3d transition metal K-shell emission spectroscopy is achievable with as few as two optics. In general, including more optics in the suite will yield θ_B closer to backscatter, θ_M closer to JNA, and smaller α for targeted emission lines.

Unlike the many discontinuities from 4 – 10 keV, we find at high energies (>10 keV) asymmetric operation makes generally any cut SBCA suitable for spectroscopy. This is a result of the many high index reflections available. Figure 6 (b) shows nearly continuous overlapping *hkl*-hopped energy ranges from 10 – 20 keV for all four surveyed analyzers. Thus, we predict any cut SBCA used asymmetrically is suitable for K-shell spectroscopy of 4d transition metals and L-shell spectroscopy of actinides in this energy range.

b. Slice orientation dependence of sagittal focus

Operation at the sagittal focus with a sliced analyzer shows a slice orientation dependence in the focal spot image. Asymmetric operation requires ϕ orientation of the optic which changes the slice orientation, and its effect on the sagittal focus is unavoidable when using a sliced SBCA. To quantify this, a study of the meridional, sagittal, and circle of least confusion (the intermediate "focus" between the two) was performed with a sliced 0.5-m Si(100) SBCA in Rowland geometry at JNA with slice orientations of $\phi = 0^o$ (slices parallel to the Rowland plane) and $\phi = 90^o$ (slices perpendicular to the Rowland plane). The high symmetry Si(100) has several asymmetric reflections at identical photon energies, θ_B, and α, separated in ϕ by 90^o and oriented

with parallel/perpendicular to the slices, making it suitable for this study. Here, the 711 and $71\bar{1}$ asymmetric reflections were used and the analyzed rays were exactly normal to the detector. Further details on this measurement are found in the SI.

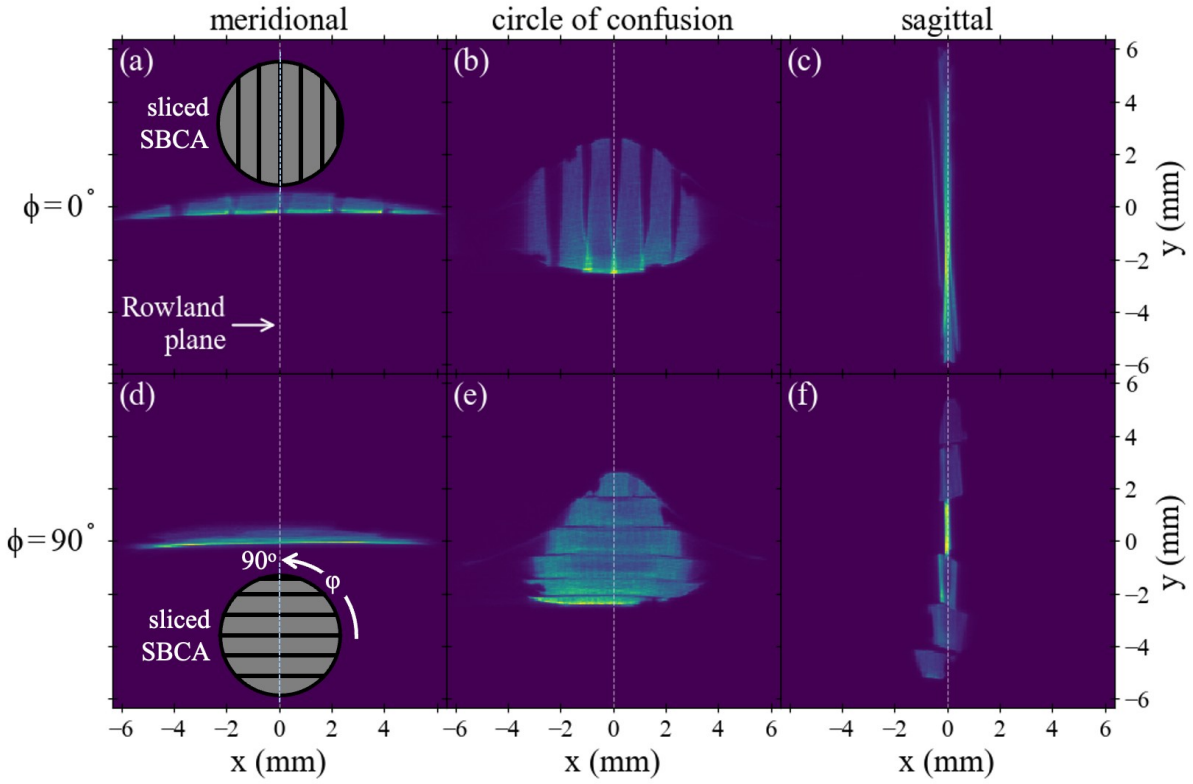

Figure 7. Effect of SBCA slice orientation on focusing behaviour, comparing slices perpendicular to Rowland plane (a,b,c) to slices parallel to Rowland plane (d,e,f) at the on-circle meridional focus (a, d), off-circle sagittal focus (c, f) and the circle of least confusion in between these foci (b, e). Here, a 0.5-m Si(100) SBCA in Rowland geometry was used and the 711 and $71\bar{1}$ reflections at JNA examined (E = 8318 eV, θ_B = 78.6°, α = 11.4°).

Slice orientation shows minimal effects at the on-circle meridional focus, as shown in Figure 7 (a) and (d). At the meridional focus, the individual stripe segments are visible in (a) and overlapping in (b). The calculated meridional extent w_m is 15.2 mm, a slight overestimation.

Slice orientation has significant effects at the sagittal focus shown in Figure 7 (c) and (f). At the sagittal focus with stripes perpendicular to the Rowland plane, each stripe has a different focal distance and only a semi-focused image is achievable (Fig. 7 (f)). This behavior is not observed when the stripes are perpendicular to the Rowland plane (Fig. 7 (e)). Again, the calculated sagittal extent h_s is 16.4 mm, slightly overestimated.

ϕ rotation is required for *hkl*-hopping and asymmetric operation – unfavorable slice orientations and a dispersed sagittal focus is occasionally unavoidable. This impacts the design of slits at the sagittal focus for background rejection, and a contributes to a worse signal to background ratio as the sagittal foci can be even more dispersed on the detector. This is particularly unfavorable for fluorescence detection of dilute samples. This sagittal defocusing behavior was also observed with the Si(211) optic reported below, and is assumed intrinsic to sliced optics. This may be solved with diced bent SBCAs, but this was not investigated.

c. Energy resolution

The overall energy resolution, ΔE, is reported by the full width half max (FWHM) of the elastic line measured with the spectrometer. Elastic lines were measured at emission peak energies, which reports both XES and HERFD resolution. Over 7 – 10 keV, the energy resolutions range from ~1.5 – 2.0 eV with the exception of Zn $K\beta_1$ shown below in Table 3. In the case of Zn $K\beta_1$, ΔE did not improve by varying ρ and the elastic energy agreed with the set spectrometer energy within 1 eV, so this is not attributed to a tracking error. The elastic line at Nd $L\alpha_1$ was too weak and was omitted, but is estimated at 1.3 eV. Energy resolution may be improved with diced bent SBCAs, detuning the beamline monochromator, or use of a secondary channel cut monochromator upstream of the spectrometer. The energy tracking of the spectrometer at each reported elastic line was within 2 eV.

Table 3. Overall energy resolution of the 0.5-m Si(211) asymmetric spectrometer and beamline at relevant emission energies assessed by FWHM of the elastic line.

Emission	**Energy**	**G_{hkl}**	**θ_B**	**α**	**θ_M**	**ΔE**
	(eV)		(°)	(°)	(°)	(eV)
Co Kα1	6930.9	(5, 3, 1)	76.99	14.96	91.95	1.4
Fe Kβ1	7059.3	(5, 3, 1)	73.06	14.96	88.02	1.5
Co Kβ1	7649.1	(5, 3, 3)	78.11	5.05	83.16	1.9
Cu Kα1	8046.3	(4, 4, 4)	79.37	19.47	98.84	1.8
Zn Kα1	8637.2	(6, 4, 2)	81.48	10.89	92.37	1.7
Re Lα1	8652.0	(6, 4, 2)	80.85	10.89	91.74	1.7
Cu Kβ1	8903.9	(5, 5, 3)	79.97	16.92	96.89	1.8
Pt Lα1	9442.0	(7, 3, 3)	81.71	4.04	85.75	2.0
Zn Kβ1	9570.4	(7, 3, 3)	77.49	4.04	81.54	2.7
As Kα1	10543.4	(7, 5, 3)	80.51	9.65	90.17	2.1

d. Asymmetric *hkl*-hopping XES

A single asymmetrically operated analyzer has an appreciable energy range for spectroscopy from 5 – 10 keV. We demonstrate this by measuring several emission spectra from 5 – 10 keV with a single Si(211) SBCA with only motorize changes to the spectrometer, shown in Figure 8 on non-dilute standards. By *hkl*-hopping, many reflections and d-spacings can be accessed, only requiring the motorized ϕ degree of freedom and the appropriate sagittal detector placement. This affords a large energy range for K- and L-shell spectroscopy with a single optic. We again note that Si(211) is not the best single optic for energy coverage in the 5 – 10 keV range, but was the optic on hand.

The XES scans were measured without tracking the detector. Thus, some highly asymmetric reflections with very large sagittal foci can move off the sensor and cause signal loss; this is observed in the decreased intensity of Nd $L\alpha_2$, for example. In the future, the spectrometer will operate with sagittal detector tracking during scans. Additionally, the θ_M range (80^o – 100^o) is limiting when constrained to operating with only a single cut of SBCA; this is observed in the Cu $K\alpha_2$ where the emission line is close to the upper limit of θ_M. This can be addressed by increasing the θ_M range (which requires more detector d_x translation) or selecting a more suitable asymmetrically operating SBCA or set of SBCAs with more favorable Rowland parameters.

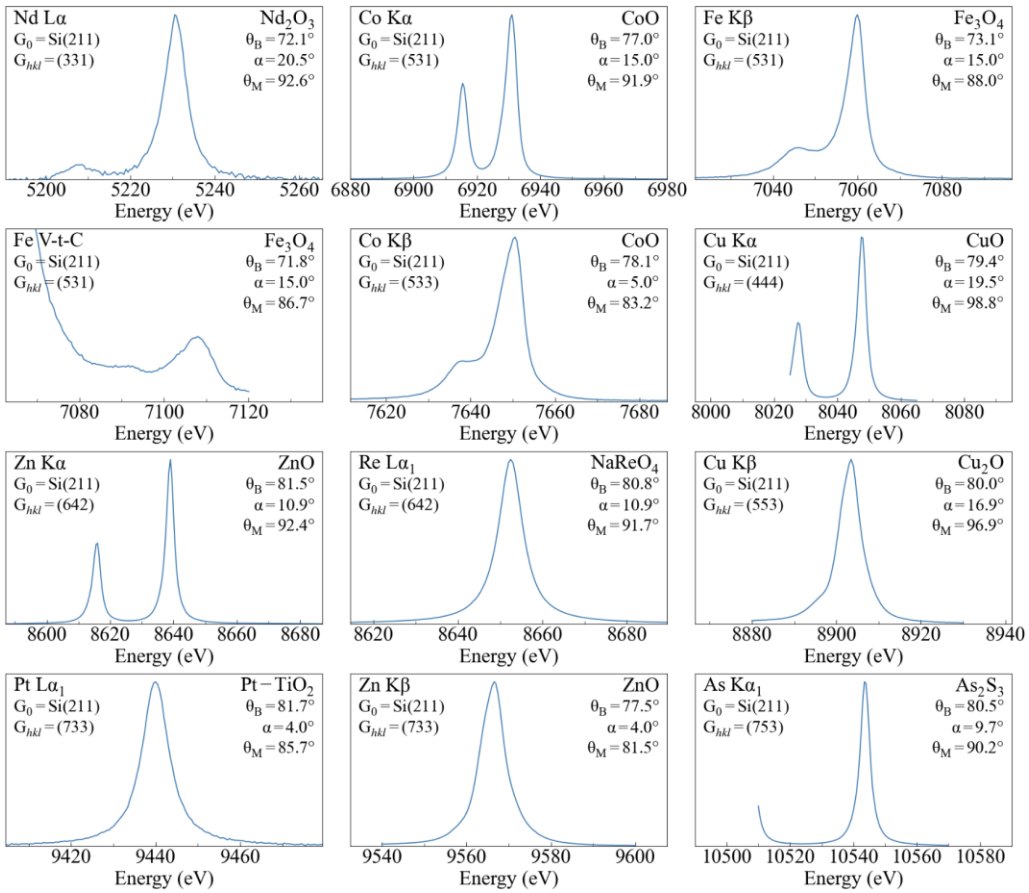

Figure 8. Emission lines asymmetrically accessed by *hkl*-hopping a Si(211) optic. Reflections and Rowland parameters are displayed for each panel.

The sagittal size can become significant when working at large α and we observe that slice orientation ϕ dependence can further impact the image quality. The sagittal images at the emission peaks of the *hkl*-hopped spectra are shown in Figure 9, ranging from 35 mm to 5 mm in extent, depending on the Rowland parameters. In general, the equation for calculating the sagittal extent overestimates the size at larger α and θ_B further from backscatter. Some imaging capability to spatially select fluorescence is shown for the samples with layers of powders on tape, this is most evident on the Re $L_{\alpha 1}$ image. Imaging resolution at the sagittal focus is degraded depending on the slice orientation w.r.t. the Rowland plane.

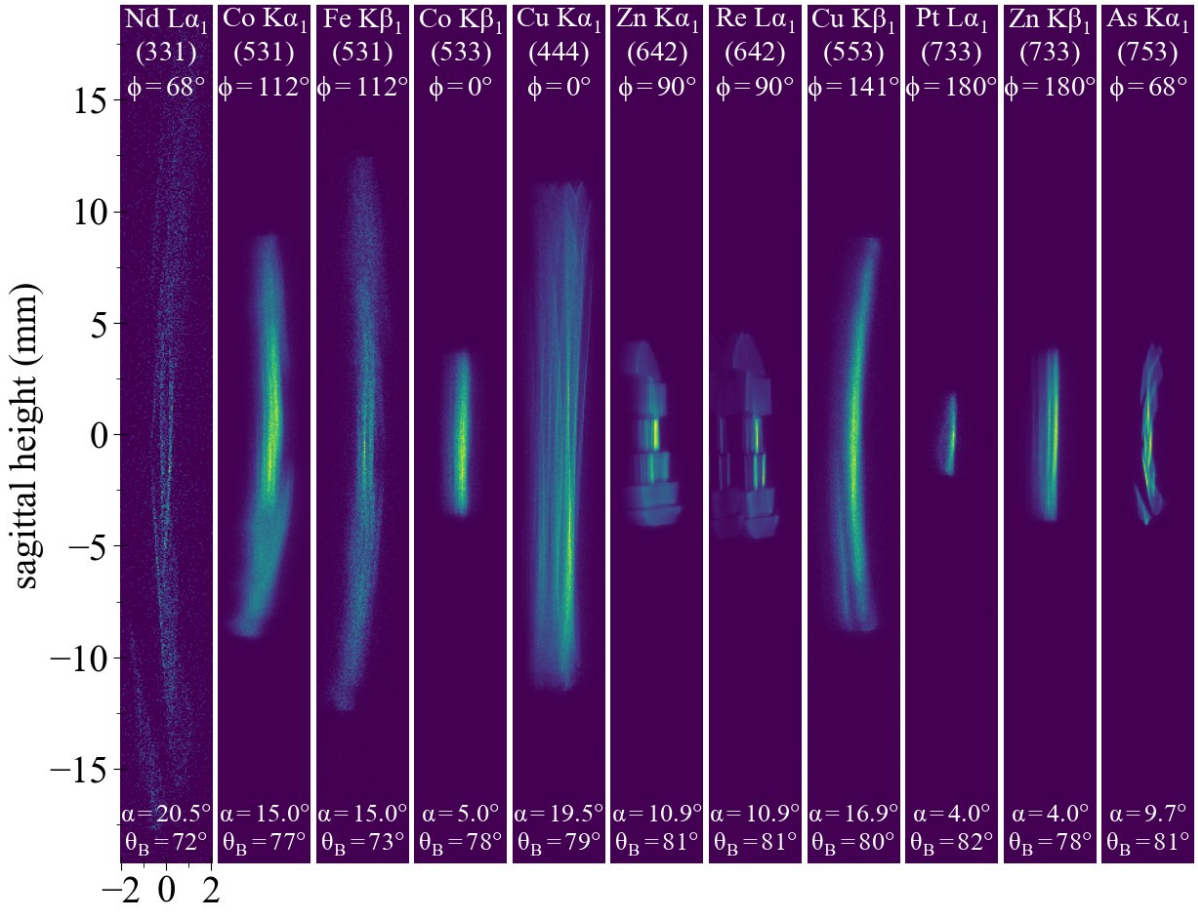

Figure 9. Corresponding sagittal foci at the corresponding to the measured *hkl*-hopped emission peaks of Figure 6. The $\mathbf{G}_{hkl}$ and Rowland circle parameters are annotated.

e. Asymmetric *hkl*-hopping HERFD

Next, given the large energy range provided by a single Si(211) optic for XES, it follows that HERFD measurements can be made with only motorized changes to the Rowland parameters. We assert that this high throughput multi-edge HERFD is both automatable and user trainable. A subset of K- and L_3-edge HERFD corresponding to some of the measured emission lines is shown in Figure 10. No changes in set-up besides swapping samples occurred between measurements. The higher resolution sharpening of HERFD spectra is demonstrated for all spectra.

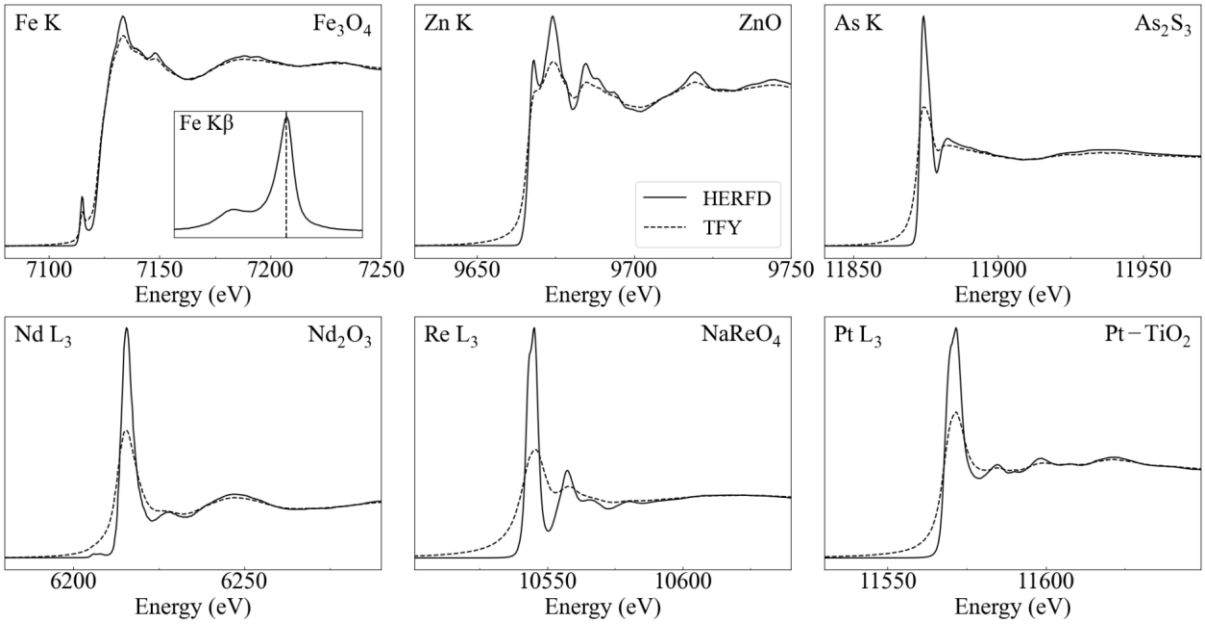

Figure 10. HERFD-XAS spectra overlaid on total-fluorescence yield (TFY) measurements, corresponding to the emission lines of Figure 5. The top row are K-edges, the bottom row L_3-edges. Spectra were measured with a single Si(211) analyzer asymmetrically. All HERFD emission channels were set to the $K_{\alpha 1}$ or $L_{\alpha 1}$ peaks except for Fe K set to $K_{\beta 1}$, shown inset.

We further demonstrate HERFD as a high-resolution fingerprinting technique sensitive to pre-edge features. Here, we compare Cu K-edge HERFD of Cu2O and CuO, shown in Figure 11. The changes in formal oxidation state result in shifts in the absorption edge. The sharpening effect of HERFD enables a better look at the pre-edge structure.

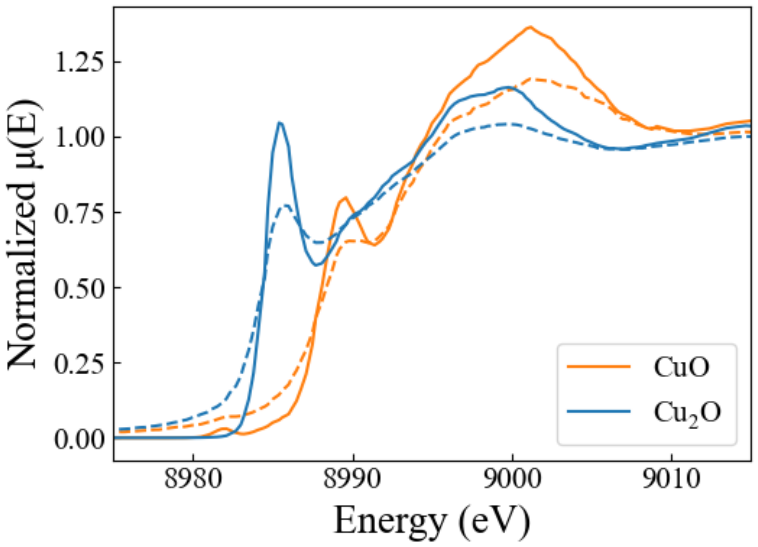

Figure 11. Asymmetrically measured HERFD of CuO and Cu_2O.

f. Applications at high energy (10 – 20 keV)

"High" energy x-ray spectroscopy is crucial for the study of actinide L-edges such as Pu, U, and Th. These species have initial to final state core-hole lifetime broadenings of 7 – 15 eV[33], thus HERFD is an important technique for obtaining high resolution spectra. We previously showed a nearly continuous *hkl*-hopped energy range above 10 keV, and purport this is generally true for any cut SBCA. As a result, any analyzer asymmetrically can be used for "high" energy x-ray spectroscopy if the energy resolution of the spectrometer/analyzer is sufficient.

We demonstrate this on 4d transition metal K-edges and K_α emissions serving as surrogates for actinide L-edges and emissions. Figure 12 shows an *hkl*-hopped study recording

the K_α XES, spectrometer resolution at the $K_{\alpha 1}$ peak, and the HERFD-XANES measurements of the Y, Zr, and Mo K-edges. The overall resolution ranges from 3.7 – 4.2 eV, which is suitable for enhancing the spectra of both 4d transition metal K-edges and actinide L-edges given their core-hole lifetime broadenings.

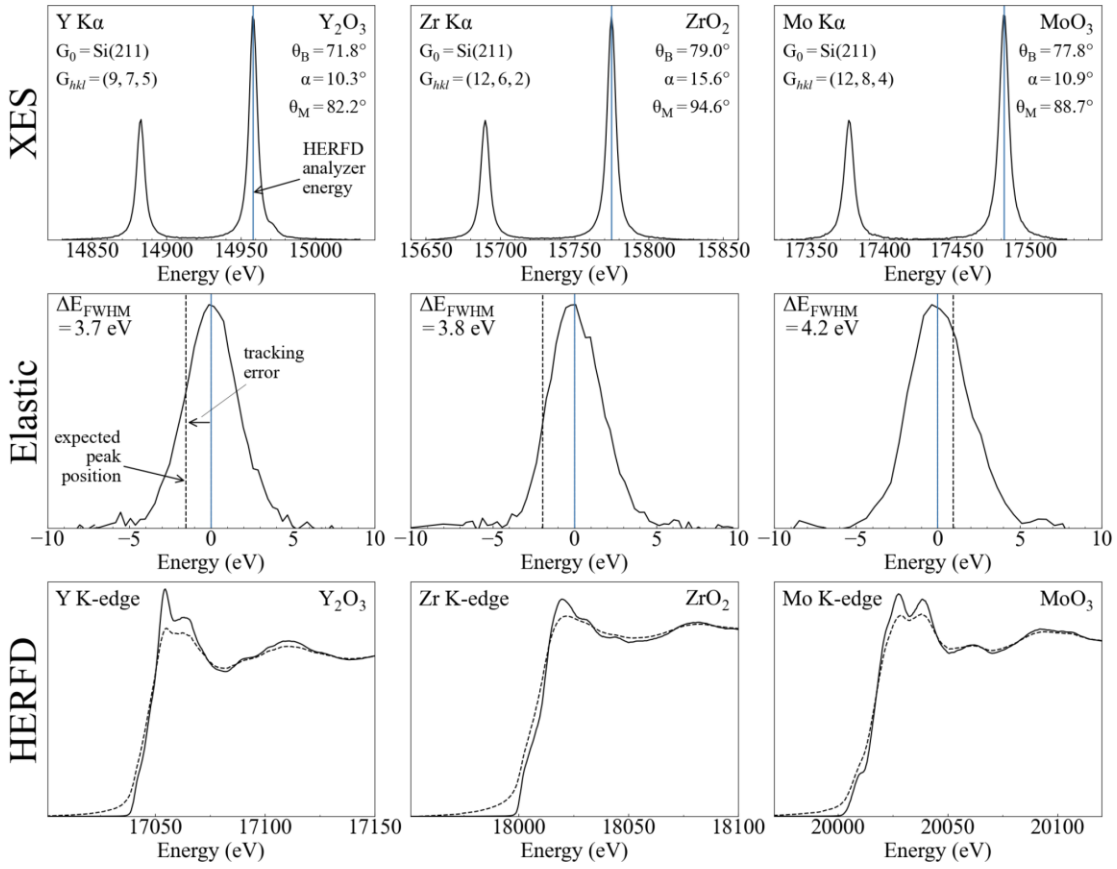

Figure 12. *hkl*-hopped measurements of K_α XES, spectrometer resolution, and HERFD of some 4d transition metal K-edges, serving as surrogates for actinide L-shell spectroscopy. All measurements used a single Si(211) analyzer asymmetrically.

7. Discussion and Outlook

An asymmetric Rowland spectrometer in tilt scan geometry with detector placement off-circle at the sagittal focus was commissioned for XES/HERFD measurements. We find many operational benefits afforded by asymmetric operation and this geometry. First, operating asymmetrically allows a massively expanded energy range of a single SBCA, which was demonstrated here from 5 – 20 keV measuring both XES and K- and L-edge HERFD. Operating this way, energy range coverage of, for example, we calculate that the first row 3d transition metal K-shell emission lines can be accomplished with a very small suite of two SBCAs compared to the many SBCAs required when only symmetric. Second, operating asymmetrically with a motorized azimuthal rotation stage enables automated *hkl*-hopping of a single optic from one reflection to another. This is both automatable and user trainable, so instrument scientists are not required if user science necessitates changing the analyzed emission line in a HERFD experiment, for example. It also poses HERFD as a rapid, dynamic spectroscopy technique for evolving science at the beamline. Third, we find generalize that any cut of SBCA is usable for X-ray analysis above 10 keV. At 17 keV, we report energy resolution of ~4 eV; we propose the entire range of 4d transition metal K-shell and actinide L-shell spectroscopy is feasible with a single SBCA of any cut in asymmetric geometry.

This presents an interesting avenue towards the future. A relatively low cost, single analyzer asymmetric spectrometer with as little as one unique SBCA in the optic suite can enable XES/HERFD of many emission lines at any hard (5 – 20 keV) X-ray beamline. Furthermore, pre-existing tilt geometry XES/HERFD spectrometers may be able to implement automated asymmetric operation with only the addition of an azimuthal rotation stage for the optic.

8. Acknowledgements

This research used resources of the Advanced Photon Source, an Office of Science User Facility operated for the U.S. Department of Energy (DOE) Office of Science by Argonne National Laboratory, and was supported by the U.S. DOE under Contract No. DE-AC02-06CH11357, and the Canadian Light Source and its funding partners.

9. References

1 U. Bergmann and P. Glatzel, *Photosynth. Res.*, 2009, **102**, 255–266.
2 K. Hamalainen, D. Siddons, J. Hastings and L. Berman, *Phys. Rev. Lett.*, 1991, **67**, 2850–2853.
3 H. Asakura and T. Tanaka, *Chem. Lett.*, 2021, **50**, 1075–1085.
4 F. M. F. de Groot, M. W. Haverkort, H. Elnaggar, A. Juhin, K.-J. Zhou and P. Glatzel, *Nat. Rev. Method. Prim.*, 2024, **4**, 45.
5 K. O. Kvashnina and S. M. Butorin, *Chem. Commun.*, 2022, **58**, 327–342.
6 W.-Q. Shi, L.-Y. Yuan, C.-Z. Wang, L. Wang, L. Mei, C.-L. Xiao, L. Zhang, Z.-J. Li, Y.-L. Zhao and Z.-F. Chai, *Adv. Mater.*, 2014, **26**, 7807–7848.
7 G. E. Cutsail and S. DeBeer, *ACS Catal.*, 2022, **12**, 5864–5886.
8 J. Singh, C. Lamberti and J. A. van Bokhoven, *Chem. Soc. Rev.*, 2010, **39**, 4754–4766.
9 K. Wojtaszek, K. Tyrala and E. Blonska-Sikora, *Appl. Sci.-Basel*, 2025, **15**, 10784.
10 A. T. Baker, G. N. George and H. H. Harris, *Metallomics*, 2025, **17**, mfaf038.
11 N. P. P. Edwards, J. R. R. Bargar, D. van Campen, A. van Veelen, D. Sokaras, U. Bergmann and S. M. M. Webb, *Rev. Sci. Instrum.*, 2022, **93**, 083101.
12 R. Verbeni, T. Pylkkänen, S. Huotari, L. Simonelli, G. Vankó, K. Martel, C. Henriquet and G. Monaco, *J Synchrotron Rad*, 2009, **16**, 469–476.
13 H. H. Johann, *Z. Physik*, 1931, **69**, 185–206.
14 R. Verbeni, M. Kocsis, S. Huotari, M. Krisch, G. Monaco, F. Sette and G. Vanko, *Journal of Physics and Chemistry of Solids*, 2005, **66**, 2299–2305.
15 J. F. Seely, E. Galtier, L. T. Hudson, A. Henins and U. Feldman, *Appl. Optics*, 2019, **58**, 5225–5232.
16 A. Bordage, M. Papai, N. S. Sas, J. Szlachetko, M. Nachtegaal and G. Vanko, *Phys. Chem. Chem. Phys.*, 2013, **15**, 11088–11098.
17 A. J. Gironda, J. E. Abramson, Y. Chen, M. Solovyev, G. E. Sterbinsky and G. T. Seidler, *J. Anal. At. Spectrom.*, 2024, **39**, 1375–1387.
18 J. E. Abramson, Y. Chen and G. T. Seidler, *J. Anal. At. Spectrom.*, 2025, **40**, 817–824.
19 Y. Chen, A. J. Gironda, Y. Shen, A. D. Taylor and G. T. Seidler, *J. Anal. At. Spectrom.*, 2025, **40**, 836–847.

20 B.-B. Mei, L.-X. Wang, S.-Q. Gu, X.-Z. Su, S. Zhang, Y. Wei, J.-Y. Ma, Z. Jiang and F. Song, *Nucl. Sci. Tech.*, 2024, **35**, 156.
21 P. Duan, S. Gu, H. Cao, J. Li and Y. Huang, *X-Ray Spectrom.*, 2017, **46**, 12–18.
22 I. Llorens, E. Lahera, W. Delnet, O. Proux, A. Braillard, J.-L. Hazemann, A. Prat, D. Testemale, Q. Dermigny, F. Gelebart, M. Morand, A. Shukla, N. Bardou, O. Ulrich, S. Arnaud, J.-F. Berar, N. Boudet, B. Caillot, P. Chaurand, J. Rose, E. Doelsch, P. Martin and P. L. Solari, *Rev. Sci. Instrum.*, 2012, **83**, 063104.
23 M. M. Sala, K. Martel, C. Henriquet, A. Al Zein, L. Simonelli, C. J. Sahle, H. Gonzalez, M.-C. Lagier, C. Ponchut, S. Huotari, R. Verbeni, M. Krisch and G. Monaco, *J. Synchrot. Radiat.*, 2018, **25**, 580–591.
24 K. O. Kvashnina and A. C. Scheinost, *J. Synchrot. Radiat.*, 2016, **23**, 836–841.
25 A. Tayal, D. S. Coburn, D. Abel, M. Rakitin, O. Ivashkevych, J. Wlodek, D. Wierzbicki, W. Xu, E. Nazaretski, E. Stavitskia and D. Leshcheva, *J. Synchrot. Radiat.*, 2024, **31**, 1609–1621.
26 E. Kleymenov, J. A. van Bokhoven, C. David, P. Glatzel, M. Janousch, R. Alonso-Mori, M. Studer, M. Willimann, A. Bergamaschi, B. Henrich and M. Nachtegaal, *Rev. Sci. Instrum.*, 2011, **82**, 065107.
27 J. M. Ablett, A. Berlioux, D. Prieur, J. Harrison, L. Heller, S. Gliga and J.-P. Rueff, *Rev. Sci. Instrum.*, 2025, **96**, 053104.
28 S. Hayama, R. Boada, J. Chaboy, A. Birt, G. Duller, L. Cahill, A. Freeman, M. Amboage, L. Keenan and S. Diaz-Moreno, *J. Phys.-Condes. Matter*, 2021, **33**, 284003.
29 P. Glatzel, A. Harris, P. Marion, M. Sikora, T.-C. Weng, C. Guilloud, S. Lafuerza, M. Rovezzi, B. Detlefs and L. Ducotte, *J. Synchrot. Radiat.*, 2021, **28**, 362–371.
30 M. M. Sala, K. Martel, C. Henriquet, A. Al Zein, L. Simonelli, C. J. Sahle, H. Gonzalez, M.-C. Lagier, C. Ponchut, S. Huotari, R. Verbeni, M. Krisch and G. Monaco, *J. Synchrot. Radiat.*, 2018, **25**, 580–591.
31 P. Suortti, T. Buslaps, P. Fajardo, V. Honkimäki, M. Kretzschmer, U. Lienert, J. E. McCarthy, M. Renier, A. Shukla, T. Tschentscher and T. Meinander, *J. Synchrot. Radiat.*, 1999, **6**, 69–80.
32 D. R. Mortensen and G. T. Seidler, *J. Electron Spectrosc. Relat. Phenom.*, 2017, **215**, 8–15.
33 M. Abbate, F. Al Shamma, J. C. Fuggle and J. E. Inglesfield, in *Unoccupied electronic states: fundamentals for XANES, EELS, IPS, and BIS*, Springer-Verlag, Berlin ;, 1992, pp. 339–351.

10. Supporting information

The following supporting information describes the prototype asymmetric spectrometer and beamline conditions used to acquire the data in Figure 7 of the results section, showing the effect of sliced SBCAs on the meridional and sagittal focus and circle of least confusion.

a. Spectrometer Design and Rowland Circle Geometry

The asymmetric prototype spectrometer was designed to function in a table scan geometry as opposed to the reported tilt scan geometry in the main article. The key feature of the table scan is the detector at the meridional focus is always vertically aligned above the sample. We found this could be accomplished by use of a "wedge" beneath the SBCA assembly. When working at a particular α in relation to the wedge angle, the detector at the meridional focus was vertically in line above the source and only translated vertically as θ_B is scanned. This table scan equivalent trajectory is only true at one value of α relating to the wedge angle, which we will now describe.

A schematic of a single module is shown in Figure 13 at an arbitrary wedge angle (i.e., not the special case approximating the table scan kinematics simply). The wedge angle, β, rotates the Rowland circle. It is evident that at a particular β, the meridional focus and detector position 'D' will align vertically with the source position, 'S'. As in the symmetric case, the table is motorized up and down (z*, Huber 5103.A20-90), but uniquely here the in/out motorization (x*, Velmex Xslide) is at an angle, corresponding to β. The analyzer is mounted on a motorized azimuthal rotation stage (ϕ, Velmex B5990TS) for asymmetric operation.

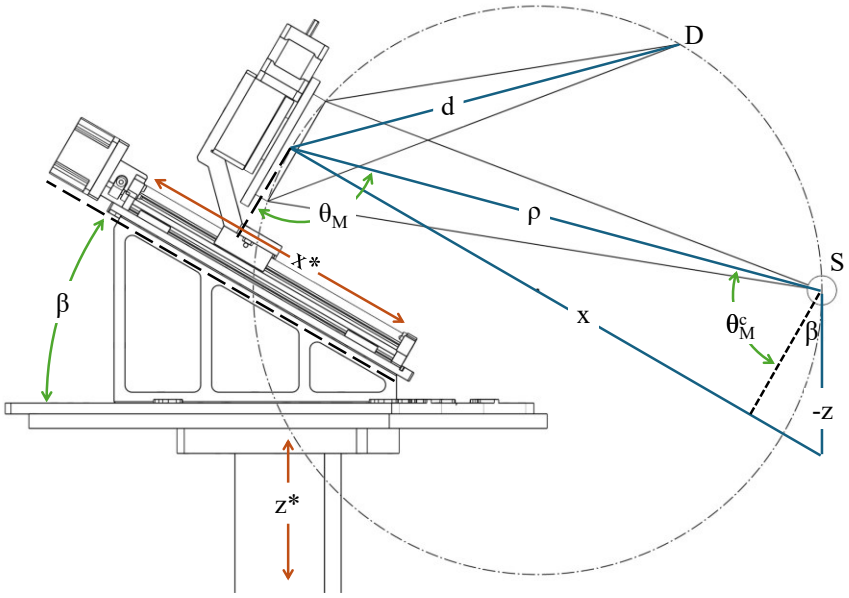

Figure 13. Diagram of the asymmetric "wedge" Rowland geometry spectrometer at an arbitrary α.

Like the symmetric case, with only two motors for the SBCA position the spectrometer can scan continuously through Bragg angle. The z and x distances, with a proper offset, correspond to motor positions in x* and z*. Analyzed photon energy, and thus θ_B, depend on θ_M and α. The kinematics are described by

$$z = \frac{\rho \cos \theta_M}{\cos \beta} \tag{S1}$$

$$x = -z \sin \beta + \rho \sin \theta_M \tag{S2}$$

$$\theta_M = \cot^{-1}\left(\frac{z \cos \beta}{x + z \sin \beta}\right) \tag{S3}$$

$$\theta_B = \theta_M - \alpha \tag{S4}$$

In the special condition where $2\alpha = \beta$, the detector position at the SBCA focus is vertical above the source across all Bragg angles, and the simple table scan kinematics from the symmetric case

are regained with the asymmetric geometry. However, in the case of the designed prototype, β was fixed, and thus enforced always working at asymmetries close to the condition $2\alpha = \beta$. When $2\alpha \neq \beta$, even when at JNA, the meridional detector trajectory became complex. The trajectories at different θ_B as a function of α and a fixed β are shown in Figure S2.

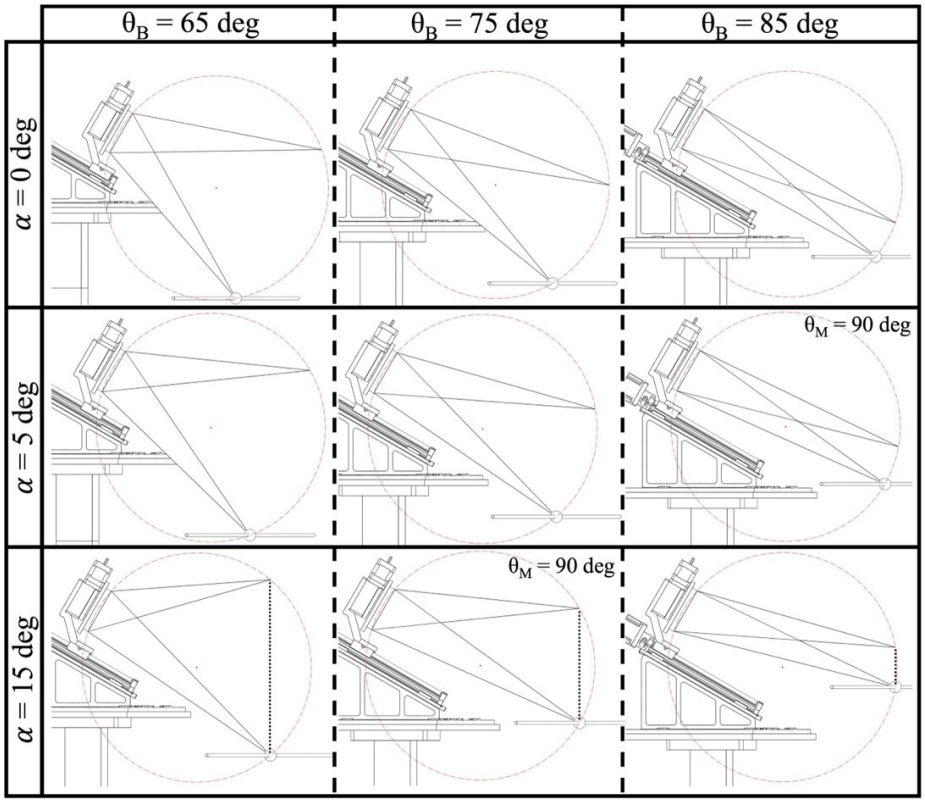

Figure 14. Rowland circle configurations for symmetric and asymmetric spectrometer operation with $\beta = 30^o$. Note the special configuration of the third row when $2\alpha = \beta$, source and detector positions remain vertically in line at any θ_B.

b. Methods

The beamline layout, operating conditions, and performance were identical to that described in the main article, with the exception of the beam dimensions. Here, the beam spot on the sample was 10 (V) x 50 (H) μm^2. The sample used for the images was an SiO2 fused quartz microscope slide at a 45^o angle to the beam.

c. Measurement

The sample layout and Rowland circle parameters are described in Figure S3. The analyzer used was a sliced Si(100) SBCA with the (711) family of reflections, which were oriented 90^o apart in ϕ and were parallel/perpendicular to the slices of the optic. The Rowland circle was configured to be at JNA, setting the analyzed energy to be 8318 eV. The monochromator was set to 8318 eV, so the images collected were composed of elastic scatter. The detector was translated parallel to the incident rays from inside the Rowland circle to behind the sagittal focus to capture images. The detector was always at normal incidence to the analyzed rays, so no smearing / image distortions occurred from detector orientation.

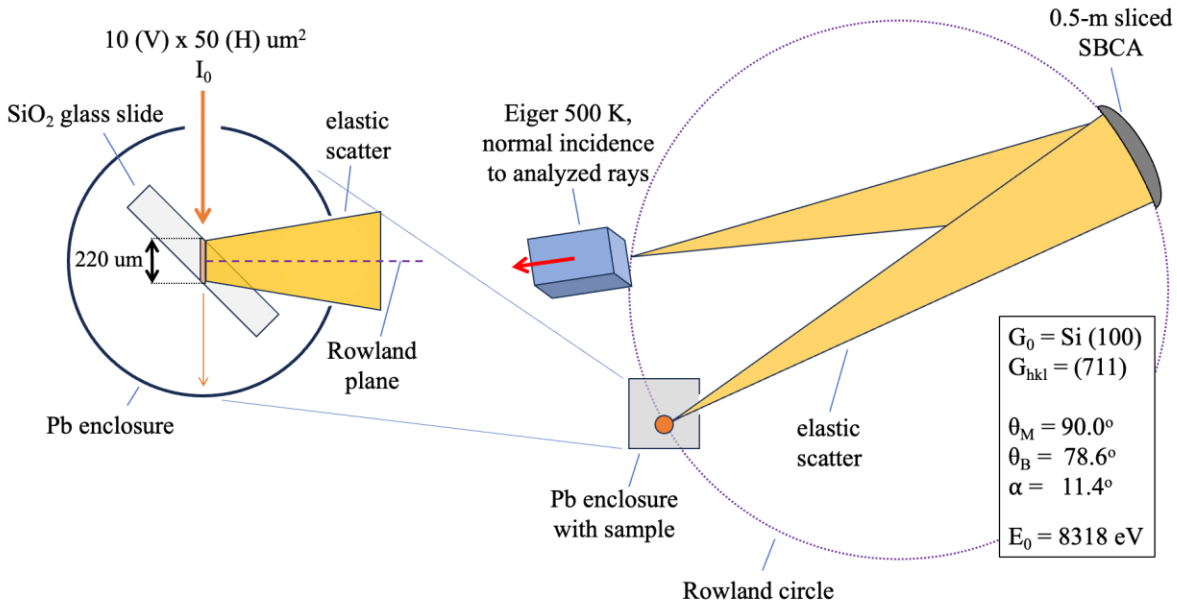

Figure 15. Rowland circle parameters and sample description for the slice orientation study. Note, the optic used was Si(100).